Quantum Teleportation and Efficient Process Verification with Superconducting Circuits

Lars Steffen

DISS. ETH NO. 21517

Quantum Teleportation and Efficient Process Verification with Superconducting Circuits

A dissertation submitted to

ETH ZURICH

for the degree of

Doctor of Sciences

presented by

Lars Steffen

Dipl. Phys., ETH Zurich

born July 29, 1983

citizen of Bellikon AG, Switzerland

accepted on the recommendation of

Prof. Dr. Andreas Wallraff, examiner
Prof. Dr. Leonardo DiCarlo, co-examiner

2013

Cover image: Detail of the photolithography mask with the chip designs for the teleportation experiment. Credits: Marek Pechal (photography), Arjan van Loo (technical equipment), Lars Steffen (editing)

Abstract

Quantum information processing has long been a field in which progress has been made mostly on its theoretical aspects. In the last decades, however, superconducting circuits have proven to be a promising candidate for the implementation of a scalable quantum information processing architecture.

In this thesis, several quantum information processing experiments with superconducting circuits are demonstrated. In order to perform quantum experiments with superconducting circuits, a setup is needed that protects the circuits from uncontrolled interactions with their environment, while still allowing to manipulate and measure the quantum state. The setup, as well as the design and fabrication of chips containing such circuits are discussed.

The building blocks of every quantum algorithm are quantum gates. We demonstrate and characterize several gates, including our realization of the Toffoli gate. This is a three-qubit gate that can be used to implement universal quantum computing and is an important part in quantum error correcting schemes.

The standard method for characterizing quantum gates and processes is known as quantum process tomography. However, with increasing system size, quantum process tomography becomes infeasible. The number of experiments to be performed as well as the computational cost for post-processing the experimental data increases exponentially with the number of qubits. In this thesis, an alternative approach known as Monte Carlo process certification is implemented on different two- and three-qubit gates and compared to quantum process tomography.

In the final part of the thesis, the implementation of quantum teleportation in superconducting circuits is discussed. Quantum teleportation is an algorithm which transfers an unknown quantum state between two parties without transferring the physical carrier of information itself. For the realization of this experiment, the setup has been extended with quantum limited amplifiers allowing to faithfully measure the qubit state in every single experiment and feed-forward electronics performing operations on a qubit based on measurement outcomes analyzed in real-time. This realization constitutes the first implementation of the complete teleportation protocol in any solid-state system and shows the highest rate of successful teleportation events observed so far in any system.

The presented results demonstrate the power of the superconducting circuit architecture for quantum information processing applications and constitute a small step further along the way of realizing a quantum computer.

Zusammenfassung

Quanteninformationsverarbeitung war lange ein Forschungsgebiet, auf dem der Fortschritt hauptsächlich theoretischer Natur war. Innerhalb der letzten Jahrzehnte haben sich jedoch supraleitende Schaltkreise als potentielle Kandidaten erwiesen, um eine skalierbare Architektur zur Quanteninformationsverarbeitung zu realisieren.

In dieser Abhandlung werden verschiedene Experimente aus dem Gebiet der Quanteninformationsverarbeitung mit supraleitenden Schaltkreisen vorgestellt. Um Experimente durchzuführen, welche erlauben Quanteneffekte in supraleitenden Schaltkreisen zu beobachten und zu kontrollieren, wird ein spezieller Messaufbau benötigt. Dieser muss einerseits die Schaltkreise von unkontrollierten Wechselwirkungen mit der Umgebung abschirmen, andererseits aber auch das Manipulieren und Auslesen der Quantenzustände erlauben. Der Messaufbau und das Design sowie die Herstellung von Chips mit supraleitenden Schaltkreisen werden in dieser Abhandlung diskutiert.

Die Grundbausteine jedes Quantenalgorithmus sind die Quantengatter. In dieser Abhandlung werden verschiedene Quantengatter in supraleitenden Schaltkreisen realisiert und charakterisiert, unter anderem auch unsere Implementation des Toffoli-Gatters. Dieses Gatter wirkt auf drei Quantenbits. Es bildet die Grundlage für universelle Berechenbarkeit im quantenmechanischen Sinne und ist ein wichtiges Element in der Quantenfehlerkorrektur.

Quantenprozess-Tomographie ist die herkömliche Methode, um Quantengatter und Quantenprozesse zu charakterisieren. Diese Methode wird allerdings undurchführbar bei wachsender Systemgrösse. Die Anzahl Experimente, die durchgeführt werden müssen und auch die für die Nachbearbeitung nötige Rechenleistung steigt exponentiell mit der Anzahl involvierter Quantenbits. In dieser Abhandlung wird eine alternative Methode, Monte Carlo Quantenprozess-Zertifizierung, implementiert. Verschiedene Quantengatter werden mit dieser Methode und mit Quantenprozess-Tomographie charakterisiert und die Resulate miteinander verglichen.

Im letzten Teil der Abhandlung wird die Implementierung von Quantenteleportation mit supraleitenden Schaltkreisen diskutiert. Quantenteleportation erlaubt den Transfer eines unbekannten Quantenzustandes zwischen einem Sender und einem Empfänger, ohne dass dabei der physikalisch Informationsträger selbst übermittelt werden muss. Um dieses Experiment zu

realisieren wurde der Messaufbau erweitert. Quantenlimitierte Verstärker erlauben das genaue Auslesen der Quantenbits bei jeder Einzelmessung und eine vorwärtsgekoppelte Regelung kontrolliert den Zustand der Quantenbits aufgrund von Messresultaten, die in Echtzeit ausgewertet werden. Diese Realisierung der kompletten Quantenteleportation ist die erste überhaupt in einem Festkörpersystem und weist die höchste Rate an erfolgreichen Telepontationsereignissen auf, die bis anhin gemessen wurde.

Die vorliegenden Resultate demonstrieren das Potential von supraleitenden Schaltkreisen für die Anwendung im Bereich der Quanteninformationsverarbeitung. Die Arbeit ist ein kleiner Schritt auf dem Weg zur Realisierung eines Quantencomputers.

Contents

1

Introduction

Quantum phenomena do not occur in a Hilbert space. They occur in a laboratory.

— Asher Peres in *Quantum theory: concepts and methods*, p. 373

The field of quantum information and quantum computing [Nielsen00] emerged in the second half of the 20$^{\text{th}}$ century. During the time when Bell's inequalities [Bell64] were studied in detail, the point of view on quantum systems underwent a change. They were no longer just considered as systems given by nature, whose properties can be studied and explained. But the possibility of designing and manipulating quantum systems was explored. This led to a proposal on how to test the predictions of quantum mechanics [Clauser69] and in the following, first experiments using polarization states of photons have been performed and refined [Freedman72, Aspect82], demonstrating the validity of quantum mechanical predictions.

In 1982, Feynman [Feynman82] published the first idea on how to use quantum systems to solve problems efficiently. He proposed to use quantum systems to simulate other quantum systems, since this cannot be done efficiently on a classical computer. Three years later, Deutsch [Deutsch85] described and investigated the properties of a "universal quantum computer".

A major step in the field of quantum information processing was the discovery of quantum key distribution [Bennett84] in 1984. This is a protocol allowing to distribute a key which can be used for encryption in a provably secure way. The protocol demonstrated the possibility to use the property of quantum entanglement in order to solve a problem (i.e. secure key distribution) which cannot be solved with classical resources.

In the following years, huge progress has been made on the theoretical aspects of the field of quantum information and computing. In 1992, Deutsch and Josza [Deutsch92] described a "problem which can be solved more efficiently by a quantum computer than by any classical computer". The presented algorithm can solve this particular problem always exponentially faster on a quantum computer than on a deterministic classical computer. However, although the problem is a nice example of quantum speed-up, it is of low practical relevance. This changed when Shor [Shor94] presented an algorithm which allows to factorize large numbers in polynomial time on a quantum computer and Grover [Grover96] described how quantum computers could be used to search entries in a large database faster than any classical computer. Especially Shor's algorithm had a great impact, since the security of one of the most frequently used cryptographic algorithms (RSA [Rivest78]) depends on the fact that the factorization of large numbers is a computationally hard task on a classical computer.

In the year 2000, Nielsen and Chuang [Nielsen00] published their famous book about quantum information and quantum computing. At that time, the book gave an almost complete overview of the field, "bringing readers near to the forefront of research". Since then, a lot of progress has been made in the field. But the most impressive progress is probably the one made on the *experimental* side. Various different implementations of quantum bits [Schumacher95] – quantum mechanical two-level systems which form the basic unit of quantum information – have been realized and quantum gates and algorithms demonstrated.

Amongst these implementations are such diverse systems [Ladd10] as the polarization states of single photons [Kok07], electronic states in Rydberg atoms [Saffman10] or trapped ions [Häffner08, Duan10, Monroe13], nuclear spins used in NMR experiments [Vandersypen04], quantum dots in solids [Hanson07, Awschalom13], electron spins in point defects of diamonds [Bernien13] and superconducting circuits [Clarke08, Devoret13].

The latter one – superconducting circuits – is the system used for the

experiments presented in this thesis. Quantum information processing with superconducting circuits has made tremendous progress in the last few years. Since the first spectroscopic measurement of a superconducting qubit in 1997 [Nakamura97], the lifetime of a single qubit was increased about four orders of magnitude – from a few nanoseconds to the order of 100 µs [Rigetti12] within 15 years! An important step was the adoption of cavity QED [Dutra05, Haroche06] – where an atom is strongly coupled to the electromagnetic field inside an optical cavity – to the field of superconducting circuits in a realization called circuit QED [Blais04, Wallraff04]. Coupling superconducting qubits to superconducting microwave resonators not only protects the qubit from decaying quickly but also offers the possibility to read out the qubit states [Bianchetti09, Filipp09] and couple several qubits [Majer07]. Today, several labs around the world perform experiments with multiple superconducting qubits [Reed12, Lucero12, Ristè13, Dewes12, Chow12, Steffen13], step-by-step approaching the realization of a real quantum computer [Devoret13].

Outline of the thesis

This thesis is a contribution to the steadily proceeding field of quantum information processing with superconducting circuits. It is organized as follows: Chap. 2 serves as an overview over the basic concepts of quantum information processing and superconducting circuits. At first it introduces the concepts of quantum information, quantum gates and algorithms. In a second part superconducting circuits are described with a focus on the transmon qubit and coplanar waveguide resonators. A significant part of the work performed in the course of this thesis consists in designing and fabricating these circuits which is the topic of Chap. 3. Once the circuits are fabricated they have to be characterized and measured. In Chap. 4 the setup which was used to perform the experiments for this thesis is described. This setup also allows to control and manipulate the quantum states of our circuits as explained in Chap. 5. The implemented quantum states and processes can be characterized in different ways as shown in Chap. 6. Since the complete characterization of a quantum process is an inefficient task, i.e. the time needed scales exponentially with the number of qubits, a way to efficiently verify a process will become important in the future. Such

a method, called Monte Carlo process certification, has been implemented in the course of this thesis for the first time in any quantum system. The method and its implementation is the main topic of Chap. 7. It is tested on different two- and three-qubit gates, including our realization of the three-qubit Toffoli gate. Chap. 8 describes our implementation of the quantum teleportation protocol which is the first realization of this algorithm in any solid-state system. Finally, Chap. 9 gives a short outlook on the topic of quantum information processing with superconducting circuits.

2

Quantum information processing with superconducting circuits

This chapter gives an introduction into the concepts which this thesis is built upon. In the first section the basic knowledge about quantum information and quantum computation is summarized. The two subsequent sections introduce the physical system used to realize the experiments presented in this thesis: Superconducting transmon qubits in a circuit quantum electrodynamics setup.

2.1. Quantum information and algorithms

In this section a summary of the basic concepts of the vast topic of quantum information and quantum computing is presented. The quantum bit, the fundamental unit of quantum information is introduced followed by a discussion of single- and multi-qubit operations, which play an important role in this thesis. As a profound introduction into the topic I can recommend the excellent book of Nielsen and Chuang [Nielsen00], which most of this section is based on.

2.1.1. Quantum bit

The fundamental unit of information in classical computation is a binary digit (*bit*). The only property of a bit is its *state*. There are only two different states – usually referred to as 0 and 1 – a bit can have. A *quantum*

bit, or *qubit*, is an analogous concept in the framework of quantum computation. It can be in a state $|0\rangle$ or $|1\rangle$, but moreover, it can also be in any superposition of these states: $|\psi\rangle = \alpha\,|0\rangle + \beta\,|1\rangle$, where α and β are complex numbers. However, such a superposition state is not directly measurable. If a measurement is performed, the result will be either 0 with probability $|\alpha|^2$, or 1 with probability $|\beta|^2$. Since the two probabilities sum up to 1, the coefficients α and β have to fulfill the condition $|\alpha|^2 + |\beta|^2 = 1$. This allows to rewrite the state of a qubit as

$$|\psi\rangle = e^{i\gamma}\left(\cos\frac{\theta}{2}\,|0\rangle + e^{i\varphi}\sin\frac{\theta}{2}\,|1\rangle\right),$$

where θ, φ and γ are real numbers. Since the global phase factor $e^{i\gamma}$ has no observable effects, i.e. no physical meaning, it can be omitted such that the prefactor of $|0\rangle$ is always real:

$$|\psi\rangle = \cos\frac{\theta}{2}\,|0\rangle + e^{i\varphi}\sin\frac{\theta}{2}\,|1\rangle\,. \tag{2.1}$$

The two real numbers θ and φ defining the state of a qubit can be interpreted as the spherical coordinates of a point on a sphere, the *Bloch sphere*, as depicted in Fig. 2.1 (a). The $|0\rangle$ state is represented by the point on the north pole, the $|1\rangle$ state by the point on the south pole. These two states are the most common basis states for describing qubits. Other frequently used bases are the pairs of states $\{|+\rangle, |-\rangle\} = 1/\sqrt{2}\,\{|0\rangle + |1\rangle, |0\rangle - |1\rangle\}$ and $\{|i\rangle, |-i\rangle\} = 1/\sqrt{2}\,\{|0\rangle + i\,|1\rangle, |0\rangle - i\,|1\rangle\}$, which represent the states lying on the x- and y-axis respectively, see Fig. 2.1 (b). These three basis pairs are an example of mutually unbiased basis states [Ivanović81, Bengtsson06], since for each of these states, all outcomes of measurements in one of the other bases occurs with equal probability.

2.1.2. Single-qubit gates

In the Bloch sphere picture, every operation (or *gate*) on a single qubit can be interpreted as a rotation around an axis of the sphere. As an example, consider the operation depicted in Fig. 2.2 (a) where the initial state $|1\rangle$ is rotated by an angle $\pi/2$ around the x-axis and ends up along the y-axis in the state $|i\rangle$.

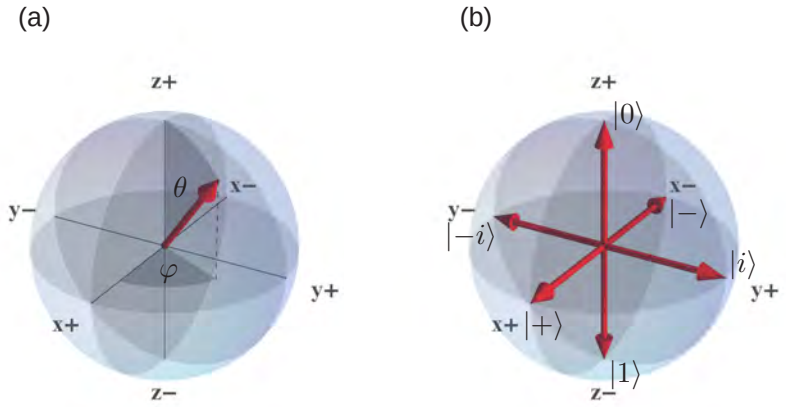

Figure 2.1: (a) Graphical representation of a single qubit quantum state $|\psi\rangle$ on the Bloch sphere. (b) The positions of the six standard mutually unbiased basis states $|0\rangle$, $|1\rangle$, $|+\rangle$, $|-\rangle$, $|i\rangle$, and $|-i\rangle$ are indicated.

Mathematically, quantum states can also be represented as vectors and operations as matrices. The state $|\psi\rangle = \alpha\,|0\rangle + \beta\,|1\rangle$ is then written as

$$\begin{bmatrix} \alpha \\ \beta \end{bmatrix}.$$

Since operations on single qubits can be described as unitary 2×2 matrices, the above example reads as follows:

$$\underbrace{\frac{1}{\sqrt{2}}\begin{bmatrix} 1 & -i \\ -i & 1 \end{bmatrix}}_{R_x^{\pi/2}} \underbrace{\begin{bmatrix} 0 \\ 1 \end{bmatrix}}_{|1\rangle} = \underbrace{\frac{1}{\sqrt{2}}\begin{bmatrix} -i \\ 1 \end{bmatrix}}_{|i\rangle} \mathrel{\widehat{=}} \underbrace{\frac{1}{\sqrt{2}}\begin{bmatrix} 1 \\ i \end{bmatrix}}_{|i\rangle},$$

where the last equivalence is due to the irrelevant global phase factor.

In analogy to classical logic circuits, *quantum circuits* can also be depicted as wire diagrams. The circuit of the above example looks as follows:

$$|1\rangle \;\text{—}\boxed{R_x^{\pi/2}}\text{—}\; |i\rangle$$

In general, rotations around the different axes can be expressed in the following way:

$$
\begin{aligned}
-\boxed{R_x^\theta}- &= e^{-i\frac{\theta}{2}\hat{\sigma}_x} = \begin{bmatrix} \cos\frac{\theta}{2} & -i\sin\frac{\theta}{2} \\ i\sin\frac{\theta}{2} & \cos\frac{\theta}{2} \end{bmatrix}, \\
-\boxed{R_y^\theta}- &= e^{-i\frac{\theta}{2}\hat{\sigma}_y} = \begin{bmatrix} \cos\frac{\theta}{2} & \sin\frac{\theta}{2} \\ \sin\frac{\theta}{2} & \cos\frac{\theta}{2} \end{bmatrix}, \\
-\boxed{R_z^\theta}- &= e^{-i\frac{\theta}{2}\hat{\sigma}_z} = \begin{bmatrix} e^{-i\theta/2} & 0 \\ 0 & e^{i\theta/2} \end{bmatrix},
\end{aligned}
$$

where $\hat{\sigma}_{x,y,z}$ are the Pauli matrices. The Pauli matrices themselves are also important single-qubit gates, since they are equivalent to π-rotations around the corresponding axis:

$$
\begin{aligned}
-\boxed{X}- &= \hat{\sigma}_x = \begin{bmatrix} 0 & 1 \\ 1 & 0 \end{bmatrix}, \\
-\boxed{Y}- &= \hat{\sigma}_y = \begin{bmatrix} 0 & -i \\ i & 0 \end{bmatrix}, \\
-\boxed{Z}- &= \hat{\sigma}_z = \begin{bmatrix} 1 & 0 \\ 0 & -1 \end{bmatrix}.
\end{aligned}
$$

Moreover, *every* single qubit operation (which is nothing else than a rotation around an arbitrary axis with an arbitrary angle) can be decomposed as a series of rotations around the z- and x-axis in the form $R_z^\alpha R_x^\beta R_z^\gamma$.

The last important single-qubit gate which is introduced in this section is the *Hadamard* gate,

$$
-\boxed{H}- = \frac{1}{\sqrt{2}} \begin{bmatrix} 1 & 1 \\ 1 & -1 \end{bmatrix}.
$$

In terms of rotations on the Bloch sphere, this gate corresponds to a π-rotation around the axis defined by the points $(0,0,0)$ and $(1,0,1)$, see Fig. 2.2 (b). Its importance comes from the fact that it acts as a *basis-changing* gate which transfers the states $|0\rangle$ and $|1\rangle$ to the states $|+\rangle$ and $|-\rangle$, respectively and vice-versa. A state $|\psi\rangle = \alpha|0\rangle + \beta|1\rangle$ is transformed by the Hadamard gate to the state $H|\psi\rangle = \alpha|+\rangle + \beta|-\rangle$, with the same

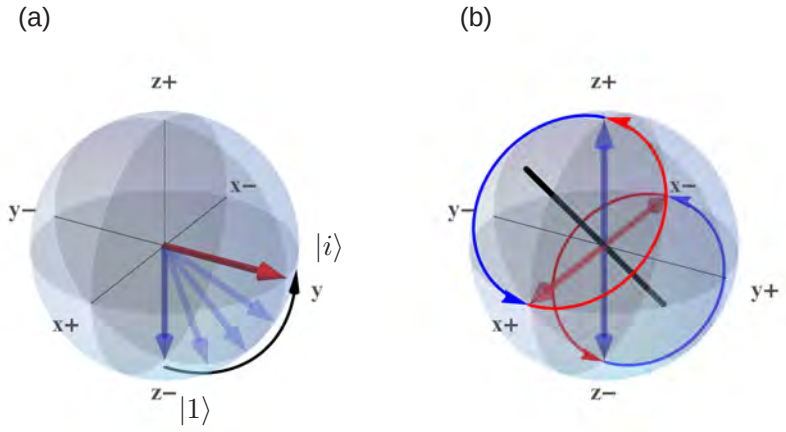

Figure 2.2: (a) Single-qubit operations can be interpreted as rotations on the Bloch sphere. (b) Action of the Hadamard gate which transforms (blue curved arrows) the $|0\rangle$ and $|1\rangle$ states (blue straight arrows) to the $|+\rangle$ and $|-\rangle$ states (red straight arrows) and vice-versa (red curved arrows). The thick black line represents the rotation axis.

coefficients α and β, but a different basis. This will become important in the discussion about the use of this gate in experiments. Like every ideal π-rotation, applying the Hadamard gate twice in series compensates its effect and leaves the state unchanged (i.e. $H^2 = \mathbb{1}$).

2.1.3. Multi-qubit gates and algorithms

An n-qubit state is the tensor product of n single-qubit states: $|\psi\rangle = |\psi_1\rangle \otimes \cdots \otimes |\psi_n\rangle$. A vector describing the state of an n-qubit system contains 2^n entries defining the complex probability amplitudes $\alpha_0, \ldots, \alpha_{2^n-1}$ of a set of basis states. In the context of qubits, one usually writes a state in the *computational basis* consisting of all 2^n possible combinations of states where qubit i is either in the ground or the excited state. In this case a state vector contains the probability amplitudes in binary order as follows:

$$\begin{matrix} |0\cdots00\rangle \\ |0\cdots01\rangle \\ \vdots \\ |1\cdots11\rangle \end{matrix}\begin{bmatrix} \alpha_0 \\ \alpha_1 \\ \vdots \\ \alpha_{2^n-1} \end{bmatrix}$$

Processes can be represented as unitary $2^n \times 2^n$ matrices describing how a given input basis state is transformed to an output combination of basis states.

The controlled-NOT or CNOT gate is one of the most fundamental two-qubit gates. Its importance comes from the fact that it forms together with arbitrary single qubit operations a universal set of gates. This means that all multi-qubit gates can be decomposed in a sequence of single-qubit gates and CNOT gates. The CNOT gate acts on two qubits, a control qubit and a target qubit. During the action of the CNOT gate, the state of the target qubit is flipped if the control qubit is in state 1. Otherwise, if the state of the control qubit is 0, the target qubit is left unchanged. The circuit symbol and the unitary 4×4 matrix representing the CNOT gate are

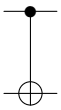

$$= \begin{bmatrix} 1 & 0 & 0 & 0 \\ 0 & 1 & 0 & 0 \\ 0 & 0 & 0 & 1 \\ 0 & 0 & 1 & 0 \end{bmatrix},$$

where $\bullet$ stands for the control qubit and $\oplus$ for the target qubit. It is interesting to note that the unitary matrix of the gate can also be seen as the classical *truth table* describing the action of the gate on the computational basis states $|00\rangle, |01\rangle, |10\rangle$, and $|11\rangle$.

Another important two-qubit gate is the controlled-PHASE (or CPHASE) gate, since it is locally equivalent to a CNOT gate (see below). It flips the phase of the two-qubit state if both qubits are in the state 1. Since both qubits act as control qubits and from all computational basis states it only modifies the $|11\rangle$ state, its circuit symbol and matrix representation are defined as follows:

$$= \begin{bmatrix} 1 & 0 & 0 & 0 \\ 0 & 1 & 0 & 0 \\ 0 & 0 & 1 & 0 \\ 0 & 0 & 0 & -1 \end{bmatrix}.$$

The action of the CPHASE gate is particularly interesting, if the input state of the first qubit is in the $|1\rangle$ state and the second qubit is $|+\rangle$ or $|-\rangle$, i.e. either $|1+\rangle = 1/\sqrt{2}(|10\rangle+|11\rangle)$ or $|1-\rangle = 1/\sqrt{2}(|10\rangle-|11\rangle)$. In this case, the CPHASE gate just switches the $|1+\rangle$ and the $|1-\rangle$ states, acting effectively as a CNOT gate with the control qubit in the $\{|0\rangle, |1\rangle\}$-basis and the target qubit in the $\{|+\rangle, |-\rangle\}$-basis. Since a Hadamard gate can be used to switch from the computational basis to the $\{|+\rangle, |-\rangle\}$-basis (see Sec. 2.1.2), the CNOT gate can be decomposed into a Hadamard gate, changing the basis of the target qubit, a CPHASE gate acting as CNOT gate on the new basis, and a final Hadamard gate to change back to the computational basis as follows:

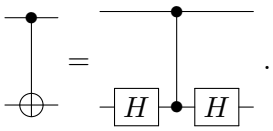

Finally, an example of a three-qubit gate is discussed, namely the Toffoli gate, which has been implemented as part of this thesis (see Sec. 7.2):

$$\begin{bmatrix} 1 & 0 & 0 & 0 & 0 & 0 & 0 & 0 \\ 0 & 1 & 0 & 0 & 0 & 0 & 0 & 0 \\ 0 & 0 & 1 & 0 & 0 & 0 & 0 & 0 \\ 0 & 0 & 0 & 1 & 0 & 0 & 0 & 0 \\ 0 & 0 & 0 & 0 & 1 & 0 & 0 & 0 \\ 0 & 0 & 0 & 0 & 0 & 1 & 0 & 0 \\ 0 & 0 & 0 & 0 & 0 & 0 & 0 & 1 \\ 0 & 0 & 0 & 0 & 0 & 0 & 1 & 0 \end{bmatrix}.$$

It acts as a controlled-controlled-NOT (or CCNOT) gate, since it flips the state of a target qubit if and only if both of the control qubits are in the state $|1\rangle$. It is an important gate in classical computing where it enables reversible computation as well as in quantum computing, since together with the Hadamard gate it forms a set of universal gates [Shi03]. Our implementation in superconducting circuits is discussed in detail in Sec. 7.2.

2.2. Superconducting transmon qubits

In the previous section we have described a number of basic conceptional aspects of qubits. Real experiments however, request for real physical im-

plementations of qubits that are controllable and measurable. This section introduces the physical realization of qubits used for the experiments presented in this thesis, the superconducting transmon qubit. After a brief overview of the field of superconducting circuits, inspired by [Clarke08], the most relevant properties of the transmon qubit are explained, closely following [Koch07].

2.2.1. Superconducting qubits

It is an remarkable fact that macroscopic structures can show quantum mechanical behavior, known normally only from atomic-scale structures. The reason is that all the Cooper pairs in a given superconductor are condensed into a single macroscopic state described by one wavefunction. This leads to the quantization of the magnetic flux Φ through a superconducting loop and a phenomenon called Josephson tunneling [Josephson62, Josephson74]: Cooper pairs can tunnel coherently through a barrier (a small insulating layer) between two superconductors, a so-called *Josephson junction*. The two relevant quantum mechanical variables for a Josephson junction are the difference between the phases of the two superconductors $\hat{\varphi}$ (which is associated with the Josephson coupling energy E_J) and the Cooper pair number difference $\hat{n}$ across the capacitance formed by the junction (associated with the charging energy E_C).

The field of superconducting qubits [Clarke08] emerged in the 1980's with the observation of the first signs of quantum behavior in Josephson junctions, namely macroscopic quantum tunneling [Voss81, Devoret85] and energy level quantization [Martinis85]. The "birth" of superconducting qubits is marked by the experiments described in [Nakamura97], which showed for the first time the superposition of two macroscopic quantum states differing by the number of Cooper pairs on a superconducting island.

In the years following this experiment several different types of superconducting qubits have been built and studied [Clarke08]: Flux-, phase-, and charge qubits. Flux qubits consist of a superconducting loop interrupted by usually three Josephson junctions. The two qubit states relate to the clockwise or anti-clockwise circulating supercurrent in the loop. The phase qubit consists of a single current-biased Josephson junction. The potential energy as a function of the phase difference $\hat{\varphi}$ resembles a tilted washboard. Thus the lowest two energy levels in one of the potential wells can form

the qubit. The charge qubit (also known as Cooper pair box) consists of a superconducting island connected with a Josephson junction to a reservoir (e.g. electrical ground). In its simplest form, the qubit states correspond to two subsequent number of Cooper pairs on the island.

2.2.2. Transmon qubit

The transmon qubit [Koch07] is a modified form of the Cooper pair box (CPB) [Bouchiat98]. Like the CPB it consists of an island that is connected via a Josephson junction to a reservoir. But in addition, it has a large shunt-capacitance C_B to decrease the charging energy E_C. As shown later in this section, this makes the transmon relatively insensitive to charge noise and as another consequence, the energy eigenstates are a combination of many CPB charge states. In our realizations of the transmon, the Josephson junction with a fixed Josephson energy E_J is replaced by two Josephson junctions in parallel forming a loop, a so called dc-SQUID, see Fig. 2.3. It acts as an effective Josephson junction with an $E_J = E_J^{\max} |\cos(\pi\Phi/\Phi_0)|$ which is tunable by the magnetic flux Φ threading the loop, where $\Phi_0 = h/(2e)$ is the magnetic flux quantum.

The effective Hamiltonian of the transmon can be written in the same form as the one for the CPB [Koch07],

$$\hat{H}/\hbar = 4E_C(\hat{n} - n_g)^2 - E_J \cos\hat{\varphi}. \tag{2.2}$$

Here $n_g = Q_r/2e + C_g V_g/2e$ is the effective offset charge in units of Cooper pairs $2e$, with V_g and C_g the gate voltage and capacitance, and Q_r the environment-induced offset charge. Due to the additional large capacitance C_B, the charging energy $E_C = e^2/2C_\Sigma$, where $C_\Sigma = C_J + C_B + C_g$ can be made small compared to the Josephson energy. This allows to operate the transmon in a regime where $E_J/E_C \gg 1$, in contrast to the standard CPB where $E_J/E_C \ll 1$.

By using Mathieu functions the transmon Hamiltonian Eq. (2.2) can be solved exactly in the phase basis. The eigenvalues are given by

$$E_m(n_g) = E_C a_{2[n_g + k(m,n_g)]}(-E_J/2E_C), \tag{2.3}$$

where $a_r(x)$ is Mathieu's characteristic value and $k(m, n_g)$ is a function appropriately sorting the eigenvalues (see [Koch07] for details).

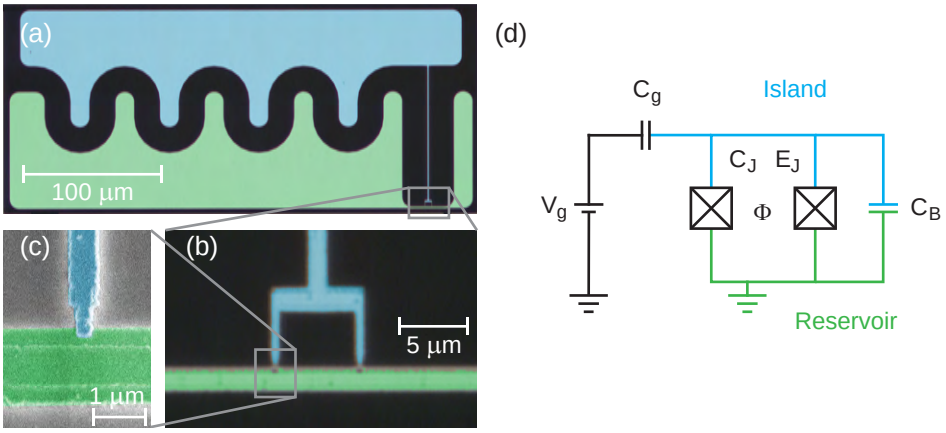

Figure 2.3: (a) False colored micrograph of a transmon qubit consisting of an island (top, blue) and reservoir (bottom, green), (b) Zoom-in of the dc-SQUID, (c) SEM-image of one of the Josephson junctions, (d) effective circuit diagram of a transmon qubit with a SQUID-loop.

It can be shown, that these eigenvalues become less sensitive to charge noise for increasing E_J/E_C, see Fig. 2.4 (a-c). Indeed, in the large E_J/E_C limit,

$$\frac{\partial E_m}{\partial n_g} \propto \epsilon_m \sin(2\pi n_g), \tag{2.4}$$

with ϵ_m the peak-to-peak value for the charge dispersion of the m^{th} energy level, which decreases exponentially fast with the E_J/E_C ratio,

$$\epsilon_m \propto e^{-\sqrt{8E_J/E_C}}. \tag{2.5}$$

The cost of the decreased sensitivity to charge noise are a lower anharmonicity $\alpha = (E_{12} - E_{01})/\hbar$, i.e. the spacing between the energy levels becomes more harmonic. Nevertheless, for using the lowest two energy levels of a transmon as a qubit, a sufficient anharmonicity is required which ensures the individual addressability of the level transitions.

For the CPB the anharmonicity is positive, i.e. the level spacing increases for higher levels. It first decreases with increasing E_J/E_C and changes sign at $E_J/E_C \approx 9$, see Fig. 2.4 (d). For larger values of E_J/E_C the transition

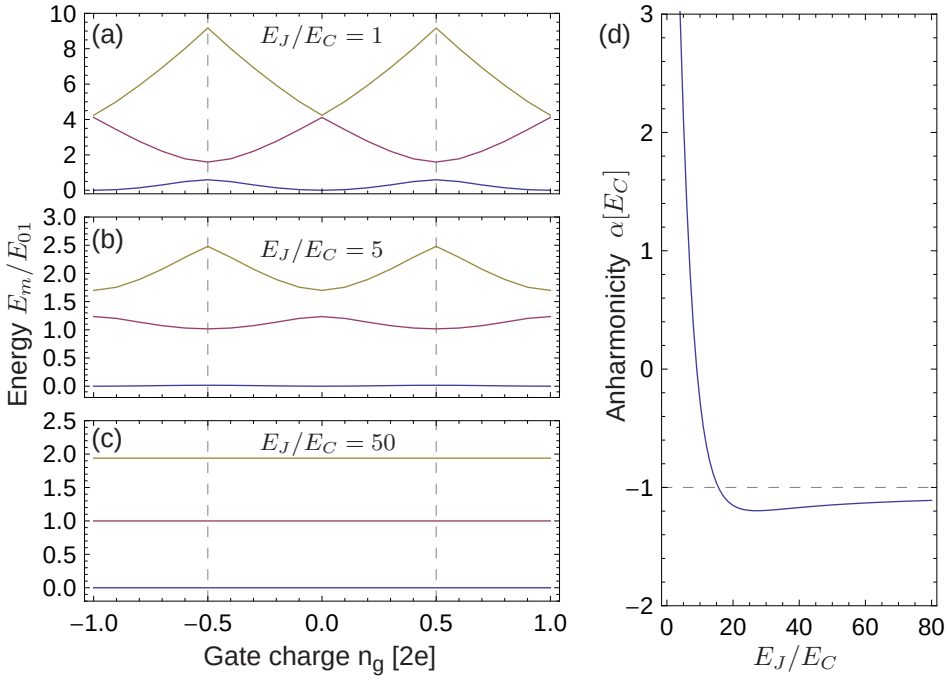

Figure 2.4: (a-c) Eigenenergies E_m (first three levels, $m = 0, 1, 2$) of the qubit Hamiltonian as a function of the effective offset charge n_g for different ratios E_J/E_C. Energies are given in units of the transition energy E_{01} at the point $n_g = 1/2$. (d) Anharmonicity in units of E_C as a function of E_J/E_C. Figure adapted from [Koch07].

energy E_{12} is therefore smaller than E_{01}. Asymptotically, the anharmonicity approaches $\alpha/\hbar \simeq -E_C$ for $E_J/E_C \to \infty$. In this limit, it is also possible to find an approximation for the eigenenergies of the transmon depending on the quantum number m:

$$E_m \simeq -E_J + \sqrt{8E_C E_J}\left(m + \frac{1}{2}\right) - \frac{E_C}{12}\left(6m^2 + 6m + 3\right). \tag{2.6}$$

Together with the flux-dependent effective Josephson energy, this results in the following formula to calculate the transition energy between

the ground and excited states (used as the qubit):

$$E_{01} = E_1 - E_0 \approx \sqrt{8E_C E_J^{\max} |\cos(\pi\Phi/\Phi_0)|} - E_C. \tag{2.7}$$

This last equation also describes the tunability of the transition frequency by means of a magnetic flux. It is periodic with the number of flux quanta penetrating the SQUID loop, with the highest frequency for integer numbers of flux quanta and the lowest frequency for half-integer number of flux quanta. As a remark, since the approximation Eq. (2.7) is only valid for $E_J/E_C \gg 1$, it also breaks down if the *effective* E_J becomes low due to the flux tuning. The exact diagonalization of the Hamiltonian shows that for half-integers the transition energy vanishes $E_{01}^{\Phi=0.5} = 0$. Nevertheless, in real implementations this is not the case due to a finite junction asymmetry, see [Koch07] for details.

Although the flux tunability is in general a wanted and useful feature, it should be considered that it makes the qubit also sensitive to flux noise. Only for integer values of flux quanta, the sensitivity vanishes to first order $\partial E_m/\partial\Phi = 0$. Especially near half-integer flux quanta, this value can become significant, leading to additional dephasing of the qubit.

2.3. Circuit quantum electrodynamics

In order to implement gates and algorithms with transmon qubits, one needs a framework which protects the qubits from the environment while still allowing the controlled interaction of many qubits as well as the possibility to read out the qubit states. Such a framework, known as *cavity quantum electrodynamics* (cavity QED) [Haroche06], has been developed in a different physical realization: atoms coupled to an electromagnetic field in a cavity defined by highly reflective mirrors. The cavity provides a small mode volume for the electromagnetic field. This can enhance its coupling to an atom inside the cavity such that the coupling strength is much larger than the decay rates of the atom or the electromagnetic field. This concept has been adapted to superconducting circuits and is usally referred to as *circuit QED*. It was first theoretically described [Blais04] and then implemented experimentally [Wallraff04] with a CPB as an "artificial" atom and a transmission-line resonator as cavity. The field of circuit QED gives the unique possibility to engineer the properties of the involved structures to

a high degree. Since these first experiments, the methods of circuit QED have been intensively used to investigate the interactions between matter and photons.

In this section at first a general model describing multi-level systems coupled to a cavity, the generalized *Janes-Cummings model*, is summarized. It is followed by a description of our actual realization of the circuit QED system with transmon qubits as multi-level systems and coplanar waveguide resonators as cavities.

2.3.1. Generalized Jaynes-Cummings model

The Hamiltonian describing a multi-level atom (or atom-like structures, e.g. a transmon) coupled to a single mode of the electromagnetic field expressed in the basis of the uncoupled atom states is

$$\hat{H}/\hbar = \underbrace{\sum_j \omega_j \left|j\right\rangle \left\langle j\right|}_{\hat{H}_{\text{transmon}}} + \underbrace{\omega_r \hat{a}^\dagger \hat{a}}_{\hat{H}_{\text{res}}} + \underbrace{\sum_{i,j} g_{ij} \left|i\right\rangle \left\langle j\right| (\hat{a} + \hat{a}^\dagger)}_{\hat{H}_{\text{int}}}. \tag{2.8}$$

Here, $\hat{H}_{\text{transmon}}$ is the Hamiltonian of the transmon with the j^{th} energy level having the energy $E_j = \hbar\omega_j$, $\hat{H}_{\text{res}}$ describes the cavity as a harmonic oscillator with resonance frequency ω_r, and $\hat{H}_{\text{int}}$ describes the interaction of the different level transitions with the cavity with coupling strength g_{ij}. It can be shown [Koch07] that the last term can be simplified in the case of a transmon: Only considering nearest-neighbor coupling $g_{i,i+1}$ and applying the rotating wave approximation yields

$$\hat{H}/\hbar = \sum_j \omega_j \left|j\right\rangle \left\langle j\right| + \omega_r \hat{a}^\dagger \hat{a} + \left(\sum_i g_{i,i+1} \left|i\right\rangle \left\langle i+1\right| \hat{a}^\dagger + \text{h.c.} \right). \tag{2.9}$$

This is the so-called generalized Jaynes-Cummings (JC) Hamiltonian, which includes many transmon levels with nearest-neighbor coupling in contrast to the regular JC-Hamiltonian [Walls08] which describes only a two-level system coupled to a harmonic oscillator. Also in contrast to the regular JC-Hamiltonian the one in Eq. (2.9) cannot be solved analytically but has to be treated numerically. However, it can be solved analytically in the so called *dispersive limit* where the detunings between transmon and cavity $\Delta_i = \omega_{i,i+1} - \omega_r$ are large.

In this limit, the effective Hamiltonian can be written [Koch07] as

$$\hat{H}_{\mathrm{disp}}/\hbar = \frac{\omega'_{01}}{2}\hat{\sigma}_z + (\omega'_r + \chi\hat{\sigma}_z)\hat{a}^\dagger\hat{a}, \tag{2.10}$$

with the dispersive shift $\chi = \chi_{01} - \chi_{12}/2$, and the renormalized frequencies $\omega'_{01} = \omega_{01} + \chi_{01}$ and $\omega'_r = \omega_r - \chi_{12}/2$, where the "partial" dispersive shifts are

$$\chi_{ij} = \frac{g_{ij}^2}{\omega_{ij} - \omega_r}. \tag{2.11}$$

The renormalized parameters come from the fact that this Hamiltonian models the transmon as an effective two-level system (qubit) but includes the effects on these levels introduced by the interaction with the third level. In the transmon limit ($E_J/E_C \gg 1$), the dispersive shift χ can be approximated as

$$\chi \simeq \frac{-g_{01}^2 E_C}{\Delta_0(\hbar\Delta_0 - E_C)}. \tag{2.12}$$

The term $\omega'_r + \chi\hat{\sigma}_z$ shows that the effective resonator frequency $\omega'_{r,\mathrm{eff}} = \omega'_r \pm \chi$ depends on the state of the qubit. This can be exploited to read out the state of the qubit as described later in Sec. 4.3.

2.3.2. Coplanar waveguide resonators

So far the cavity was just modeled as a harmonic oscillator. This subsection describes our actual implementation of the cavity as a superconducting coplanar waveguide resonator. At first, general properties of coplanar waveguides are introduced, followed by a discussion about the implementation of a one-dimensional cavity in such a system. The basics (and much more) of microwave engineering needed to understand this structures is discussed in [Pozar11]. For a detailed study of coplanar waveguide circuits I recommend the two books [Simons01] and [Wolff06]. The use of coplanar waveguides for superconducting circuits is studied in [Göppl08].

The coplanar waveguide (CPW) [Wen69, Simons01] is a type of transmission line [Pozar11] supporting quasi-TEM modes [Wolff06]. It is the planar counterpart of a co-axial cable, having the ground and the center conductor in the same plane, as shown in Fig. 2.5 (a). The geometry is defined by the center conductor width W and the gap width S. Alternatively, the half-width of the center conductor a and the half-with of the whole structure b

can used to describe the CPW. Other important design parameters are the relative permittivity ε_1 and the height h of the substrate. Another parameter would be the thickness of the conducting film, however, it is normally much smaller than the other involved dimensions and the conducting layer is therefore usually modeled as flat.

The characteristic impedance Z_0 for a lossless transmission line can be written [Pozar11] in terms of its capacitance and inductance per unit length C_ℓ and L_ℓ as

$$Z_0 = \sqrt{\frac{L_\ell}{C_\ell}}. \tag{2.13}$$

For a CPW on a dielectric (and non-magnetic) substrate one can calculate the capacitance per unit length C_ℓ by using conformal mapping techniques [Gevorgian95, Simons01] which results in

$$C_\ell = 4\varepsilon_0\varepsilon_{\text{eff}}\frac{K(k_0)}{K(k_0')}, \tag{2.14}$$

where ε_{eff} is the effective relative permittivity discussed below, K the complete elliptic integral with modulus $k_0 = W/(W+2S)$ and $k_0' = \sqrt{1-k_0^2}$. By using the following expressions for the phase velocity v_{ph} [Pozar11, Simons01]

$$v_{\text{ph}} = \frac{1}{\sqrt{L_\ell C_\ell}} = \frac{c}{\sqrt{\varepsilon_{\text{eff}}}}, \tag{2.15}$$

an expression for the inductance per unit length can be found:

$$L_\ell = \frac{\varepsilon_{\text{eff}}}{c^2 C_\ell} = \frac{\mu_0}{4}\frac{K(k_0')}{K(k_0)}. \tag{2.16}$$

The inductance L_ℓ hence solely depends on the geometry of the CPW in contrast to the capacitance C_ℓ, which also depends on the effective relative permittivity ε_{eff}. Combining Eqs. (2.13), (2.14), and (2.16) leads to the following expression for Z_0 for coplanar waveguides,

$$Z_0 = \frac{1}{4}\sqrt{\frac{\mu_0}{\varepsilon_0\varepsilon_{\text{eff}}}}\frac{K(k_0')}{K(k_0)}. \tag{2.17}$$

The effective relative permittivity ε_{eff} depends on the geometry of the CPW, the height h of the substrate and the relative permittivity ε_1 of the

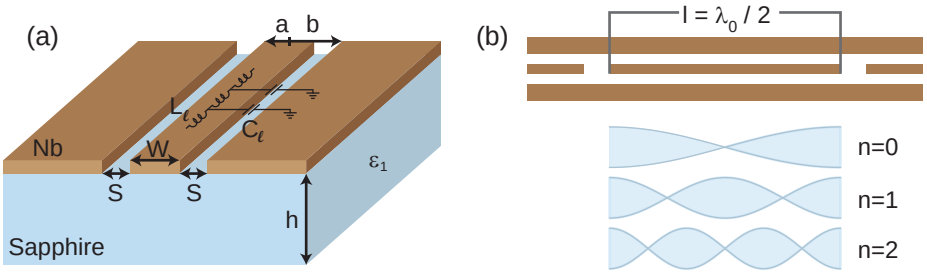

Figure 2.5: (a) Schematic representation of a CPW, (b) CPW resonator with the electric field of the first three modes indicated.

substrate. It can be shown [Gevorgian95] to be

$$\varepsilon_{\text{eff}} = 1 + \frac{\varepsilon_1 - 1}{2} \frac{K(k_1)}{K(k_1')} \frac{K(k_0')}{K(k_0)}, \tag{2.18}$$

with $k_1 = \sinh(\pi W/4h_1)/\sinh\left[(\pi(W+2S))/4h_1\right]$ and $k_1' = \sqrt{1-k_1^2}$. In the limit where $h_1 \to \infty$, k_1 becomes k_0 and

$$\lim_{h_1 \to \infty} \varepsilon_{\text{eff}} = 1 + \frac{\varepsilon_1 - 1}{2} = \frac{1+\varepsilon_1}{2}. \tag{2.19}$$

This can be intuitively interpreted as that half of the electric field energy between ground planes and center conductor is in the vacuum ($\varepsilon_r = 1$) and the other half is in the substrate ($\varepsilon_r = \varepsilon_1$), hence the effective permittivity is just the mean value of both.

For sapphire as a substrate, as used in our experiments, the relative permittivity is anisotropic. We use sapphire that is cut perpendicular to the C-axis of the crystal, such that the in-plane permittivity is isotropic, but different from the permittivity along the vertical axis of the wafer. The permittivity perpendicular and parallel to the C-axis of the crystal is $\varepsilon_{xy} = 9.3$ and $\varepsilon_z = 11.5$ at room temperature, respectively. At cryogenic temperatures they are slightly lower [Krupka94]. A value of $\varepsilon_{\text{eff}} \approx 5.8$ was found to agree with the experimental data.

Based on these values we used a CPW with dimensions $W = 10\,\mu\text{m}$ and $S = 4.5\,\mu\text{m}$, which results in a characteristic impedance of $Z_0 \approx 50\,\Omega$

compatible with the rest of the microwave equipment in our setup (see also Chap. 4).

A cavity is formed by introducing gaps into the center conductor of the coplanar waveguide as schematically shown in Fig. 2.5 (b). The gaps impose boundary conditions onto the electromagnetic field: the current vanishes at the gaps and accordingly the electric field has an antinode. The lowest possible mode for a standing electromagnetic wave is where the length l of the resonator is half of the wavelength, i.e. $l = \lambda_0/2$, therefore this type of resonator is also called a $\lambda/2$-*resonator*. The fundamental frequency is given by

$$f_0 = \frac{c}{\sqrt{\varepsilon_{\text{eff}}}} \frac{1}{2l}, \tag{2.20}$$

and the higher harmonics $f_{n-1} = nf_0$ are integer multiples of the fundamental frequency.

For frequencies close to a resonance $f \approx f_n$, the CPW can be mapped to a parallel RLC-circuit [Pozar11, Göppl08] with the following substitutions:

$$L_{n-1} = \frac{2L_\ell l}{n^2\pi^2}, \qquad C = \frac{C_\ell l}{2}, \qquad R = \frac{Z_0}{\alpha l}, \tag{2.21}$$

with α an attenuation constant. By neglecting the loss, this circuit corresponds to a harmonic LC-oscillator which can be described quantum-mechanically by the Hamiltonian

$$\hat{H} = \hbar\omega_0 \left(\frac{1}{2} + \hat{a}^\dagger \hat{a}\right), \tag{2.22}$$

with $\omega_0 = 2\pi f_0$ the angular resonance frequency and $\hat{a}^{(\dagger)}$ the usual ladder operators for a harmonic oscillator.

2.4. Conclusion

In this chapter, we have discussed quantum bits as quantum mechanical two level systems and represent the quantum analog to bits, capable of storing quantum information. Operations can be performed on single qubits or also on multiple qubits. The qubits used for the experiments presented in this thesis are implemented as the two lowest energy levels of a transmon. This is a circuit which has a quantized anharmonic level-spectrum and consists

of two superconducting islands interconnected by Josephson junctions. Circuit QED is an appropriate framework to protect the transmon from the environment while still allowing to read out its state and couple it to other qubits. The implementation of this framework needs an additional building block, the coplanar waveguide resonator. This chapter serves as an overview of the presented topics. As further reading or for a more detailed introduction, I recommend the following books: *The* introduction for quantum information and quantum computation is the book by Nielsen and Chuang [Nielsen00]. The book by D. M. Pozar [Pozar11] is a comprehensive introduction into microwave engineering in general. The two books specifically focused on coplanar waveguides are [Simons01] and [Wolff06]. In the following chapters, these building blocks and the mechanisms which allow to perform quantum computing experiments are discussed in more detail.

3

Sample design and fabrication

The transmon and the coplanar waveguide resonator, introduced in Sec. 2.2 and Sec. 2.3, are the main building blocks of the circuits used for the experiments presented in this thesis. In addition, the circuits contain bias lines which also consist of coplanar waveguides — their functionality is discussed in Chap. 5. One focus of this thesis was the design and fabrication of the coplanar waveguide structures, i.e. the resonators and bias lines, which is the topic of this chapter. The design and fabrication of the transmon qubits are described in [Göppl09, Fink10a, Burkhard12].

3.1. Sample design

3.1.1. Resonator coupling

The resonator is normally coupled to input- and output-transmission lines that allow to measure the transmission of microwaves through the resonator. A transmission measurement [Göppl08] shows a Lorentzian line shape around the resonance frequency f_0:

$$F_{\mathrm{Lor}}(f) = A_0 \frac{\delta f^2}{4(f - f_0)^2 + \delta f^2}, \tag{3.1}$$

where A_0 is the amplitude at resonance frequency f_0, and δf is the full width at half maximum. From such a measurement, one can also extract

the loaded quality factor $Q_\mathrm{L} = f_0/\delta f$ which is linked to the photon decay rate $\kappa/2\pi = f_0/Q_\mathrm{L}$.

The quality factor (or the photon decay rate) is an important design property. It influences the time with which a transmission measurement can be performed and also the time with which coherent operations between a qubit and the cavity can be performed. Smaller Q allow a faster population of the resonator and therefore shorter readout times, while larger Q (i.e. larger photon lifetime) allow longer resonant qubit-resonator operations. The resonator is capacitively coupled to the in- and output leads (c.f. Fig. 3.1 (a)), either by a gap capacitor with variable width or with finger capacitors with variable length and number of fingers [Göppl08]. The capacitances of a certain design can be simulated with finite-element methods (using e.g. the software *Ansoft Maxwell 3D*). For typical designs, these values are in the range of 1 fF – 0.1 fF for gap capacitors of width 1 µm – 30 µm, and 1 fF – 20 fF for finger capacitors with up to 5 fingers of length 100 µm.

In the following, a formula for the quality factor for asymmetrically coupled resonators is derived, similarly as for the formula for symmetrically coupled resonators in [Göppl08].

As known from Eqs. (2.21), the resonator itself can be approximated as a parallel RLC circuit. The quality factor for an RLC circuit is given as $Q = R\sqrt{C/L} = \omega_0 RC$ [Pozar11]. In our model, we approximate the coupled resonator as an RLC circuit coupled via two capacitances $C_\mathrm{in}, C_\mathrm{out}$ to a load resistance usually equal to the characteristic impedance of the circuitry $R_\mathrm{L} = 50\,\Omega$, as shown in Fig. 3.1 (a). To map the whole circuit to an equivalent RLC circuit, we first map the capacitances and resistances in series $(C_\mathrm{in,out}, R_\mathrm{L})$ onto equivalent parallel circuit elements $(C^*_\mathrm{in,out}, R^*_\mathrm{L})$, as shown in the green parts of Fig. 3.1 (a,b). By rearranging the elements, we get an equivalent RLC circuit for the coupled resonator with the effective parameters

$$C_\mathrm{eff} = C + C^*_\mathrm{in} + C^*_\mathrm{out}, \quad R_\mathrm{eff} = \frac{1}{\frac{1}{R} + \frac{1}{R^*_\mathrm{in}} + \frac{1}{R^*_\mathrm{out}}}, \quad \omega^*_n = \frac{1}{\sqrt{L_{n+1} C_\mathrm{eff}}}, \tag{3.2}$$

with

$$C^*_\mathrm{in,out} = \frac{C_\mathrm{in,out}}{1 + \omega_n^2 R_\mathrm{L}^2 C_\mathrm{in,out}^2}, \qquad R^*_\mathrm{in,out} = \frac{1 + \omega_n^2 R_\mathrm{L}^2 C_\mathrm{in,out}^2}{\omega_n^2 R_\mathrm{L} C_\mathrm{in,out}^2}. \tag{3.3}$$

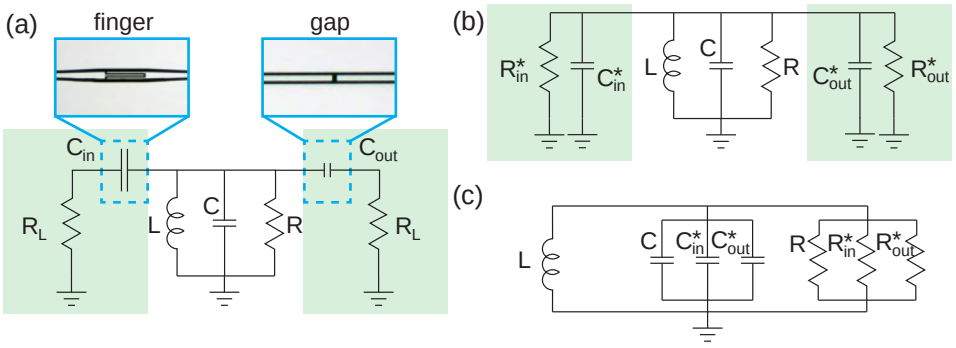

Figure 3.1: (a) Circuit diagram of the resonator modeled as an RLC circuit, coupled (green background) with in- and output capacitances $C_{\mathrm{in}}, C_{\mathrm{out}}$ to a load impedance R_{L}. (b) Equivalent parallel circuit of (a). (c) Rearranging (b) gives the RLC circuit of the coupled resonator.

From $1 \gg \omega_n^2 R_{\mathrm{L}}^2 C_{\mathrm{in,out}}^2 (\approx 10^{-4}$ for $\omega/2\pi = 7\,\mathrm{GHz}, R_{\mathrm{L}} = 50\,\Omega, C_{\mathrm{in,out}} = 5\,\mathrm{fF})$ it follows that $C_{\mathrm{eff}} \approx C$ and $\omega_n^* \approx \omega_n$ are good approximations and one can write the loaded quality factor Q_{L} as

$$Q_{\mathrm{L}} = \omega_n R_{\mathrm{eff}} C = \omega_n C \frac{1}{\frac{1}{R} + \frac{1}{R^*_{\mathrm{in}}} + \frac{1}{R^*_{\mathrm{out}}}}. \tag{3.4}$$

The loaded quality factor can be considered as a combination of the internal quality factor Q_{int} only depending on the intrinsic losses of the resonator, and the external quality factor Q_{ext} defined by the coupling capacitors,

$$\frac{1}{Q_{\mathrm{L}}} = \underbrace{\frac{1}{\omega_n C R}}_{1/Q_{\mathrm{int}}} + \underbrace{\frac{1}{\omega_n C R^*_{\mathrm{in}}} + \frac{1}{\omega_n C R^*_{\mathrm{out}}}}_{1/Q_{\mathrm{ext}}}. \tag{3.5}$$

Since the resonators used in this thesis are designed to be in the overcoupled regime where $Q_{\mathrm{ext}} \sim 10^3 \ll Q_{\mathrm{int}} \sim 10^5$, the loaded quality factor will be governed by Q_{ext}. Using $\omega_n = 1/\sqrt{L_n C}$, Eqs. (2.21), and $Z_0 = \sqrt{L_\ell / C_\ell}$ one can write

$$\omega_n C = \frac{C}{\sqrt{L_n C}} = \frac{n\pi}{2Z_0}, \tag{3.6}$$

and combining this with Eqs. (3.5), (3.3) and $\omega_{n-1} = n\omega_0$ leads to an expression for Q_{ext} that does only depend on the mode number n ($n = 1$ for the fundamental mode), the characteristic impedance of the resonator Z_0, the load impedance R_{L} and the input and output capacitances $C_{\text{in,out}}$ as follows:

$$Q_{\text{ext},n-1} = \frac{n\pi}{2Z_0} \frac{1}{n^2\omega_0^2 R_{\text{L}}} \frac{\left(1 + n^2\omega_0^2 R_{\text{L}}^2 C_{\text{in}}^2\right)\left(1 + n^2\omega_0^2 R_{\text{L}}^2 C_{\text{out}}^2\right)}{C_{\text{in}}^2\left(1 + n^2\omega_0^2 R_{\text{L}}^2 C_{\text{out}}^2\right) + C_{\text{out}}^2\left(1 + n^2\omega_0^2 R_{\text{L}}^2 C_{\text{in}}^2\right)}. \tag{3.7}$$

For $C_{\text{in}} = C_{\text{out}} = C_\kappa$, the formula for symmetric coupling given in [Göppl08] is recovered:

$$Q_{\text{sym},n-1} = \frac{n\pi}{4Z_0}\left(\frac{1}{n^2\omega_0^2 R_{\text{L}} C_\kappa^2} + R_{\text{L}}\right). \tag{3.8}$$

It is also possible to not couple the resonator to input and output leads, but terminate each end with a CPW-open (i.e. a small capacitance to ground). In this case the resonator quality factor will be close to the intrinsic quality factor, unless it is coupled to other structures (like transmons, gate lines etc.) which provide loss channels. Such a resonator is used in the teleportation experiment, see Chap. 8.

3.1.2. Airbridges

In our experiments we usually want to couple the transmon qubits to a single mode of the electromagnetic field approximated as a harmonic oscillator. We therefore want to suppress any other parasitic modes which the transmon could also couple to. In this subsection, we discuss two possible parasitic modes, the slot-line mode and parasitic modes induced by gate lines, and how to suppress those with airbridges. Subsequently the use of airbridges to enable resonator cross-overs is discussed.

Parasitic mode suppression

Coplanar waveguides are capable of supporting two types of modes, the even- and odd-modes (sometimes also referred to as coplanar waveguide modes and slot-line modes), see Fig. 3.2 (a,b). In our experiments we want the CPW to support only the even mode. The odd mode shows a much stronger dependence of its effective dielectric constant on frequency and geometry than the even mode [Wolff06]. It is therefore harder to predict

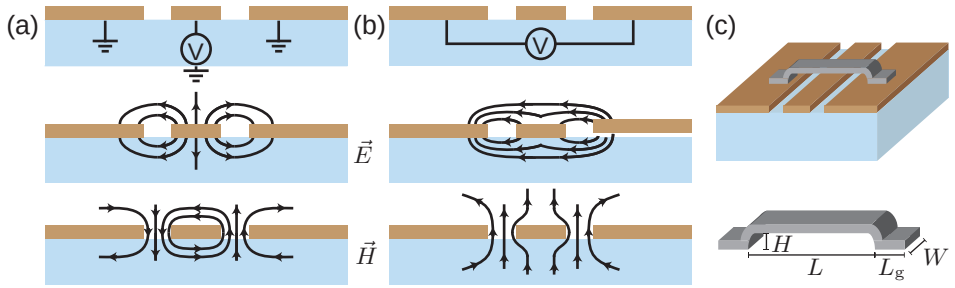

Figure 3.2: (a) Even (coplanar waveguide) mode and (b) odd (slot-line) mode of the CPW. Top: Excitation of the modes. Middle: Schematic of the transversal electric field. Bottom: Schematic of the transversal magnetic field. (c) Schematics of an airbridge connecting the two ground planes, suppressing the odd mode.

its exact frequencies. The odd mode can be effectively suppressed by using airbridges [Koster89, Simons01, Wolff06], metallic bridges connecting the ground planes on both sides of the center conductor, see Fig. 3.2 (c).

Another possibility for introducing parasitic modes are gate lines, leading from the edge of the chip to the transmon qubit. The gate lines cut the ground plane into several possibly unconnected areas which hinders the electromagnetic wave in the CPW to propagate in the desired way and introduces unwanted modes. This can also be avoided by using airbridges placed over the gate lines to connect the different ground plane areas with each other as depicted in Fig. 3.3.

Airbridges introduce an additional capacitance and therefore locally change the characteristic impedance of the underlying CPW. By numerically simulate the additional capacitance between the CPW and ground due to the presence of the airbridge, the characteristic impedance for the part of the CPW below the airbridge was calculated to be $\approx 40\,\Omega$. There are known possibilities [Wolff06] to correct for this impedance mismatch. Since the length on which this impedance mismatch occurs is small compared to the wavelength, and the impedance mismatches introduced due to the transmon gaps are even larger, this effect has been neglected when designing the chips.

The designed airbridges have a height $H = 2\,\mu\text{m}$ (see Fig. 3.2 (c) for

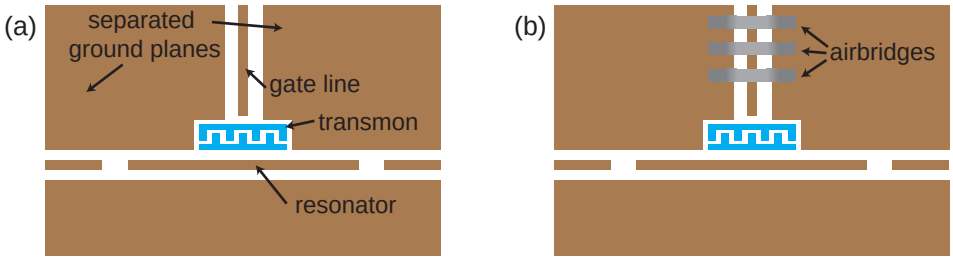

Figure 3.3: (a) A gate line can split the ground plane in two unconnected parts, disturbing signal propagation in the resonator. (b) Airbridges reconnect the ground planes and enable proper signal propagation.

the dimensions), a width $W = 10\,\mu\text{m}$, and a length $L = 40\,\mu\text{m}$. The part connected to the ground has a length of $L_g = 30\,\mu\text{m}$. For suppressing the odd mode, one or two airbridges per resonator placed symmetrically around the center of the resonator showed the complete extinction of the odd mode. For the gate lines the airbridges are placed every $100\,\mu\text{m} - 200\,\mu\text{m}$ to ensure a good connection between the different ground planes.

Resonator cross-overs

Airbridges can also be used to cross two resonators. This allows to design complex networks of resonators [Helmer09] which would not be possible in a fully planar geometry. A chip with crossed resonators is used for the teleportation experiment discussed in Chap. 8. A micrograph of a cross-over is depicted in Fig. 3.7 (a).

3.2. Fabrication

The fabrication of the resonators, gate-line structures, and airbridges is performed by photolithography in the FIRST cleanroom at ETH Zurich. This technique requires masks (a patterned chromium layer on a glass substrate) which have to be fabricated beforehand[1] on the basis of digitized graphics data. During the thesis, a *Mathematica* program has been developed which

[1] Our masks have been fabricated by the commercial supplier *ML&C GmbH, Jena, D*

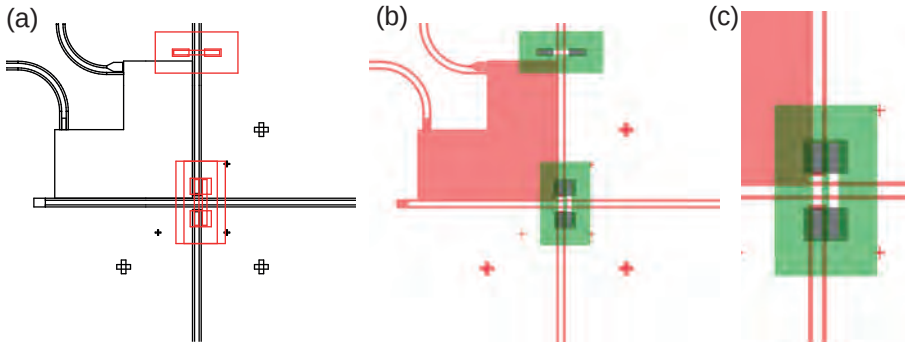

Figure 3.4: (a) *Mathematica* output of the mask design for a resonator cross-over with space for a transmon qubit which is fabricated in a separate step, see also Chap. 8 for a discussion of this sample. (b) After conversion to GDS-format. Different colors correspond to different masks. Filled areas will be transparent on the final masks. (c) Zoom-in of (b)

simplifies the task of generating the digital mask data by providing flexible drawing functions. The program outputs connected lines in a *DXF*-file format [Autodesk] (Fig. 3.4 (a)). This file can then be converted to an industry-standard GDSII-file [Rubin94] (Fig. 3.4 (b)), where the connected lines are transformed to areas. This areas will become transparent on the final mask, everything else stays opaque.

The fabrication of the airbridges requires two additional photolithography masks, one defining the area where the bridge contacts the metal layer of the chip (grey areas in Fig. 3.4 (b,c)) and one for the bridge outline (green areas in Fig. 3.4 (b,c)).

After the photolithography process, large unmetallized gaps are left into which a transmon qubit can be fabricated (large red area in Fig. 3.4). The transmons are fabricated in a separate step with an electron-beam lithography process.

In the following, the two fabrication processes for the CPW structures and the airbridges are explained. The detailed recipes are provided in Appendix A.

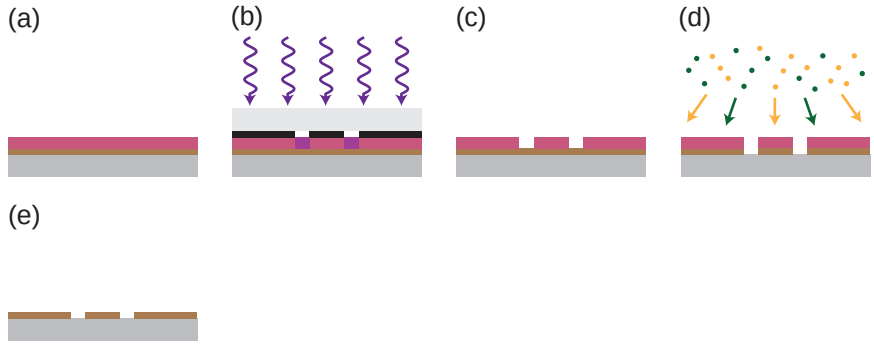

Figure 3.5: Resonator and gate-line etch process. (a) Spin resist layer. (b) Exporsure. (c) Development. (d) Reactive ion etching. (e) Resist stripping.

3.2.1. Resonators, gate lines

To efficiently fabricate many devices usually a whole 2-inch wafer is processed at once. We use sapphire (crystalline Al_2O_3) wafers with a thickness of 500 µm and a diameter of 2 inches, cut parallel to the C-plane of the crystal. The smallest standard chip we use has dimensions of 2 mm × 7 mm. A mask can contain 88 of these chips with a spacing of 300 µm between each chip needed for dicing. Larger chips have dimensions such that they use the same space on the mask/wafer as a multiple of the smallest chip, i.e. 4.3 mm × 7 mm and 6.6 mm × 7 mm.

The fabrication starts with a sapphire wafer coated with a 150 nm thick layer of niobium (Nb) from a commercial supplier[2], see Fig. 3.5 for a graphical representation of the fabrication steps. After spinning a positive resist (a), the wafer is pressed against the photolithography mask and exposed in a mask aligner (b). In the exposed areas (clear areas on the mask) the resist becomes soluble in the appropriate developer and is removed (c). The Nb layer is then removed in a reactive ion-etching process with a mixture of argon (Ar) ions and sulfur hexafluoride (SF_6) ions (d). As a final step, the remaining resist is removed chemically (with DMSO or acetone) or with oxygen plasma (e).

As a photoresist either one of the positive resists AZ 5214 E [Clariant GmbH]

[2]STAR Cryoelectronics, Santa Fe, NM

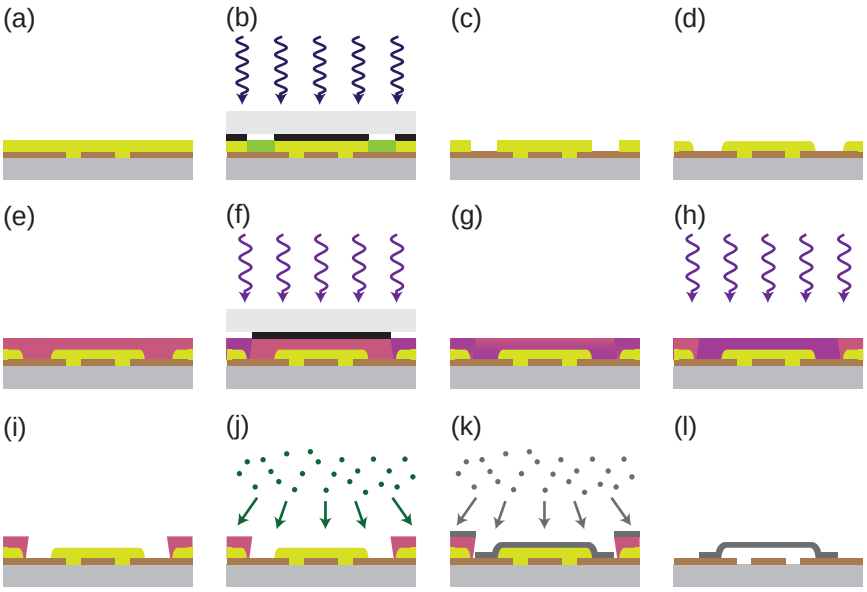

Figure 3.6: Airbridge process. (a) Spin PMMA layer. (b) Exporsure in DUV. (c) Development. (d) Reflow. (e) Spin AZ5214E layer. (f) Exposure in UV. (g) Image reversal bake. (h) Flood exposure. (i) Development. (j) Ar sputtering. (k) Al evaporation. (l) Final lift-off.

or PMMA 950K [MicroChem Corp.] is used. The first one has the advantage that it is more resistant to the reactive ion etching process, it is therefore appropriate for structures of size $\geq 2\,\mu m$. PMMA is etched at a similar rate as the niobium but allows a better resolution and should be used if the resolution is critical.

3.2.2. Airbridge fabrication

Once the resonator/gate line structures are fabricated the airbridge process can be performed. The airbridge process is schematically depicted in Fig. 3.6. In the first step the patterned wafer is spin coated with PMMA 950K (a). This layer defines the height of the bridges above the niobium layer (typically $2\,\mu m$). The first exposure (b) in deep ultra-violet (DUV) light at 220 nm defines the bridge support, i.e. the contacts to the

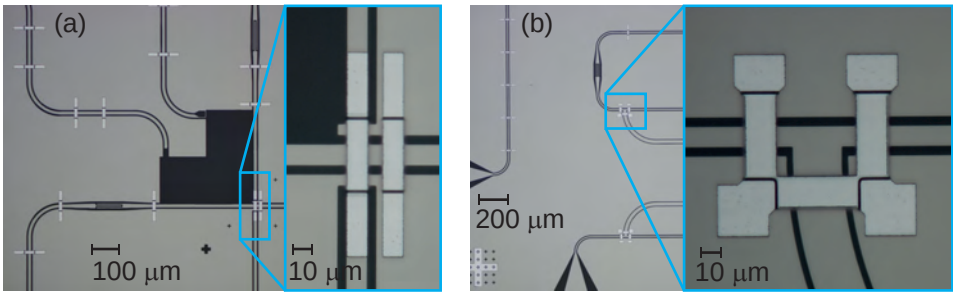

Figure 3.7: (a) Resonator crossing and transmon gap, zoom-in of airbridges at the crossing, (b) Two ports of a beam splitter and an additional gate line going upwards, zoom-in of an airbridge at a T-junction of the beam-splitter.

metal layer of the chip (see also grey areas in Fig. 3.4 (b,c)). The exposed areas become soluble in the appropriate developer and are removed (c). The resist is then heated to 180 °C which causes it to soften and rounds off the edges (reflow), defining a continuous bridge profile (d). To define the planar structure of the bridge a second photolithography step is necessary. For this step, the photoresist AZ 5214E is chosen. It can be exposed at UV-light with a wavelength of 365 nm which does not expose the underlying PMMA and it can be used as an image reversal resist [Clariant GmbH], allowing an undercut-profile which is needed for the metal evaporation. After spin coating (e) the area around the bridge is exposed (f), but not the area of the bridge itself as can be seen from the mask design (green areas in Fig. 3.4 (b,c)). By heating the sample above 110 °C the exposed areas get cross-linked and become insoluble in the developer (g). A flood exposure (exposure without mask) makes the previously unexposed parts of the resist soluble in the developer (h). Developing will result in a negative wall profile, i.e. an undercut (i). The wafer is then transferred into a physical vapor depositon (PVD) system with included ion gun. There it is sputtered with Ar ions which remove the oxide layer on the Nb film (j), before it is coated with a 800 nm thick aluminum (Al) film (k). A final lift-off in DMSO, acetone and isopropyl alcohol removes the remaining resist and the Al structures which are not connected to the Nb film (l).

A micrograph of the final airbridges is shown in Fig. 3.7, where im-

age (a) corresponds to the part of the mask shown in Fig. 3.4. Image (b) shows an airbridge at a CPW T-junction connecting all three ground planes with each other. The structures in (b) were fabricated for the experiments in [Bozyigit11, Lang13b] (not discussed here).

For the experiments presented in this thesis, the aluminum airbridges have a thickness of 800 nm. Despite the high thickness the airbridges are sensitive and sometimes collapse during dicing or transmon fabrication. We also tested airbridges made from titanium (Ti) which are much more stable (for 400 nm thick and 40 µm long Ti-bridges we never observed a collapsed bridge). But the Ti film did not become superconducting at cryogenic temperatures, hinting at a non-optimal film quality. This is however a crucial requirement for using the airbridges in resonator cross-overs. A possibility for enhancing the stability while maintaining the superconductivity is to fabricate bridges with different layers, e.g. an aluminum layer with a thin titanium layer on top.

3.3. Conclusion

In this chapter the design and fabrication of the CPW structures and airbridges has been presented. The CPWs are used to implement the cavity to which the transmon qubits couple and provide a method for reading out the qubit state as discussed in Sec. 4.3. Asymmetrically coupled cavities with a higher coupling at the output port than at the input port offer the possibility to increase the readout efficiency for a given quality factor. A method to estimate the quality factor for such cavities has been presented. During the course of this thesis, several samples with asymmetric cavity coupling have been designed and fabricated, e.g. the samples used and described in [Bozyigit11, Baur12b, Lang13b]. CPW structures can also be used to create charge- and flux-bias lines for individual qubit control (see Chap. 5), $\lambda/4$-resonators for the implementation of parametric amplifiers (see Sec. 4.4) or the implementation of on-chip microwave beam-splitters as used in [Bozyigit11, Lang13b].

The airbridges crossing a CPW serve mainly to suppress spurious CPW modes. In contrast to manually placed wirebonds, the fabrication of airbridges produces uniform and reproducible results. This was a key element in [Lang13b] where it was important to obtain two resonators with nearly

identical resonance frequencies. In the chip used for the teleportation experiment (see Chap. 8) airbridges are used to create resonator cross-overs which allow to build complex resonator networks with arbitrary connecting topology in a planar technology.

4

Measurement setup and principles

To observe the quantum mechanical properties of an electrical circuit, all interactions with its environment must be well controlled. Uncontrolled interaction of a quantum system with its environment alters the state in an unpredictable and possibly irreproducible way. The design of the measurement setup and its working principles are therefore crucial factors for the success of a quantum experiment and are discussed in this chapter.

In our system the energy scales are in the GHz range, therefore one of the key points is to protect the structures on our chip from thermal GHz radiation. Since the temperature scale associated with a single photon of a frequency $\nu = 5\,\mathrm{GHz}$ is $T = h\nu/k_\mathrm{B} = 240\,\mathrm{mK}$, the ambient temperature of the chip must be well below this temperature to allow the qubits to be in the ground state. In our setup this is accomplished by operating the chip inside a dilution refrigerator at a temperature of $T \approx 20\,\mathrm{mK}$. In contrast, the electronics to generate the signals for manipulating and measuring the qubits and resonators are at room temperature. Therefore a careful design of the cryogenic setup is required in order to maintain a low temperature while enabling the control and readout of the quantum systems, as discussed in Sec. 4.1. An important aspect of the setup is the sample holder which is discussed in Sec. 4.2. Apart from being the connection between the chip and the rest of the cryogenic setup, it also shields the chip from electromagnetic radiation and residual magnetic fields. The working principle of the readout by transmission measurements and its implementation in our setup is described in Sec. 4.3. For the teleportation

experiment (see Chap. 8) we extended the readout circuitry to perform single-shot readout by including Josephson parametric amplifiers into the setup, as explained in Sec. 4.4.

4.1. Cryogenic setup

The sample is mounted at the lowest temperature stage of a ^{3}He/^{4}He-dilution refrigerator (*Oxford Instruments Kelvinox 400HA*). This system consists of an inner vacuum chamber (IVC) which is pre-cooled to 4.2 K by immersing it into a bath of liquid helium (He). A small part of the He in the bath is transferred to the *1K pot*, a pot with a needle valve for admitting liquid He which is constantly cooled by evaporative cooling (i.e. pumping on it). This allows to pre-cool the second stage of the cryogenic system to about 1.5 K. The main part inside the IVC is the dilution unit (DU) in which a mixture of the two helium isotopes ^{3}He and ^{4}He is circulated. During operation most of the mixture is condensed in the *mixing chamber* at the base plate, where it forms two phases, a ^{3}He-rich phase which floats on top of a ^{3}He-poor phase. The concentration of ^{3}He in the two phases is constant for a given temperature. By actively pumping ^{3}He out of the ^{3}He-poor phase a phase transition of the ^{3}He from the ^{3}He-rich into the ^{3}He-poor phase is induced which removes energy from the environment. One can also consider this process as evaporative cooling process where ^{3}He is evaporated from one phase into the other. Heat exchangers at different stages in the DU use the cooling power of the upwards flowing ^{3}He to gradually cool down the downwards flowing ^{3}He and effectively produce a temperature gradient along the DU [Oxford Instruments, Pobell06].

Since all the electronics for signal generation is located at room temperature, wiring inside the IVC is needed that respects the following two points: First, since the cables provide a connection between the sample and room temperature they cause a *heat load* onto the base plate, adversely affecting the lowest achievable temperatures. Second, the cables directly transmit thermal radiation at the qubit/resonator frequencies from room temperature to the sample, inducing excitation or emission of the qubits/resonators. In the following we explain how these points are considered in the design of the wiring.

There are four main types of lines used in our setup, two to perform

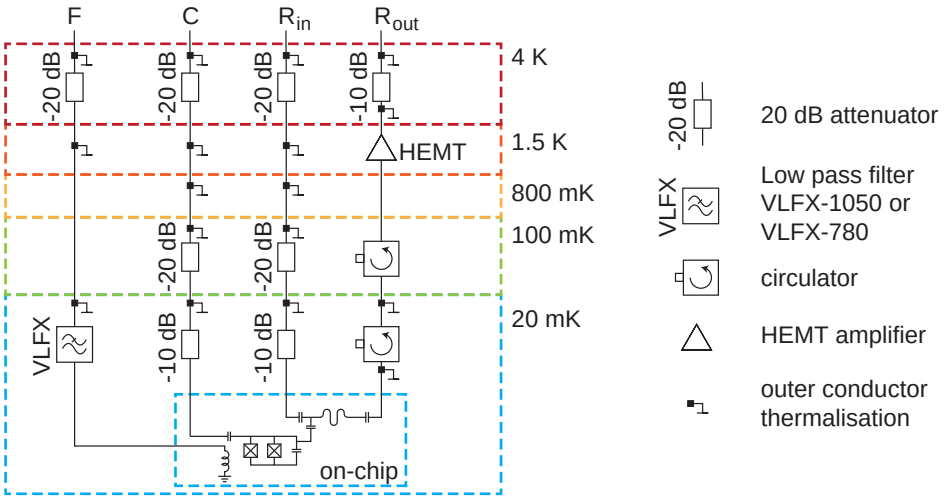

Figure 4.1: Schematic of the cryogenic wiring of typical components: Resonator in- and output line (R_{in}, R_{out}), qubit charge- (C) and flux- (F) bias line.

transmission measurements of the resonator (an input- and an output line) and two different types of bias lines to control the qubits, a charge bias line coupling capacitively to the qubit and a flux bias line coupling inductively to the qubit. A graphical representation of the components used in the lines is shown in Fig. 4.1.

The resonator input line and the charge gate line are designed in the same way, since the purpose of both of these lines is to bring a coherent microwave signal to the chip. The required signal at the chip has a very low power, e.g. down to $-140\,\mathrm{dBm}$ for the resonator input line, which is lower than the Johnson-Nyquist (thermal) noise at room temperature ($P_{\mathrm{th}} = 4k_{\mathrm{B}}T\Delta f \approx -110\,\mathrm{dBm}$ for $T = 300\,\mathrm{K}$ and $\Delta f = 1\,\mathrm{MHz}$). The straightforward solution would therefore be to generate a signal that has a much higher power than the thermal noise power and attenuate it at the lowest temperature stage, where the added thermal noise is low due to the small temperature. However attenuation always means that power is dissipated which can heat up the environment. As the lowest temperature stage has also the lowest cooling power it makes it unfavorable to

dissipate energy there. As shown in [Bianchetti10a], a good solution is to distribute the power dissipation in a way such that the attenuated noise is on the order of the thermal noise generated at a certain temperature stage. This is implemented by installing a 20 dB attenuator at 4 K, another 20 dB attenuator at the 100 mK stage and a 10 dB attenuator at the base stage. To reduce the heat load onto the base plate, all cables connecting different temperature stages are made from stainless steel whose thermal conductivity is about 10^3 times lower at low temperatures than that of copper. The inner conductor of each cable is thermalized via the attenuators, which are thermally connected with copper clamps and copper braid to the respective temperature stage. Additionally, the outer conductor is thermally anchored at every temperature stage with copper braid.

The flux bias lines have to carry a current pulse to the sample with a current of $\sim$ 1 mA at the sample. It is therefore not possible to use attenuators at lower temperature stages, since the power dissipation would be much too high. The only attenuator (20 dB) is placed at the 4 K-stage which has a high cooling power from the liquid helium bath. Instead of the attenuators, coaxial low-pass filters with a 40 dB stopband in the range of 2 GHz to 20 GHz are placed at the base stage of the cryostat, efficiently shielding noise in the relevant frequency range. The coaxial cables are either of stainless steel or NbTi which becomes superconducting below 9 K. The superconducting cable allows the application of a constant current which would produce a too high heat dissipation in stainless steel cables while still having a low thermal conductivity comparable to that of stainless steel.

The resonator output line fulfills a set of different requirements. While it should provide an as high as possible transmission of the signal from the low temperature stage to room temperature, the transmission in the reverse direction should be suppressed as much as possible. This can be implemented by using circulators with one of the three ports terminated with a resistor matching the characteristic impedance of the transmission lines (50 Ω). A circulator used in this way allows the upwards going signal to pass with an insertion loss of typically only $\sim$ 0.5 dB while the noise going downwards is dumped in the matched load, effectively leading to an isolation of $\sim$ 20 dB due to some finite cross coupling between the ports. Since the signal transmitted through the resonator for qubit measurements is very small (typically −140 dBm) it has to be amplified in order to be detectable. Therefore we installed a high-electron-mobility transistor (HEMT) amplifier

at the 1.5 K stage (1K pot) which has a noise temperature of ~ 4 K and a gain of 35 dB. In Sec. 4.4 it is explained how the readout wiring is modified to include Josephson parametric amplifiers allowing amplification at base temperature.

4.2. 16-port sample holder

For the experiments performed in our lab before the teleportation experiment (see Chap. 8) we used a sample holder which allows to connect 8 coaxial cables to a PCB on which the chip is mounted. This sample holder is described in [Baur12a]. In this section the sample holder with 16 connections which has been developed for the new generation of experiments [Häusler12, Liu12] is described.

The sample holder consists of several parts as shown in Fig. 4.2. The sample is glued into a cutout of a printed circuit board (PCB) with silver paint or PMMA and the on-chip CPWs are connected to CPWs on the PCB with wirebonds. The PCB is then mounted onto the bottom part of the sample holder (a). To suppress standing waves in a cavity which is formed by the PCB/bottom cover and the top cover of the sample holder, a cover [Marx09, Liu12] which has 500 µm deep cutouts around the region of the chip and the CPWs is placed on top of the PCB (a,b). In the next step, SMP bullets are inserted into the SMP-PCB-connectors and the bottom part is connected with the top part (c) through which the coaxial cables are fed through via an SMP connector. The bottom and top part as well as the PCB cover are made from oxygen-free copper (OFC) and are connected with an OFC copper rod to the base plate of the cryostat to maximize thermal conductivity.

The bottom part of the sample holder (c) has slots which allow to insert miniature superconducting coils [Bianchetti10a] to provide static flux offsets for the transmon qubits.

The housing of our sample holder provides also a good protection of the sample from external radiation. This can be concluded from experiments in which the 8-port version of the sample holder was covered by an absorptive medium (*Eccosorb CR-124*) protecting it better from external radiation but no effect on the qubit lifetime was observed [Peterer12]. This is in contrast to the experiments described in [Córcoles11], where this technique

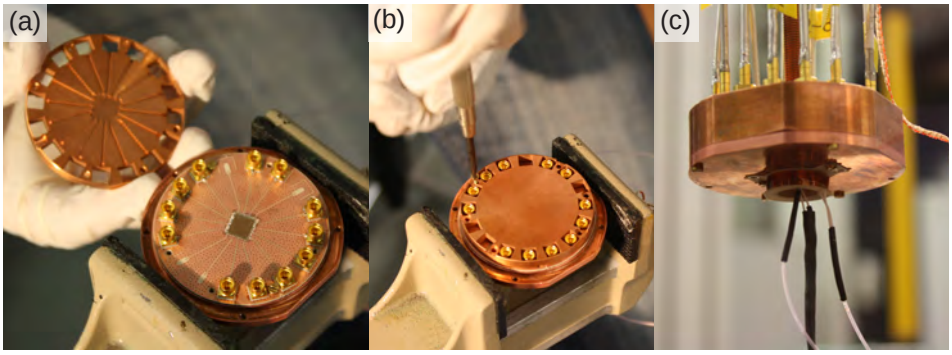

Figure 4.2: (a) 16-port PCB mounted on bottom part of the sample holder. Lid for covering the PCB. (b) Bottom part of the sample holder with PCB and attached lid. (c) Bottom part with coils inserted into top part of the sample holder.

applied to a sample holder which provided bad shielding resulted in drastic improvements of the qubit lifetime. However, the fact that we did not observe an improvement of the qubit lifetime might just show that our sample holder protects the qubit well enough such that another (unknown) factor is dominating the qubit decay. Once this factor has been identified and eliminated, a better shielding might still be necessary to further increase qubit lifetimes.

Since the sample is sensitive to magnetic fields it is necessary to protect it from external magnetic field fluctuations. This is done by cylindrical shields made from a metal alloy with high magnetic permeability (*Cryoperm*), reducing the external magnetic field at the location of the sample. The shields for the 8-port and 16-port-sample holder have a wall thickness of 1 mm, an inner diameter of 48 mm and 65 mm and a length of 188 mm and 200 mm, respectively. For the measurements where only the 8-port sample holder is used, both shields are mounted to provide better magnetic shielding.

4.3. Readout schemes

The readout of the qubit state is based on the dispersive shift which affects the effective resonator frequency to be $\omega'_{r,\mathrm{eff}} = \omega'_r \pm \chi$, depending on the state of the qubit, see Eqs. (2.10)–(2.12). By measuring the transmission of the resonator it is therefore possible to infer the state of the qubit. In the first part of this section the technical aspects of resonator transmission measurements in our setup is discussed, followed by an explanation of the experimental procedures for reading out the qubit state. A detailed description of the dispersive qubit-state readout is given in [Bianchetti09, Bianchetti10a], and an approach to understand this measurement in terms of density operators is presented is Sec. 6.2.1.

The resonator transmission is measured with a microwave signal at a frequency ν_{RF} close to the resonance frequency (4 GHz to 10 GHz). The path of the signal inside the cryostat is described in Sec. 4.1 and depicted in Fig. 4.1. The output signal is then processed further at room temperature. The corresponding circuitry is displayed in Fig. 4.3. At first the signal is further amplified by 25 dB with an ultra-low noise amplifier (ULN, *Miteq AFS3-ULN*), high-pass filtered to suppress (amplified) low-frequency noise before amplified again by 27 dB with a low noise filter (LN, *Miteq AFS3-LN*). The additional 3 dB attenuator suppresses standing waves between the two amplifiers. The signal is then down-converted to an intermediate frequency (IF) of typically 25 MHz or 10 MHz with an *IQ*-mixer (*Marki IQ-0714* or *Miteq IRM0408LC2Q*) and a local oscillator. This IF-frequency signal is then low-pass filtered and amplified again with a low-noise filter (LN, *Mini-Circuits ZFL-500LN+*), before it is digitized in a data acquisition (DAQ) board (*Acquiris AP240* or *Nallatech XtremeDSP* with a *Xilinx Virtex 4*-FPGA). The DAQ boards have a sampling rate of 1 GS/s and 100 MS/s, respectively, and are capable of averaging the recorded time traces. The averaging is needed when the signal-to-noise ratio is small, which is typically the case except for the single-shot measurement when using Josephson parametric amplifiers (see Sec. 4.4). DC blocks (*Inmet 8039*) isolate the down-conversion circuitry from the cryostat and the data-acquisition hardware to avoid ground loops in the system.

An example of a resonator transmission readout is shown in Fig. 4.4 (a), where the transmission of a signal is shown as a function of drive frequency and time (blue for low transmission, red for high transmission). The signal

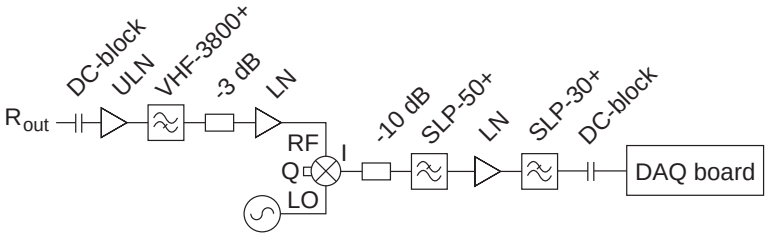

Figure 4.3: Schematics of the down-conversion circuitry. The resonator output R_{out} (see also Fig. 4.1) is amplified and filtered several times down-converted to an intermediate frequency and finally digitized in a data acquisition board. See text for details.

is turned on at a time $\tau = 1.5\,\mu s$ after the beginning of the measurement. Every time trace is a result of many (typically 10^4 to 10^5) averages over the same experimental settings. Far away from the resonance at a frequency $\nu = 7.67\,GHz$ the transmission stays low after turning on the measurement, while at the resonance frequency $\nu_{r0} = 7.695\,GHz$ the transmission rises to a higher value for the rest of the measurement. By integrating every time trace from 1.5 µs to 2.5 µs the spectral lineshape shown in Fig. 4.4 (c) (blue dots) is obtained.

The readout of the qubit state is based on the dispersive shift which changes the effective resonator frequency $\omega'_{r,\mathrm{eff}} = \omega'_r \pm \chi$, depending on the state of the qubit, see Eqs. (2.10)–(2.12). The dispersive shift can be measured experimentally with pulsed spectroscopy. In addition to the measurement above, the same experiment is performed with the qubit transferred to the excited state just before the transmission measurement. In this case the effective resonator frequency is shifted by $2\chi/2\pi$ as shown in Fig. 4.4 (b) and (c) (red dots). These measurements also show that the qubit is decaying during the measurement. For increasing time, the transmission signal at the resonance frequency for the qubit in the excited state $\nu_{r1} = 7.69\,GHz$ becomes weaker while the transmission at the resonance frequency for the qubit in the ground state ν_{r0} becomes stronger. When calculating the spectrum from the time traces the decay is visible as a small peak as indicated with the black arrow in (c). This peak becomes stronger as the integration time is increased.

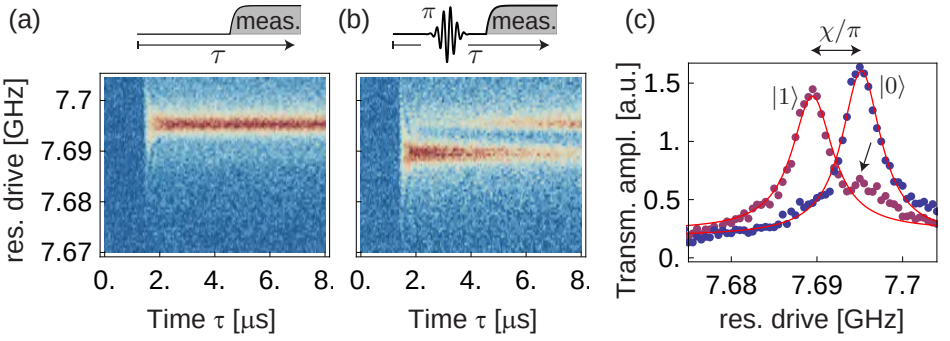

Figure 4.4: (a) Transmission measurement as a function of time for varying resonator drive frequencies with the qubit in the ground state and (b) the qubit in the excited state. (c) Transmission spectra extracted from the measurements in (a,b) and Lorentzian fits (solid red lines). The decay of the excited state is visible in the spectrum (black arrow).

Inferring the excited-state population of an arbitrary qubit state is possible by comparing the time trace of a cavity response of this state to time traces where the qubit is prepared in the ground and excited states. The excited-state population is proportional to the area between the ground state curve and the curve of the state to test, see Fig. 4.5. The linear dependence of the excited state population on the area under the time trace can be understood easiest in the context of single measurements. For every point in time for each single measurement the qubit is either in the ground or the excited state with a certain probability. An average over many realizations gives therefore in time a value which depends linearly on the fraction of qubits that were in the excited state for each point in time.

It should be noted that by using this technique to infer the excited state population, one implicitly assumes that the reference measurements (Fig. 4.5 (a)) are exact. In reality there is typically a small thermal population which leads to a finite probability that the qubit is in the excited state although it is assumed to be in the ground state and vice versa. However this thermal population is not discernible in the presented way of averaged only measurements. Only with single shot measurements it becomes easily possible to detect and quantify it.

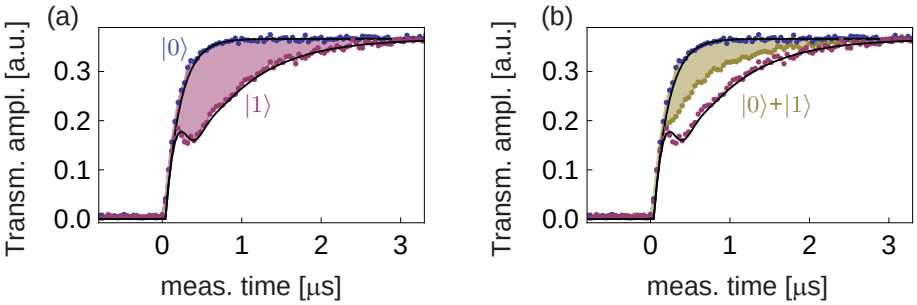

Figure 4.5: (a) Measured time traces for the qubit in the ground (blue dots) and excited (red dots) state. The black lines are fits to cavity Bloch equations [Bianchetti10a]. (b) The area between the time trace of an arbitrary state and the ground state response is proportional to the excited state population.

4.4. Josephson parametric amplifiers

The readout circuitry based on conventional semiconductor amplifiers presented in Sec. 4.3 allows to infer the expectation value of the state of one or several (c.f. Sec. 6.2) qubits by *averaging* over many measurement outcomes. But due to the low signal-to-noise ratio it is not possible to extract useful information from a single measurement. The bottleneck of the readout circuitry is the HEMT-amplifier with a noise temperature of 4 K. The added noise constitutes the dominant part of the measured signal, since it exceeds the signal power coming from the resonator measurement typically by a factor of ~ 40. However, several protocols (e.g. the teleportation protocol presented in Chap. 8) require single-shot readout explicitly, whereas for all other protocols single-shot readout is at least no disadvantage.

The ability to perform single-shot readout in circuit-QED experiments [Mallet09, Vijay11] came only up recently thanks to development of low-noise amplifiers based on Josephson junctions such as Josephson bifurcation amplifiers [Siddiqi04, Vijay09] or Josephson parametric amplifiers (JPA) [Castellanos-Beltran08, Yurke06]. These amplifiers made from superconducting circuits can be operated at the lowest temperature stage of the dilution refrigerator and can amplify a certain signal with theoretically no additional noise.

In this section JPAs are introduced as building blocks enabling single-shot readout and their integration into our measurement setup is described.

4.4.1. Working principle and design

The JPAs were first realized in the QUDEV-Lab by Christopher Eichler as part of his PhD thesis [Eichler13a]. A detailed introduction into the topic can be found therein, a summary of the relevant parts is also given in [Eichler13b].

The JPAs used in our experiments are realized as CPW $\lambda/4$ resonators shunted by an array of SQUIDs, see Fig. 4.6. In contrast to a $\lambda/2$ resonator (Sec. 2.3.2), a $\lambda/4$ resonator has a capacitance on only one end and is shorted to ground on the other end. This imposes the condition that it can support only modes with a voltage anti-node at the capacitor and a voltage node at the short. In a regular $\lambda/4$-resonator the incident wave is reflected and the phase of the reflected wave depends only on the frequency. Since the inductance of SQUIDs depends on the current flowing through them, shunting a $\lambda/4$-resonator with SQUIDs realizes a non-linear oscillator. Its reflection coefficient therefore additionally depends on the *power* of the incident signal. Amplification can be achieved in such a device when it is constantly driven at a frequency and power at which the phase of the reflected signal depends sensitively on the power. In this case an additional small signal at the input will induce a large change in the reflected signal.

The SQUIDs also provide flux tunability of the effective resonator frequency. Since the band of amplification is usually a small range around the resonator frequency, the flux tunability allows to match the amplification band to the frequency of the signal to be amplified.

4.4.2. Integration into the setup

To operate a JPA it is necessary to drive ("pump") it at a certain frequency and power. The frequency at which the JPA is operated is determined by the readout frequency of the associated resonator. Therefore the two parameters that have to be tuned are the *magnetic flux* through the SQUIDs and the applied *pump power*. This requires additional circuitry inside the cryostat and – as shown later in this section – also on the room temperature end of the setup.

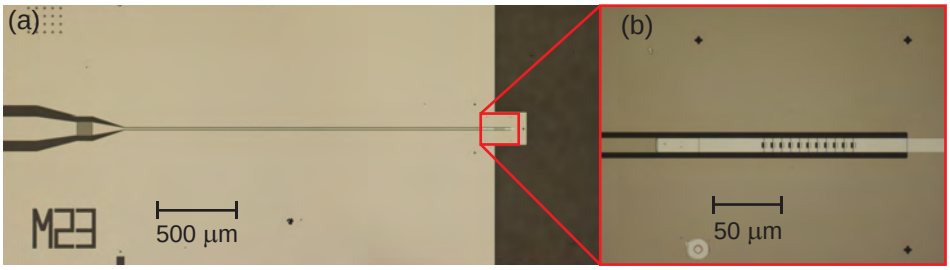

Figure 4.6: (a) Micrograph of one of the used chips with a $\lambda/4$-resonator terminated by an array of 11 SQUIDs. (b) Zoom of the SQUID-array.

The additional cryogenic wiring needed for the integration of one JPA is depicted schematically in Fig. 4.7 (a). In our setup we implemented two JPAs, allowing to read out two resonators at different frequencies in parallel. A photograph of this implementation is shown in Fig. 4.7 (b,c).

The flux tuning is realized with miniature superconducting coils mounted at the bottom of the sample holder as presented in Sec. 4.2. The pump tone (P) is applied to the $\lambda/4$-resonator using a directional coupler. The signal coming from the sample is directed by a circulator (C2 in Fig. 4.7) through the directional coupler (D) into the resonator where it is amplified and reflected. Passing the directional coupler again it is then guided by the circulator (2) towards the room temperature circuitry.

Since the reflected (amplified) signal has a high power compared to the measurement tone applied to the resonator ($\sim +20\,\mathrm{dB}$) and the circulator has a only a finite isolation between its port ($\sim 20\,\mathrm{dB}$), a signal of similar power as the measurement tone would be applied to the sample from its output port, inducing a measurement itself. Therefore, another circulator (1) is placed in between the sample and circulator 2 to further isolate the sample from the leaking amplified signal.

To suppress the reflected pump signal in steady state (i.e. if no measurement signal is applied) a cancellation tone (Cn) is applied to the directional coupler which cancels the reflected pump signal by destructive interference. The cancellation tone must have the same frequency as the pump tone but an amplitude and phase adjusted to cancel the pump tone. This is achieved with the circuitry depicted in Fig. 4.8 (a). The signal form a generator (RF 1/2) is split with a power splitter such that one half of the signal is guided to

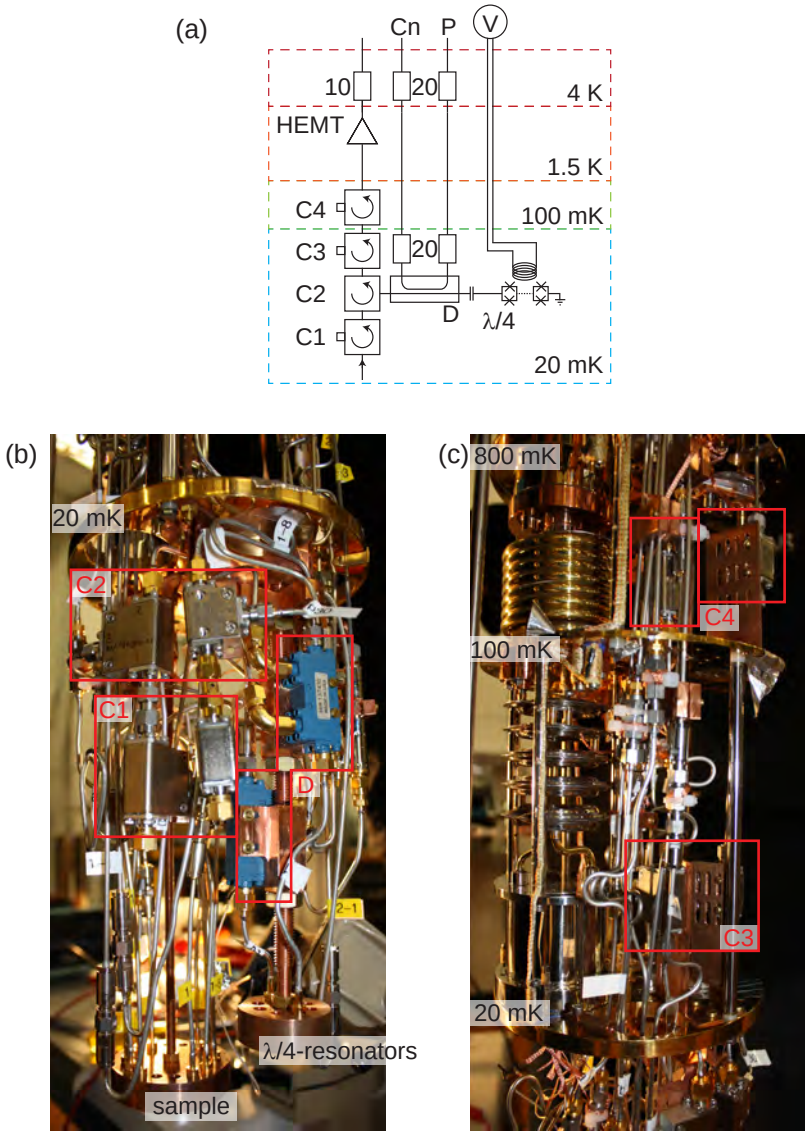

Figure 4.7: (a) Schematic of cryogenic circuitry of the JPA pump and cancellation. (b) Wiring and components connected to the base plate (20 mK) of the dilution refrigerator. (c) Dilution unit and wiring of the cryostat between the base plate (20 mK), 100 mK-plate and still-plate (800 mK).

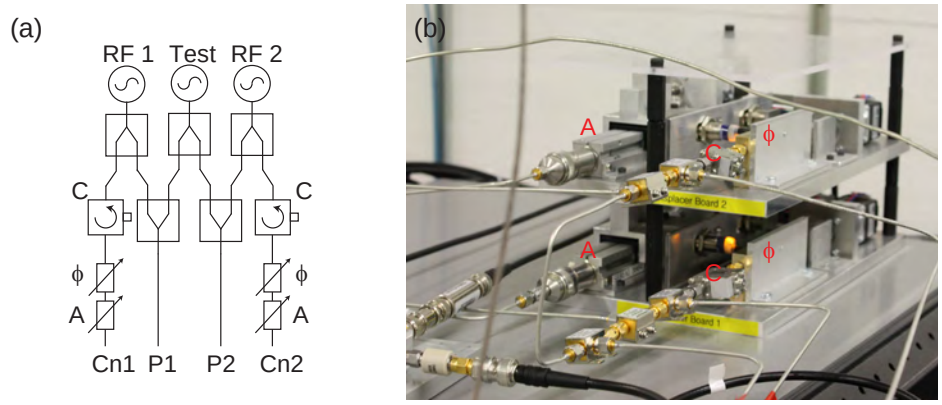

Figure 4.8: (a) Schematic of the room temperature JPA pump and cancellation circuitry. (b) Photograph of the implementation.

the pump line and the other half goes through computer-controlled variable attenuator and phase shifter which allow to adjust the cancellation tone. A circulator is included into the cancellation path to suppress reflections coming from the variable attenuator and phase shifter. To automate the calibration of the JPAs and the cancellation circuitry and to make it independent of the used sample, another signal generator (Test) is connected to the pump lines of both JPAs which can be used to inject a signal simulating the measurement signal into the $\lambda/4$ resonator.

Typical characterization measurements for one of the JPAs used in the teleportation experiment (Chap. 8) are shown in Fig. 4.9. In (a) the resonance frequency of the $\lambda/4$ resonator is shown as a function of the applied magnetic field. This measurement is performed in the linear regime, i.e. in the regime with a very weak power dependence of the reflection. The fact that it shows an irregular behavior comes from the anisotropic coupling of the SQUIDs to the coil. In general, if more SQUIDs are used the flux dependency of the resonance frequency becomes more irregular. The plot in (b) shows the reflection coefficient of the real and imaginary part at one particular coil bias voltage. In (c), a characterization of the system noise is shown in analogy to the measurements in [Eichler11]. From this measurement a system noise $N_{\mathrm{system}} \approx 29$ noise photons dominated by the HEMT amplifier noise can be extracted.

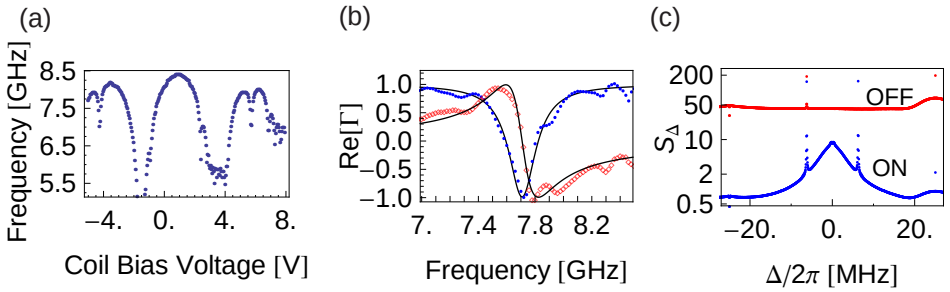

Figure 4.9: (a) Measured resonance frequency versus magnetic coil bias voltage. (b) Measured real (blue dots) and imaginary (red diamonds) parts of the reflection coefficient Γ in the linear regime. (c) Measured gain G_Δ (blue dots) and power spectral density (red dots) for a fixed pump tone as a function of detuning Δ.

Once a coil bias voltage with the desired resonance frequency has been found, the pump power and the coil bias are swept around this point in order to find the optimal settings. The coil bias has also to be swept, since due to the current dependent inductance of the SQUIDs, the pump power also changes the resonance frequency. For a chosen pair of coil bias/pump power one can then record the *gain curve* of the JPA at this point. This is done by measuring the reflection as a function of the test-signal frequency, once with the pump tone on, and once without the pump tone to calculate the absolute amplification. The gain curves for the two JPAs at the points used for the teleportation experiment are shown in Fig. 4.10. Whereas the gain curve shown in (a) shows a Lorentzian line shape (red line), the curve in (b) shows a broadened curve. This behavior can occur when higher-order non-linearities become significant and can no longer be explained by a simple model [Eichler13a].

As a remark it should be noted that even with the JPA circuitry implemented it is still possible to perform measurements without using the JPA, since turning off the pump tone will just reflect any incoming signal of a given frequency with a constant phase shift. However, there will be an extra loss due to the additional components in comparison to a circuit without the JPA.

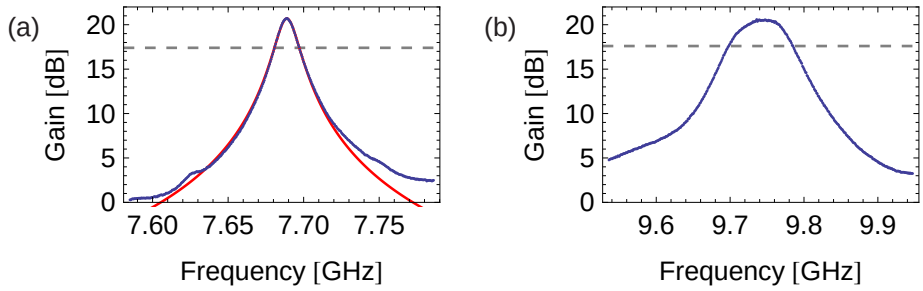

Figure 4.10: Gain curves of the two parametric amplifiers at the frequencies used for the teleportation experiments. The red curve in (a) is a Lorentzian-shaped fit. The dashed lines are drawn 3 dB below the maximal gain.

4.4.3. Single-shot readout

An example of single-shot traces is shown in Fig. 4.11. At first the data acquisition is turned on (I.) without a measurement pulse applied to the resonator. It shows the noise coming mostly from the various amplification stages. Then a first measurement pulse of 500 ns length is sent to the resonator (II.). In this measurement the readout was tuned such that the amplitude is either higher ($|1\rangle$) or lower ($|0\rangle$) than the noise signal. In most cases the qubit is measured to be in the ground state as expected (colored traces). However in $\approx 5 - 10\,\%$ of the traces, depending on the exact qubit frequency, the qubit is found to be in the excited state due to thermal excitation (black trace). This first measurement can be used to herald a proper ground state before doing any operations. In post-processing the measurements where the qubit did not start in the ground state can be discarded. After this heralding measurement operations can be executed while the measurement tone is off (III.) before the measurement tone is turned on again to measure the final qubit state (IV.). In the data shown either no pulse has been applied (blue trace) or a π pulse has been applied (other traces) to the qubit. It can be seen that the blue curve (no pulse) is still in the $|0\rangle$ state while the other colored curves show the qubit to be in the $|1\rangle$-state. The qubit that was in the $|1\rangle$ state before the operation (black curve) has been transferred to the $|0\rangle$-state. It is also

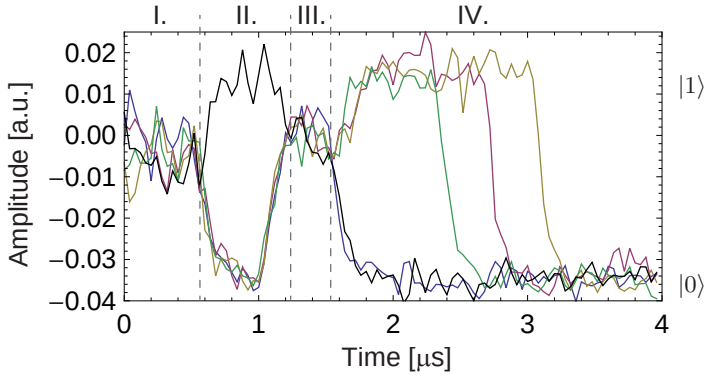

Figure 4.11: Different single-shot traces. (I.) The data acquisition is running but no measurement pulse is applied to the resonator. (II.) A measurement pulse is applied to herald the ground state. (III.) Either no pulse (blue trace) or a π pulse (other traces) is applied to the qubit, followed by turning on the measurement signal again (IV.).

visible that the excited state decays at random times, with a distribution related to the energy relaxation time. However during measurement the qubits normally decay faster than with the typical energy relaxation time T_1 since with high measurement power, non-linear interactions neglected in the dispersive approximation become apparent [Boissonneault08]. These spontaneous "quantum jumps" have been first observed in superconducting circuits in [Vijay11].

For obtaining the final qubit state, every trace in (IV.) is integrated for a time τ_{int} and the resulting value is compared to a threshold determining whether the qubit is in a $|0\rangle$ or $|1\rangle$ state. The optimal threshold can be found as follows. By preparing the qubit in a state $|0\rangle$ and $|1\rangle$ and integrating many time traces, one obtains histograms which show the distribution of integrated values for the two cases, as shown in Fig. 4.12 (a,b). By integrating the counts and normalizing the value to the number of total counts, the "S curves" shown in (c) are obtained. The difference of the two curves is a measure for the readout fidelity as a function of the chosen threshold. The maximum is at the optimal threshold for distinguishing the two states for the integration time τ_{int}. The data in Fig. 4.12 has been integrated for 200 ns, to find the overall maximum readout fidelity, the same

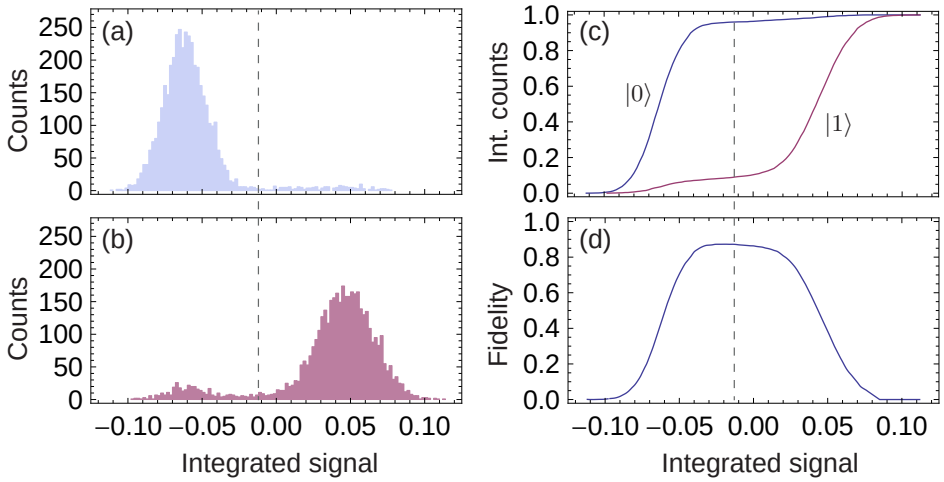

Figure 4.12: Histograms of the integrated single-shot traces when preparing the qubit in the (a) $|0\rangle$ and (b) $|1\rangle$ state. (c) The integrated counts of the two histograms in (a,b) allow to calculate the readout fidelity F (d). Its maximum $F_{\max} = 87.3\,\%$ is at the optimal threshold (dashed line) for distinguishing $|0\rangle$ and $|1\rangle$ states.

measurements have to be performed for different integration times.

The histogram in (b) when the qubits are prepared in the excited state shows more false counts (small peak on the left) than the histogram for the ground state (a). This indicates that the readout fidelity is limited by the qubit decay.

As mentioned in Sec. 4.3, by passive initialization (i.e. waiting for a long time such that the qubit decays into the ground state) the measurements which are not initialized properly are nevertheless averaged with the other measurements. By normalizing to reference measurements these effects are corrected implicitly and are not discernible in the final data. Single-shot readout however allows to observe the amount of thermally excited qubits and can be used for heralding the ground state.

The heralding can be viewed as an initialization by measurement [Ristè12b] in contrast to passive initialization which does not provide a high-quality ground state. In addition, active initialization schemes have been imple-

mented in superconducting circuits using sideband-cooling [Valenzuela06], coupling to spurious two-level systems [Mariantoni11], temporal control of the relaxation rate [Reed12], or using a feed-back loop [Ristè12a].

4.5. Conclusion

In this chapter our setup is presented which is used to measure samples with a circuit QED architecture. To be able to observe quantum effects in the sample, it has to be cooled down to millikelvin temperatures with a dilution refrigerator. Carefully designed cabling allows to send control and readout microwave signals to the sample while still isolating it from room-temperature noise. To be able to implement a new generation of experiments, a sample holder and a PCB were introduced which allow to connect up to 16 microwave transmission lines to a chip. The method to read out the qubit state is based on a transmission measurement of the resonator. Since the effective resonance frequency of the cavity depends on the qubit state, the transmission of a microwave signal contains information about the qubit state. By repeatedly preparing a certain qubit state and recording the time-resolved cavity transmission, the expectation value of the excited state population of the qubit can be inferred. Finally the Josephson parametric amplifier is introduced which amplifies the signal transmitted through the cavity while at the same time introducing only a negligible amount of noise. This allows to perform single-shot measurements, a crucial element of the teleportation experiment in Chap. 8.

5

Qubit manipulation

In this chapter we show how to manipulate a transmon qubit in order to implement single- and multi-qubit gates. We use two different methods to control the qubit: Applying microwave radiation to control the state of the qubit and changing the magnetic flux to control the transition frequency. For both methods we implemented individual control lines which couple to a specific qubit and have little cross-talk to other qubits.

5.1. Microwave control

The state of a qubit is controlled by applying a coherent microwave signal with frequency $\omega_\mathrm{d}/2\pi$ near the qubit transition frequency $\omega_\mathrm{q}/2\pi$. For a qubit drive with drive amplitude $\mathcal{E}(t)$ and phase φ, the effective Hamiltonian for a qubit in a frame rotating at the drive frequency $\omega_\mathrm{d}/2\pi$ can be written as [Blais07, Baur12a]

$$H_\mathrm{drive} = \frac{\Delta_\mathrm{q}}{2}\hat{\sigma}_z + \frac{\Omega_\mathrm{Rabi}(t)}{2}\left(\cos(\varphi)\hat{\sigma}_x + \sin(\varphi)\hat{\sigma}_y\right), \tag{5.1}$$

with $\Delta_\mathrm{q} = \omega_\mathrm{q} - \omega_\mathrm{d}$ the detuning of the qubit transition frequency from the drive and $\Omega_\mathrm{Rabi}(t) \propto \mathcal{E}(t)$ the Rabi frequency. This Hamiltonian shows several important aspects of the qubit drive. At first since the operators $\hat{\sigma}_x$ and $\hat{\sigma}_y$ represent rotations around the x- and y-axis of the Bloch sphere, qubit rotations around arbitrary axes lying on the equator of the Bloch sphere can be realized by changing the phase φ of the qubit drive. Second,

a detuning between the drive and qubit frequency induces a rotation about the z-axis of the Bloch sphere.

In practice, a drive pulse is generated by amplitude and phase modulation of a coherent and phase-stable constant microwave signal. This is implemented with an IQ-mixer which multiplies the coherent signal with the complex amplitude of an envelope function generated by an arbitrary waveform generator (AWG) [Schmidlin09, Baur12a].

The pulses are applied to the transmon qubit via charge gate lines. These are CPW transmission lines which couple capacitively to the qubit as shown in Fig. 5.1. The gap between the end of the transmission line and the transmon qubit allows for some flexibility in choosing the coupling during the design/fabrication of the transmon by changing the length of the extension from the transmon to the gate line. The coupling properties of a charge bias line to a transmon qubit are discussed in [Steffen08].

In the Hamiltonian (5.1) the transmon is approximated as a two-level system. For short pulses however, this approximation becomes inaccurate since the bandwidth $B = 1/2\pi\sigma$ of a Gaussian pulse with standard deviation σ can become similar to the anharmonicity of the transmon (e.g. $B = 320\,\mathrm{MHz}$ for $\sigma = 2\,\mathrm{ns}$). In this case a pulse can induce a temporary population of the $|2\rangle$-level during the pulse inducing an additional phase rotation which reduces the pulse fidelity. This problem can be eliminated by using optimal pulse control as theoretically described in [Motzoi09, Gambetta11] and first used in [Chow10a]. In addition to the normal pulse envelope used to modulate one field quadrature (I), the so-called DRAG pulse uses the derivative of this envelope to modulate the other drive field quadrature (Q).

The standard single-qubit gate calibration measurements are shown in Fig. 5.2. In a Rabi oscillation experiment [Rabi37, Vion03] (a) a single Gaussian shaped microwave pulse with constant length (typically $\sigma \in [2, 5]\,\mathrm{ns}$) is applied and the resulting $|1\rangle$-population is measured as a function of the pulse amplitude. According to Eq. (5.1), this induces a rotation around the x-axis of the Bloch sphere for the time of the pulse. Since the speed of this rotation – the Rabi frequency Ω_{Rabi} – is proportional to the drive amplitude, the $|1\rangle$-population evolves sinusoidally with the drive amplitude. A sinusoidal fit (red line in (a)) can be used to extract the amplitude for $\pi/2$ and πpulses. As an alternative, the Rabi experiment can also be performed with constant amplitude and varying pulse length

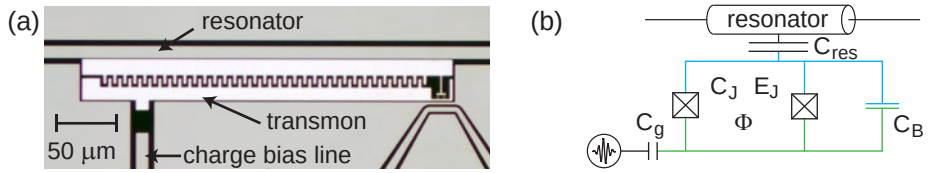

Figure 5.1: (a) Micrograph of a transmon qubit coupled to a resonator and a charge bias line, (b) simplified equivalent circuit.

as described in [Bianchetti09]. It should be mentioned that all these measurements are averaged measurements which potentially suffer from some residual thermal population as discussed in Sec. 4.3 and Sec. 4.4.

The Ramsey experiment [Ramsey50, Vion03] (b) consists of two $\pi/2$ pulses around the x-axis with a variable time delay τ between the pulses, and a measurement of the excited state population directly after the second pulse. The first $\pi/2$ pulse will bring the qubit to a superposition state (equator of the Bloch sphere). In case of no delay time ($\tau = 0$) the second pulse immediately brings the qubit to the excited state. From Eq. (5.1) it can be seen that if the drive frequency is detuned from the pulse frequency a rotation around the z-axis is induced, even if the pulse amplitude is zero, i.e. also during the waiting time. The action of the second $\pi/2$ pulse onto the qubit can also be interpreted as that it maps the population of the y-axis onto the z-axis. Therefore the result shows the $|i\rangle$ population just before the application of the second pulse. The measured population therefore oscillates with the detuning frequency and can be used to extract the exact qubit frequency. An exponentially damped sinusoidal fit allows to extract the detuning as well as the decoherence time T_2^* (see Appendix B). In order to calibrate the drive frequency, a certain offset (typically 4 MHz) is set intentionally in order to facilitate the fitting since a low frequency oscillation can be hard to distinguish from decay.

The experiment presented in (c) serves to calibrate the DRAG [Motzoi09, Chow10a, Gambetta11] pulse. As stated above, the pulse envelope on the Q quadrature is the derivative of the envelope of the I quadrature, but multiplied by a constant factor (Q scaling factor) which needs to be determined in a calibration measurement. To do so, two consecutive pulses are applied, the first one a $\pi/2$ pulse around the x-axis and the second one a π pulse

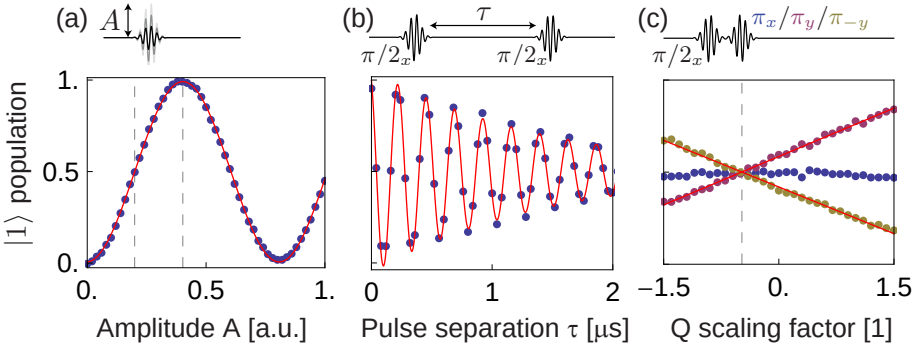

Figure 5.2: Pulse schemes and data of standard single-qubit calibration measurements: (a) Rabi oscillations for calibrating π and $\pi/2$ pulses (dashed lines), (b) Ramsey oscillations for calibrating the detuning, (c) Q-scale measurement for calibrating the DRAG pulses (see text for more details).

around the x-, y- or $-y$-axis respectively. For the case in which both pulses are around the same axis the resulting $|1\rangle$-population is always $1/2$ (blue dots) independent of the scaling factor, since it is calibrated with the Rabi experiment to behave in such a way. However if the first pulse induces a phase error, this can be made visible when the second pulse rotates around the y or $-y$ axis (red and yellow dots, respectively). The deviation of the final population from $1/2$ is expected to depend linearly from the scaling factor and is opposite for y- and $-y$-rotations, respectively. A linear fit (red lines) to these deviations allows to extract the scaling factor at which all three pulse sequences result in a population of $1/2$ as expected.

During the calibration procedure, these experiments are performed iteratively since a change in one parameter might influence the optimal setting for another parameter.

5.2. Magnetic flux control

As mentioned in Sec. 4.2 the sample holder has miniature superconducting coils attached to it which can provide a flux offset to tune the qubits to a certain operation frequency. But due the large inductance of the coils

and the low pass filtering of the bias voltage, they can only be used to provide a *static* offset, changeable on timescales of milliseconds. Our experiments however require qubit transition frequency control on a timescale of nanoseconds. Fast frequency modulation during the experiment can be achieved with on-chip flux bias lines [DiCarlo09]. These are implemented as CPW transmission lines which pass near the SQUID loop of the transmon qubit. A current applied to the flux bias line induces a magnetic field changing the flux in the SQUID loop and therefore modulating the transition frequency of the qubit. Two different flux line designs used in our lab are shown in Fig. 5.3. The design shown in (a) consists of a CPW transmission line passing by the SQUID. The current is guided away from the transmon to the edge of the chip where the flux line is shorted to the ground of the PCB. This flux line design provides a high bandwidth since the line on the chip has an impedance of 50 Ω everywhere. A drawback of this design is its high capacitive coupling to the qubit which leads to an increased decoherence (c.f. Appendix B). The ground in between the flux line and the SQUID loop was put to decrease the capacitive coupling. The flux line shown in (b) goes into a narrow constriction shortly before the transmon structure passing by the SQUID loop and is then shorted to ground on the chip. This type of flux line has a lower capacitive coupling compared to the type in (a) but since its impedance changes gradually it reflects a part of the current pulse.

The current pulses are generated with an arbitrary waveform generator (*Tektronix* AWG 5014) which has a sampling rate of 1.2 GS/s and a bandwidth of 600 MHz. Since the wiring and other components of the setup act as a filter for these pulses distorting their pulse shape, special care has to be taken in order to control the effective pulse shape that is seen by the qubit. From measuring the response of the setup to a short pulse it is possible to infer corrections that have to be applied to the generated pulse. This procedure is described in detail in [Bozyigit10].

The fast flux lines allow control over the qubit transition frequencies and their interaction with each other through their frequency dependent interaction with the resonator, or the interaction of a qubit with the resonator. By detuning the qubit for a certain time τ by a frequency $\Delta\nu$, the excited state acquires a phase $\phi = \tau\Delta\nu$, similar to a Ramsey experiment. We use this technique to implement z-rotations e.g. in the Toffoli gate as described in Sec. 7.2. In the following Sec. 5.2.1 it is shown how to use the frequency

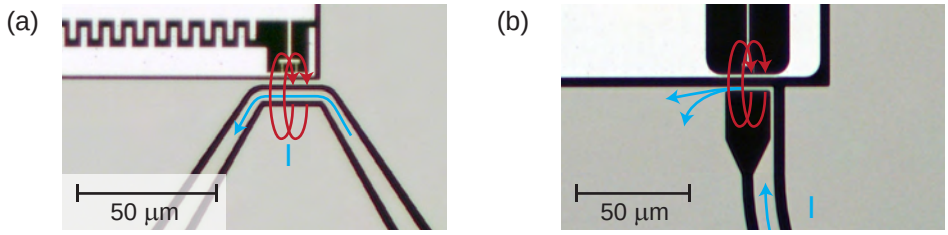

Figure 5.3: Micrograph of two different fast flux bias line designs. Current flow is indicated with blue arrows, magnetic flux with red arrows. (a) Flux bias line which guides the current away from the chip and is shorted to ground at the PCB (b) flux bias line which is shorted to ground directly on chip.

tuning to allow a controlled interaction of the qubit with the resonator to investigate its properties. In Sec. 5.2.2 the fast flux tuning is used to realize two-qubit gates.

5.2.1. Qubit-resonator interaction

Solving the Jaynes-Cummings Hamiltonian Eq. (2.8) for a two-level system and a single mode of the electromagnetic field (see e.g. [Yamamoto99, Walls08, Scully97]) reveals the phenomenon of *vacuum Rabi oscillations*: If the system is prepared in a state $|1\rangle \otimes |n = 0\rangle = |1, n = 0\rangle$ where the qubit is in the excited state and the cavity is empty, then as soon as the Jaynes-Cummings interaction is turned on the two systems start to coherently exchange the excitation with an (angular) frequency $\Omega_\mathrm{R} = \sqrt{(2g)^2 + \Delta_0^2}$, called the vacuum Rabi oscillation frequency, with $\Delta_0 = \omega_{01} - \omega_\mathrm{r}$ the detuning.

The exchange of the excitation is however only complete when the qubit and cavity are on resonance $\Delta_0 = 0$. In the case of a finite detuning the maximal theoretical cavity population will be $(2g)^2/((2g)^2 + \Delta_0^2)$. This allows to control the strength of the interaction by tuning the frequency of the qubit into or out of the resonator, effectively turning the interaction on or off. Of course the analog conditions apply in the situation where the cavity is initially in the one-photon Fock state and the qubit in the ground state.

In spectroscopic measurements, these oscillations manifest themselves as the vacuum Rabi mode splitting (or normal-mode splitting) and have been first observed in a cavity QED experiments with atoms in a cavity reported in [Thompson92] and in superconducting circuits in [Wallraff04]. Time resolved vacuum Rabi oscillations have been first observed in [Brune96] in cavity QED and in [Johansson06, Hofheinz08] in superconducting circuits. It should be noted that the observation of a vacuum Rabi mode splitting or oscillations is only possible in systems with strong coupling, i.e. where the coupling g is larger than the cavity or qubit decay rates.

In our experiments performed in [Fink10b], we used this technique to tune a qubit in the ground state into a resonator to which white noise with different power spectral densities S_n was applied as shown in the pulse sequence in Fig. 5.4 (a). The noise generates a quasi-thermal field inside the cavity with an average photon number $n_{\mathrm{th}} = S_n/\hbar\omega_{\mathrm{r}} + n_0$ with $n_0 \approx 0.04$ photons the thermal background field. This thermal photon number can also be expressed in terms of an equivalent cavity field temperature T_c through $n_{\mathrm{th}} = [\exp(\hbar\omega_{\mathrm{r}}/k_{\mathrm{B}}T_c) - 1]^{-1}$.

By measuring the qubit population after bringing the qubit into resonance with the resonator as a function of the interaction time we can observe vacuum Rabi oscillations with a low final qubit population as shown in Fig. 5.4 (b). By fitting the measured data to a master equation simulation (see Appendix B) incorporating two qubit states, six cavity states, the qubit and cavity decay the equivalent cavity field temperature T_c can be extracted for different noise powers S_n =−214 dBm/Hz to −202 dBm/Hz in steps of 3 dBm/Hz.

The oscillations at low noise power show long coherence times but low contrast. For an increasing thermal field, the amplitude of the coherent oscillations increases while the coherence time decreases, as expected for a thermal distribution of photon numbers. For higher noise powers the qubit approximation breaks down and one would have to measure the population of the higher excited transmon states to reliably fit the data. However with spectroscopic measuremnts it is possible to fit the spectrum of the system where the qubit is permanently tuned into the cavity for equivalent resonator field temperatures of up to $T_c \sim 100$ K as discussed in detail in [Fink10b, Fink10a].

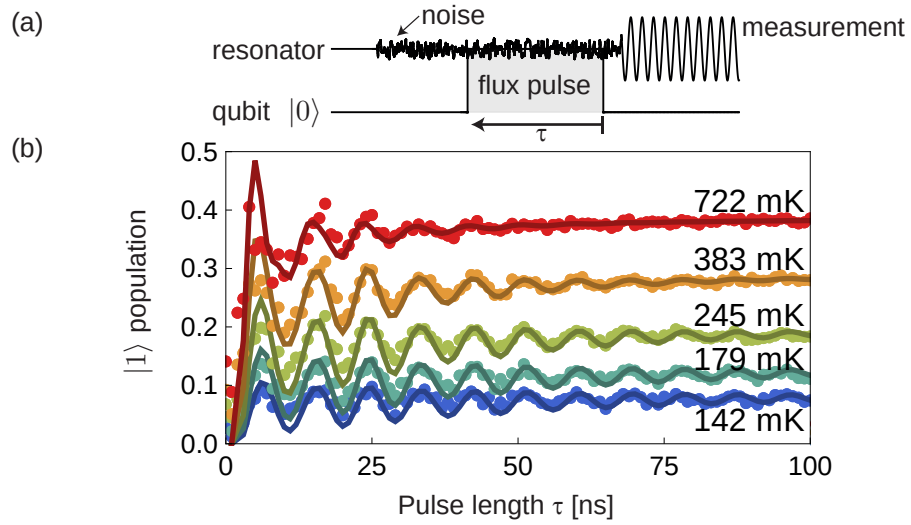

Figure 5.4: (a) Pulse sequence for measuring the qubit excited state population as a function of the resonant cavity interaction time τ, (b) data (dots) and master equation simulation (lines) for different noise levels.

5.2.2. Two-qubit gates

Mulit-qubit gates are necessary for implementing quantum algorithms. Since a two-qubit CPHASE-gate together with arbitrary one-qubit operations form a universal set of quantum gates, this gate is particularly interesting for an implementation.

In the dispersive regime the Hamiltonian of two qubits coupled to a single mode of a cavity can be written as [Blais07]

$$H_{2q}/\hbar = \sum_{j=1,2} \frac{\omega_{01}^{(j)}}{2}\hat{\sigma}_z^{(j)} + (\omega_r + \sum_{j=1,2} \chi_j \hat{\sigma}_z^{(j)})\hat{a}^\dagger\hat{a} + J_{00}(\sigma_-^{(1)}\sigma_+^{(2)} + \sigma_-^{(2)}\sigma_+^{(1)}). \tag{5.2}$$

In addition to the terms known from Eq. (2.10), the last term (called J-coupling or transverse coupling) describes a coupling between the $|01\rangle \leftrightarrow |10\rangle$-states of the qubits which enables a coherent exchange of a single quan-

tum between them at a rate

$$J_{00} = \frac{g_{01}^{(1)} g_{01}^{(2)} (\Delta_{01}^{(1)} + \Delta_{01}^{(2)})}{2\Delta_{01}^{(1)}\Delta_{01}^{(2)}}, \tag{5.3}$$

where $g_{01}^{(i)}$ and $\Delta_{01}^{(i)}$ are the qubit-resonator coupling and the qubit-resonator detuning for qubit i, respectively.

This coupling is an effective qubit-qubit coupling mediated via the exchange of virtual cavity photons [Blais04, Gywat06]. It is present in the complete absence of any direct qubit-qubit coupling and allows to use the cavity as a "quantum bus" [Majer07, Sillanpää07] for long-range non-local interactions between two or more distant qubits. In addition, since only virtual photons are exchanged via the cavity, the cavity-induced relaxation (Purcell effect, see Appendix B) does not affect this type of interaction. Furthermore, the coupling term is only energy conserving when both qubits have the same transition frequencies. This process is effectively suppressed when the detuning between the qubits becomes large compared to J. This gives us the possibility to control this process by controlling the qubit transition frequencies.

In the case of transmon qubits coupled to a cavity, similar processes are present also for non-computational states. In particular the coupling between the $|11\rangle \leftrightarrow |20\rangle$ states is interesting as it allows to implement a CPHASE-gate. This mechanisms was first proposed in [Strauch03] and then implemented in superconducting circuits in [DiCarlo09, DiCarlo10]. The relevant coupling term in this case is $J_{10}(|20\rangle\langle 11| + |11\rangle\langle 20|)$, where J_{10} is analog to J_{00} in Eq. (5.3) but with coupling constant $g_{12} = \sqrt{2}g_{01}$ [Fink08] and detuning $\Delta_{12} = \omega_{12} - \omega_r$ for the first qubit. In case of large qubit-resonator detuning where $\Delta_{01} \approx \Delta_{12}$ this gives $J_{10} \approx \sqrt{2}J_{00}$.

In experiments this can be used to implement a CPHASE-gate (see Sec. 2.1.3) as follows. The qubits are tuned to idle frequencies, i.e. kept at constant frequencies, such that their interaction is strongly suppressed. This is done by applying a flux offset with the miniature coils such that the states $|01\rangle$ and $|10\rangle$ are well separated in frequency space, typically >0.5 GHz to 1 GHz. A fast current pulse applied to the magnetic flux line of one qubit changes its frequency such that the $|11\rangle$ state becomes degenerate with the $|20\rangle$ state. This is the case when $\omega_{01}^{(1)} + \omega_{01}^{(2)} = \omega_{02}^{(1)} = 2\omega_{01}^{(1)} + \alpha$ which leads to the condition $\omega_{01}^{(2)} = \omega_{01}^{(1)} + \alpha^{(1)}$. Note that the anharmonicity α is a negative

number for transmons and hence the transition frequency $\omega_{01}^{(1)}$ of $|10\rangle$ is higher than $\omega_{01}^{(2)}$ of $|01\rangle$. If the state of the qubits was $|11\rangle$ before the pulse, it will now start to coherently oscillate between the $|11\rangle$ and the $|20\rangle$ state. In time steps of $\pi/2J_{10}$ the state of the two qubits will evolve as

$$|11\rangle \rightarrow i\,|20\rangle \rightarrow -\,|11\rangle \rightarrow -i\,|20\rangle \rightarrow |11\rangle\,, \tag{5.4}$$

returning to the original state after a time $2\pi/J_{10}$. A CPHASE-gate is realized if the interaction is turned off after a time π/J_{10}, when the initial state of the system $|11\rangle$ has evolved to $-\,|11\rangle$. All other computational basis states $|00\rangle$, $|01\rangle$ and $|10\rangle$ have not been affected since neither at the idle frequency nor the $|11\rangle \leftrightarrow |20\rangle$ position do these states interact with any other state.

So far, the *dynamical phase* has not yet been considered. As can be seen from Eq. (5.1), a detuning of the qubit from the drive frequency induces a rotation around the z-axis, i.e. it corresponds to a phase-gate, changing the relative phase between the $|0\rangle$ and $|1\rangle$ state. Tuning the frequency of a qubit with a flux pulse will induce such a phase gate with a phase proportional to the detuning and the time of the pulse. However the extra phase acquired of the qubit that is tuned can be compensated by another phase-gate just after the pulse. This phase-gate can also be implemented by changing the phase of all succeeding single-qubit pulses (which is equivalent to redefining the x- and y-axis on the Bloch sphere). In the experiment we always have to adjust the phases of both qubits, since a finite cross-coupling of the flux lines (typically on the order of 1 – 10 %) also shifts the ideally static qubit.

In general a CPHASE gate can be realized either with the $|11\rangle \leftrightarrow |20\rangle$ or the $|11\rangle \leftrightarrow |02\rangle$ interaction. It is however favorable to tune the qubits in such a way that the $|10\rangle$ and $|01\rangle$ levels do not cross, i.e. the sign of their relative detuning is not changed. Otherwise the $|01\rangle \leftrightarrow |10\rangle$ interaction can induce additional phases that cannot be compensated with additional phase-gates.

In this thesis we always tune the qubits non-adiabatically into and out of the interaction as first realized in [DiCarlo10]. However, adiabatic gates using the discussed transitions are also possible and have been implemented e.g. in [DiCarlo09] or (by also incorporating the third excited state $|3\rangle$) in [Reed12].

The calibration of the flux pulse works as follows, see also Fig. 5.5. A pattern is applied where at first both qubits are excited such that the system

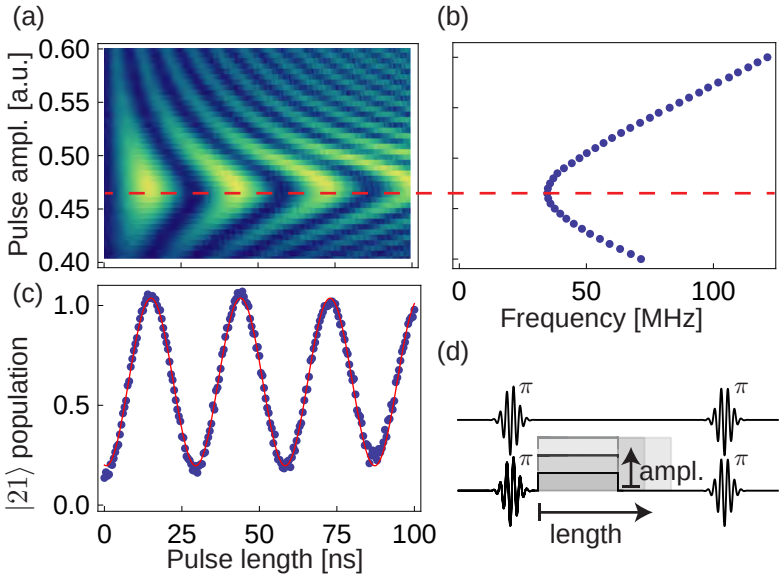

Figure 5.5: Calibration of the flux pulse amplitude and length. (a) Color density plot of an pulse amplitude and length sweep, (b) extracted oscillation frequencies, (c) data and fit of the trace in (a) with the smallest frequency (red dashed line in (a,b)), (d) pulse scheme for the calibration procedure.

is in the $|11\rangle$-state. Then a flux pulse of varying length and amplitude is applied, finally π pulses are applied to both qubits, see (d) for the pulse sequence. After the flux pulse the system is in a superposition state of the form $|\psi\rangle = \alpha\,|11\rangle + \beta\,|20\rangle$. The final π pulses will change this state to $|\psi\rangle = \alpha\,|00\rangle + \beta\,|21\rangle$ which shows a better contrast in the readout.

For every pulse amplitude one can observe an oscillation between these states with a frequency $\Omega/2\pi = \sqrt{(2J_{10})^2 + \Delta^2}/2\pi$, where $\Delta = \omega_{|20\rangle} - \omega_{|11\rangle}$ is the detuning between the two levels. In (a) a color density plot of such a measurement is shown. The corresponding oscillation frequencies, plotted in (b), are extracted by fitting sinusoidals to each time trace. When the two levels are exactly on resonance ($\Delta = 0$) the oscillation frequency is minimal $\Omega_{\min}/2\pi = 2J_{10}/2\pi$ (red line). From the time trace (c) of the corresponding

amplitude one can extract the interaction time. The population in (c) does not go to $|00\rangle$ since the temporal distance between the two π pulses on each qubit is kept constant for every experiment (typically $\approx 200\,\mathrm{ns}$) such that a decay of the initial $|11\rangle$ state is visible as a small offset.

The procedure described above gives a good first estimate for the time and amplitude to use for implementing a CPHASE gate. In a next step these parameters are fine tuned with a Ramsey type experiment where on one qubit two $\pi/2$ pulses are applied with a fixed delay between them and on the other qubit two π pulses are applied at the same times as the pulses on the first qubit. By varying the phase of the second $\pi/2$ pulse an oscillating population for the first qubit is observed. For an optimal CPHASE gate the flux pulse applied in between the two $\pi/2$ pulses should result in an oscillation of the population with a phase shift of 180° compared to the case without flux pulse. The pulse amplitude and time are then changed adaptively until this condition is fulfilled.

5.3. Conclusion

We have seen in this chapter how the quantum states of single and multiple transmon qubits can be manipulated. Microwave pulses applied to gate lines coupling capacitively to the transmon qubits allow to perform single-qubit rotations around an arbitrary axis in the xy-plane of the Bloch sphere. Current pulses applied to gate lines coupling inductively to the SQUID loop allow to tune the qubit transition frequency on a nanosecond timescale. This can be used to implement rotations of the qubit around the z-axis or to tune a qubit to a frequency at which it interacts with the resonator or other qubits by real or virtual photon exchange. This mechanism allows to implement two-qubit CPHASE gates.

6

Measurement of quantum states and processes

In the previous chapters we reviewed how to fabricate a sample with superconducting circuits and implement it into a setup in which it is possible to manipulate the state of a single qubit, perform two-qubit gates and read out the excited state population of a qubit.

In this chapter we will focus on how to characterize quantum states and processes and will present different ways how to visualize this information. In Sec. 6.1 we will see how to describe quantum states, represent this information graphically and how to compare different states. The process of extracting this information from a given quantum state in an experiment is explored in Sec. 6.2 for single-qubit as well as multi-qubit states. Considerations similar as to the ones for quantum states can also be made for quantum processes. This is explained in Sec. 6.3.

6.1. Representation of quantum states

6.1.1. Density matrix and Pauli set

In Sec. 2.1, any one-qubit state was always described as a pure state $|\psi\rangle$, a state on the surface of the Bloch sphere. In reality, however, one can rarely be certain that a given system is in a known pure state. Decoherence in the system or residual coupling of the qubit to the environment reduce our knowledge about the precise nature of the state. Rather we just know that the system is in a certain state $|\psi_i\rangle$ with some probability p_i.

The appropriate way how to describe quantum systems when the exact state is not known with certainty is to use *density matrices* (or "density operators") which are defined as [Nielsen00]

$$\rho = \sum_i p_i \left|\psi_i\right\rangle \left\langle\psi_i\right| . \tag{6.1}$$

The density matrix of a single qubit state is a 2×2 matrix of the form

$$\begin{bmatrix} a & c+id \\ c-id & b \end{bmatrix}, \tag{6.2}$$

with $a, b, c, d \leq 1$ real numbers and $a + b = 1$. The entries a, b represent the probability to find the qubit in the state $|0\rangle$,$|1\rangle$ respectively. The state which is represented by a vector $\vec{r} = (r_x, r_y, r_z)$ on the Bloch sphere (Bloch vector) can be written in the form of a density matrix as

$$\rho = \frac{\mathbb{1} + \vec{r} \cdot \vec{\sigma}}{2}, \tag{6.3}$$

with $\vec{\sigma} = (\hat{\sigma}_x, \hat{\sigma}_y, \hat{\sigma}_z)$ the vector of Pauli matrices. In the Bloch sphere picture, states described by a density matrix can also lie *inside* the Bloch sphere, i.e. $|\vec{r}| \leq 1$, whereas for pure states $|\vec{r}| = 1$.

One special state is the *completely mixed* state, the state lying in the center of the Bloch sphere,

$$\rho_{\text{cm}} = \frac{\mathbb{1} + (0,0,0) \cdot \vec{\sigma}}{2} = \begin{bmatrix} 1/2 & 0 \\ 0 & 1/2 \end{bmatrix}, \tag{6.4}$$

representing the state of a qubit of which we do not have any information. Its density matrix is distinguished from other states on the xy-plane by having vanishing off-diagonal elements.

The state of one qubit can be graphically represented in several different ways as shown in Fig. 6.1. In (a), the equal superposition state $|\psi\rangle = 1/\sqrt{2}\,|0\rangle + (1+i)/2\,|1\rangle$ is shown as a point on the Bloch sphere by calculating the relevant angles as in Eq. (2.1). A graphical representation of the corresponding density matrix is shown in (b) as bar charts of the real and imaginary part respectively. Another way to display the state of a qubit is shown in (c). This is the so called "Pauli set" [Chow10b], the expectation values of the Pauli operators $X = \hat{\sigma}_x$, $Y = \hat{\sigma}_y$, $Z = \hat{\sigma}_z$. In terms of

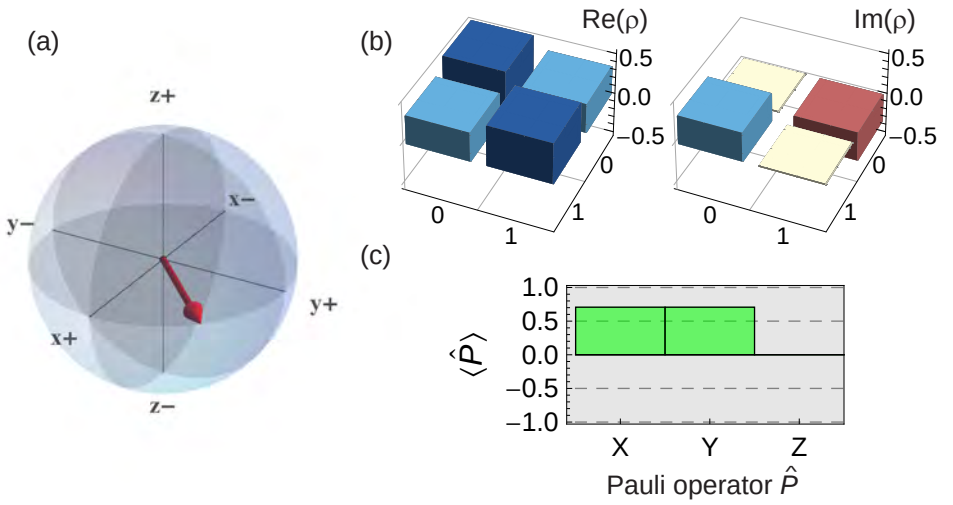

Figure 6.1: Graphical representation of a single-qubit state. State represented as (a) a point on the Bloch sphere, (b) bar charts of the real and imaginary parts of the density matrix, (c) the expectation values of the Pauli operators.

optics, these are also called "Stokes parameters" [Stokes52, Collett93] (and the Bloch sphere is known as "Poincaré sphere"). As expected from a state on the equator of the Bloch sphere, the diagonal elements of the density matrix are both 1/2 and the expectation value of the σ_z-operator vanishes. It is worth to note that for one qubit the Pauli set is just a description of the Bloch vector $\vec{r}$. Hence, since the depicted state lies on the line bisecting the x- and y-axes in the Bloch sphere picture, it has the same expectation values for the Pauli X and Y operators.

In the case of many qubits there is no equivalent of a Bloch sphere picture, but the depiction of the density matrix and the Pauli set can give complementary insights (although they contain exactly the same information) as discussed in the following.

The density matrix for n qubits can be expanded in terms of the compu-

tational basis states

$$\rho_{\mathrm{n}} = \sum_{i,j}^{2^n} m_{ij} \left|i\right\rangle \left\langle j\right|$$

$$= \begin{array}{c} \\ |0\cdots00\rangle \\ |0\cdots01\rangle \\ \vdots \\ |1\cdots11\rangle \end{array} \begin{array}{c} \begin{array}{cccc} |0\cdots00\rangle & |0\cdots01\rangle & \cdots & |1\cdots11\rangle \end{array} \\ \begin{bmatrix} a_{0\cdots00} & & & \\ & a_{0\cdots01} & & \\ & & \ddots & \\ & & & a_{1\cdots11} \end{bmatrix} \end{array} \tag{6.5}$$

with m_{ij} the entries of the matrix where the diagonal elements $a_i = m_{ii}$ are real and the off-diagonal elements $m_{ij} = m_{ji}^*$ are complex numbers, and i, j are a binary representation of an n-qubit computational basis state. This gives a total of 4^n parameters (or $4^n - 1$ if the condition $\mathrm{Tr}[\rho] = 1$ is considered) that are needed to describe the state of an n-qubit system.

The Pauli set for n qubits is the analog of the generalized Stokes parameters in optics. In superconducting circuits it has been first used in [Chow10b] and later in [DiCarlo10, Neeley10]. It is the set of expectation values for all possible operators $\hat{\sigma}_{i1} \otimes \ldots \otimes \hat{\sigma}_{in}$ where each $\hat{\sigma}_i$ is one of the three Pauli matrices and the identity, resulting in 4^n different expectation values that describe an n-qubit quantum state. The n-qubit identity operator which is built only from single-qubit identity operators is usually not shown, since its expectation value is always 1 for any n-qubit state.

6.1.2. Fidelity

For an experimentally implemented quantum state, it is usually interesting to compare it to an ideally expected state. The *fidelity* of two states is a quantification of the similarity of two states. In terms of experimental quantum information processing usually the the fidelity F of a measured density matrix ρ and a pure state $|\psi\rangle$ is defined as the trace of the product of the two corresponding density matrices:

$$F = \mathrm{Tr}[\rho \left|\psi\right\rangle \left\langle\psi\right|]. \tag{6.6}$$

Note that this definition differs from the definition usually used in theory books (e.g. [Nielsen00]), where the fidelity $F' = \sqrt{F}$ is defined as the square

root of our definition. Since $F \leq 1$, F always has a smaller value than F'.

6.2. Measurement of quantum states

In this section, the process of measuring the state of a qubit is explained for three different cases. Sec. 6.2.1 describes the basic case in which one qubit is coupled to a readout resonator. In the case of more than one qubit there are two different possibilities which are examined. The case when two qubits couple to one readout resonator is described in Sec. 6.2.2. The case when two qubits couple to different readout resonators is fundamentally different from the aforementioned case and is the topic of Sec. 6.2.3.

6.2.1. Single-qubit states

The excited-state population of a single qubit in state ρ can be inferred by comparing averaged integrated time-traces of the resonator transmission as described in Sec. 4.3. Here we first revisit this technique in terms of density matrices and explain in the following how to obtain a complete description of a single-qubit quantum state.

The expectation value of a measurement of an observable (measurement operator) $\hat{\mathcal{M}}$ in the state ρ is $\langle\hat{\mathcal{M}}\rangle = \mathrm{Tr}[\rho\hat{\mathcal{M}}]$. Since in our setup we can directly infer the expectation value of the excited-state population from repeated measurements, we effectively perform a measurement in the computational basis. Therefore the measurement operator can be written as

$$\hat{\mathcal{M}}_{\mathrm{1qb}} = \alpha_0 \left|0\right\rangle \left\langle 0\right| + \alpha_1 \left|1\right\rangle \left\langle 1\right|, \tag{6.7}$$

where α_0 and α_1 are the integrated signals of a ground- and excited state response of the resonator, respectively. Integrating the averaged time-trace over many realizations of a state ρ gives an expectation value $\langle\hat{\mathcal{M}}_{\mathrm{1qb}}\rangle_\rho = \mathrm{Tr}[\rho\hat{\mathcal{M}}_{\mathrm{1qb}}]$ from which the excited state population $P_1(\rho)$ can be calculated as

$$P_1(\rho) = \frac{\langle\hat{\mathcal{M}}_{\mathrm{1qb}}\rangle_\rho - \langle\hat{\mathcal{M}}_{\mathrm{1qb}}\rangle_{\rho=|0\rangle}}{\langle\hat{\mathcal{M}}_{\mathrm{1qb}}\rangle_{\rho=|1\rangle} - \langle\hat{\mathcal{M}}_{\mathrm{1qb}}\rangle_{\rho=|0\rangle}} = \frac{\langle\hat{\mathcal{M}}_{\mathrm{1qb}}\rangle_\rho - \alpha_0}{\alpha_1 - \alpha_0}. \tag{6.8}$$

Since the polarization along the z-axis of the Bloch sphere is related to the excited-state population as $\langle\hat{\sigma}_z\rangle = -2(P_1 - 1/2)$, our measurement is

equivalent to a measurement of $\langle\hat{\sigma}_z\rangle$. This can also be seen by rewriting the measurement operator in Eq. (6.7) as

$$\hat{\mathcal{M}}_{1\mathrm{qb}} = \frac{\alpha_0 + \alpha_1}{2}\mathbb{1} + \frac{\alpha_0 - \alpha_1}{2}\hat{\sigma}_z. \tag{6.9}$$

The measurement of $\langle\hat{\sigma}_z\rangle$ alone is not sufficient for the complete characterization of a single-qubit state. One needs the expectation value of the three Pauli matrices (i.e. the Bloch vector) to calculate the density matrix according to Eq. (6.3). If a $\pi/2$ rotation around the x-axis of the Bloch sphere is performed just before the measurement, the state is rotated such that the original polarization along the y-axis now lies on the z-axis. A subsequent measurement allows to infer the polarization along the y-axis before the last $\pi/2$ rotation. Such a measurement, including the $\pi/2$ pulse can therefore be used to obtain an estimate of the expectation value $\langle\hat{\sigma}_y\rangle$. In the same way, a $\pi/2$ rotation around the y-axis just before the measurement allows to estimate $\langle\hat{\sigma}_x\rangle$. In a more formal way this can be understood as

$$\langle\hat{\mathcal{M}}_k\rangle = \mathrm{Tr}[\rho \underbrace{\hat{U}_k^\dagger \hat{\mathcal{M}} \hat{U}_k}_{\hat{\mathcal{M}}_k}] = \mathrm{Tr}[\underbrace{\hat{U}_k \rho \hat{U}_k^\dagger}_{\rho_k} \hat{\mathcal{M}}], \tag{6.10}$$

where $\hat{\mathcal{M}}$ is the measurement operator of the system and $\hat{U}_k$ is one of the mentioned rotations. In the experiments however we always use the *four* different operators $\{\hat{U}_k\} = \{\mathbb{1}, e^{-i\frac{\pi}{4}\hat{\sigma}_x}, e^{-i\frac{\pi}{4}\hat{\sigma}_y}, e^{-i\frac{\pi}{2}\hat{\sigma}_x}\}$, leading to the expectation values of the operators $\hat{\mathcal{M}}_k = \{\hat{\sigma}_z, \hat{\sigma}_y, -\hat{\sigma}_x, -\hat{\sigma}_z\}$. Having these expectation values and putting the following relation (which is a generalization of Eq. (6.3)) into Eq. (6.10),

$$\rho = \frac{r_1\mathbb{1} + r_2\hat{\sigma}_x + r_3\hat{\sigma}_y + r_3\hat{\sigma}_z}{2}, \tag{6.11}$$

we can solve for all the r_i and then calculate the density matrix ρ. The advantage of this method using four measurements is that we do not assume $\mathrm{Tr}[\rho] = 1$, and any deviation from this value hints at systematic errors in the measurement.

As an example of this method typically referred to as quantum state tomography the evolution of a quantum state has been measured as shown in Fig. 6.2. The qubit has been driven with a finite detuning to an initial superposition state and then state tomography was performed as a function

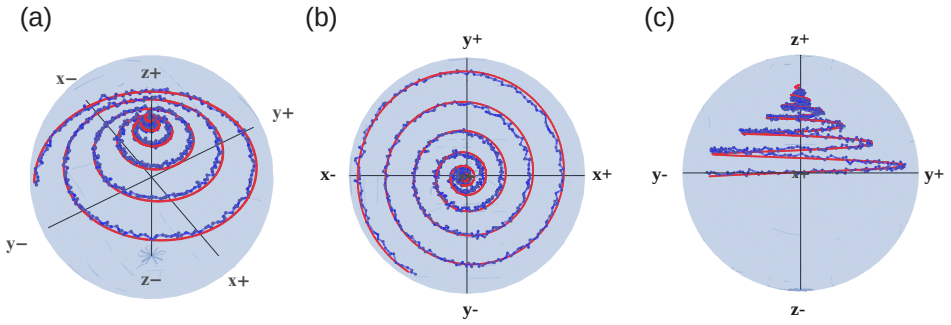

Figure 6.2: Evolution of the state during a Ramsey type experiment. Blue dots are measured data, red solid line is a master equation simulation. (a) General view, (b) view on the xy-plane shows the decoherence, (c) view along the z-axis shows the energy relaxation.

of the waiting time. At first, the detuning is visible as a rotation around the z-axis, the dephasing is visible as the decreasing radius of the spiral and finally also the energy relaxation shows a decrease of z-polarization. To simulate the behavior, we used a master equation (see Appendix B) incorporating the finite detuning, the dephasing- and energy-relaxation times obtained from independent measurements. The good agreement of the data (blue points) with the master equation simulation (red line) shows that the system is well described by the used model.

6.2.2. Joint qubit readout

In the case of n qubits the decomposition of the density matrix in Eq. (6.11) can be generalized to

$$\rho = \frac{\sum_{\vec{v}} r_{v_1,\ldots,v_n} (\hat{\sigma}_{v_1} \otimes \hat{\sigma}_{v_2} \otimes \cdots \otimes \hat{\sigma}_{v_n})}{2^n}, \tag{6.12}$$

where the sum is over all vectors $\vec{v}$ whose entries are $v_i \in \{0, x, y, z\}$ and $\hat{\sigma}_0 \equiv \mathbb{1}$. In order to obtain the 4^n different coefficients $r_{v_1,\ldots,v_n}$, one has to measure 4^n linearly independent expectation values to reconstruct the density matrix. But measuring single expectation values with joint readout

is not as straightforward as in the case for a single qubit or if separate qubit readout would be available (see Sec. 6.2.3).

The measurement operator for two qubits coupled to a resonator reads as follows [Filipp09, DiCarlo09, Chow10b]

$$\hat{\mathcal{M}}_{\mathrm{2qb}} = \beta_{00}\mathbb{1}\otimes\mathbb{1} + \beta_{10}\hat{\sigma}_{z1}\otimes\mathbb{1} + \beta_{01}\mathbb{1}\otimes\hat{\sigma}_{z2} + \beta_{11}\hat{\sigma}_{z1}\otimes\hat{\sigma}_{z2}, \tag{6.13}$$

with $\hat{\sigma}_{zk}$ the Pauli z-operator for qubit k and β_{ij} constants that depend on the resonator decay κ, the dispersive shifts χ_{q1}, χ_{q2}, the relaxation time of the qubits $T_{1,q1}, T_{1,q2}$ and the integration time. In the experiment the constants β_{ij} are derived from time-resolved transmission measurements of the four computational basis states $|00\rangle, |01\rangle, |10\rangle$, and $|11\rangle$, similarly to the case for one qubit described in Sec. 4.3. The integrated signal gives the constants α_{ij} from the measurement operator

$$\hat{\mathcal{M}}_{\mathrm{2qb}} = \alpha_{00}\,|00\rangle\langle 00| + \alpha_{01}\,|01\rangle\langle 01| + \alpha_{10}\,|10\rangle\langle 10| + \alpha_{11}\,|11\rangle\langle 11|\,. \tag{6.14}$$

By subtracting the ground-state response and appropriate scaling, the coefficients can always be chosen such that $\alpha_{00} = 0$ and $\alpha_{11} = 1$. The coefficients β_{ij} can then be calculated as

$$\beta_{ij} = 1/4\left(\alpha_{00} + (-1)^j\alpha_{01} + (-1)^i\alpha_{10} + (-1)^{i+j}\alpha_{11}\right). \tag{6.15}$$

Single-qubit operations $\hat{U}_k = \hat{U}_{k1}\otimes\hat{U}_{k2}$ are used to effectively transform the Pauli z-operators $\hat{\sigma}_z$ in Eq. (6.13) into other Pauli operators as described in Sec. 6.2.1, allowing to get the required 4^n different measurement operators. However, single-qubit operations alone cannot be used to generate non-trivial correlation terms like $\hat{\sigma}_z\otimes\hat{\sigma}_z$ from terms containing the identity operator $\mathbb{1}$ since e.g. $\hat{U}_k^\dagger(\mathbb{1}\otimes\hat{\sigma}_z)\hat{U}_k = \mathbb{1}\otimes(\hat{U}_{k2}^\dagger\hat{\sigma}_z\hat{U}_{k2})$. Therefore it is important that none of the β_{ij} vanishes. Otherwise some coefficients r_{ij} of the density matrix ρ would not be determined as $\mathrm{Tr}[(\hat{\sigma}_k\otimes\hat{\sigma}_l)(\hat{\sigma}_m\otimes\hat{\sigma}_n)] = \delta_{km}\delta_{ln}$, for $k,l,m,n\in\{0,x,y,z\}$ [Filipp09], and full state tomography would not be possible.

As an example for this approach we present a measurement of all four maximally entangled two-qubit states (Bell states) as shown in Fig. 6.3 with an average fidelity for the states of $F = 94.8\,\%$ (after a maximum likelihood procedure [Ježek03, Smolin12, Baur12a] which assesses the most likely physical state for the given measurement data). For this experiment

the qubits Q1 and Q2 of the sample for the teleportation experiment were used. The sample and its parameters are described in Chap. 8. The Bell states are prepared by using single qubit rotations and the CPHASE gate described in Sec. 5.2.2. The first qubit is prepared in a superposition state $|\psi_1\rangle = |0\rangle + |1\rangle$ and the second qubit in one of the states $|\psi_2\rangle = |0\rangle \mp |1\rangle$ by applying $\pi/2$ pulses around the $\pm y$-axis to the qubits. After the CPHASE gate they are in a state $|\psi_{12}\rangle = |00\rangle \mp |01\rangle + |10\rangle \pm |11\rangle$. Applying a $-\pi/2$ pulse to the first qubit and either no pulse or a π pulse around the y-axis to the second qubit allows to generate all four Bell states $|\Phi^{\pm}\rangle = 1/\sqrt{2}\,(|00\rangle \pm |11\rangle)$, $|\Psi^{\pm}\rangle = 1/\sqrt{2}\,(|01\rangle \pm |10\rangle)$. A circuit diagram of this Bell-state preparation algorithm looks as follows:

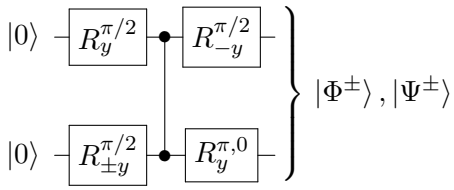

In Fig. 6.4 the Pauli sets of the same measurement data as used to generate Fig. 6.3 is presented. It can be easily calculated from the density matrix ρ as $\langle\hat{\sigma}_i \otimes \hat{\sigma}_j\rangle = \mathrm{Tr}[\rho(\hat{\sigma}_i \otimes \hat{\sigma}_j)]$, for $i, j \in \{0, x, y, z\}$. As expected for maximally entangled states, the single-qubit terms vanish, the only non-zero terms are two-qubit correlations.

The procedure for joint readout is theoretically easily extendable to n qubits. However in practice it will become difficult to perform joint readout with many qubits in one resonator. Not only the number of measurements scales exponentially with the number of qubits, but also the properties of the qubits (i.e. dispersive shifts) need to be such that the qubits can be easily distinguished according to their time trace. Currently, no more than three-qubit joint readout has been implemented [DiCarlo10, Baur12b, Fedorov12, Steffen12].

6.2.3. Separate qubit readout

In the sample described in Chap. 8 it is also possible to create Bell states between the two qubits Q2 and Q3. These qubits couple to a common resonator used as quantum bus for generating entanglement. But this resonator does not couple to any in- and output leads and can therefore not

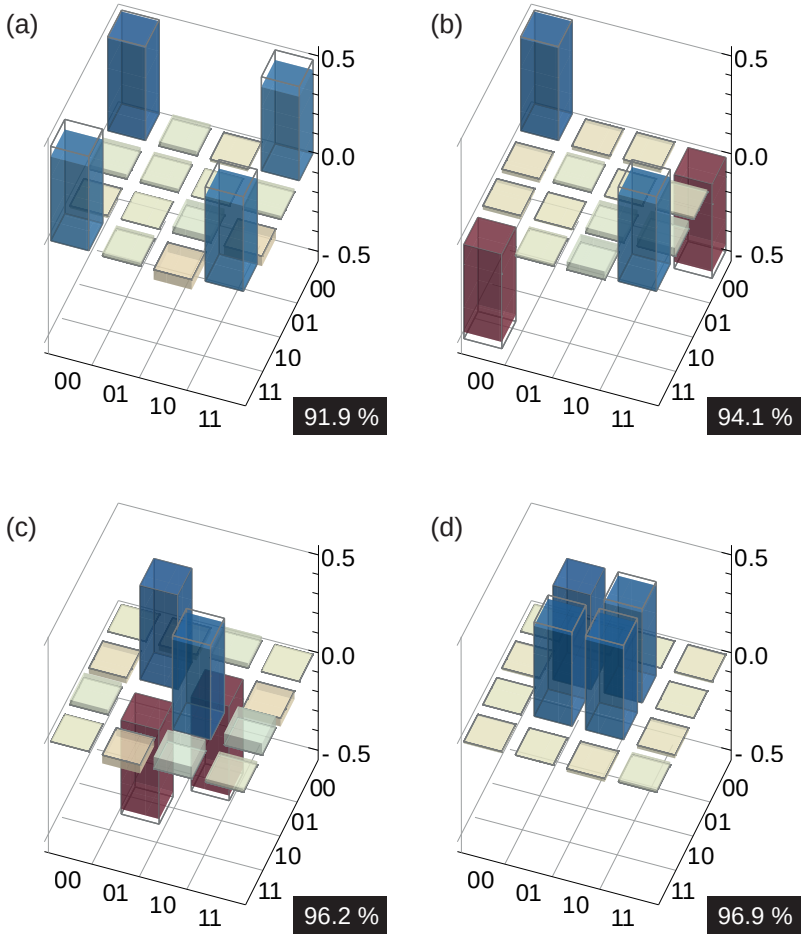

Figure 6.3: Measured real parts of the density matrices of the four Bell states (a-d) $|\Phi^+\rangle, |\Phi^-\rangle, |\Psi^-\rangle, |\Psi^+\rangle$. Wireframes are ideally expected values, colored bars measurement data, the fidelity is indicated in the black boxes.

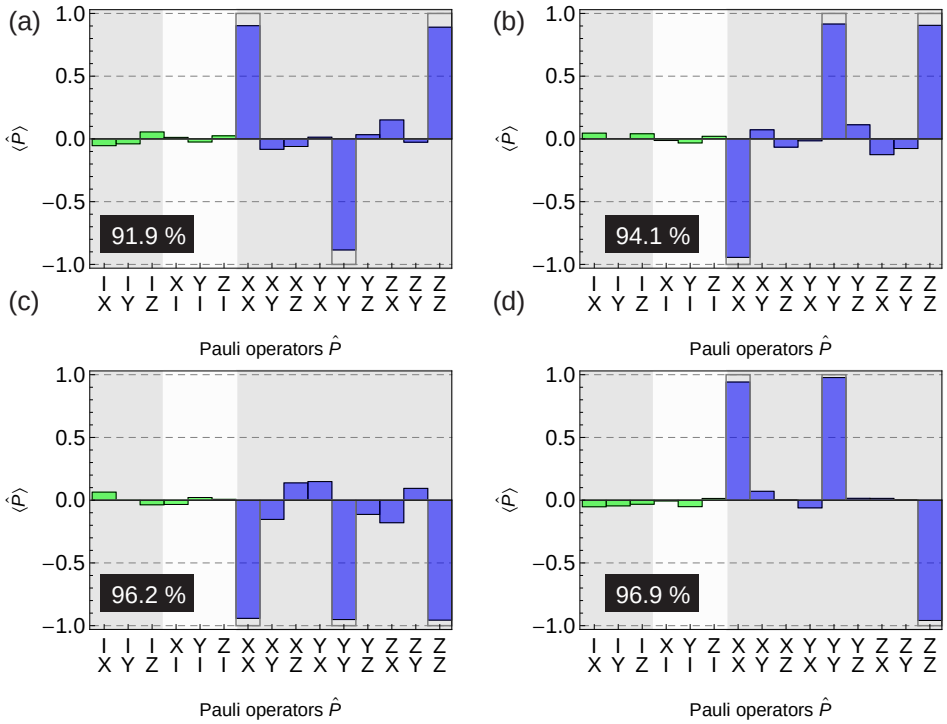

Figure 6.4: Measured Pauli sets of the four Bell states (a-d) $|\Phi^+\rangle, |\Phi^-\rangle, |\Psi^-\rangle, |\Psi^+\rangle$. Wireframes are ideally expected values, colored bars measurement data, the fidelity is indicated in the black boxes.

be used to read out the two-qubit state. Instead, each qubit also couples to an individual readout resonator. In this configuration it is not possible to reconstruct the complete two-qubit density matrix by performing an averaged readout of the individual qubits. The measurement operator for each qubit is the same as for a single qubit, see Eq. (6.9). By only averaging the measurement outcomes for each qubit separately it is therefore not possible to retrieve any information about the correlation term $\hat{\sigma}_z \otimes \hat{\sigma}_z$, but only the expectation values for the individual Pauli operators. As seen in Sec. 6.2.2 the measurement of the correlation term is also not achievable by performing single qubit rotations on the individual qubits. Since every single-qubit measurement realizes a measurement of the $\hat{\sigma}_z$ operator, it is possible to get a measurement of the $\hat{\sigma}_z \otimes \hat{\sigma}_z$ operator by multiplying the individual qubit measurement outcomes before the averaging. Note that in our system the measurement value is derived from the *area* under the time trace, this means one would have to multiply the area of both traces and not the time traces.

For the experiments presented here we exploit the possibility to perform single-shot readout enabled by the JPAs in the setup, see Sec. 4.4. This allows us to obtain a measurement value of ± 1 for every single measurement of the $\hat{\sigma}_z$ operator on each qubit separately, and then obtain the corresponding value for the correlation $\hat{\sigma}_z \otimes \hat{\sigma}_z$ by multiplying the two single-measurement outputs. Averaging the single- and two-qubit operators gives directly the expectation values of the corresponding Pauli operator, i.e. the components of the Pauli set. Again, single-qubit operations performed before the measurement allow to infer all combinations of the $4^n - 1$ non-unity Pauli operators.

As seen in Sec. 4.4, an important difference between the averaged readout and the single-shot readout is that with averaged readout one implicitly corrects for measurement errors due to finite thermal excitation of the qubits and spontaneous qubit relaxation.

In single-shot readout this is not the case. The finite thermal excitation can be suppressed by heralding the ground state as shown in Sec. 4.4. The finite readout fidelity due to qubit relaxation or excitations occurring during qubit operation is however not corrected implicitly. Qubits that decay before or during the measurement will induce measurement errors that reduce the fidelity of the final state compared to an averaged readout. To be able to compare the fidelities of the two readout methods, one can

correct the results from the single-shot measurements for these errors. In the following the error-correction procedure, similar to the one described in the supplementary material of [Steffen06a, Bialczak10], is described.

For one qubit, let f_0 and f_1 be the probabilities of correctly identifying the states $|0\rangle$ and $|1\rangle$, respectively. These probabilities can be determined experimentally. By repeatedly preparing and measuring these states in single-shot experiments, one can extract f_0 and f_1 as the fraction of correct identifications. By defining P_0 and P_1 as the real ground- and excited-state populations of the qubit, the measured populations $P_{\mathrm{m}0}$ and $P_{\mathrm{m}1}$ can be written as

$$\underbrace{\begin{bmatrix} P_{\mathrm{m}0} \\ P_{\mathrm{m}1} \end{bmatrix}}_{\vec{P}_{\mathrm{m}}} = \underbrace{\begin{bmatrix} f_0 & 1-f_1 \\ 1-f_0 & f_1 \end{bmatrix}}_{F} \underbrace{\begin{bmatrix} P_0 \\ P_1 \end{bmatrix}}_{\vec{P}}. \tag{6.16}$$

The real (or rather the corrected) populations can now be calculated as $\vec{P} = F^{-1}\vec{P}_{\mathrm{m}}$ with

$$F^{-1} = \frac{1}{f_0 + f_1 - 1} \begin{bmatrix} f_1 & f_1 - 1 \\ f_0 - 1 & f_0 \end{bmatrix}. \tag{6.17}$$

To calculate the corrected polarization $\langle\hat{\sigma}_z\rangle_{\mathrm{corr}}$ from the measured ones $\langle\hat{\sigma}_z\rangle_{\mathrm{meas}}$, one can use the fact that $\langle\hat{\sigma}_z\rangle = -2(P_1 - 1/2)$ or equivalently $\langle\hat{\sigma}_z\rangle = P_0 - P_1$, since $P_0 + P_1 = 1$. This leads then to an expression for the corrected polarization

$$\langle\hat{\sigma}_z\rangle_{\mathrm{corr}} = P_0 - P_1 = \frac{\langle\hat{\sigma}_z\rangle_{\mathrm{meas}} + f_1 - f_0}{f_0 + f_1 - 1}. \tag{6.18}$$

For the single-qubit terms, it is not relevant whether the single measurements are averaged before or after the correction. For the two-qubit terms $\langle\hat{\sigma}_z \otimes \hat{\sigma}_z\rangle_{\mathrm{corr}}$ however, the correction of the single-qubit terms has to be performed before averaging:

$$\langle\hat{\sigma}_z \otimes \hat{\sigma}_z\rangle_{\mathrm{corr}} = \frac{1}{N}\sum_{i}^{N} \frac{\langle\hat{\sigma}_z^{(1)}\rangle_{\mathrm{meas}}^{i} + f_1^{(1)} - f_0^{(1)}}{f_0^{(1)} + f_1^{(1)} - 1} \cdot \frac{\langle\hat{\sigma}_z^{(2)}\rangle_{\mathrm{meas}}^{i} + f_1^{(2)} - f_0^{(2)}}{f_0^{(2)} + f_1^{(2)} - 1}, \tag{6.19}$$

where the superscript $^{(j)}$ indicates the qubit number j and $\langle\hat{\sigma}_z\rangle_{\mathrm{meas}}^{i}$ is the measurement outcome of the i^{th} single-shot measurement (with result ± 1)

out of a total of N measurements. Alternatively, by first calculating all two-qubit populations ($\vec{P}_{\mathrm{m,2qb}} = \{P_{\mathrm{m00}}, P_{\mathrm{m01}}, P_{\mathrm{m10}}, P_{\mathrm{m11}}\}$) out of the measurement data, a similar procedure as described above can be performed with $\vec{P}_{\mathrm{2qb}} = \{P_{00}, P_{01}, P_{10}, P_{11}\} = (F \otimes F)^{-1}\vec{P}_{\mathrm{m,2qb}}$. The corrected value for the correlation term reads then

$$\langle \hat{\sigma}_z \otimes \hat{\sigma}_z \rangle_{\mathrm{corr}} = P_{00} + P_{11} - P_{01} - P_{10}. \tag{6.20}$$

As an example, the measurement of the $|\Psi^-\rangle$-state is shown in Fig. 6.5. In (a, b) the real part of the density matrix and the Pauli set of the uncorrected data is shown. The fidelity is $F = \mathrm{Tr}[\rho_{\mathrm{meas}} |\Psi^-\rangle \langle\Psi^-|] = 75.4\,\%$ which is considerably lower than for the states measured with joint readout on similar qubits (see Sec. 6.2.2). After the readout correction the fidelity is increased to $F = 94.2\,\%$, see (c, d). This is close to the fidelity measured with joint readout for similar qubits, and shows that the entangling gate itself works fine, the observed lower fidelity in the uncorrected case is purely due to the initialization and readout errors.

6.3. Description of quantum processes

6.3.1. Process tomography

Process matrix

It is possible to characterize quantum processes experimentally in a similar way as quantum states. The procedure is known as *quantum process tomography* and has been first described in [Chuang97].

Every quantum process $\mathcal{E}(\rho)$ acting on a state ρ can be decomposed as

$$\mathcal{E}(\rho) = \sum_{mn} \tilde{E}_m \rho \tilde{E}_n^\dagger \chi_{mn}, \tag{6.21}$$

where $\tilde{E}_i$ are a basis set of operators and χ_{mn} are the complex components of the *chi matrix* (also referred to as the process matrix). The matrix χ is a positive Hermitian matrix and is a complete description of the process for a given given set of operators $\tilde{E}_i$. It describes how any given input density matrix is transformed to an output density matrix and therefore also includes dissipation and other non-unitary behavior.

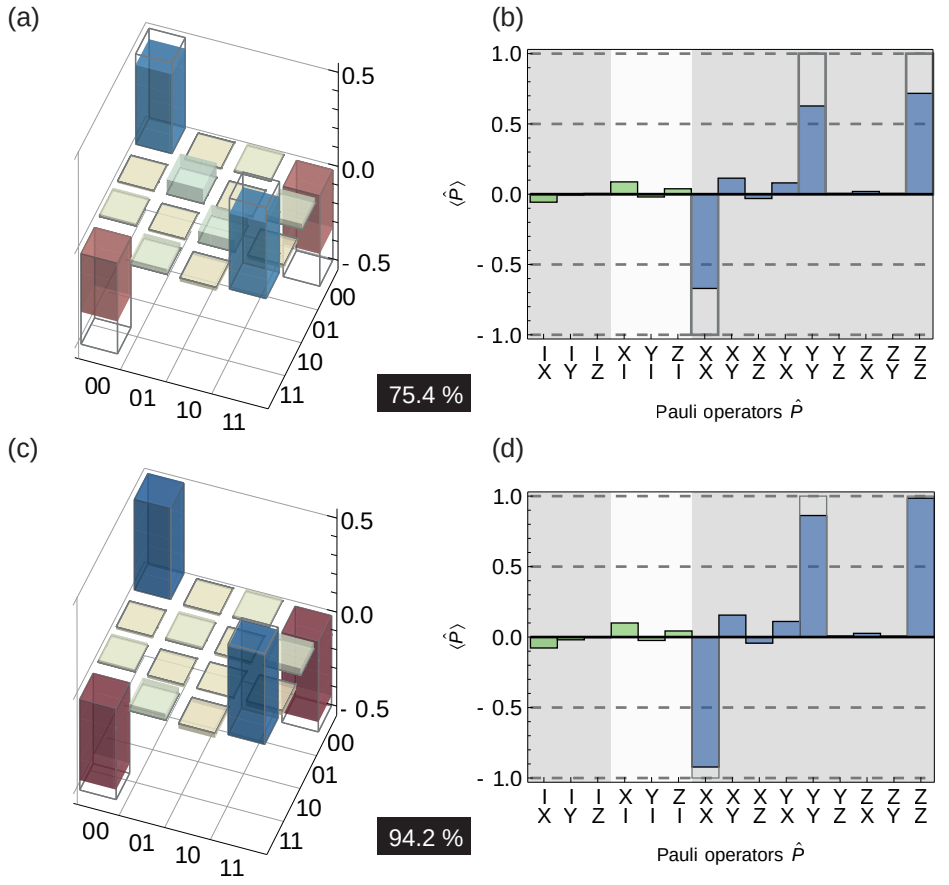

Figure 6.5: (a) Real part of the measured density matrix of the $|\Phi^-\rangle$-state when using separate qubit readout. (b) Pauli set of (a). (c,d) Density matrix and Pauli set of the data in (a,b) after correcting for readout errors. The fidelities are indicated in the black boxes.

The operators normally chosen for a process acting on an n-qubit state are all possible combinations of Pauli operators $\tilde{E} = \{I, X, \tilde{Y}, Z\}^{\otimes n} = \{\mathbb{1}, \hat{\sigma}_x, -i\hat{\sigma}_y, \hat{\sigma}_z\}^{\otimes n}$. The Pauli y-operator is multiplied by $-i$ to have only real elements in χ when the corresponding process can be described by an operator U with only real entries.

The χ matrix of an n-qubit system can be measured in an experiment by performing state tomography on the output of the process for a set of 4^n linearly independent input states, usually the set of states $\{|0\rangle, |1\rangle, |+\rangle, |-\rangle\}^{\otimes n}$, leading to a total of 4^{2n} different experimental settings. This can be understood as follows. Let $\{\tilde{\rho}_j\}$ be a set of linearly independent basis states for the space of $2^n \times 2^n$ matrices. The measured output of all $\mathcal{E}(\tilde{\rho}_j)$ can also be written as a linear combination of the basis states,

$$\mathcal{E}(\tilde{\rho}_j) = \sum_k \lambda_{jk} \tilde{\rho}_k, \tag{6.22}$$

from which the matrix λ can be calculated. Since one can also express the term $\tilde{E}_m \tilde{\rho}_j \tilde{E}_n^\dagger$ as combinations of basis states

$$\tilde{E}_m \tilde{\rho}_j \tilde{E}_n^\dagger = \sum_k \beta_{jk}^{mn} \tilde{\rho}_k, \tag{6.23}$$

for which β_{jk}^{mn} can be calculated from the set of $\{\tilde{E}_i\}$, one can write the following equation:

$$\mathcal{E}(\tilde{\rho}_j) = \sum_{mn} \tilde{E}_m \tilde{\rho}_j \tilde{E}_n^\dagger \chi_{mn} = \sum_{mn} \sum_k \beta_{jk}^{mn} \tilde{\rho}_k \chi_{mn} = \sum_k \lambda_{jk} \tilde{\rho}_k. \tag{6.24}$$

This shows that once the matrices λ and β have been calculated, the χ matrix can be obtained with linear inversion from the equation

$$\sum_{mn} \beta_{jk}^{mn} \chi_{mn} = \lambda_{jk}. \tag{6.25}$$

The *process fidelity* [Schumacher96], a measure of the similarity between an experimentally implemented process χ_{exp} and the ideal process χ_{ideal} is given by

$$F = \text{Tr}[\chi_{\text{exp}} \chi_{\text{ideal}}]. \tag{6.26}$$

Note that this fidelity is sometimes also called "entanglement fidelity".

Processes can be represented graphically as bar charts of the corresponding χ matrix. An example of such a graphical representation is the χ matrix of a CPHASE gate is shown in Fig. 6.6. It is the same implementation which is analyzed in more detail in Sec. 7.1.

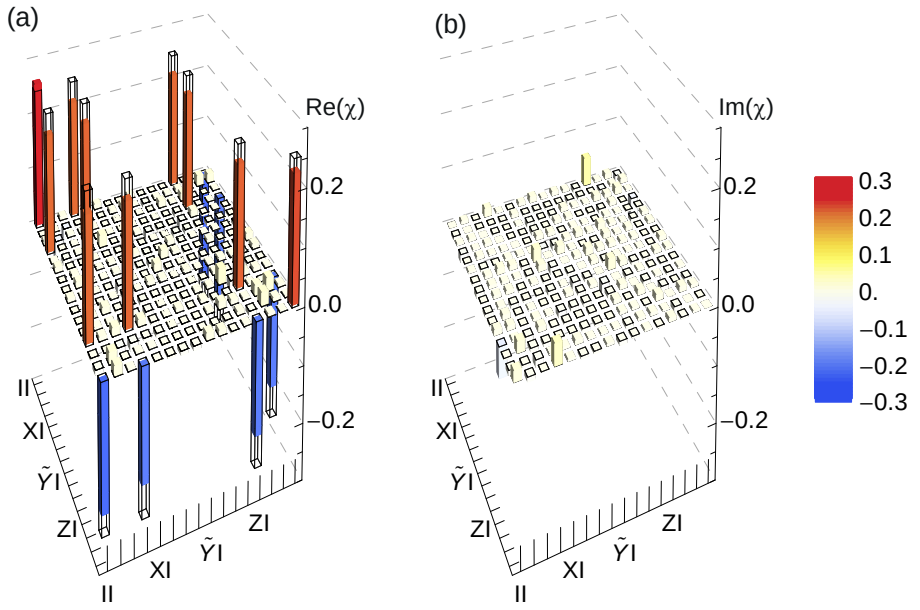

Figure 6.6: Real (a) and imaginary (b) part of the χ matrix of a CPHASE gate with fidelity $F \approx 86\,\%$.

Pauli transfer matrix

An alternative visualization of a process has been introduced as the *Pauli transfer matrix* (PTM) in [Chow12]. The Pauli transfer matrix $\mathcal{R}$ of a process describes how this process transfers an input Pauli set to an output Pauli set. Formally this can be described by defining a Pauli state vector $\vec{p}$ whose components are the expectation values of the n-qubit Pauli operators $\{\mathbb{1}, \hat{\sigma}_x, \hat{\sigma}_y, \hat{\sigma}_z\}^{\otimes n}$. The Pauli transfer matrix can then be used to calculate the Pauli state vector $\vec{p}_{\text{out}}$ of an output state, given a Pauli state vector $\vec{p}_{\text{in}}$ of an input state as $\vec{p}_{\text{out}} = \mathcal{R}\vec{p}_{\text{in}}$. Note that the components of the Pauli set and the Pauli state vector are identical (by definition), but the order in which the elements are displayed can differ. Pauli sets normally show all one-qubit terms before showing the two-qubit terms and so on. The elements of the Pauli state vector can be in the "lexicographic order" for the Pauli operators. In Fig. 6.7 the CPHASE gate form Sec. 6.3.1 is shown

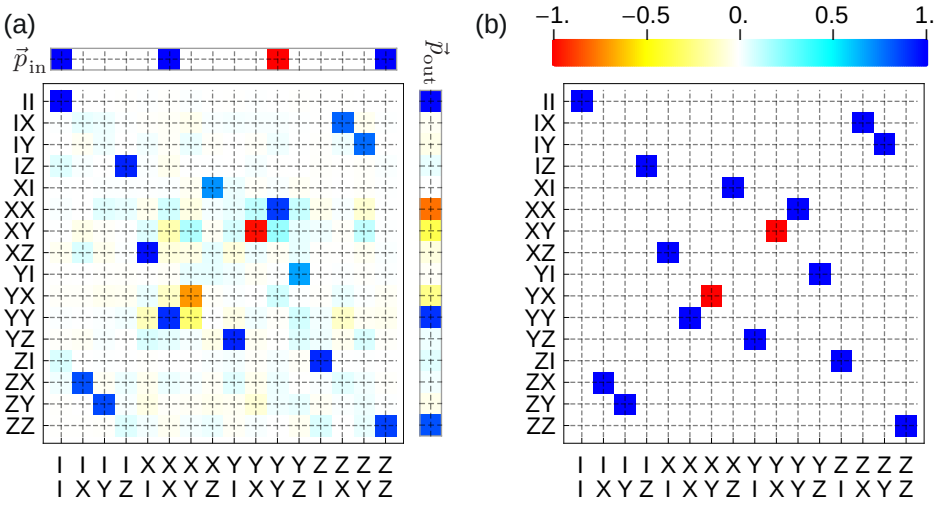

Figure 6.7: Experimental (a) and ideal (b) PTM of the CPHASE gate (same data as Fig. 6.6). As an example, the effect of the gate on an input state $|00\rangle + |11\rangle$ is show by plotting the in- and output Pauli state vector $\vec{p}_{\text{in/out}}$. The figure is adapted with our own data from [Chow12].

as a PTM, both the (a) measured and (b) ideal case.

According to [Chow12], the advantages of the PTM over the χ matrix are that they consist only of real numbers, it is simple to tell whether the map is trace preserving ($\mathcal{R}_{II,jk} = \delta_{Ij}\delta_{Ik}$ for all $j,k \in \{I,X,Y,Z\}$) and unital ($\mathcal{R}_{jk,II} = \delta_{Ij}\delta_{Ik}$). The elements are bounded by ± 1, and for all Clifford operations there is exactly one ± 1 element in each row and column.

The gate fidelity between a measured PTM $\mathcal{R}$ and the ideal PTM $\mathcal{R}_{\text{ideal}}$ stated in [Chow12] is $F_{\text{g}} = (\text{Tr}[\mathcal{R}^{\dagger}_{\text{ideal}}\mathcal{R}] + d)/(d^2 + d)$ with $d = 2^n$ (note that in the original paper it is stated wrongly as $d = 2n$). However this is not the process fidelity F as defined in Eq. (6.26) but corresponds to the average output state fidelity, related to the process fidelity as $F = \frac{(d+1)F_{\text{g}}-1}{d}$. The process fidelity can be directly calculated from the Pauli transfer matrix as $F = \text{Tr}[\mathcal{R}^{\dagger}_{\text{ideal}}\mathcal{R}]/d^2$.

The PTM is a nice alternative to the χ matrix. However, since both PTM and χ-matrices have 4^{2n} elements, it becomes impractical for systems with many qubits. For example, for five qubits ($n = 5$), the PTM (and also

the χ matrix) is a 1024×1024 matrix. At this level it becomes impossible to understand such a matrix "by looking at it."

6.3.2. Randomized benchmarking

Process tomography is a powerful tool to characterize a given gate. However, it has several drawbacks. The gate is only examined as an isolated gate. Process tomography does not tell us anything about the stability of the error behavior when the gate is used in long sequences. Moreover, state preparation and measurement (SPAM) errors limit the capability of process tomography. A method that overcomes these drawbacks is called *randomized benchmarking* (RB). It has been developed and first implemented with trapped ions [Knill08] for estimating the error rate of single-qubit gates. Later is has also been implemented with superconducting circuits [Chow09] for single-qubit gates. The extension to multi-qubit gates followed, first with trapped ions [Gaebler12] and then also with superconducting circuits [Córcoles13]. A related method that allows to measure the error rate of one particular gate independent of SPAM errors is called interleaved RB [Magesan12]. In the following, a short description of randomized benchmarking – following the description in [Knill08, Chow09] – together with experimental data from our setup is presented.

The main idea behind RB is that a random sequence of gates of varying length is applied to a standard initial state. The last gate is also chosen randomly but such that the qubit is ideally in a computational basis state. A subsequent measurement is performed and the outcome is compared to the expected value. This gives a measure of the accumulated error in long sequences. The average error per gate is deduced from the increase of the error probability as a function of sequence length. It turns out to be sufficient if the random gates are taken from the Clifford group, i.e. all possible $\pi/2$-rotations $e^{\pm i\hat{\sigma}\pi/4}$ where $\hat{\sigma}$ is an n-qubit Pauli operator.

The following recipe [Knill08] describes how to generate the pulse sequences for RB in an experiment:

1. Choose a maximum length l_{N_l} of the computational sequence.

2. Choose N_G different computational sequences $\{G_1, \ldots G_{l_{N_l}}\}$ of length l_{N_l} (the maximum length) and sequence elements G_i. The computational sequences in the one-qubit case are just a sequence of random

$\pi/2$ rotations around the x- or y-axis of the Bloch sphere, i.e. $e^{\pm i\hat{\sigma}_i \pi/4}$ with $\hat{\sigma}_i \in \{\hat{\sigma}_x, \hat{\sigma}_y\}$.

3. Truncate every computational sequence at N_l different lengths $l_1 < l_2 < \ldots < l_{N_l}$.

4. Add a final gate R such that for every length every computational sequence transforms the initial state $|0\rangle$ into an eigenstate of the Pauli z-operator, i.e. a computational basis state.

5. Add "Pauli randomization pulses". For every length l_k of every sequence choose N_P random sequences $\{P_1, \ldots P_{l_k+2}\}$ of Pauli pulses, i.e. π pulses of the form $e^{\pm i\hat{\sigma}\pi/2}$ with $i = 0, x, y, z$. Put these pulses alternately to the computational pulses. The Pauli randomization pulses ensure that the outcomes are not correlated with a subsequence of pulses and randomize the errors.

6. Apply each sequence $P_{l_k+2} R P_{l_k+1} G_{l_k} P_{l_k} \ldots G_1 P_1$ to the state $|0\rangle$, see Fig. 6.8, and measure its expectation value.

In total there are N_G different computational sequences, each truncated to N_l different length with, each randomized with N_P Pauli randomization sequences, in total $N_\mathrm{G} N_l N_\mathrm{P}$ different experimental settings. Additionally every sequence is averaged N_e times, which gives a total of $N_\mathrm{G} N_l N_\mathrm{P} N_\mathrm{e}$ experimental runs.

The analysis proceeds as follows:

1. Calculate the expected outcome for each sequence.

2. Compare the expectation with the measured expectation value.

3. Calculate the fidelity of the output states (1 - probability of incorrect measurement outcome).

4. The fidelity of the output state versus the number of computational gates decays exponentially to a value of 0.5. This decay constant is fitted and the error per gate ε is extracted.

The last step is understood as follows. The data is fit to a function $1/2(1 + e^{kl})$ with l the number of computational gates and k the fit parameter.

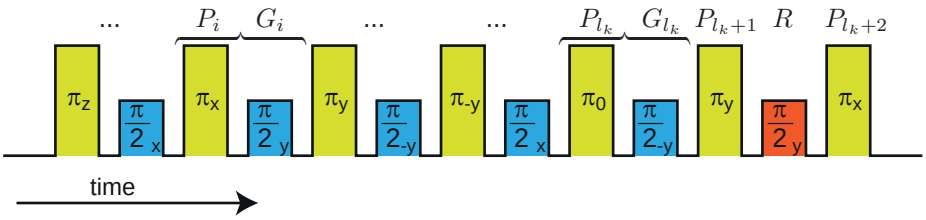

Figure 6.8: Example of an RB sequence of length l_k for one qubit.

With an error per gate ε, the gate fidelity is $F_\mathrm{g} = (1-\varepsilon)^l$. When the gate fidelity approaches zero $F_\mathrm{g} \to 0$, the output state fidelity $F_\mathrm{out} \to 0.5$. It can therefore be written as $F_\mathrm{out} = 1/2\left(1+(1-\varepsilon)^l\right)$, which gives the relation between the fit parameter k and the error per computational gate ε as $\varepsilon = 1 - e^k \approx -k$. A computational gate consists of a Pauli randomization gate and an element of the Clifford group, i.e. a π and a $\pi/2$ pulse. The average error per single-qubit rotation ε_rot is therefore linked to the error of a computational gate as $\varepsilon = 1-(1-\varepsilon_\mathrm{rot})^2 \Rightarrow \varepsilon_\mathrm{rot} \approx \varepsilon/2 = -k/2$.

We implemented the randomized benchmarking procedure with the same parameters used in the original implementation [Knill08], namely $N_\mathrm{G} = 4$ random computational sequences truncated to $N_l = 17$ different lengths $\{2, 3, 4, 5, 6, 8, 10, 12, 16, 20, 24, 32, 40, 48, 64, 80, 96\}$ and randomized each sequence $N_\mathrm{P} = 8$ times which leads to a total of 544 different pulse sequences. An example measurement is shown in Fig. 6.9. The exponential fit gives a single-qubit rotation error of $\varepsilon_\mathrm{rot} = 0.8\,\%$.

6.4. Conclusion

We have seen that the state of a quantum system can be completely characterized by its density matrix. A completely equivalent way to describe a state of qubits is the Pauli set, the set of expectation values of the Pauli operators. In an experiment, the density matrix of a repeatedly prepared qubit state can be determined using quantum state tomography. It requires the measurement of the qubit with different measurement operators. This procedure can be generalized to multi-qubit systems. However it is important that one has access to the correlation information of the different qubits. In

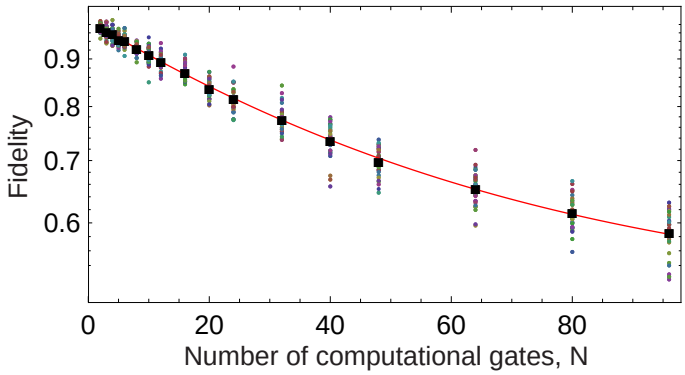

Figure 6.9: Example of an RB data analysis. The colored dots are measurements of different computational sequences, the black squares are the average fidelities of all computational sequences with the corresponding length, the red solid line is an exponential fit.

the case where many qubits couple to the same readout cavity, this is naturally given even in the case of averaged measurements. When the qubits couple to separate readout cavities, one has to resort to single-shot analysis to have access to the correlation information. The similarity of a measured quantum state to an ideal one can be quantified with a measure known as fidelity. Quantum processes can be characterized in a similar way with a procedure called quantum process tomography. The procedure requires to perform state tomography on the output states of the process for a set of different input states. The two most often used ways to describe quantum processes are the χ matrix and the Pauli transfer matrix. Quantum process tomography is useful to characterize a single process, however it is sensitive to state preparation and measurement errors. A method insensitive to these errors is randomized benchmarking. It allows to determine the average gate error in a long computational sequence.

7

Monte Carlo process certification and the Toffoli gate

Monte Carlo quantum process certification is a method which allows to measure the fidelity of an experimentally implemented process relative to an ideal one in a way that is much more efficient than quantum process tomography. This method has been proposed in [Flammia11, daSilva11] and experimentally implemented in the course of this thesis [Steffen12]. In Sec. 7.1.1, the general principles of the method are described. Sec. 7.1.2 presents the sample with which the measurements shown in this chapter have been performed. The properties of the sample impose some experimental constraints which require a special protocol to perform Monte Carlo process certification, this is discussed in Sec. 7.1.3. The protocol was used to characterize two-qubit and three-qubit gates as presented in Sec. 7.1.4.

Monte Carlo process certification has also been applied to our implementation of the Toffoli gate [Fedorov12], where its higher efficiency compared to process tomography has been demonstrated. The experimental implementation of the Toffoli gate is presented in Sec. 7.2.1 and its characterization with Monte Carlo process certification and quantum process tomography is discussed in Sec. 7.2.2.

7.1. Monte Carlo process certification

7.1.1. Principle of process certification

As discussed in Sec. 6.3, quantum process tomography of an n-qubit state requires to measure the expectation value of 4^{2n} different experimental settings. In addition the computational cost of the post-processing increases also exponentially with the number of qubits. With the ongoing experimental progress and growth in system size, quantum process tomography is already impractical and will soon become infeasible in state-of-the-art experiments. Even the most recent tomography algorithms would need days of data post-processing in order to yield a process tomography estimate for as few as 8 qubits [Smolin12].

There are more drawbacks to the approach of quantum process tomography: Statistical fluctuations in the measured expectation values must be dealt with in order for the estimated process matrix to be physical. However, the most appropriate method to produce a physical estimate from a perturbed dataset is still under active debate [Blume-Kohout10]. The resulting exponential amount of data is often reduced to a single number, the average fidelity, which quantifies the similarity between the experimental process and some ideal physical process, and thus the exponential amount of data collected is extremely redundant. Monte Carlo process certification [Flammia11, daSilva11] has been proposed as an efficient method to estimate the average fidelity of an experiment to a large class of ideal processes while completely sidestepping the exponential overhead associated with the reconstruction of process matrices. This method estimates the fidelity of an implemented process to an ideal one without completely characterizing the process. Hence the ideal process has to be chosen before doing the experiment, i.e. the experimental settings depend on the ideal process, as described in the following.

Monte Carlo process certification relies on the fact that an n-qubit process $\mathcal{E}$ can be described by a $2n$-qubit density matrix $\hat{\rho}_\mathcal{E}$, known as the Choi matrix [Jamiołkowski72, Choi75] via

$$\hat{\rho}_\mathcal{E} = (\mathbb{1} \otimes \mathcal{E})(|\phi\rangle\langle\phi|) \tag{7.1}$$

where $|\phi\rangle = \frac{1}{\sqrt{d}} \sum_{i=1}^{d} |i\rangle \otimes |i\rangle$ is a maximally entangled state and $d = 2^n$ is the dimension of the Hilbert space used to describe the states of the

system. When comparing an experimentally realized process $\mathcal{E}_{\text{exp}}$ to an ideal unitary process $\mathcal{E}_{\text{ideal}}$, the fidelity expression for the two Choi matrices [Schumacher96] simplifies to

$$F(\hat{\rho}_{\mathcal{E}_{\text{ideal}}}, \hat{\rho}_{\mathcal{E}_{\text{exp}}}) = \text{Tr}\left[\hat{\rho}_{\mathcal{E}_{\text{ideal}}} \hat{\rho}_{\mathcal{E}_{\text{exp}}}\right], \tag{7.2}$$

which in turn is related to the unitarily invariant average fidelity by $\overline{F} = (dF + 1)/(d + 1)$ [Horodecki99]. The problem of determining the fidelity of a process is therefore identical to finding the fidelity of a state. The fidelity of an experimentally implemented state $\hat{\sigma}$ with respect to a theoretical pure state $\hat{\rho}$ can be written as

$$F(\hat{\rho}, \hat{\sigma}) = \text{Tr}\hat{\rho}\hat{\sigma} = \sum_i \frac{\rho_i \sigma_i}{d}, \tag{7.3}$$

where $\rho_i = \text{Tr}\hat{\rho}\hat{P}_i$, $\sigma_i = \text{Tr}\hat{\sigma}\hat{P}_i$, d the dimension of the Hilbert space, and $\hat{P}_i$ an orthonormal Hermitian operator basis chosen as the 4^n tensor products of the Pauli matrices and the identity. By defining the relevance distribution $\Pr(i) = \frac{\rho_i^2}{d}$, one can write the fidelity as

$$F(\hat{\rho}, \hat{\sigma}) = \sum_i \Pr(i) \frac{\sigma_i}{\rho_i}, \tag{7.4}$$

where the sum is taken over only the i with $\rho_i \neq 0$. The distribution $\Pr(i) = \frac{\rho_i^2}{d}$ reflects the relevance of the observation of $\hat{P}_i$ for the fidelity calculation. In particular, observables with zero expectation value in the ideal case do not contribute to the fidelity and need not be measured in actual experiments. One can then estimate the fidelity by randomly sampling from the observables to be measured according to the relevance distribution $\Pr(i)$. The number of observables required for an estimate with error ϵ is independent of n [Flammia11, daSilva11], unlike tomography which would require 4^{2n} different experiments. The scaling of the precision with which each observable must be measured depends on the process in question, but for Clifford group [Gottesman97, Gottesman99] operations such as CNOT and CPHASE, this scaling is independent of the number of qubits.

The straightforward implementation of Monte Carlo process certification as described above is rather impractical, since the preparation of the state $\hat{\rho}_{\mathcal{E}}$, representing the Choi matrix of the process $\mathcal{E}$, would require preparing

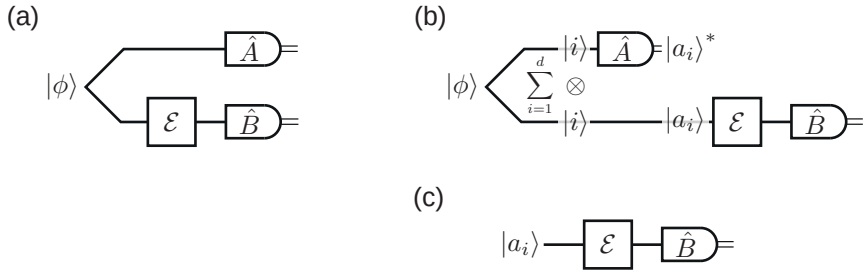

Figure 7.1: (a) Straightforward implementation of the algorithm requires the preparation of a $2n$-qubit entangled state and the application of $\mathcal{E}$ on the second half of this state. (b) Illustration of the effect of the measurement on the first half of the state $|\phi\rangle$ on the second half. (c) Experimentally implemented algorithm. Figure adapted from [daSilva11].

the maximally entangled state $|\phi\rangle = \frac{1}{\sqrt{d}} \sum_{i=1}^{d} |i\rangle \otimes |i\rangle$, where $d = 2^n$ the dimension of the state Hilbert space, to obtain $\hat{\rho}_{\mathcal{E}} = (\mathbb{1} \otimes \mathcal{E})(|\phi\rangle\langle\phi|)$. This requires $2n$ qubits for an n-qubit gate, as well as perfect storage of the n ancillary qubits, see Fig. 7.1 (a).

A more experimentally relevant approach is to prepare and measure only the n-qubit states on which $\mathcal{E}$ acts [Flammia11, daSilva11]. The key idea (Fig. 7.1 (b)) is that the effect of the measurement of the first half of the state $|\phi\rangle$, on which no gate is applied, corresponds to a projection of the second half of the state $|\phi\rangle$ onto complex conjugates (in the computational basis) of eigenstates of the first half of the measurement operator. The measurement of $\hat{\rho}_{\mathcal{E}}$ with randomly chosen operators $\hat{P}_i = \hat{A} \otimes \hat{B}$, where $\hat{A}, \hat{B}$ are tensor products of n Pauli matrices or identities, can be expressed as

$$\begin{aligned} \mathrm{Tr}\left[(\hat{A} \otimes \hat{B})\hat{\rho}_{\mathcal{E}}\right] &= \mathrm{Tr}\left[(\hat{A} \otimes \hat{B})(\mathbb{1} \otimes \mathcal{E})(|\phi\rangle\langle\phi|)\right] \\ &= \frac{1}{d} \sum_{i=1}^{d} a_i \mathrm{Tr}\left[\hat{B}\ \mathcal{E}(|a_i\rangle\langle a_i|)\right]. \end{aligned} \tag{7.5}$$

Here $|a_i\rangle$ is the complex conjugate of the i^{th} eigenstate of the operator $\hat{A}$ with eigenvalue a_i. This final expression corresponds to the action of the process $\mathcal{E}$ on the state $|a_i\rangle$ followed by a measurement of the observable $\hat{B}$

(Fig. 7.1 (c)). The results for different input eigenstates are then summed up to obtain an estimate of $\mathrm{Tr}\left[(\hat{A}\otimes\hat{B})\hat{\rho}_{\mathcal{E}}\right]$.

7.1.2. The sample

The sample used for the experiments presented in this chapter is shown in Fig. 7.2. It has been used for experiments published in [Baur12b, Fedorov12, Steffen12]. It consists of three superconducting transmon qubits (A,B,C) coupled to a coplanar waveguide resonator. The resonator has a bare resonance frequency $\nu_{\mathrm{res}} = 8.625\,\mathrm{GHz}$ and a quality factor $Q = 3300$. The qubits were tuned to their maximum transition frequencies $\nu^{\mathrm{max}}_{\mathrm{A,B,C}} = \{6.714, 6.050, 4.999\}$ GHz. They have charging energies $E_{\mathrm{C}}/h = \{0.264, 0.296, 0.307\}$ GHz and coupling strengths to the resonator $g/2\pi = \{0.36, 0.30, 0.34\}$ GHz. At these bias points the energy relaxation times are $T_1 = \{0.55, 0.70, 1.10\}$ µs and the phase coherence times are $T_2^* = \{0.45, 0.60, 0.65\}$ µs. All three qubits are equipped with individual charge and flux gate lines that allow to implement one-qubit and two-qubit operations as described in Chap. 5.

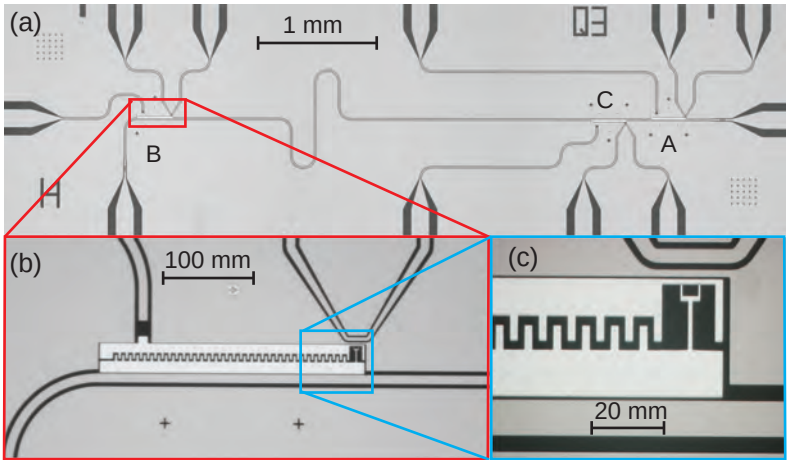

Figure 7.2: (a) Optical microscope image of the sample [Baur12b] used for the experiments discussed in this chapter. (b) Magnification of qubit B with individual charge- and flux-bias lines. (c) Magnification of the SQUID-loop of qubit B.

7.1.3. Experimental protocol

The approach described in Sec. 7.1.1 allows us to implement Monte Carlo quantum process certification with our sample for processes involving up to three qubits. The following recipe summarizes the experimental protocol we used. It is generally applicable for measuring the fidelity of an n-qubit process in any n-qubit system:

1. For a given ideal process $\mathcal{E}$ calculate the Choi matrix $\hat{\rho}_{\mathcal{E}_{\text{ideal}}}$.
2. Find Pauli operators $\hat{P}_i = \hat{A}_i \otimes \hat{B}_i$ which have non-vanishing expectation values $\rho_i = \text{Tr}\hat{\rho}_{\mathcal{E}_{\text{ideal}}}\hat{P}_i \neq 0$.
3. For every Pauli operator $\hat{P}_i$ find the $|a_{i_1}\rangle, |a_{i_2}\rangle, \ldots, |a_{i_d}\rangle$ (complex conjugates of the eigenvectors of $\hat{A}_i$, c.f. Appendix C.1.1 for an example), and do the following:
   a) Prepare the input of the gate operation in the state $\left|a_{i_j}\right\rangle$.
   b) Apply the process $\mathcal{E}_{\text{exp}}$ to the state prepared in (a).
   c) Measure the expectation value of $\hat{B}_i$ given the output of (b).
   d) Compute the weighted average of the expectation value of $\hat{B}_i$ over all the complex conjugates of the eigenstates, using the corresponding eigenvalues as the weight. This gives an estimate of σ_i for the computation of the gate fidelity.
4. Calculate the average of the estimated outcomes σ_i weighted with the relevance distribution $\Pr(i)$ according to Eq. (7.4).

Our 3-qubit system is small enough such that we can measure all relevant operators and do not need to resort to random sampling. This still allows for a significant saving in the number of measurements because many of the measurements required to perform process tomography are irrelevant for the fidelity estimate. In other words, we measure all operators which have a non-zero expectation value for the ideal gate, and calculate the accordingly weighted average to compute the gate fidelity.

The protocol requires the preparation of qubits in eigenstates of Pauli operators $\hat{A}$ and the measurement of Pauli operators $\hat{B}$. The preparation of the qubit input states is straightforward by using amplitude and phase

controlled coherent microwave pulses applied to the individual charge control lines. In our setup, the implementation of the measurement using joint dispersive readout of all qubits is a more complex procedure than it would be if single-qubit readout would be available. The measurement operator is

$$\hat{M} = \sum_{i_1,\ldots,i_n \in \{0,1\}} \alpha_{i_1,\ldots,i_n} |i_1\rangle\langle i_1| \otimes |i_2\rangle\langle i_2| \otimes \cdots \otimes |i_n\rangle\langle i_n| , \tag{7.6}$$

where $|0\rangle, |1\rangle$ are the computational basis states. The coefficients $\alpha_{i_1,\ldots,i_n}$ are obtained from measurements of the resonator transmission amplitude for each computational basis state [Filipp09, Bianchetti10a, Chow10b]. $\hat{M}$ expressed in terms of individual qubit identity and $\hat{\sigma}_z$ Pauli operators is

$$\hat{M} = \sum_{\hat{j}_1,\ldots,\hat{j}_n \in \{\mathbb{1},\hat{\sigma}_z\}} \beta_{j_1,\ldots,j_n} \hat{j}_1 \otimes \hat{j}_2 \otimes \cdots \otimes \hat{j}_n, \tag{7.7}$$

with coefficients $\beta_{j_1,\ldots,j_n}$ calculated as combinations of the $\alpha_{i_1,\ldots,i_n}$. By averaging many measurement outcomes of the same operator, we are able to perform a measurement of the expectation value of the operator in question.

In general, the measurement operator has 2^n different elements. However, in Monte Carlo process certification for each input state the expectation value of only one specific element is needed. This element can be obtained by adding measurement outcomes with different signs of $\hat{\sigma}_z$ operators of different qubits, realized by π pulses applied to the corresponding qubits just before the measurement. Since the first element $\mathbb{1} \otimes \cdots \otimes \mathbb{1}$ has always an expectation value of one, one needs to measure 2^{n-1} different expectation values to extract a single operator $\hat{B}$. We emphasize that this particular property and the overhead associated with it relate to our joint readout, and are not a consequence of the Monte Carlo certification method.

As an example, the joint readout procedure of the operator $\hat{\sigma}_y \otimes \hat{\sigma}_x$ for two qubits is presented in the following. The joint readout operator is

$$\begin{aligned} \hat{M} = {} & \alpha_{00} |0\rangle\langle 0| \otimes |0\rangle\langle 0| + \alpha_{01} |0\rangle\langle 0| \otimes |1\rangle\langle 1| \\ & + \alpha_{10} |1\rangle\langle 1| \otimes |0\rangle\langle 0| + \alpha_{11} |1\rangle\langle 1| \otimes |1\rangle\langle 1| , \end{aligned} \tag{7.8}$$

which is equivalent to

$$\hat{M} = \beta_{00} \mathbb{1} \otimes \mathbb{1} + \beta_{01} \mathbb{1} \otimes \hat{\sigma}_z + \beta_{10} \hat{\sigma}_z \otimes \mathbb{1} + \beta_{11} \hat{\sigma}_z \otimes \hat{\sigma}_z. \tag{7.9}$$

The prefactors β_{ij} are determined from measurements of the α_{ij} as described above. To measure the given combination of Pauli operators, we rotate the measurement basis of the individual qubits accordingly. For the example above, we apply a $-\pi/2$ rotation around the x-axis to the first qubit and a $\pi/2$ rotation around the y-axis to the second qubit. The resulting measurement operator is

$$M = \beta_{00}\mathbb{1}\otimes\mathbb{1} + \beta_{01}\mathbb{1}\otimes\hat{\sigma}_x + \beta_{10}\hat{\sigma}_y\otimes\mathbb{1} + \beta_{11}\hat{\sigma}_y\otimes\hat{\sigma}_x. \tag{7.10}$$

To extract only the last term in the measurement operator, a second measurement with an additional π pulse on both qubits is performed. This results in a measurement operator with two minus signs:

$$M = \beta_{00}\mathbb{1}\otimes\mathbb{1} - \beta_{01}\mathbb{1}\otimes\hat{\sigma}_x - \beta_{10}\hat{\sigma}_y\otimes\mathbb{1} + \beta_{11}\hat{\sigma}_y\otimes\hat{\sigma}_x. \tag{7.11}$$

Adding the measurement outcomes of the two experiments (for the same input state) results in the expectation value for the operator $2(\beta_{00}\mathbb{1}\otimes\mathbb{1} + \beta_{11}\hat{\sigma}_y\otimes\hat{\sigma}_x)$. Since the expectation value for $\mathbb{1}\otimes\mathbb{1}$ is always equal to 1 and β_{00} and β_{11} are known, the expectation value of $\hat{\sigma}_y\otimes\hat{\sigma}_x$ can be extracted in this way.

Hence, it is possible in our experiments to extract any expectation value of two-qubit Pauli operators from two measurements (or three-qubit Pauli operators from four measurements), using the corresponding single qubit rotations. Having found the expectation values $\sigma_i = \mathrm{Tr}\left[\hat{\rho}_{\mathcal{E}_{\mathrm{exp}}}\hat{P}_i\right]$, the fidelity can be directly calculated using Eq. (7.4).

According to Eq. (7.5), a measurement of one of the expectation values σ_i consists of averaging measurement outcomes over different input states. To achieve this, one can also Monte Carlo sample from the eigenvectors to be prepared as input states. The weighting factor for the sampling is given by the absolute value of the eigenvalue. Since the system size is small in our experiments but a high accuracy is desired, we measured all eigenstates.

The fact that we use joint readout in our setup increases the number of different expectation values that we have to measure. This is a particular property of our readout scheme and not of the Monte Carlo certification method and is explained in more detail below.

To extract a single operator $\hat{B}$ from a joint readout in our experiments, we sum the expectation values of 2^{n-1} different measurement operators $\hat{M}$.

For each measurement operator $\hat{M}$, we prepare the qubits in a different initial state and then average many outcomes to obtain the corresponding expectation value. This means that the number of *different* measurement settings to obtain the expectation value of an operator $\hat{B}$ increases exponentially with the number of qubits. However the *total* number of measurements (including averages) does not need to grow exponentially as long as the number of averages to measure the expectation value of one operator $\hat{M}$ is large compared to the number of different measurement settings (i. e. 2^{n-1}): In this case one can just reduce the number of averages to measure the expectation value of one $\hat{M}$, such that the total number of averages for all measurements used to calculate the operator $\hat{B}$ stays constant. This approach has been taken for the experiments presented here, since the number of averages for a single expectation value of $\hat{M}$ is on the order of $10^5 - 10^6$ whereas the number of different expectation values which need to be measured for obtaining one specific operator $\hat{B}$ is 2 and 4 (for $n = 2$ and $n = 3$ respectively). The implementation of simultaneous single-shot, single-qubit readout [Steffen06b, Mallet09, Vijay11, Groen13] would overcome these restrictions and would allow to measure the expectation value of an operator $\hat{B}$ with only one experimental setting, independent of the number of qubits n.

7.1.4. Experimental implementation

We tested Monte Carlo process certification on 2-qubit CNOT and CPHASE gates, on the sequential application of two CPHASE gates on three qubits and as described in Sec. 7.2 on the Toffoli gate. The CNOT and the CPHASE gates are particularly interesting for Monte Carlo process certification, since these gates map elements of the Pauli group to other elements of the Pauli group. Such gates are Clifford operations and their Choi matrices are stabilizer states [Gottesman97, Gottesman99] for which the number of relevant Pauli operators is minimal with uniform relevance distribution. For any stabilizer state $\hat{\rho}_{\mathcal{E}}$ there is a subgroup S of the Pauli group with elements $\hat{S}_i$ such that the pure state corresponding to $\hat{\rho}_{\mathcal{E}_{\text{ideal}}}$ is an eigenvector of all $\hat{S}_i$ with eigenvalue $+1$. The expectation value of each operator in this stabilizer group is $+1$. Therefore, the relevance distribution $\Pr(i) = 1/4^n$ is uniform for all $i \in \{1, \ldots, 4^n\}$. All other operators of the Pauli group have expectation value zero, and therefore have no impact on the estimation of

the fidelity of a gate.

All experimentally realized gates have been characterized by calculating their fidelity using Monte Carlo process certification (F_{MC}), unconstrained tomography data (F_{tom}) and tomography data constrained by maximum-likelihood [Smolin12, Baur12a] estimation (F_{ML}).

The CNOT gate, which changes the state of a target qubit if the control qubit is in the state $|1\rangle$, is described by a Choi matrix whose stabilizer group is generated by

$$\begin{array}{lcccc} g_1 & = & \hat{\sigma}_x & \mathbb{1} & \hat{\sigma}_x & \hat{\sigma}_x, \\ g_2 & = & \hat{\sigma}_z & \mathbb{1} & \hat{\sigma}_z & \mathbb{1}, \\ g_3 & = & \mathbb{1} & \hat{\sigma}_x & \mathbb{1} & \hat{\sigma}_x, \\ g_4 & = & \mathbb{1} & \hat{\sigma}_z & \hat{\sigma}_z & \hat{\sigma}_z. \end{array} \tag{7.12}$$

This indicates that, e.g. eigenstates of the $\hat{\sigma}_x \otimes \mathbb{1}$ operator are mapped to eigenstates of the $\hat{\sigma}_x \otimes \hat{\sigma}_x$ operator by the CNOT operation. The relevant Pauli operators are products of the elements of each subset of these generators. A complete list of the relevant operators is shown in Tab. 7.1 (a). A visualization of the expectation value of the 16 Pauli operators with non-vanishing relevance distribution is shown in Fig. 7.3 (a), where each row of the plot corresponds to a block of four operators in Tab. 7.1 (a). For the CNOT gate, the total number of different measurement settings is 120. For each of the 15 non-unity Pauli operators we prepare 4 different input states and measure 2 different operators (required only by the joint readout). In contrast, the total number of different measurement settings for process tomography is $4^{(2\times 2)} = 256$.

The CPHASE gate, which changes the phase of the $|1\rangle$ state of the target qubit by π if the control qubit is in the state $|1\rangle$, has been characterized in a way similar to the CNOT gate as these gates are locally equivalent. The relevant Pauli operators are found with the same procedure as for the CNOT gate and are listed in Tab. 7.1 (b). A visualization of the expectation value of the 16 Pauli operators with non-vanishing relevance distribution is shown in Fig. 7.3 (b).

A sequence of 2 CPHASE gates first acting on qubits 1 and 2, and then on qubits 2 and 3 was characterized as an example of a 3-qubit gate with a stabilizer state Choi matrix. This Choi matrix has $4^3 = 64$ Pauli operators with non-vanishing expectation value. The stabilizer group generators as well as a list of the relevant Pauli operators are presented in Appendix C.1.2.

(a)

$\mathbb{1}$	$\mathbb{1}$	$\mathbb{1}$	$\mathbb{1}$
$\mathbb{1}$	$\hat{\sigma}_x$	$\mathbb{1}$	$\hat{\sigma}_x$
$\mathbb{1}$	$\hat{\sigma}_y$	$\hat{\sigma}_z$	$\hat{\sigma}_y$
$\mathbb{1}$	$\hat{\sigma}_z$	$\hat{\sigma}_z$	$\hat{\sigma}_z$
$\hat{\sigma}_x$	$\mathbb{1}$	$\hat{\sigma}_x$	$\hat{\sigma}_x$
$\hat{\sigma}_x$	$\hat{\sigma}_x$	$\hat{\sigma}_x$	$\mathbb{1}$
$\hat{\sigma}_x$	$\hat{\sigma}_y$	$\hat{\sigma}_y$	$\hat{\sigma}_z$
$\hat{\sigma}_x$	$\hat{\sigma}_z$	$\hat{\sigma}_y$	$\hat{\sigma}_y$
$\hat{\sigma}_y$	$\mathbb{1}$	$\hat{\sigma}_y$	$\hat{\sigma}_x$
$\hat{\sigma}_y$	$\hat{\sigma}_x$	$\hat{\sigma}_y$	$\mathbb{1}$
$\hat{\sigma}_y$	$\hat{\sigma}_y$	$\hat{\sigma}_x$	$\hat{\sigma}_z$
$\hat{\sigma}_y$	$\hat{\sigma}_z$	$\hat{\sigma}_x$	$\hat{\sigma}_y$
$\hat{\sigma}_z$	$\mathbb{1}$	$\hat{\sigma}_z$	$\mathbb{1}$
$\hat{\sigma}_z$	$\hat{\sigma}_x$	$\hat{\sigma}_z$	$\hat{\sigma}_x$
$\hat{\sigma}_z$	$\hat{\sigma}_y$	$\mathbb{1}$	$\hat{\sigma}_y$
$\hat{\sigma}_z$	$\hat{\sigma}_z$	$\mathbb{1}$	$\hat{\sigma}_z$

(b)

$\mathbb{1}$	$\mathbb{1}$	$\mathbb{1}$	$\mathbb{1}$
$\mathbb{1}$	$\hat{\sigma}_x$	$\hat{\sigma}_z$	$\hat{\sigma}_x$
$\mathbb{1}$	$\hat{\sigma}_y$	$\hat{\sigma}_z$	$\hat{\sigma}_y$
$\mathbb{1}$	$\hat{\sigma}_z$	$\mathbb{1}$	$\hat{\sigma}_z$
$\hat{\sigma}_x$	$\mathbb{1}$	$\hat{\sigma}_x$	$\hat{\sigma}_z$
$\hat{\sigma}_x$	$\hat{\sigma}_x$	$\hat{\sigma}_y$	$\hat{\sigma}_y$
$\hat{\sigma}_x$	$\hat{\sigma}_y$	$\hat{\sigma}_y$	$\hat{\sigma}_x$
$\hat{\sigma}_x$	$\hat{\sigma}_z$	$\hat{\sigma}_x$	$\mathbb{1}$
$\hat{\sigma}_y$	$\mathbb{1}$	$\hat{\sigma}_y$	$\hat{\sigma}_z$
$\hat{\sigma}_y$	$\hat{\sigma}_x$	$\hat{\sigma}_x$	$\hat{\sigma}_y$
$\hat{\sigma}_y$	$\hat{\sigma}_y$	$\hat{\sigma}_x$	$\hat{\sigma}_x$
$\hat{\sigma}_y$	$\hat{\sigma}_z$	$\hat{\sigma}_y$	$\mathbb{1}$
$\hat{\sigma}_z$	$\mathbb{1}$	$\hat{\sigma}_z$	$\mathbb{1}$
$\hat{\sigma}_z$	$\hat{\sigma}_x$	$\mathbb{1}$	$\hat{\sigma}_x$
$\hat{\sigma}_z$	$\hat{\sigma}_y$	$\mathbb{1}$	$\hat{\sigma}_y$
$\hat{\sigma}_z$	$\hat{\sigma}_z$	$\hat{\sigma}_z$	$\hat{\sigma}_z$

Table 7.1: All relevant Pauli operators for the verification of a (a) CNOT and a (b) CPHASE gate.

For each of these operators we sample 8 different eigenvectors, each by measuring 4 different operator combinations required by the joint readout. In total this gives 2016 different measurement settings, again without making use of random sampling. In contrast, process tomography for any three-qubit gate requires $4^{2\times3} = 4096$ different measurement settings. A visualization of the expectation value of the 64 relevant Pauli operators is shown in Fig. 7.3 (c).

All resulting fidelities are summarized in Tab. 7.2. Errors are stated as 90 % confidence intervals. For Monte Carlo process estimation the error was calculated by Gaussian error propagation of the errors of the single measurements. For the error of the process tomography, the confidence interval of the distribution of fidelities was calculated based on a resampling of the measurement outcomes according to the inferred error statistics of the experiments. All fidelities found with Monte Carlo process certification have tighter error bounds than the fidelities obtained from process tomography. This is mainly due to the fact that the post-processing for the Monte Carlo certification only consists of averaging the relevant measured values whereas full process tomography must impose collective physical constraints on the entire dataset, and errors of the expectation values from the irrelevant observables can only add to the errors relating to the relevant observables.

Gate	F_{MC}	F_{tom}	F_{ML}
CNOT	$81.7 \pm 2.1\,\%$	$80 \pm 3\,\%$	$79 \pm 3\,\%$
CPHASE	$86.6 \pm 3.0\,\%$	$86 \pm 4\,\%$	$83 \pm 4\,\%$
2 CPHASES	$65.0 \pm 0.8\,\%$	$67 \pm 5\,\%$	$67 \pm 5\,\%$

Table 7.2: Fidelities obtained by Monte Carlo process certification (F_{MC}) compared to the values obtained with process tomography (F_{tom}) and subsequent application of a maximum likelihood algorithm (F_{ML}).

7.2. Implementation of the Toffoli gate

The Toffoli gate is a three-qubit operation which inverts the state of a target qubit conditioned on the state of two control qubits. It is therefore sometimes referred to as a controlled-controlled-NOT (CCNOT) gate.

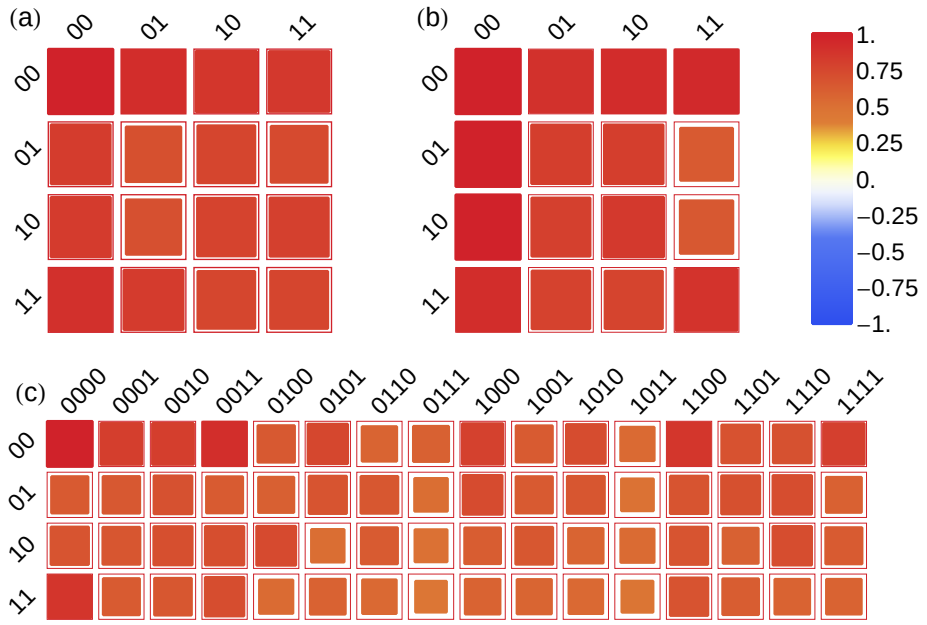

Figure 7.3: Hinton diagrams [Hinton86] of the measured data for (a) a two-qubit CNOT-gate, (b) a two-qubit CPHASE-gate, and (c) a three-qubit 2-CPHASE-gate. The thin border shows the ideal expected values, the colored squares are the estimated values. The (00, 00) and (00, 0000) entries are the expectations of the identity, so they have sizes corresponding to absolute value 1 and the area of the other squares are adjusted proportionally. The column label corresponds to the most-significant digits of the binary expansion of the index of the observable, while the row label corresponds to the least significant digits. The order of the operators corresponds to the order in Tab. 7.1 and Tab. C.2 shown in the appendix.

It enables universal reversible classical computation [Toffoli80] and forms a universal set of gates in quantum computation together with the Hadamard gate [Shi03]. It is also a key element in quantum error correction schemes (for theoretical aspects of quantum error correction see [Nielsen00], implementations are described e.g. in [Cory98, Knill01, Chiaverini04, Pittman05, Aoki09, Reed12]).

The Toffoli gate can be constructed out of two-qubit and single-qubit gates. If one is restricted to CNOT gates as two-qubit gates, the optimal decomposition of the Toffoli gate needs six CNOT gates and ten single qubit operations [Nielsen00, Shende09] as depicted in Fig. 7.4. If one has the possibility of implementing arbitrary two-qubit gates, the optimal decomposition consists of five two-qubit gates [Barenco95], two CNOT gates and three controlled-$\sqrt{\text{NOT}}^{(\dagger)}$ gates as shown in Fig. 7.5.

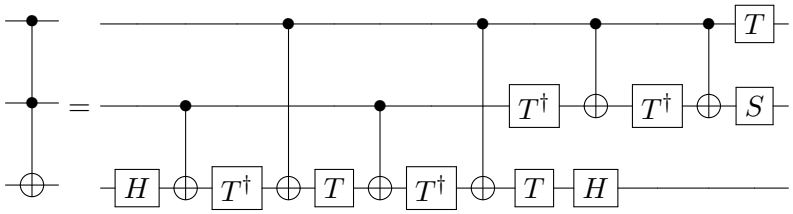

Figure 7.4: Decompositon of the Toffoli gate into two-qubit CNOT-gates and single-qubit gates. Here, $T = R_z^{\pi/4}$, $S = R_z^{\pi/2}$ and H is the Hadamard gate.

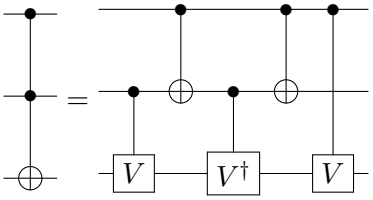

Figure 7.5: Decompositon of the Toffoli gate into the minimal possible amount of two-qubit gates. Here, $V = \sqrt{\text{NOT}}$.

7.2.1. Experimental realization

During the course of this thesis we experimentally implemented the Toffoli gate using the chip described in Sec. 7.1.2. The work described in this section closely follows the original publication [Fedorov12].

Besides our implementation, in superconducting circuits a Toffoli-class gate (i.e. a gate switching the state of the target qubit if at least one of the control qubits is in the $|1\rangle$ state) has been implemented using two qubits and a resonator [Mariantoni11]. However, the characterization was limited to the phase fidelity since full process tomography including the resonator state was not available. Also, a Toffoli gate (i.e. a controlled-controlled-$e^{i\phi}Z$ gate) has been implemented using the third excited state of the transmon qubits and used to demonstrate three-qubit quantum error correction [Reed12].

In our experimental realization of the Toffoli gate, we exploit the presence of additional (non-computational) higher excited states in the energy level spectrum of the transmon. Using the transmons as quantum mechanical three-level systems (*qutrits*), allows us to implement the Toffoli gate with only two qubit-qutrit gates, one two-qubit gate and two single-qubit gates.

In the conventional realization of the Toffoli gate, a NOT operation is applied to the target qubit (C) if the control qubits (A, B) are in the state $|11\rangle$. In our setup it is more natural to realize a variant of the Toffoli gate shown in Fig. 7.6 (a) in which the state of the target qubit is inverted if the control qubits are in $|01\rangle$. This gate can easily be transformed to the conventional Toffoli gate by a redefinition of the computational basis states of qubit A or by adding two π pulses on qubit A.

The Toffoli gate can be constructed from a controlled-controlled-phase gate (CCPHASE) sandwiched between two Hadamard gates acting on the target qubit as shown in Fig. 7.6 (a). A CCPHASE gate leads to a π phase shift for the $|1\rangle$ state of the target qubit if and only if the control qubits are in the state $|01\rangle$. This corresponds to a sign change of only one out of the 8 computational three-qubit basis states: $|011\rangle \leftrightarrow -|011\rangle$.

The basic idea of 'hiding' states into non-computational states to simplify the implementation of a Toffoli gate was theoretically proposed in [Ralph07, Borrelli11] and experimentally implemented for linear optics and ion trap systems [Monz09, Lanyon09]. The implementation of the scheme of [Ralph07] in our setup would require 3 CPHASE gates, 6 single-qubit and 2 single-qutrit

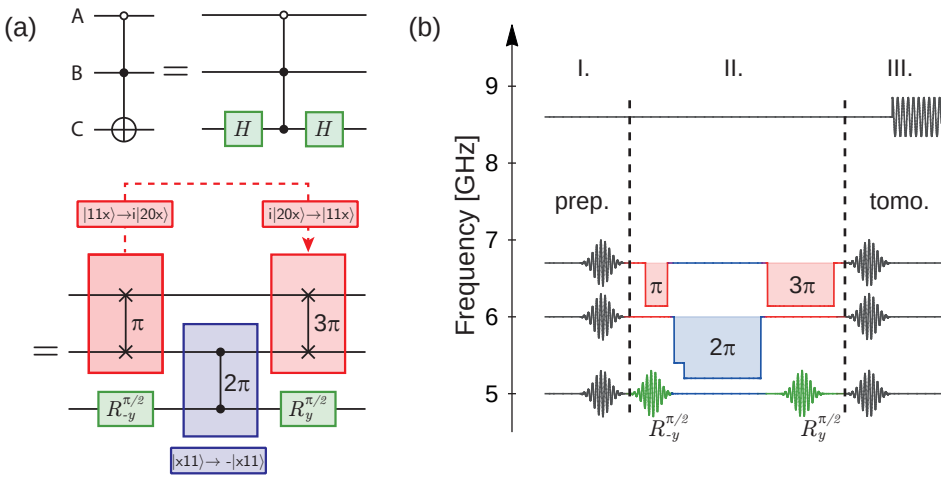

Figure 7.6: (a) The Toffoli gate which changes the state of the target qubit ($\oplus$) when the control bits are in state '0' ($\circ$) or '1' ($\bullet$) can be decomposed into Hadamard- and CCPHASE-gates (top). The CCPHASE-gate is implemented as a sequence of two-qubit and qubit-qutrit gates (see text for details). (b) Pulse sequence used for the implementation of the Toffoli gate.

operations. Instead, we construct the controlled phase gate from a single two-qubit CPHASE gate and two qubit-qutrit gates denoted as a π-SWAP and a 3π-SWAP shown in Fig. 7.6 (a). The application of a single CPHASE gate on qubits B and C (shown in the blue frame) inverts the sign of both the $|111\rangle$ and $|011\rangle$ states. To create the CCPHASE operation the computational basis state $|111\rangle$ is transferred to the non-computational state $i\,|201\rangle$ by the first π-SWAP (shown in left red frame), effectively 'hiding' it from the CPHASE operation acting on qubits B and C. After the CPHASE operation, the $|111\rangle$ state is recovered from the non-computational level $i\,|201\rangle$ by an additional 3π-SWAP. Also, alternative approaches using optimal control of individual qubits for implementing a Toffoli gate in a single step have been theoretically proposed [Spörl07] and recently analyzed in the context of the circuit QED architecture [Stojanović12].

All three-qubit basis states show three distinct evolution paths during our CCPHASE gate (see also Tab. 7.3). Only the input state $|011\rangle$ is affected by the CPHASE gate acting on qubits B and C which transfers $|011\rangle$ to the

Initial state	after π-SWAP	after CPHASE	after 3π-SWAP
$\|011\rangle$	$\|011\rangle$	$-\|011\rangle$	$-\|011\rangle$
$\|110\rangle$	$i\|200\rangle$	$i\|200\rangle$	$\|110\rangle$
$\|111\rangle$	$i\|201\rangle$	$i\|201\rangle$	$\|111\rangle$
$\|x0y\rangle$	$\|x0y\rangle$	$\|x0y\rangle$	$\|x0y\rangle$
$\|010\rangle$	$\|010\rangle$	$\|010\rangle$	$\|010\rangle$

Table 7.3: Evolution of the three-qubit states during the CCPHASE gate. The state $|011\rangle$ acquires a phase shift of π during the CPHASE pulse; the states $|11x\rangle$ are transferred to $i\,|20x\rangle$, "hiding" them from the CPHASE gate; and the initial states $|x0y\rangle$ (with $x, y \in \{0, 1\}$) and $|010\rangle$ do not change during the sequence.

desired state $-\,|011\rangle$. The states $|11x\rangle$ ($x \in \{0, 1\}$) are transferred by the π-SWAP gate to the states $i\,|20x\rangle$. The following CCPHASE gate then has no influence on the resulting state. The last gate, a 3π-SWAP, transfers $i\,|20x\rangle$ back to $|11x\rangle$. The two swap gates (π and 3π) realize a full 4π rotation such that the state $|11x\rangle$ does not acquire any extra phase compared to the other states. The states of the last group ($|010\rangle, |x0y\rangle$ with $x, y \in \{0, 1\}$) do not change during the CPHASE gate sequence.

The actual experimental implementation of the Toffoli gate consists of a sequence of microwave and flux pulses applied to the qubit local control lines (Fig. 7.6 (b)). The rotations about the x- and y-axes are realized with resonant microwave pulses applied to the charge gate line at each qubit. We use 8 ns long Gaussian-shaped DRAG pulses [Motzoi09, Gambetta11] to prevent population of the third level during the single-qubit operations which would lead to phase errors. Few nanosecond long current pulses passing through the transmission line next to the SQUID loop of the respective qubits control the qubit transition frequency realizing z-axis rotations. All two-qubit/qutrit gates are implemented by tuning a qutrit non-adiabatically to the avoided crossing between the $|11x\rangle \leftrightarrow |20x\rangle$ or $|x11\rangle \leftrightarrow |x20\rangle$ states, respectively (see Sec. 5.2.2). During this time the

system oscillates between these states with a frequency $2J_{11,20}^{AB/BC}$. With interaction times $\pi/(2J_{11,20}^{AB}) = 7$ ns, $3\pi/(2J_{11,20}^{AB}) = 21$ ns and $2\pi/(2J_{11,20}^{BC}) = 23$ ns we realize a π-SWAP and a 3π-SWAP between qubits A and B and a CPHASE gate between qubits B and C, respectively. The use of qubit-qutrit instead of single-qutrit operations allows for a more efficient construction of the Toffoli gate. Direct realization of the scheme proposed in [Ralph07] in our system would require 8 additional microwave pulses (used to implement 6 single-qubit and 2 single-qutrit gates) with a two-fold increase of overall duration of the pulse sequence with respect to our scheme. The pulse sequence used introduces dynamical phases which we compensated for as described in Appendix C.2.1.

7.2.2. Characterization

We have characterized the performance of the realization of the Toffoli gate described above using three methods: By measuring the truth table, by full process tomography, and by Monte Carlo process certification. The truth table depicted in Fig. 7.7 shows the population of all computational basis states after applying the Toffoli gate onto each of the computational basis states prepared at the input of the circuit. It clearly reveals the characteristic properties of the Toffoli gate, namely that a NOT operation is applied on the target qubit (C) if the control qubits (A,B) are in the state $|01\rangle$. The fidelity of the output states show a significant dependence on qubit lifetime. In particular, input states with qubit A (with the shortest lifetime) in the excited state exhibit generally the worst fidelity, indicating that the protocol is mainly limited by the qubit lifetime. The fidelity of the measured truth table, $F = (1/8)\mathrm{Tr}\,[U_{\mathrm{exp}}U_{\mathrm{ideal}}] = 76.0\,\%$, shows the average performance of our gate when acting onto the eight basis states.

To completely characterize the quantum features of the Toffoli gate, we have performed full three-qubit process tomography and reconstructed the process matrix χ_{exp}, overcoming the limited characterization provided by measurements of the phase fidelity only [Mariantoni11]. The process matrix χ_{exp} reconstructed directly from the data has a fidelity of $F = \mathrm{Tr}[\chi_{\mathrm{exp}}\chi_{\mathrm{ideal}}] = 70 \pm 3\,\%$ (the error represents a 90 % confidence interval). Using a maximum likelihood procedure [Ježek03, Smolin12] to correct for unphysical properties of χ_{exp} the obtained process matrix $\chi_{\mathrm{exp}}^{\mathrm{ML}}$ has a fidelity of $F = \mathrm{Tr}[\chi_{\mathrm{exp}}^{\mathrm{ML}}\chi_{\mathrm{ideal}}] = 69\,\%$ with errors expected on the level of 3 %. The

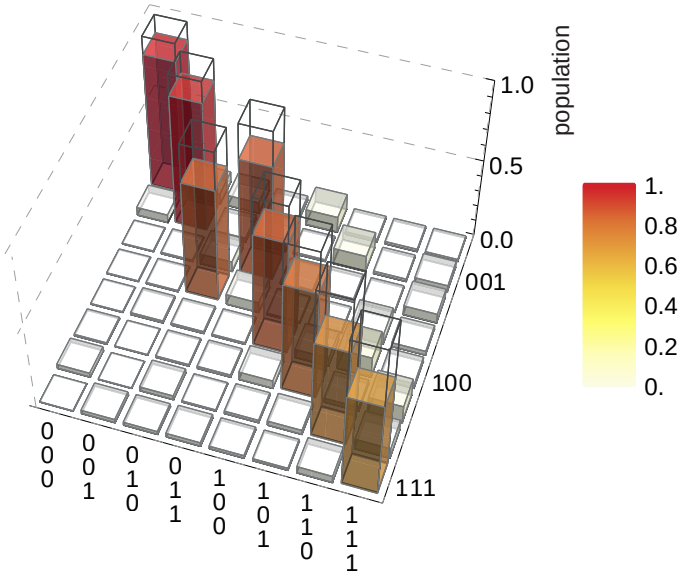

Figure 7.7: Barchart of the measured truthtable showing the population of the output state (right axis) given a certain input state (front axis). The state of qubit C is inverted if qubits A and B are in the state $|01\rangle$. Wireframes show ideally expected populations.

measured process matrix χ_{exp} displays the same key features as the ideal process matrix χ_{ideal} as demonstrated in Fig. 7.8.

We also used Monte Carlo process certification to characterize our implementation of the Toffoli gate. The Choi matrix of the Toffoli gate is not a stabilizer state. Therefore, the list of relevant Pauli operators has no group structure and the relevance distribution $\Pr(i)$ is not uniform. We find that there are 232 Pauli operators with non-zero expectation value of 1 or ± 0.5 out of 4096 possible ones. The list of all relevant operators is given in Appendix C.1.3. The total number of different relevant experimental settings is $231 \times 8 \times 4 = 7392$, since for each of the 231 different non-unity Pauli operators we prepare 8 different input states and measure 4 different operators.

For the Monte Carlo process estimation, we averaged each measurement setting $\sim 330\,000$ times, resulting in a total number of $\sim 2.4 \times 10^9$ mea-

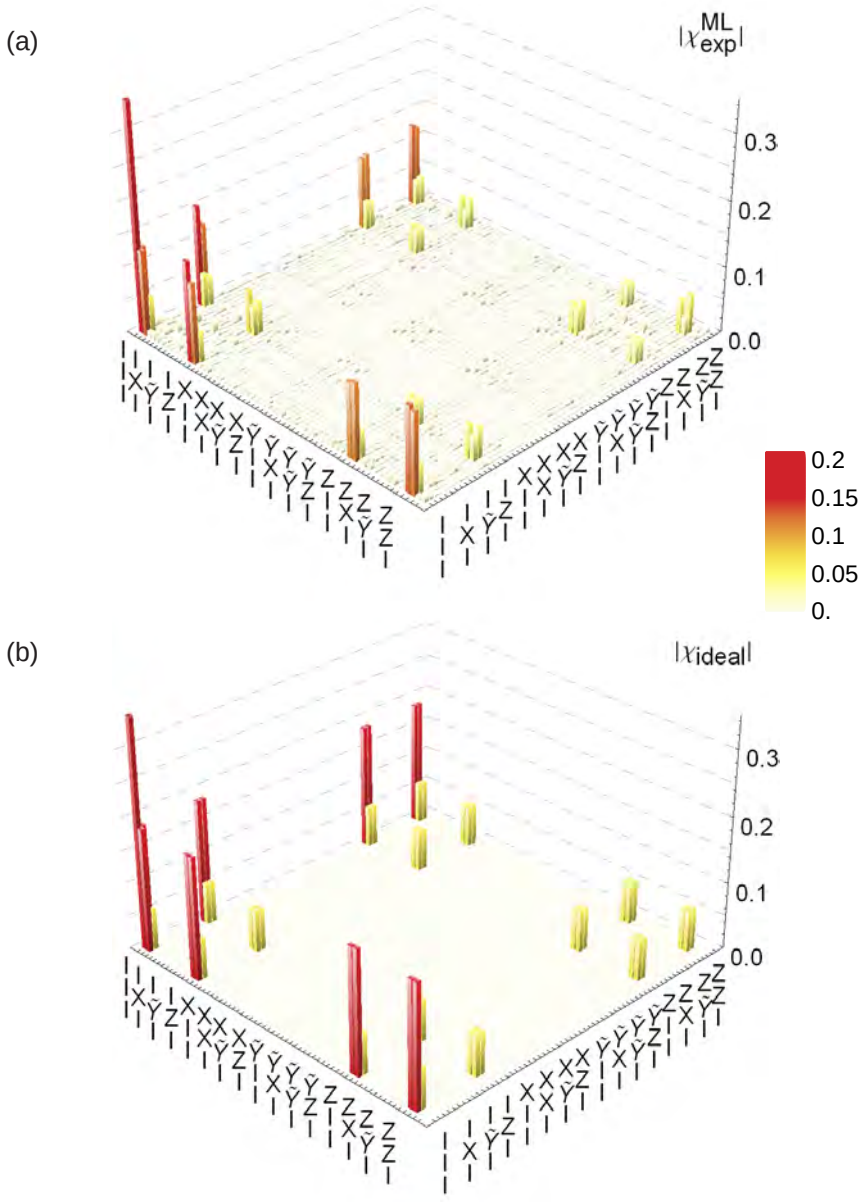

Figure 7.8: Bar chart of the absolute value of the (a) measured and (b) ideal process matrix χ of the Toffoli gate. The 4096 elements are displayed in the operator basis $\{III, IIX, II\tilde{Y}, \ldots, ZZZ\}$. The process fidelity is $F = 69 \pm 3\,\%$.

surements and an error of the fidelity of 0.5 %, whereas for the process tomography we averaged each measurement setting for $\sim$ 790 000 times, resulting in a total number of $\sim 3.2 \times 10^9$ measurements and an error of the fidelity of 3 %. This shows that even without random sampling, the total number of measurements (including repeated measurements used for averaging) to achieve a smaller error is less for Monte Carlo process certification than for process tomography. The measurement outcomes for the different operators are shown in Fig. 7.9.

As discussed before, the significant advantage of Monte Carlo process estimation is that one can estimate the fidelity of a process also without sampling over all relevant Pauli operators, at the expense of a higher uncertainty. If all relevant Pauli operators have been measured like in our experiments, the only error in the fidelity is due to the experimental uncertainty in the estimation of the different expectation values. In the case that an incomplete set of Pauli operators is sampled, there is an additional error. An asymptotic bound for this error is calculated in the supplementary material of [daSilva11], and it is shown that these bounds scale polynomially

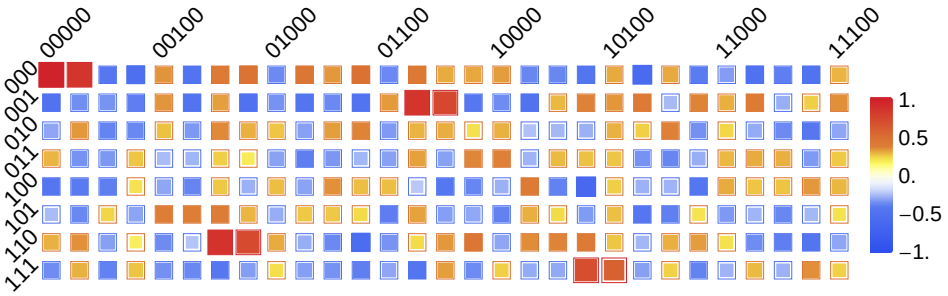

Figure 7.9: Hinton diagram of the measured expectation values of all relevant operators of the Toffoli gate Choi matrices. The thin border shows the ideally expected values, the colored squares are the estimated values. The (000, 00000) entry is the expectation of the identity, so they have sizes corresponding to absolute value 1 and the area of the other squares are adjusted proportionally. The column label corresponds to the most-significant digits of the binary expansion of the index of the observable, while the row label corresponds to the least significant digits (see Appendix C.1.3).

with the number of measured samples. However, the bounds are not tight and therefore too pessimistic to be used in the calculation of error bars. The error in the fidelity estimate when performing non-exhaustive sampling of the Pauli operators can be obtained by non-parametric resampling methods such as bootstrapping [Efron81]. However, given that we have measured all the relevant Pauli operators for each of the gates we characterized, we can simply gather statistics for estimates with non-exhaustive sampling. The corresponding data for the Toffoli gate is shown in Fig. 7.10. For our data one finds e. g. an additional error of 2 % for sampling 100 Pauli operators or an additional error of 3.2 % when sampling only 50 Pauli operators. This illustrates that Monte Carlo sampling leads to significant reduction in the number of measurements required to determine the fidelity with a given error bound.

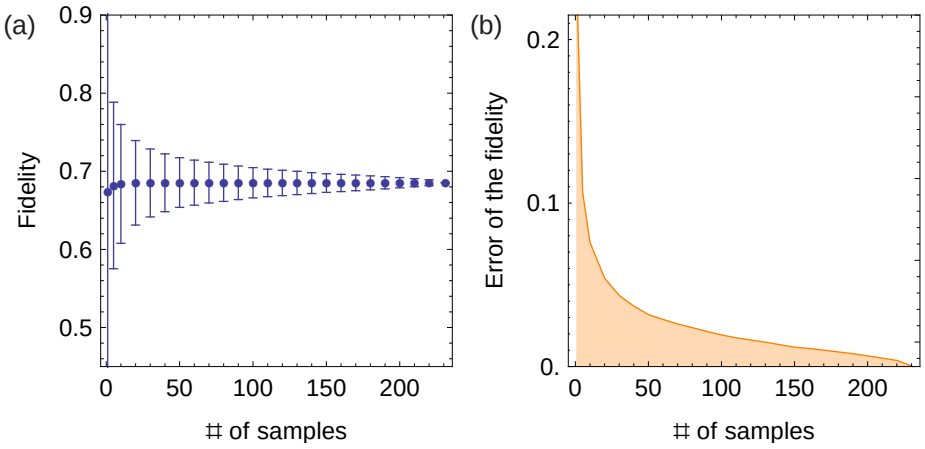

Figure 7.10: (a) Mean of the estimated average output fidelity of a Toffoli gate as a function of the number of sampled observables. The error bars correspond to the 90 % confidence interval, which in turn gives an estimate of the additional error due to the non-exhaustive sampling of relevant observables. (b) Half width of the 90 % confidence intervals vs. the corresponding number of samples.

7.3. Conclusion

Monte Carlo process certification allows to estimate the fidelity of an experimentally implemented process to an ideal one more efficiently than with quantum process tomography. It estimates the fidelity without completely characterizing the process since operators which do not contribute to the fidelity are not measured. In this way we characterized different two- and three-qubit gates, namely our implementation of the CNOT and CPHASE gate, a combination of two CPHASE gates on three qubits as well as the Toffoli gate. Monte Carlo process certification allows also to estimate the fidelity without measuring all operators which actually would contribute to the fidelity. In this case the random non-complete sampling induces an additional error which has been characterized experimentally for the Toffoli gate. We compared the results from full process tomography with Monte Carlo process certification and found that they give consistent results, but Monte Carlo process certification gives more accurate estimates of the fidelity with fewer measurements. In future systems with more qubits, Monte Carlo process certification could become an important method for the estimation of the fidelity of multi-qubit gates and processes since performing process tomography will become impossible due to the exponential scaling.

8

Quantum teleportation of a solid-state qubit

Everybody really knows if you are ever going
to make a real quantum computer,
it must be solid state.

— Benjamin Schumacher

One of the most interesting and also surprising quantum algorithms is *quantum teleportation*, since it allows to transfer a quantum state without transporting the actual information carrier. In this chapter we describe the implementation of this algorithm with superconducting circuits. The reported experiments demonstrate the first implementation of the full teleportation algorithm in any solid-state system.

The teleportation algorithm is explained in Sec. 8.1 accompanied by an overview of the implementations of the protocol in other systems (Sec. 8.1.1). In Sec. 8.1.2 the optimal simulation of the teleportation algorithm with only classical resources is described. Our implementation of the protocol [Steffen13] is presented in detail in Sec. 8.2.

8.1. Quantum teleportation

Quantum teleportation [Bennett93] describes the process of transferring an unknown quantum state between two parties at two different physical lo-

cations without transferring the physical carrier of quantum information itself. This especially means that neither the physical carrier of information itself is transferred nor a SWAP-operation between the sender and the receiver is performed. Instead teleportation makes use of the non-local correlations provided by an entangled pair shared between the sender and the receiver and the exchange of classical information. This concept plays a central role in extending the range of quantum communication using quantum repeaters [Gisin02, Briegel98] and can also be used to implement logic gates for universal quantum computation [Gottesman99].

In the original teleportation protocol [Bennett93], the unknown state $|\psi_{\text{in}}\rangle$ of qubit Q1 in possession of the sender is transferred to the receiver's qubit Q3 (Fig. 8.1 (a)). To enable this task, sender and receiver prepare in advance a maximally-entangled (Bell) state between an ancillary qubit Q2 which remains with the sender and Q3 which is located at the receiver. Then the sender performs a measurement of Q1 and Q2 in the Bell basis which projects the two qubits in the sender's possession onto one of the four possible Bell states $|\Phi^{\pm}\rangle = (|00\rangle \pm |11\rangle)/\sqrt{2}$ and $|\Psi^{\pm}\rangle = (|01\rangle \pm |10\rangle)/\sqrt{2}$. As a consequence, the receiver's qubit Q3 is projected, instantaneously and without ever having interacted with the senders qubit Q1, onto a state $|\psi_{\text{out}}\rangle = \{\mathbb{1}, \hat{\sigma}_x, \hat{\sigma}_z, i\hat{\sigma}_y\}\,|\psi_{\text{in}}\rangle$, which differs from the input state $|\psi_{\text{in}}\rangle$ only by a single qubit rotation, depending on the four possible measurement results. To always recover the original state $|\psi_{\text{in}}\rangle$ the receiver may rotate the output state of Q3 conditioned on the outcome of the Bell measurement communicated to the receiver as two bits of information via a classical channel. This final step is frequently referred to as feed-forward, since the outcome of a measurement performed on one part is used to control the other part of the same quantum system. This is in contrast to acting back on the same quantum system, which we call a feed-back process.

The protocol we implemented is shown in Fig. 8.1 (b) and is equivalent to the original teleportation protocol as described in Sec. 8.2.

8.1.1. Realization of quantum teleportation in other systems

In pioneering work, the teleportation protocol was first implemented with single photons [Bouwmeester97] over lab-scale distances and later also over km-scale distances in free space [Marcikic03, Yin12, Ma12]. However, in these experiments only two out of four Bell states were distinguished un-

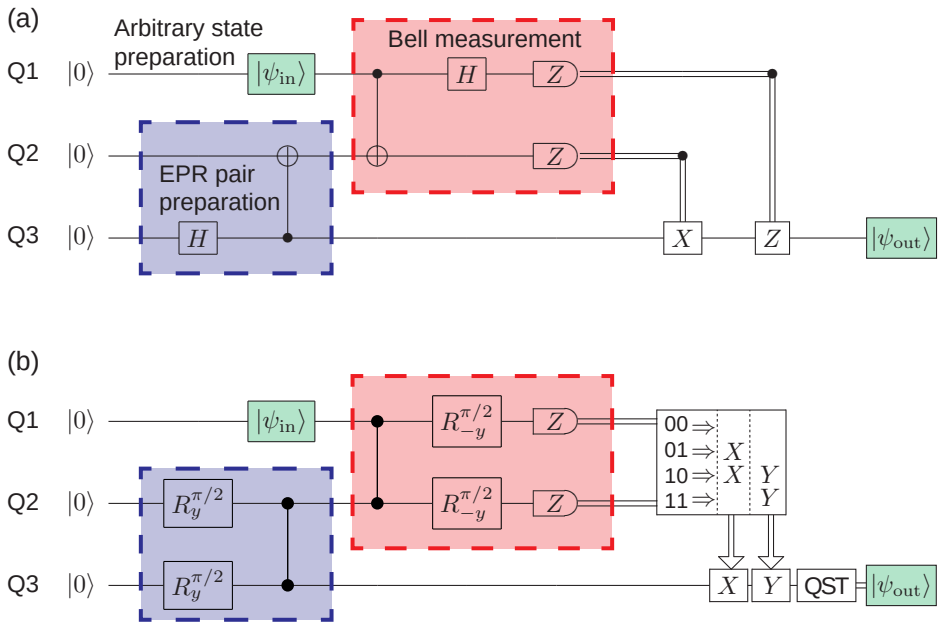

Figure 8.1: (a) Standard protocol of the teleportation scheme. The standard protocol starts with the preparation of a Bell state between Q2 and Q3 (blue box) followed by the preparation of an arbitrary state $|\psi_{\text{in}}\rangle$ (green box) and a Bell state measurement of Q1 and Q2 (red box). The classical information extracted by the measurement of Q1 and Q2 is transferred to the receiver to perform local gates conditioned on the measurement outcomes. After the protocol Q3 is in a state $|\psi_{\text{out}}\rangle$ which ideally is identical to $|\psi_{\text{in}}\rangle$ (also colored in green). (b) Implemented scheme. The protocol implemented in our experiment uses CPHASE gates and single-qubit rotations. To finalize the teleportation we either post-select on any single one of the four measurement outcomes $00, 01, 10, 11$, or we deterministically use all four outcomes which we then may use to implement feed-forward. The feed-forward operators X and Y are applied to Q3 conditioned on the four measurement outcomes according to the table presented in the figure. At the end, quantum state tomography (QST) is performed to characterize the output state.

ambiguously, limiting the efficiency of the protocol to 50 % at best. A proof of principle experiment which can distinguish all four Bell states was implemented using non-linear photon interaction [Kim01] but the efficiency of the detection step was much below 1 %. With photonic continuous-variable states teleportation has been achieved deterministically for all measurement outcomes and the final conditional rotation has been implemented to complete the teleportation protocol [Furusawa98, Lee11]. Along with the publication of the results presented in this chapter [Steffen13], the deterministic teleportation of photonic qubits was reported in [Takeda13] by using a continuous-variable technique. In atomic qubits, fully deterministic quantum teleportation has been realized over micrometer scale distances with ions in the same trap [Riebe04, Barrett04]. Non-deterministically, the protocol has also been implemented between ions in different traps [Olmschenk09], in atomic ensembles [Bao12], and single atoms [Nölleke13]. Using nuclear magnetic resonance techniques for spin ensembles a teleportation-like protocol was implemented over interatomic distances by replacing the readout and feed-forward step with dephasing and conditioned unitary operations [Nielsen98].

8.1.2. Optimal classical algorithm

By fully implementing the teleportation protocol it is possible to always recover the initial state with unit fidelity. Moreover, although two bits of classical information are needed to recover the original state, they do not provide *any* information about the original state itself. In this subsection we discuss how well one can classically simulate a teleportation protocol.

A "classical" version of the teleportation protocol does not make use of an entangled state shared by the two parties. Instead the only resources are the projective measurement of the initial state and a classical communication channel. In [Massar95] it is shown that the information extracted from the projective measurement of one qubit allows to recreate the qubit state with an average fidelity of $\langle \mathcal{F} \rangle = 2/3$. In the classical protocol the initial state can therefore be transferred only with a limited fidelity and the information transferred over the classical channel contains information about the original state.

Another point of view is presented in [vanEnk07], where teleportation is discussed as a method to verify entanglement. Indeed, if a teleportation

protocol is executed and the average output state fidelity is above 2/3, it unambiguously shows that the two parties shared an entangled state (not considering a potential hidden-variable model [vanEnk07]).

An algorithm which achieves this classically optimal state transfer can be implemented as follows: The sender performs a projective measurement of the qubit and sends the outcome to the receiver who prepares his qubit just in the state which was measured at the sender. We now calculate explicitly the average fidelity achieved by this algorithm to demonstrate that it achieves the theoretically maximal value of $\langle \mathcal{F} \rangle = 2/3$. Assume the unknown state is $|\psi\rangle = \alpha |0\rangle + \beta |1\rangle$, where $\alpha = \cos(\theta/2)$ and $\beta = e^{i\phi} \sin(\theta/2)$. Since the density matrix of this state is

$$\rho = \begin{pmatrix} \alpha^2 & \alpha\beta^* \\ \beta\alpha^* & \beta^2 \end{pmatrix}, \tag{8.1}$$

the fidelity $\mathcal{F}_\sigma = \mathrm{tr}[\rho.\sigma]$ of this state relative to the ground (excited) state $|0\rangle$ ($|1\rangle$) is $\mathcal{F}_0 = \alpha^2$ ($\mathcal{F}_1 = \beta^2$). A projective measurement onto the z-axis of the Bloch-sphere will give the outcome "0" with probability α^2 and the outcome "1" with probability β^2. If the target qubit is then prepared in the measured state, its expected fidelity relative to the original state $|\psi\rangle$ is

$$\mathcal{F}_\psi = \alpha^2\alpha^2 + \beta^2\beta^2 = \cos(\theta/2)^4 + \sin(\theta/2)^4. \tag{8.2}$$

It is easy to see that the fidelity of our guess is always $\mathcal{F}_{0,1} = 1$ if the original state was one of the basis states $|0\rangle, |1\rangle$ ($\theta = 0, \pi$). For an equal superposition state ($\theta = \pi/2$), the expected fidelity is always $\mathcal{F}_{\theta=\pi/2} = 0.5$. To get the expected fidelity for an arbitrary input state, one has to integrate Eq. (8.2) over the whole Bloch sphere S:

$$\begin{aligned} \langle \mathcal{F} \rangle &= \frac{1}{4\pi} \int \cos(\theta/2)^4 + \sin(\theta/2)^4 \mathrm{d}S \\ &= \frac{1}{4\pi} \int_{\theta=0}^{\pi} \int_{\phi=0}^{2\pi} \left(\cos(\theta/2)^4 + \sin(\theta/2)^4 \right) \sin\theta \mathrm{d}\theta\mathrm{d}\phi \\ &= 2/3. \end{aligned} \tag{8.3}$$

However, this threshold is only valid if one samples a large number of points equally distributed over the Bloch sphere. For finite sets of

states, the threshold depends on the chosen set and is generally higher than 2/3 [vanEnk07]. If one tests only the four states typically used for quantum process tomography ($|0\rangle, |1\rangle, |0\rangle + |1\rangle, |0\rangle + i|1\rangle$), the classical threshold would be 3/4 (since $|0\rangle$ and $|1\rangle$ can be reproduced with unit fidelity and $\{|0\rangle + |1\rangle, |0\rangle + i|1\rangle\}$ with fidelity 1/2 each).

As pointed out in [Fuchs03], finite sets of states exist for which the classical threshold can be the theoretical minimum, i.e. 2/3. These are all sets of states, whose representation on the Bloch sphere are the corners of a Platonic solid, e.g. a tetrahedron, a cube, or an octahedron. Since the states defined by the intersection of the the Bloch sphere with the x, y, z-axes form an octahedron ($|0\rangle, |1\rangle, |0\rangle + |1\rangle, |0\rangle + i|1\rangle, |0\rangle - |1\rangle$ and $|0\rangle - i|1\rangle$), it is sufficient to show that the average fidelity of these six states is higher than 2/3. A set of such states is also called a set of six *mutually unbiased basis states* [Bengtsson06]. This means that every state belonging to one of the bases is in an equal superposition state with respect to the other two bases.

8.2. Realization of the teleportation protocol

In superconducting circuits, the coherent part of teleportation protocol (i.e. the part before the single-shot measurement, c.f. Fig. 8.1) has previously been implemented and characterized in our lab [Baur12b, Baur12a]. Performing full three-qubit quantum state tomography shows that the resulting state of all qubits right before measurement is a genuine tripartite entangled state. By projecting this three-qubit state onto the four basis states of the sender's qubits and subsequently tracing out the sender's qubits, the teleported states can be reconstructed with an average fidelity of $F = 86\,\%$.

The implementation of fully deterministic quantum teleportation with feed-forward places additional requirements on the sample and the setup: The possibility to read out the sender's qubits independently of the receiver's qubit, the ability to perform single-shot readout of the Bell-state, as well as an active feed-forward circuitry. In the following we show how these tasks have been addressed in our lab in order to successfully demonstrate deterministic quantum teleportation with feed-forward.

8.2.1. Sample and protocol

In order to enable separate readout of the sender's and receiver's qubits, a novel sample geometry has been developed. Based on ideas in [Helmer09], we have realized a circuit QED based architecture in which cross-overs allow to create complex networks with arbitrary connecting topology in a planar technology. A design of the sample is shown in Fig. 8.2 (a). The sample consists of three superconducting transmon qubits (Q1, Q2, Q3) capacitively coupled to three superconducting coplanar waveguide resonators (R1, R2, R3). The individual resonators R1 and R3 allow the sender and the receiver to perform independent measurements of their qubits as detailed below. In addition, Q2 and Q3 are coupled to R2. The resonators R2 and R1 act as quantum buses to realize two-qubit controlled-PHASE (CPHASE) gates used to create a shared Bell state distributed between the sender and the receiver and to perform a deterministic Bell state analysis at the sender. Airbridges are used to realize cross-overs for the resonator lines which enhances scalability of this planar design and to suppress spurious electromagnetic modes by connecting the ground planes across the coplanar wave guides.

Each quibt has individual charge gate lines to perform single qubit rotations as well as individual fast flux bias lines to control its transition frequency. In total 12 ports are used for connecting the qubit charge- and flux-gate lines and the resonator in-/output lines to coaxial cables. This requires the use of the new sample holder discussed in Sec. 4.2 which provides 16 ports — twice as many as the one used during the past few years by our group.

The resonators R1 and R3 have bare resonance frequencies $\nu_\mathrm{r} = \{7.657, 9.677\}$ GHz, respectively. They are coupled by gap- and finger capacitors to their in- and output lines. The overcoupled resonator decay rates are measured to be $\kappa/2\pi = \{2.4, 2.5\}$ MHz. The coupling capacitances are designed asymmetrically such that the decay rate through the input port is approximately 100 times lower than through the output port. The resonator R2 is not coupled to any in- or output line. Its resonance frequency is approximately 8.7 GHz and its decay rate is expected to be close to the internal decay rate of $\kappa < 50$ kHz [Göppl08]. From spectroscopic measurements we determine the maximum transition frequencies $\nu_\mathrm{max} = \{6.273, 7.373, 8.390\}$ GHz and charging energies $E_\mathrm{C}/h = \{0.297, 0.303, 0.287\}$ GHz of the qubits Q1, Q2, and Q3, respectively, where h is

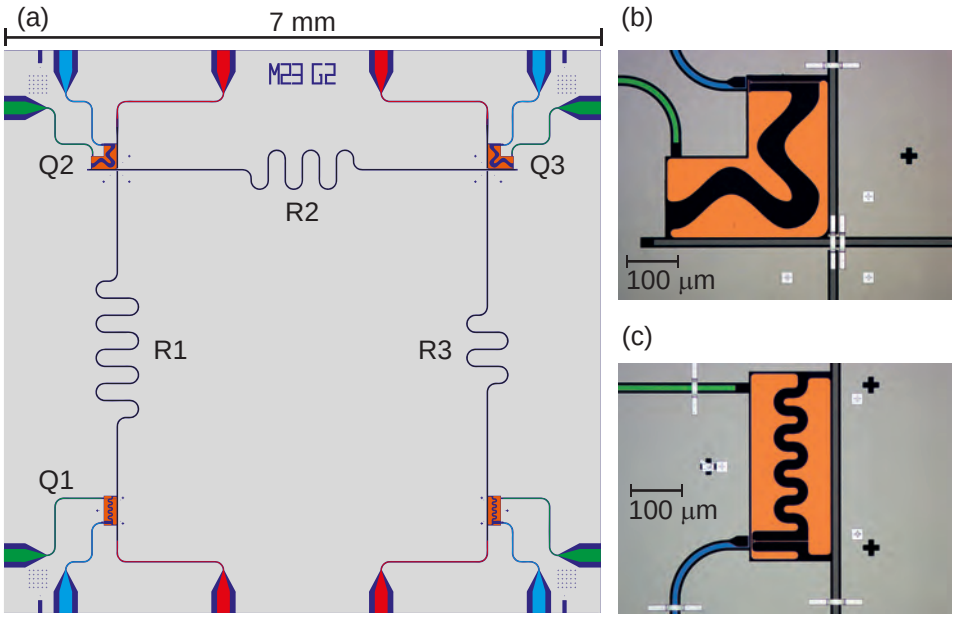

Figure 8.2: Schematics of the sample. (a) Chip-design including three resonators R1, R2 and R3 (black) with corresponding in- and output lines (red) used for readout and coupling of three transmon qubits Q1, Q2 and Q3 (orange). The fourth qubit in the lower right corner of the chip is not used. The local microwave charge gate lines (green) are used for single-qubit rotations while the local flux-bias lines (blue) allow for nanosecond time control of the qubit frequencies to implement two-qubit operations. (b, c) False-color micrographs of Q1 coupled to resonator R1 and of Q2 coupled to both resonators R1 and R2. The micro-fabricated aluminum airbridges visible as bright white strips.

Planck's constant.

Qubits Q1 and Q2 are coupled to resonator R1 with coupling strengths $g/2\pi = \{0.260, 0.180\}$ GHz, and Q3 is coupled to resonator R3 with a coupling strength of $g/2\pi = 0.240$ GHz. The coupling of Q2 and Q3 to R2 is estimated from the transverse coupling strength (see below) to be $g/2\pi = 0.2$ GHz each.

For the presented experiments, the qubits were tuned to idle state transition frequencies $\nu = \{4.776, 5.311, 6.354\}$ GHz with miniature superconducting coils mounted underneath the chip [Bianchetti10a]. At these frequencies we have determined the qubit energy relaxation $T_1 = \{5.5, 3.6, 2.5\}$ µs and coherence times $T_2 = \{1.6, 1.1, 1.4\}$ µs.

The dynamical phases arising from the flux pulses can be compensated just by adjusting the phase of all single qubit gates following a flux pulse (this is in contrast to the Toffoli gate, see Sec. 7.2 and Appendix C.2.1). As an example, the procedure for determining the dynamical phase of Q1 is depicted in Fig. 8.3 (a). A Ramsey-type experiment is performed on Q1, where the temporal separation between the pulses stays constant, but the phase of the second pulse is varied. Depending on the initial state of Q2 and Q3, one either expects (in the absence of dynamical phases) no phase shift (for Q2 in the $|0\rangle$ state) or a 180° phase shift (for Q2 in the $|1\rangle$ state) compared to the case when no flux pulse is present. The additional phase shift observed in the measurement (Fig. 8.3 (b)) corresponds then to the dynamical phase. The full calibration procedure is discussed in Appendix C.3.1.

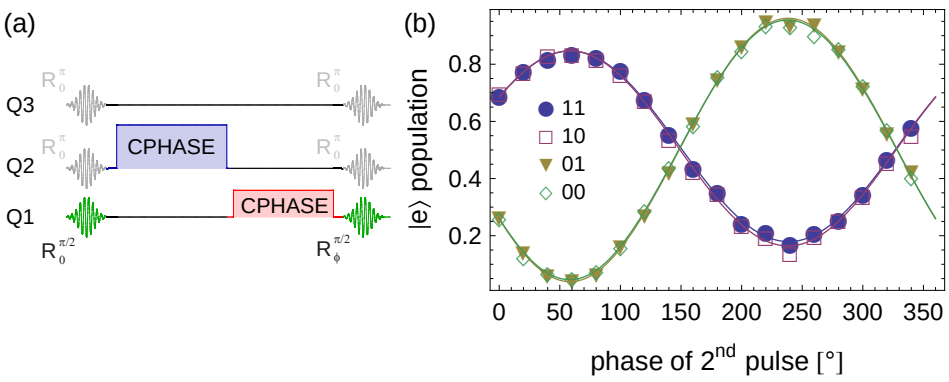

Figure 8.3: (a) Pulse sequence for the calibration of the dynamical phase of Q1. On Q1 a Ramsey-type experiment is performed where the phase of the second pulse is varied. (b) Experimental data for which Q2 and Q3 are at the beginning of the sequence in the state $|11\rangle$ (blue solid dots), $|10\rangle$ (red open squares), $|01\rangle$ (yellow solid triangles), $|00\rangle$ (green open diamonds).

As an essential part of the protocol, we perform a Bell measurement of qubits Q1 and Q2. Since a measurement in our setup is naturally a projective measurement in the computational basis $|00\rangle, |01\rangle, |10\rangle, |11\rangle$ [Blais04, Filipp09], the Bell measurement (Fig. 8.1, red part) consists of a mapping of the Bell basis onto the computational basis and a subsequent measurement in the computational basis as first described and implemented in [Brassard98, Nielsen98]. We realize this basis transformation by using single-qubit rotations and a CPHASE gate. Then we perform a projective joint readout of the states of Q1 and Q2 by measuring the transmission amplitude and phase of resonator R1. A given Bell state is transformed to the corresponding computational basis state resulting in the corresponding output state $|\psi_{\text{out}}\rangle = \{\mathbb{1}, \hat{\sigma}_x, \hat{\sigma}_z, i\hat{\sigma}_y\} |\psi_{\text{in}}\rangle$ of Q3 as follows:

$$\begin{aligned}
\left|\Phi^-\right\rangle &\Rightarrow |00\rangle \quad &\longrightarrow \quad & |\psi_{\text{out}}\rangle = |\psi_{\text{in}}\rangle \\
\left|\Psi^-\right\rangle &\Rightarrow |01\rangle \quad &\longrightarrow \quad & |\psi_{\text{out}}\rangle = \hat{\sigma}_x |\psi_{\text{in}}\rangle \\
\left|\Phi^+\right\rangle &\Rightarrow |10\rangle \quad &\longrightarrow \quad & |\psi_{\text{out}}\rangle = \hat{\sigma}_z |\psi_{\text{in}}\rangle \\
\left|\Psi^+\right\rangle &\Rightarrow |11\rangle \quad &\longrightarrow \quad & |\psi_{\text{out}}\rangle = i\hat{\sigma}_y |\psi_{\text{in}}\rangle \,.
\end{aligned} \tag{8.4}$$

In our realization (Fig. 8.1 (b)) the CNOT gate of the original protocol (Fig. 8.1 (a)) is decomposed into a CPHASE gate and two single-qubit operations, and the Hadamard gate is replaced by an appropriate single-qubit rotation. This protocol is implemented with the pulse scheme depicted in Fig. 8.4. In the figure, Gaussian shaped sinusoids represent the microwave pulses applied to the respective charge bias lines of the qubits, sinusoids on the resonators represent the readout tones, and the squares labeled "CPHASE" represent the flux pulses that shift the frequency of a qubit to implement a controlled-PHASE gate between the marked qubits, where the interaction is mediated through the resonator indicated with a bar of the same color as the flux pulse. Single-qubit rotations are implemented by 12 ns long resonant gaussian-shaped DRAG microwave pulses [Motzoi09, Gambetta11] with average fidelity of greater than 98% as determined by randomized benchmarking (see Sec. 6.3.2). The controlled-PHASE gate is implemented by shifting the qubits with fast magnetic flux pulses to the avoided level crossing between the $|11\rangle$ and $|02\rangle$ states of the involved qubits as described in Sec. 5.2.2. The transverse coupling strengths of $J_{11,02}^{\text{Q1,Q2}}/2\pi = 11.0$ MHz

(between qubits Q1 and Q2) and $J_{11,02}^{Q2,Q3}/2\pi = 10.5$ MHz (between Q2 and Q3) lead to pulse lengths for the CPHASE gates of $t = \{45.6, 47.6\}$ ns, respectively.

The Bell measurement (Fig. 8.4, red elements) allows to map any of the four Bell states to the $|00\rangle$ state by adding π pulses to Q1 and Q2 to flip their states right before commencing the measurement. Instead of applying these π pulses directly we change the phases of the preceding $\pi/2$ pulses accordingly, which can easily be verified to be equivalent.

8.2.2. Experimental setup

A schematic of the experimental setup is shown in Fig. 8.5 (a). The main components shown in (b-e) are described in the following: (b) Amplitude and phase controlled microwave pulses are applied to the qubits using side band modulation of an up-conversion in-phase quadrature (I,Q) mixer driven by a local oscillator (LO) and modulated by an arbitrary waveform generator (AWG). (c) The measurement signals transmitted through R1 and R3 are amplified using JPAs (see Sec. 4.4) pumped by an LO through a directional coupler (D), which is also used for phase (ϕ) and amplitude (A) controlled cancellation of the pump leakage, and coupled to and isolated from the sample by two circulators (C) (see also Sec. 4.4). (d) The signal is further amplified by high-electron-mobility transistor (HEMT) amplifiers at 4 K and chains of ultra low noise (ULN) and low noise (LN) room temperature (RT) amplifiers. (e) The transmission signal of both resonators is down-converted to an intermediate frequency (IF) in an IQ mixer pumped by a dedicated LO, digitized, and fed into field programmable gate array (FPGA) logic for real-time data analysis and triggering the conditioned feed-forward step (see Sec. 8.2.6).

A total of nine signal generators are used – three for controlling the qubits, two to pump the two JPAs, and four for the readout of the two resonators (one drive and one LO for each resonator). Eight AWG channels are used to control the qubits – for each qubit two channels for the amplitude and phase controlled microwave pulses and two more channels for the flux pulses on Q1 and Q2. In addition four AWG channels are used for the feed-forward loop described in Sec. 8.2.6.

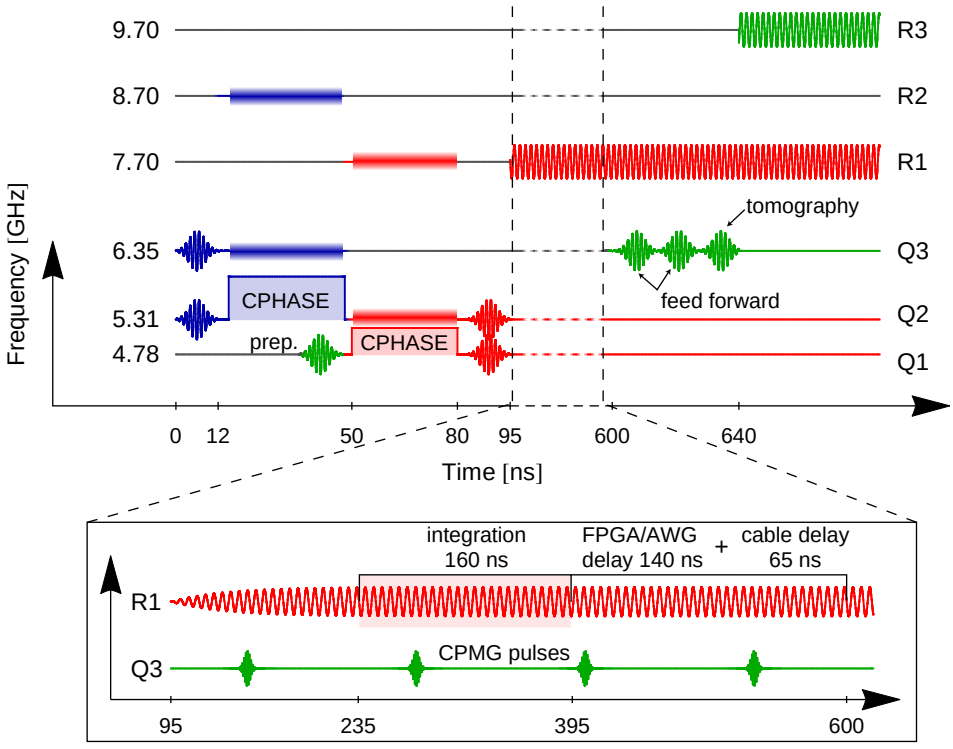

Figure 8.4: Pulse sequence of the teleportation protocol with feed-forward. The color code of the preparation circuit is identical to the one in Fig. 8.1. The inset shows the time used for implementing the conditional feed-forward rotations. The total feed-forward time is the sum of the ramp up time of the measurement tone, the integration time of the measurement signal and the delay times induced by the FPGA signal processing, the AWG trigger and the cables.

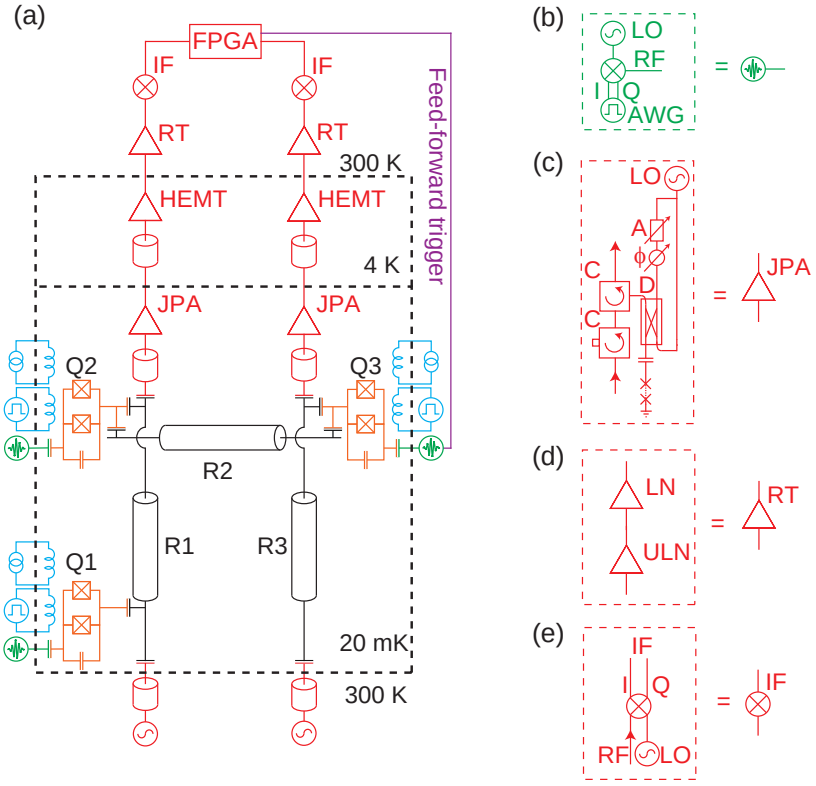

Figure 8.5: (a) Simplified schematic of the measurement setup with the same color code as in Fig. 8.2. (b) – (e) show individual components as described in the text.

8.2.3. Single-shot readout

In order to realize single-shot measurement, the output signals of resonators R1 and R3 are amplified by individual Josephson parametric amplifiers as described in Sec. 4.4. The maximum frequencies for the two parametric amplifiers are $\nu_{\max} = \{8.349, 10.141\}$ GHz for R1 and R3 respectively. To provide a fast response large input capacitors were fabricated which result in a measured JPA linewidth of $\kappa/2\pi = \{334, 548\}$ MHz in the linear regime. For the experiments the parametric amplifiers were tuned to a maximum gain of $G = \{25.4, 22.2\}$ dB with a 3 dB bandwidth of $B/2\pi = \{9, 61\}$ MHz at the frequencies $\nu_{\text{exp}} = \{7.690, 9.740\}$ GHz.

We also use the single-shot measurement technique to herald the ground state of the three-qubit system as described in Sec. 4.4.3. Before each individual experimental realization of the teleportation protocol, we apply a 500 ns long measurement tone to both resonators, to verify that all the qubits are in their ground states. This heralds the ground state with a total efficiency of more than 60%.

8.2.4. Teleportation with post-seletion

To perform a post-selected teleportation protocol, it is sufficient to distinguish only one of the four Bell states, say $|00\rangle$, ideally occurring with a probability of 1/4, with high fidelity from all other states ($|01\rangle, |10\rangle, |11\rangle$). For this purpose we amplify a measurement tone applied to R1 with a JPA operated in the phase sensitive mode in which no or only very little noise is added to the signal [Castellanos-Beltran08]. The transmission of R1 was measured at the readout frequency $\nu_{\text{ro}} = 7.686\,48$ GHz which is the mean value of the effective resonator frequencies for the qubits Q1 and Q2 in the states $|00\rangle$ and $|01\rangle$. The parametric amplifier is used in the phase-sensitive mode by tuning its transition frequency such that the maximum gain was achieved at the readout frequency ν_{ro} at which it was also pumped. Preparing the four computational basis states $|00\rangle, |01\rangle, |10\rangle, |11\rangle$, applying a measurement tone to R1 and integrating the amplified transmission signal for 160 ns results in a distribution of the integrated measurement signals as shown in Fig. 8.6 (a). Since we optimized for the readout contrast between $|00\rangle$ and and all other states, the mean values of the distributions of the integrated signals for these two states (blue and yellow bars in Fig. 8.6 (a))

have the largest separation. However due to the finite qubit lifetime, some of the $|01\rangle$ and $|10\rangle$ population decays into the ground state and are visible in the data as such. We choose a threshold for the integrated quadrature values to discriminate 00 from all other measurement outcomes $01, 10, 11$ with a fidelity of $91.0 \pm 0.1\,\%$, where the error represents the statistical error.

If the measurement of Q1 and Q2 returns 00, qubit Q3 is instantaneously projected to the desired state $|\psi_{\text{in}}\rangle$ not requiring any additional rotations at the receivers qubit to complete teleportation. As described above, by adding π pulses to Q1 and Q2 right before the measurement we map any of the Bell states to the $|00\rangle$ state. This allows us to post-select individually on any of the four Bell states. To characterize the state transfer from Q1 to Q3 we performed full process tomography (see Sec. 6.3.1) to determine the corresponding process matrices $\chi_{00,01,10,11}$. We use *six* different input states $|\psi_{\text{in}}\rangle = |0\rangle, |1\rangle, (|0\rangle+|1\rangle)/\sqrt{2}, (|0\rangle-|1\rangle)/\sqrt{2}, (|0\rangle+i\,|1\rangle)/\sqrt{2}, (|0\rangle-i\,|1\rangle)/\sqrt{2}$ in order to meet even the most strict criteria when comparing to classical thresholds (c.f. Sec. 8.1.2).

The experimentally obtained process matrices (Fig. 8.8 (a)) agree well with the expected processes. The average output state fidelity $\bar{\mathcal{F}}_s^{\text{ps}} = (81.6 \pm 1.2)\,\%$ of all four processes is clearly above the classical limit of $2/3$. This results in an average process fidelity of $\bar{\mathcal{F}}_p^{\text{ps}} = (72.3 \pm 0.7)\,\%$ when post-selecting on a single Bell state, well above the classical limit of $1/2$. The output state fidelity is predominantly limited by relaxation and dephasing of our qubits which affects both the effective gate- and readout fidelity (see Appendix C.3.2).

8.2.5. Deterministic teleportation

To uniquely and simultaneously identify the four randomly distributed outcomes of the Bell state measurement at the sender in a deterministic way (instead of using post-selection) we use high fidelity dispersive single-shot qubit readout enabled by a Josephson parametric amplifier operated in the phase preserving mode [Eichler11].

The readout frequency $\nu_{\text{ro}} = 7.6836\,\text{GHz}$ is chosen to be the mean of the effective resonator frequencies for the qubits Q1 and Q2 in the state $|01\rangle$ and $|10\rangle$. The parametric amplifier is operated in the phase-preserving mode by detuning the pump frequency 6.25 MHz from the readout frequency. In

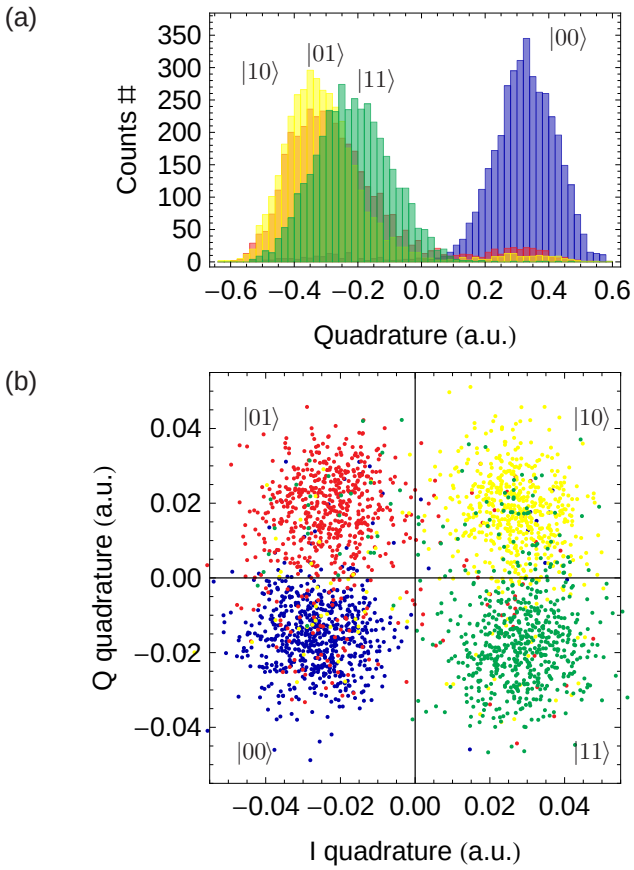

Figure 8.6: (a) Histogram of the integrated signal quadrature amplitude amplified phase sensitively when preparing the states $|00\rangle$ (blue), $|01\rangle$ (red), $|10\rangle$ (yellow), and $|11\rangle$ (green). (b) Scatter plot of integrated (I, Q) quadratures of the measurement signal amplified in the phase preserving mode when preparing the states $|00\rangle$ (blue), $|01\rangle$ (red), $|10\rangle$ (yellow), and $|11\rangle$ (green).

	00	01	10	11
$\|00\rangle$	0.91	0.06	0.01	0.02
$\|01\rangle$	0.13	0.81	0.03	0.03
$\|10\rangle$	0.02	0.04	0.83	0.11
$\|11\rangle$	0.05	0.02	0.09	0.83

Table 8.1: Probabilities of identifying a prepared input state (rows) as the indicated output state (columns). Correct identifications are diagonal elements, misidentifications are off-diagonal elements.

this way the gain $G = 19.8\,\mathrm{dB}$ at the readout frequency and the effective bandwidth are smaller than for phase sensitive amplification, but both quadratures of the electromagnetic field are amplified. By preparing the computational basis states and integrating the transmitted signals of both quadratures (I, Q) simultaneously for 160 ns, we can map every measurement outcome to a point on the complex plane. The choice of integration time digitally filters out the parametric amplifier pump tone which is detuned by 6.25 MHz from the measurement tone. By adjusting the pump power and the readout power we find settings which maximize the distinguishability of all four states by their location in the complex plane, see Fig. 8.6 (b).

Adjusting the phase of the local oscillator and implementing small linear offsets directly in the FPGA we are able to choose the $I = 0$ and $Q = 0$ axes of the complex plane as thresholds to identify the four different output states in real-time (Fig. 8.6 (b)). By assigning our best estimate of the corresponding states to every measurement outcome according to a quadrant in the I, Q-plane, we identify $(84.6 \pm 0.4)\,\%$ of the prepared states correctly. The probabilities of either correctly identifying a prepared state or misidentifying it as a different state are listed in Tab. 8.1 for all four input basis states.

Correlating the four single-shot Bell state measurement outcomes at the sender with the single-shot measurement outcomes at the receiver and performing state and process tomography we find an average deterministic

output state fidelity of the transferred state of $\bar{\mathcal{F}}_s^{\mathrm{det}} = (78.1 \pm 0.9)\,\%$ and an average process fidelity of $\bar{\mathcal{F}}_p^{\mathrm{det}} = (67.2 \pm 0.5)\,\%$ well above the classical limits of 2/3 and 1/2, respectively. The process matrices (Fig. 8.8 (b)) prominently show the characteristic features of the expected processes. The fidelities obtained with this method are lower compared to the post-selected teleportation due to the lower fidelity of the deterministic Bell state readout (see Appendix C.3.2).

8.2.6. Feed-forward

To implement the feed-forward, the measurement data of the Bell measurement is analyzed in real-time and based on its result, a certain operation has to be performed on Q3. For the real-time analysis, our custom built firmware for the FPGA used for data acquisition was extended. The implementation of this firmware was performed by Yves Salathe [Salathe13] based on previous work by Christian Lang [Lang13a]. Depending on the measurement outcome, the FPGA triggers up to two different arbitrary waveform generators (AWGs) which realize σ_x- and σ_y-rotations.

The implementation also requires additional hardware for the control of Q3. A schematic of the extended part of the setup is depicted in Fig. 8.7 (a). In order to ensure phase stability of the pulses applied to Q3, there is only one signal generator providing the carrier signal for all mixers. Its signal is split by two power splitters to pump three different IQ-mixers. The two additional mixers are modulated with *Tektronix* AWG 520 arbitrary waveform generators. The reason for using this type of AWG is their small delay of 38 ns between the arrival of a trigger and the output of the stored pattern, compared to ~ 400 ns for the AWG 5014 model. Since the AWG 520 does not allow to set bias voltages for each channel individually, the bias voltages for the mixer inputs were added to the AWG outputs using bias-tees. The outputs of all mixers were combined again with power combiners before they are fed into the line connected with the charge gate line of Q3. Not shown in Fig. 8.7 (a) are attenuators to equalize all mixer input powers and suppress standing waves, and DC-blocks (inner- and outer-conductor) to prevent ground loops.

The pulses generated with the different AWGs in general have different absolute phases. In order to realize phase controlled pulses, the relative phases between the pulses from different AWGs is compensated for. We

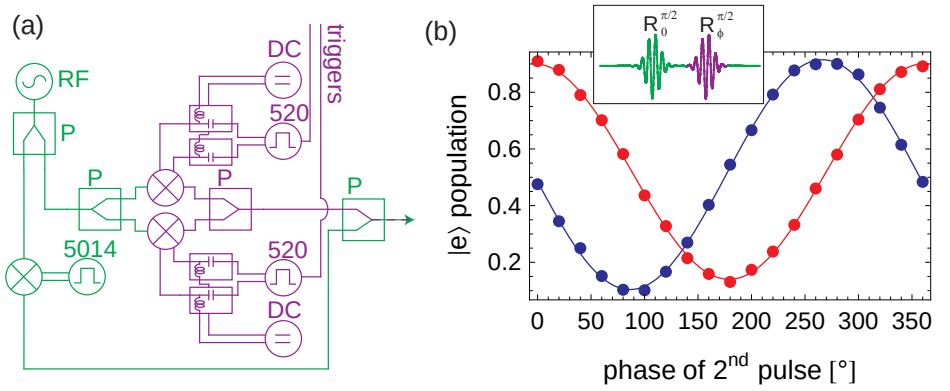

Figure 8.7: (a) Simplified schematic of the room-temperature feed-forward circuitry. Three different IQ-mixers ($\otimes$) are driven by the same source (RF) via power splitters/combiners (P) and modulated via three different AWGs (5014, 520). For more details see text. (b) Calibration measurement of the phase between the different AWGs: The pulse sequence (inset) consists of a $\pi/2$ pulse around the x-axis given by the first AWG (5014, green) followed by a $\pi/2$ pulse on one of the feed-forward AWGs (520, purple). The phase of this second pulse is varied. The dots are measurements with the relative phase uncalibrated (blue) and calibrated (red), solid lines are sinusoidal fits from which the relative phase is extracted.

measure these phases with a Ramsey-type experiment (Fig. 8.7 (b)) in which the first pulse is always a $\pi/2$ pulse with no extra phase, given by the AWG 5014, and the second pulse is a $\pi/2$ pulse whose phase is varied, generated by one of the feed-forward AWGs. The relative phase is then determined by fitting the resulting oscillation to a sinusoid. This phase is then added to all pulses generated with the corresponding AWG.

The total time needed for the feed-forward loop is crucial, since the qubit decay during the waiting time lowers the fidelity of the process. In order to minimize the time needed for data analysis within the FPGA, it assigns a certain state to a measured signal solely based on the quadrant of the complex plane it lies in, see Fig. 8.6 (b). To optimize the readout fidelity we calibrate the phase of the down-conversion local oscillator to rotate the data such that the four different states can be distinguished by thresholds

parallel to the I- and Q-axes of the complex plane. Additionally a small offset is subtracted digitally before the real-time analysis is completed.

With a fixed integration time of 160 ns (see above) we experimentally determine a maximum readout fidelity by starting the integration time 140 ns after the initial rise of the pulsed measurement tone applied to the resonator. A finite delay to achieve the optimal readout fidelity is expected, since the signal-to-noise ratio during the rise time of the resonator is reduced. The FPGA board used for data analysis and the AWG used for generating the feed-forward pulses introduce a combined delay of 140 ns and the total cable delay is 65 ns. As a result, the conditional rotations are applied to Q3 505 ns after the measurement tone has been applied to the readout resonator R1 (Fig. 8.4). To mitigate dephasing of Q3 during this feed-forward delay time, we apply a series of four dynamical decoupling pulses to Q3 (see Appendix B for more information about dynamical decoupling).

We have also fully characterized the fidelity of the feed-forward process. After preparing the state indicated in the rows of Tab. 8.2 and performing the conditional rotations indicated in the columns of Tab. 8.2, the fidelity of the applied feed-forward process was determined. The diagonal elements indicate the fidelity of the desired feed-forward operations occurring with the probabilities shown in Tab. 8.1. The off-diagonal elements indicate the fidelity of the unwanted rotations, occurring with a smaller probability (Tab. 8.1) but a similar fidelity.

We analyzed more than 250 000 single-shot experiments and found a deterministic state transfer fidelity of $\bar{\mathcal{F}}_s^{\mathrm{ff}} = (69.5 \pm 0.1)\,\%$ with a process fidelity $\mathcal{F}_p^{\mathrm{ff}} = (54.2 \pm 0.1)\,\%$, clearly above the classical thresholds. The limited fidelity can be traced back to the fidelities of single- and two-qubit operations, the readout fidelities and the time required for the feed-forward in relation to the coherence times of the employed qubits.

When averaging and appropriately normalizing the measurement results of Q3 directly in the FPGA we are able to circumvent the limited single-shot readout fidelity of Q3 (see also Sec. 6.2.3). In this case, the deterministically teleported states including the feed-forward step have an average fidelity of $\bar{\mathcal{F}}_s^{\mathrm{avg}} = (78.5 \pm 1.0)\,\%$ with a corresponding process fidelity of $\mathcal{F}_p^{\mathrm{avg}} = (67.7 \pm 0.6)\,\%$.

Fig. 8.9 shows the measured density matrices of the teleported states for post-selection and averaged readout using deterministic teleportation with

feed-forward.

	I	X	Y	Z
$\|00\rangle \otimes \|\psi\rangle$	0.75	0.59	0.70	0.67
$\|01\rangle \otimes \hat{\sigma}_x\|\psi\rangle$	0.66	0.74	0.67	0.68
$\|10\rangle \otimes \hat{\sigma}_z\|\psi\rangle$	0.70	0.75	0.71	0.67
$\|11\rangle \otimes i\hat{\sigma}_y\|\psi\rangle$	0.68	0.75	0.70	0.72

Table 8.2: Process fidelities of the feed-forward pulses. After preparing the indicated input states (rows) and performing the conditional operations (columns), the fidelity of the expected process is determined (elements of the table). The rows indicate the fidelity of the performed rotation conditioned on the measurement result of Q1 and Q2, which occur with the probabilities shown in Tab. 8.1. Note that the off-diagonal elements are calculated with fewer events, leading to a higher variation in the fidelity.

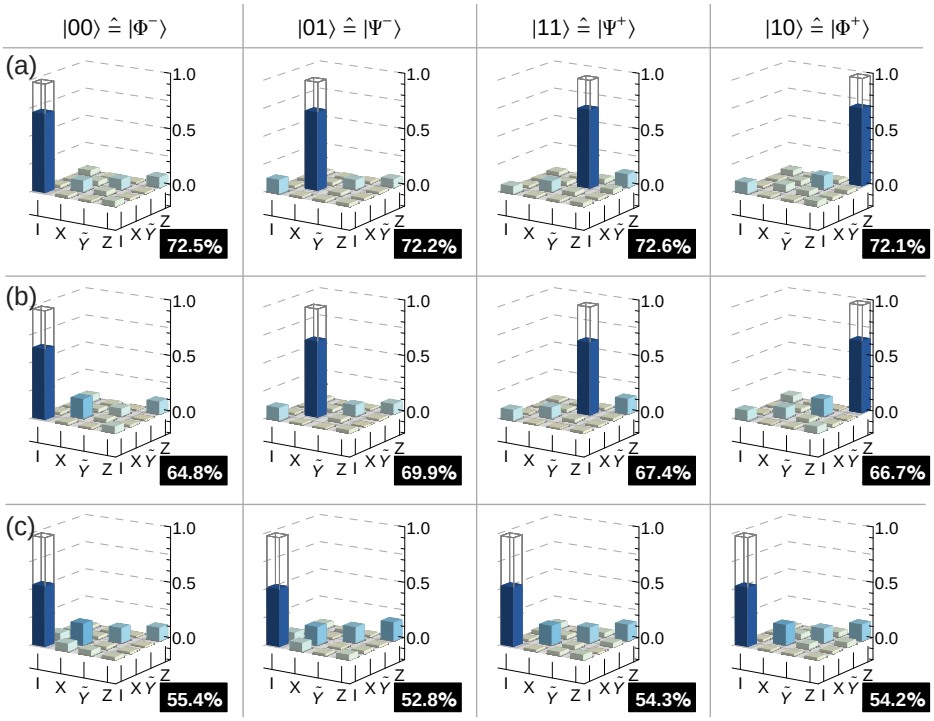

Figure 8.8: **State transfer process matrix for quantum teleportation.** The experimentally obtained (solid bars) absolute values of the process matrices $|\chi|$ describing the state transfer from Q1 to Q3 by teleportation are displayed for: (a) Post-selection on any single one of the Bell-measurement outcomes $00, 01, 10, 11$, (b) simultaneous deterministic measurement of all four outcomes, and (c) with feed-forward. The respective process fidelities are indicated in black boxes. The ideal $|\chi|$ is indicated by wire frames.

8.2.7. Comparison with other implementations

Our implementation of the quantum teleportation protocol stands out due to the high efficiency and high rate at which teleportation events take place. To illustrate this, a comparison of different implementations of quantum teleportation with qubits is presented in Tab. 8.3. Approximate numbers (with the "≈" sign) are estimated from data provided in plots of the original

publications. For several experiments, no number for the distance between the two parties is given in the publication, but something on the order of 1 m seems to be a reasonable distance for a quantum-optics experiments (indicated with (≈ 1)). Compared are at first the success probability of an experiment, the repetition rate and the product of these two quantities which is the number of successful events per second. Comparing these properties, our implementation teleports ≈ 100 times more qubits per second than the implementation with the highest number of events before (ions in one trap). Also the success probability of 0.6 of our implementation, limited due to the passive ground state preparation, is only outperformed by the implementation with ions in one trap. Further compared are the distance, the average state fidelity (the number for our experiment is the one with feed-forward) and whether the teleportation was deterministic (i.e. all four Bell states could be distinguished) and whether feed-forward was used (for at least two states).

In addition to the teleportation of qubits, continuous-variable teleportation [Vaidman94, Braunstein98] has been realized [Furusawa98, Lee11] in optical systems. There the teleported states are not qubits, but continuous-variable states as e.g. coherent states. In contrast to qubit teleportation, also the information transmitted over the classical channel consists of continuous variables, e.g. an analogue photocurrent. These experiments are usually driven continuously and work therefore only on narrow frequency bandwidths which made them unable to be used with (broad frequency bandwidth) photonic qubits as input states. Published simultaneously with our results, Takeda *et al.* reported in [Takeda13] the first qubit teleportation using a continuous-variable setup. They used a broadband continuous-variable teleporter combined with a compatible narrowband time-bin qubit and reached a deterministic teleportation rate of $\approx 5000\,\mathrm{s}^{-1}$.

Figure 8.9: **(next page) Characterization of the output states.** Real (blue) and imaginary (red) parts of the reconstructed density matrices of the state $|\psi_{\mathrm{out}}\rangle$ for the indicated input states $|\psi_{\mathrm{in}}\rangle$ obtained from state tomography when (a) post-selecting data on a 00 outcome of the Bell measurement (b) using averaged readout on Q3 while performing fully deterministic teleportation with feed-forward. The ideally expected outcomes are indicated with wireframes. The state fidelities are indicated in the black boxes.

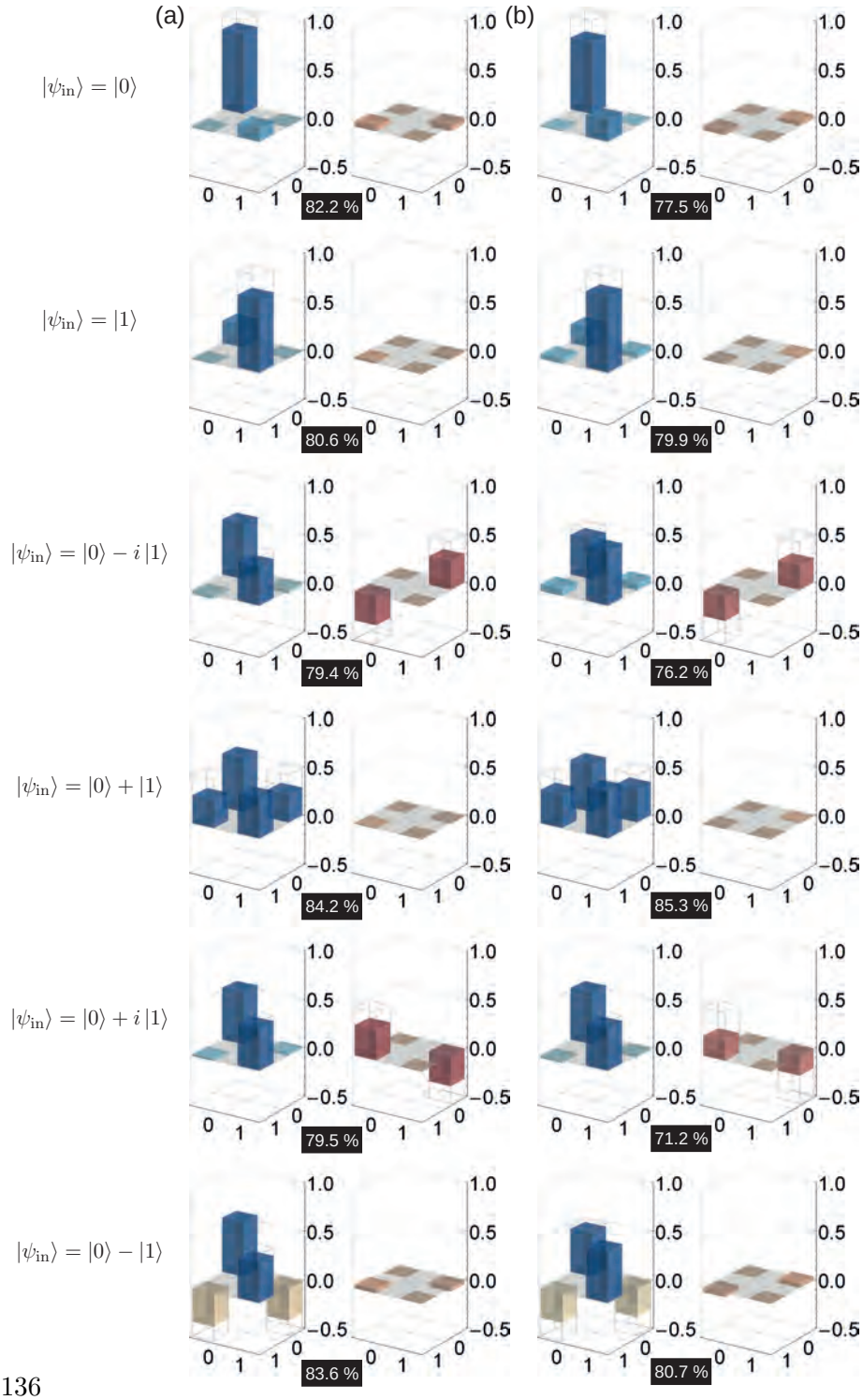
(a)
(b)
$|\psi_{\mathrm{in}}\rangle = |0\rangle$
$|\psi_{\mathrm{in}}\rangle = |1\rangle$
$|\psi_{\mathrm{in}}\rangle = |0\rangle - i\,|1\rangle$
$|\psi_{\mathrm{in}}\rangle = |0\rangle + |1\rangle$
$|\psi_{\mathrm{in}}\rangle = |0\rangle + i\,|1\rangle$
$|\psi_{\mathrm{in}}\rangle = |0\rangle - |1\rangle$
82.2 %
77.5 %
80.6 %
79.9 %
79.4 %
76.2 %
84.2 %
85.3 %
79.5 %
71.2 %
83.6 %
80.7 %

Implementation		Success probability	Rate [Hz]	Events [1/s]	Distance [m]	Avg. state fidelity	Det	FF
Photons	first[1]	$\approx 3 \times 10^{-10}$	76×10^6	≈ 0.025	(≈ 1)	0.68	–	–
	furthest[2]	$\approx 3 \times 10^{-10}$	80×10^6	≈ 0.026	$143\ 10^3$	0.863	–	–
	furthest[2]	$\approx 3 \times 10^{-10}$	80×10^6	≈ 0.026	$143\ 10^3$	0.78	–	✓
	determ.[3]	$\approx 8 \times 10^{-11}$	82×10^6	≈ 0.007	(≈ 1)	0.83	✓	–
Ions	one trap[4]	1	250	250	$5\ 10^{-6}$	0.78	✓	✓
	two traps[5]	$2.2\ 10^{-8}$	75 000	$1.65\ 10^{-3}$	1	0.9	–	–
Neutral atoms	[6]	10^{-3}	10 000	10	(≈ 1)	0.789	–	–
Atomic ensembles	[7]	10^{-4}	71.4	0.007	150	0.95	–	–
Circuit QED		0.6	40 000	24 000	0.006	0.695	✓	✓

Table 8.3: Comparison of different implementations of quantum teleportation with qubits. "Det" indicates whether all four Bell states could be separated, "FF" indicates whether feed-forward was implemented for at least two Bell-state outcomes.

[1] [Bouwmeester97] [2] [Ma12] [3] [Kim01]
[4] [Barrett04] [5] [Olmschenk09] [6] [Nölleke13]
[7] [Bao12]

8.3. Conclusion

The experiments presented in this chapter demonstrate the first implementation of quantum teleportation with solid-state qubits. We implemented a novel device geometry, two independent single-shot readout channels and a feed-forward loop. The independent single-shot readout channels are realized with two Josephson parametric amplifiers connected to two readout resonators. The feed-forward step is implemented with an FPGA with custom firmware that analyzes the outcome of the Bell measurement in real-time and triggers up to two different AWGs.

The results demonstrate the progress made in the field of superconducting circuits and mark an important step on the way to the realization of quantum computing and quantum communication with superconducting circuits. The presented scheme may find application in quantum repeaters [Gisin02] or schemes allowing universal quantum computation [Gottesman99].

9

Conclusion and Outlook

9.1. Conclusion

The presented thesis summarizes the quantum information processing experiments I have been working on in the QUDEV-Lab at ETH Zürich during the last years. At the beginning we performed characterization measurements of one [Bianchetti09, Baur09, Bianchetti10b] and two [Filipp09] qubits. Increased control over the quantum systems was gained by the implementation of charge [Leek09, Leek10] and flux [Fink10b, Bozyigit11] gate lines. Extending the setup to operate a three qubit quantum processor allowed us to demonstrate and characterize quantum gates and algorithms [Baur12a, Fedorov12, Steffen12]. Finally, the inclusion of parametric amplifiers [Eichler11] and real-time feed-forward led to the deterministic teleportation of a qubit in superconducting circuits [Steffen13].

9.2. Outlook

9.2.1. General outlook

The field of superconducting circuits has made extraordinary progress in the last few years. But still it is a long way towards the implementation of a quantum computer than can solve problems faster (on an absolute time scale) than a classical computer.

At the current state of the art, superconducting circuits are at a stage

where simple multi-qubit algorithms have been demonstrated [DiCarlo09, Steffen13] and first error correcting schemes have been implemented [Reed12].

The next big step on the way to a fault-tolerant [Preskill97] quantum computer will involve the implementation of a logical qubit with a longer lifetime than the physical qubits which it is made of [Devoret13]. This however requires also the continuous development and improvement of more "basic" properties such as longer coherence times, more stable single- and two-qubit operations or novel device topologies.

The coherence times of superconducting qubits improved steadily over the last few years. The limiting factor at the current stage is suspected to be the surface loss from metal-substrate and substrate-air interfaces [Martinis05, Wenner11]. Addressing this issue e.g. through novel device geometries using three-dimensional cavities [Paik11] or stripline cavities [Sandberg13], advances in fabrication [Chang13] or new qubit designs [Barends13] has shown promising results. The approach of placing a transmon qubit into a three-dimensional cavity [Paik11] has demonstrated coherence time on the order of 100 µs [Rigetti12], which are the highest reported with transmon qubits so far. In these three-dimensional cavities most of the electromagnetic energy is stored in the vacuum, thus minimizing the surface loss from interfaces. This geometry has been used successfully in several experiments [Ristè12b, Kirchmair13, Abdumalikov13, Murch13, Ristè13].

Also single- and two-qubit operations are further developed. By using microwave-only control with fixed-frequency single-junction transmon qubits, a universal set of quantum gates approaching fault-tolerant thresholds [Chow12] has been demonstrated. New schemes of entangling gates exploiting non-computational states in fixed-frequency qubits have been proposed and implemented [Chow13]. Moreover, potentially noise-resilient geometric gates have been realized [Abdumalikov13].

Novel device architectures have been proposed [DiVincenzo09, Helmer09, Steffen11] which allow to increase the complexity of on-chip networks to reach scalability and fault-tolerance, and first implementations have been studied [Underwood12, Steffen13]. More complex architectures, like implementations of surface codes [Fowler12] are also studied theoretically in the context of superconducting circuits.

Besides the efforts to pursue this "conventional" way of gate-based quantum computing, a different approach known as *quantum annealing* is explored experimentally with superconducting circuits [Johnson11, Dickson13].

Quantum annealing [Das08] is a sort of "analog quantum computation" used to solve certain hard optimization problems. The solution of the problem is thereby encoded in the ground state of the final Hamiltonian, into which the system is adiabatically transferred. It has been shown [Boixo13b] that present realizations of quantum annealers (e.g. *D-Wave System's* D-Wave One [Johnson11]) indeed perform quantum annealing with more than one hundred qubits, despite the limited qubit coherence time of tens of nanoseconds [Boixo13a]. However, it should be noted that these devices are not universal quantum computers but special purpose quantum optimizers [Troyer13].

In addition to the progress on superconducting quantum processors, other hardware is developed and refined steadily: Current advances made in the development of quantum limited amplifiers based on superconducting circuits [Eichler13b, Abdo13, Mutus13] allow for increasingly faithful readout of quantum states. Combining these with recent advances in feed-back techniques [Ristè13, Campagne-Ibarcq13, Steffen13] enables superior control over the quantum systems.

But the field is not limited to more and more powerful superconducting chips. Hybrid systems, superconducting circuits coupled to other quantum systems [Xiang13], are promising candidates for realizing quantum memories. These "other systems" include e.g. Rydberg atoms [Hogan12], semiconductor quantum dots [Frey12] or nitrogen-vacancy centers in diamonds [Kubo11]. Combining superconducting "CPUs" with a memory made from any of these systems (and using e.g. teleportation for the state transfer) could allow to implement a hybrid quantum von Neumann architecture [Mariantoni11].

Besides quantum information processing, superconducting circuits could also be used in quantum communication by using propagating microwave photons [Eichler13a, Pechal13, Srinivasan13]. Once larger distances can be overcome, the schemes demonstrated in this thesis will allow the construction of quantum repeaters [Gisin02] for quantum communication at microwave frequencies or might even allow to realize a loophole-free test of Bell's inequality [Bell64].

9.2.2. Next experiments

There are several possible experiments with superconducting circuits that could be realized in the near future. Using the same sample as used for the teleportation experiment (Fig. 8.2), it will be possible to implement e.g. digital quantum simulations of spin chain models [Las Heras13]. A quantum simulator [Georgescu13] allows to model the behavior of a certain quantum system, for instance a chain of spins. *Digital* in this context means that the corresponding Hamiltonian can be approximated by discrete stepwise unitaries. Models like the Heisenberg model or the frustrated Ising model only need nearest neighbor interaction and could therefore be implemented using one- and two-qubit gates.

Amongst the experiments which involve or develop further the teleportation experiment is e.g. entanglement swapping [Żukowski93]. Entanglement swapping is a key resource (together with entanglement distillation [Bennett96a, Bennett96b]) for the realization of a quantum repeater, which allows to distribute entanglement over large distances. The working principle of entanglement swapping can be described as follows: Two remote parties, (A and B) have each a pair of entangled qubits. Each party sends one part of its entangled pair to an intermediate party (C) which then performs a quantum teleportation to transfer the state of A's qubit to B. Hence, A and B share an entangled pair of qubits. The modification of the chip design (see Fig. 8.2) needed for this experiment would be the possibility to read out resonator R2. Initially entangling Q1 and Q2 as well as Q3 and Q4 (the qubit not labeled in Fig. 8.2) and then performing a teleportation of the state of Q2 to Q4 would leave Q1 and Q4 in an entangled state, thus realizing entanglement swapping.

Entangling qubits on different chips can be used for the above mentioned distribution of entanglement via quantum repeaters or the teleportation of information between a "processor"-chip and a "memory"-chip. In order to realize entanglement on different chips, a faithful conversion of stationary qubits (e.g. transmons) to flying qubits (e.g. propagating microwave photons) and vice versa will be a key resource in future experiments. First experiments demonstrating photon shaping have already been carried out [Pechal13, Srinivasan13], and ongoing research will soon enable also the absorption of a propagating microwave qubit and the mapping of its state to a stationary qubit.

9.2.3. Quantum engineering

The field of superconducting circuits has now matured to a point where it is not only investigating fundamental physics, but it is now one of the most active topics in *quantum engineering*. Several companies do research on exactly this topic (groups at *IBM*, *Raytheon BBN*, *NEC*) or it is even their core business (*D-Wave Systems*).

Quantum engineering has already arrived in everyday live. Many technical applications rely on the exploitation of quantum effects, e.g. the use of quantum tunneling in flash memory cells [Pavan97]. But taking quantum effects into account will become even more important in future technologies, as shrinking structures more and more automatically leads to an emergence of "quantum behavior". From there, it is only a small step to actively engineering quantum systems. Quantum computing is thereby not the only application. Novel technologies based on quantum engineering – such as quantum dot solar cells [Kamat08] or highly efficient light-emitting diodes [Sun07] based on quantum dots, to give two examples – have the potential to dramatically change the future.

A

Fabrication recipes

A.1. Resonators, gate lines

The following recipes can be used for fabricating resonators and gate lines as described in Sec. 3.2.1. The etching parameters are for a 150 nm thick Nb layer. At first the process is given where the AZ5214E resist is used as a positive resist, followed by the process where PMMA is used as resist.

AZ5214E positive process

Process step	Description	Comments
Chip cleaning	Acetone, ultrasonic bath for 5 min, 50 °C Isopropanol, ultrasonic bath for 5 min, 50 °C Rinse with DI water for 2 min N_2 blow dry	
Resist spinning	Prebake on hot plate for 10 min, 180 °C	

	Cool down for 3 min	
	Set up spinner	Step 0: 500 rpm, 2 s, 2 s ramp up time Step 1: 4000 rpm, 45 s, 3 s ramp up time
	Spin AZ5214E	
	Revome resist from back of the wafer	
	Bake on hotplate for 60 s at 105 °C	
	Cool down for $\geq$ 3 min	Thickness should be $\approx$ 1.4 µm
Photo lithography	Warm up MA6 mask aligner	
	Measure intensity at 365 nm	Typically $\approx$ 5 mW/cm^2
	Set exposure time for a dose of 50 mJ/cm^2 at 365 nm	
	Align mask and expose	Use “Vacuum contact” mode
	Develop for 30 s in MIF 726	
	Rinse under flowing DI water for 60 s	
	N_2 blow dry for 60 s	Inspect wafer under microscope
RIE etching	Load sample into RIE etcher	Use microscope slides to stabilize wafer
	Run “Nb-etch” recipe for 2’30”	Ar: 10 sccm, SF_6: 20 sccm; pressure: 130 µbar, 150 W RF power

Cleaning	Clean with Acetone and Isopropanol in ultrasonic bath each for 5 min at 50 °C	

PMMA positive process

Process step	Description	Comments
Chip cleaning	Acetone, ultrasonic bath for 5 min, 50 °C Isopropanol, ultrasonic bath for 5 min, 50 °C Rinse with DI water for 2 min N_2 blow dry	
Resist spinning	Prebake on hot plate for 10 min, 180 °C Cool down for 3 min Set up spinner Spin PMMA 950K in EL Revome resist from back of the wafer Bake on hotplate for 180 s at 180 °C Cool down for $\geq$ 3 min	 Step 0: 1000 rpm, 2 s, 2 s ramp up time Step 1: 2000 rpm, 90 s, 2 s ramp up time Thickness should be $\approx$ 400 nm

DUV photo lithography	Warm up DUV mask aligner, use 220 nm mirror, DUV channel and CP mode	
	Measure intensity at 220 nm	Typically $\approx 20\,\mathrm{mW/cm^2}$
	Set exposure time for a dose of $6400\,\mathrm{mJ/cm^2}$ at 220 nm	
	Align mask and expose	
	Develop for 60 s in MIBK:IPA 1:1	
	Rinse under flowing DI water for 30 s	
	N_2 blow dry for 30 s	Inspect wafer under microscope
RIE etching	Load sample into RIE etcher	Use microscope slides to stabilize wafer
	Run "Nb-etch" recipe for 2'30"	Ar: 10 sccm, SF_6: 20 sccm; pressure: 130 µbar, 150 W RF power This will also etch PMMA!
Cleaning	Flood exposure with a dose $> 6400\,\mathrm{mJ/cm^2}$ at 220 nm in DUV mask aligner	
	Clean with Acetone and Isopropanol in ultrasonic bath each for 5 min at 50 °C	

A.2. Airbridges

The following process is used to fabricate the airbridges as described in Sec. 3.2.2. They have a height above the waver of $\sim 2\,\mu m$ and are stable up to a length of $50\,\mu m$. Some points to consider:

- "Rounder" bridges (longer reflow time) are more stable than rectangular bridges.
- Do not use ultrasound for cleaning devices with air bridges, they will also be "cleaned" away.
- Do not plasma ash devices with air bridges in the Tepla asher or any other asher with a magnetron. These will produce random fields inducing currents on the chip which can burn the air bridges. For plasma clean the samples use the reactive ion etcher with just oxygen plasma, since the fields produced parallel to the wafer are constant at a given point of time.

Air bridge process

Process step	Description	Comments
Chip cleaning	Acetone, ultrasonic bath for 5 min, 50 °C Isopropanol, ultrasonic bath for 5 min, 50 °C Rinse with DI water for 2 min N_2 blow dry	
Spinning of the support layer	Prebake on hot plate for 10 min, 180 °C Cool down for 3 min	

	Set up spinner	Step 0: 500 rpm, 2 s, 2 s ramp up time Step 1: 5000 rpm, 45 s, 5 s ramp up time
	Spin PMMA(8.5)MAA in EL 12	Use separate PMMA spinner bowl
	Wait 3 min	
	Revome resist from back of the wafer	
	Bake on hotplate for 180 s at 180 °C	
	Cool down for 1 min	
	Repeat 4 times, each layer adds ≈ 500 nm	
	Bake last layer for 300 s	Final layer thickness is 2 µm
DUV photo lithography	Warm up DUV mask aligner, use 220 nm mirror, DUV channel and CP mode	
	Measure intensity at 220 nm	Typically ≈ 20 mW/cm^2
	Set exposure time for a dose of 7700 mJ/cm^2 at 220 nm	
	Align bridge foot mask and expose	Check alignment in contact vacuum mode
	Develop for 60 s in MIBK:IPA 1:1	
	Rinse under flowing DI water for 30 s	
	N_2 blow dry for 30 s	Inspect wafer under microscope

Reflow	Bake on hotplate for 10 min at 180 °C Visual inspection	
Spinning of the image reversal layer	Set up spinner	Step 0: 500 rpm, 2 s, 2 s ramp up time Step 1: 3000 rpm, 50 s, 30 s ramp up time Step 2: 5500 rpm, 2 s, 2 s ramp up time
	Spin AZ5214E Wait 3 min Revome resist from back of the wafer Bake on hotplate for 60 s at 100 °C Cool down for 1 min	
Photo lithography	Warm up MA6 mask aligner	
	Measure intensity at 365 nm	Typically $\approx 5\,\mathrm{mW/cm^2}$
	Set exposure time for a dose of $50\,\mathrm{mJ/cm^2}$ at 365 nm	
	Align bridge definition mask and expose	Use “Vacuum contact” mode
	Image reversal bake on hotplate for 50 s at 112 °C	This is a critical step!

	Flood exposure, 200 mJ/cm^2 at 405 nm	
	Wait 5 min	
	Develop for 60 s in MIF 726	
	Rinse under flowing DI water for 60 s	
	N_2 blow dry for 60 s	Inspect wafer under microscope
Metal deposition	Place samples in Plassys PVD system	
	Run ion gun recipe	300 V, 10 mA, 180 s
	Deposit 800 nm of aluminum	
	Visual inspection	
Lift-off	DMSO for 2-3 h at 70 °C	in a stirrer, 150 rpm
	Visual inspection in IPA	
	Acetone for 10 min at 50 °C	in a stirrer, 150 rpm
	IPA for 5 min at 50 °C	in a stirrer, 150 rpm
	N_2 blow dry for 60 s	Inspect wafer under microscope

B

Decoherence & Co.

This chapter introduces different terms and concepts used in the context of *decoherence*. A profound introduction into the subject, especially in the framework of superconducting circuits, is presented in the PhD-thesis of G. Ithier [Ithier05a]. A detailed discussion of decoherence, including power spectral densities and dynamical decoupling sequences can be found in the lecture notes by W. D. Oliver [Oliver13]. The subsequent sections mostly follow these two sources.

B.1. Depolarization, decoherence and dephasing

This section introduces the relaxation processes occurring during free evolution of a qubit and explains how they are characterized in the experiment. The main processes are longitudinal relaxation (usually called *depolarization* or *energy relaxation*) characterized by the time T_1 and transverse relaxation (*decoherence*) characterized by the time T_2.

B.1.1. Longitudinal relaxation, T_1

The longitudinal relaxation describes the random switching of the qubit state ($|0\rangle \leftrightarrow |1\rangle$), i.e. the rate at which the qubit *depolarizes*. In general the depolarization rate Γ_1 includes both random excitations ($|0\rangle \rightarrow |1\rangle$) with rate $\Gamma_{1\uparrow}$ as well as random relaxations ($|1\rangle \rightarrow |0\rangle$) with rate $\Gamma_{1\downarrow}$. However at low temperatures, the relaxation process $|1\rangle \rightarrow |0\rangle$ dominates and Γ_1 is

therefore usually referred to as "energy relaxation" rate. The characteristic time associated to this process is the energy relaxation time T_1 defined as

$$\Gamma_1 \equiv \frac{1}{T_1} = \Gamma_{1\downarrow} + \Gamma_{1\uparrow}. \tag{B.1}$$

Energy relaxation comes from the coupling of the qubit to noise at the qubit frequency, e.g. thermal noise from the environment to which the qubit is coupled capacitively. This noise is usually "well behaved" [Oliver13] in superconducting circuits, i.e. short-correlated and weakly coupled. Therefore the polarization of a qubit shows an exponential decay. In the experiment, the time T_1 is measured by exciting the qubit and measuring the population as a function of the waiting time after preparation. A fit to the observed exponential decay gives directly the energy relaxation time T_1, see Fig. B.1 (a).

B.1.2. Transverse relaxation, T_2

The transverse relaxation or *decoherence* describes the loss of quantum coherence. For a qubit this means that the phase information between the states $|0\rangle$ and $|1\rangle$ is lost, or equivalently in terms of the Bloch sphere, the azimuthal angle of the state is randomized. In a density matrix this corresponds to a decrease in magnitude of the off-diagonal terms.

In the regime of weak coupling between the qubit and its environment and short-correlated noise, the decoherence rate Γ_2 has two contributions, described by the Bloch-Redfield approach [Ithier05b, Wangsness53, Redfield57]: The depolarization rate Γ_1 and the pure dephasing rate Γ_φ combined as

$$\Gamma_2 = \frac{1}{2}\Gamma_1 + \Gamma_\varphi. \tag{B.2}$$

The pure dephasing rate Γ_φ describes the longitudinal low-frequency noise, e.g. flux noise which shifts the qubit frequency and therefore introduces an unknown phase. In this approach, the decay of the coherence is exponential, and the characteristic decay time is $T_2 = 1/\Gamma_2$. However, in general the dephasing can be non-exponential, especially in the presence of $1/f$-noise [Ithier05a]. In this case, T_2 is defined as the time at which the initial population in a Ramsey experiment is decayed by a factor e^{-1}.

The experimental procedure to measure the decoherence time is the Ramsey experiment (see also Sec. 5.1). The pulse sequence (Fig. B.1 (b)) consists

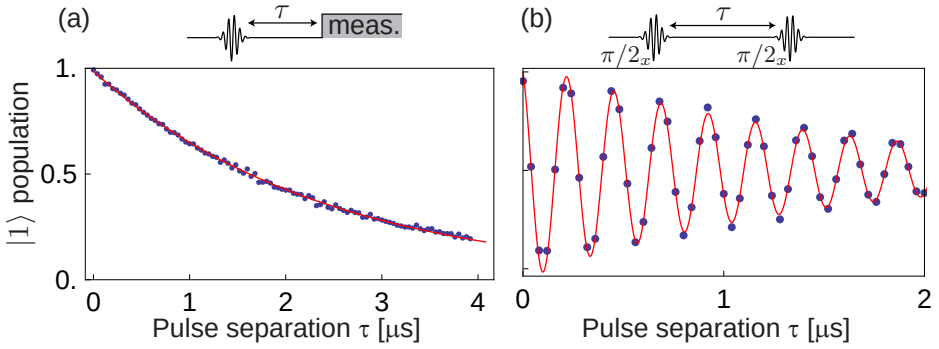

Figure B.1: Measurement of (a) the energy relaxation time T_1 and (b) decoherence time T_2^*. The blue dots are measured values, the red lines are exponentially decaying fits.

of two $\pi/2$ pulses with a varying time delay in between. Usually a finite detuning between the qubit and drive frequency is introduced which produces the characteristic oscillations as shown in Fig. B.1 (b). Without detuning the data would just show an exponential decay of the population as a function of the waiting time. In this situation the experiment is also referred to as "free-induction decay" [Ithier05b]. However, since low frequency detuning and decay are hard to distinguish, the experiment is usually performed with a detuning (typically 4 MHz) which is higher than the decoherence rate. The data can be fitted with an exponentially damped sinusoid, giving directly the Ramsey decay time T_2^*. The Ramsey decay time T_2^* generally differs from the "intrinsic" decay time T_2 since it is the result of an ensemble measurement. The ensemble in the case of superconducting qubits is the temporal ensemble formed by the repeated and averaged experiments of a single qubit, which is necessary to acquire sufficient data [Clarke08]. Fluctuations on the timescale of a single experimental run then lead to a reduced observed coherence time $T_2^* < T_2$. In Sec. B.2 it is shown how to measure a more intrinsic decay time.

B.2. Dynamical decoupling

Dynamical decoupling refers to different methods for prolonging the decoherence time in qubit systems. The first pulse sequence was implemented in the context of nuclear magnetic resonance to refocus a spatial ensemble of spins and is referred to as *Hahn echo* or *spin echo* [Hahn50]. In superconducting qubits it was first studied in [Vion03, Bertet05]. The sequence is a modified Ramsey sequence with a π pulse in the middle of the waiting time as depicted in Fig. B.2. Low frequency noise causing a drift of the transition frequency will induce a random rotation of the qubit state during the waiting time. The π pulse turns the rotated state such that in the following waiting time, the state will rotate back to its original position. Hence, noise that does not change on the timescale of one experimental sequence can be filtered out. The resulting decay time T_{2E} measured with this method is closer to the intrinsic decay time T_2 than T_2^*.

In a next step, more π pulses can be added as shown by Carr, Purcell, Meiboom and Gill [Carr54, Meiboom58]. In these "CPMG"-sequences, the spacing between the π pulses is always twice as large as the spacing between the $\pi/2$ and π pulse, see Fig. B.3. For a given total sequence length, the time between two refocusing pulses is shorter with increasing number of pulse. Such sequences therefor shift the filter function which defines the noise affecting the qubit to higher frequencies [Bylander11]. The resulting decay times $T_2^{(N)}$ for a sequence with N π pulses approach the intrinsic decay time for increasing N.

The results of an experimental implementation of free-induction decay (a Ramsey sequence without detuning), Hahn echo and CPMG sequences with $N = 2$ and $N = 3$ π pulses is shown in Fig. B.4. In (a) a sample was used which showed high sensitivity to flux noise due to a superconducting loop formed around the qubit by wirebonds and the ground plane. It showed a $T_2^* \approx 95\,\text{ns}$ much smaller than $T_1 = 650\,\text{ns}$. Spin echo pulses increased the measured coherence time efficiently up to a factor of 4.8 to $T_2^{(3)} \approx 460\,\text{ns}$. The black lines in Fig. B.4 (a) are Gaussian fits, indicating a $1/f$-noise environment [Ithier05a, Oliver13]. The measurements shown in (b) are performed with a qubit almost insensitive to flux noise. It has a $T_2^* = 670\,\text{ns}$ and a $T_1 = 900\,\text{ns}$. The exponential decay (black lines) hint at a white noise environment, which cannot be filtered out efficiently with CPMG sequences.

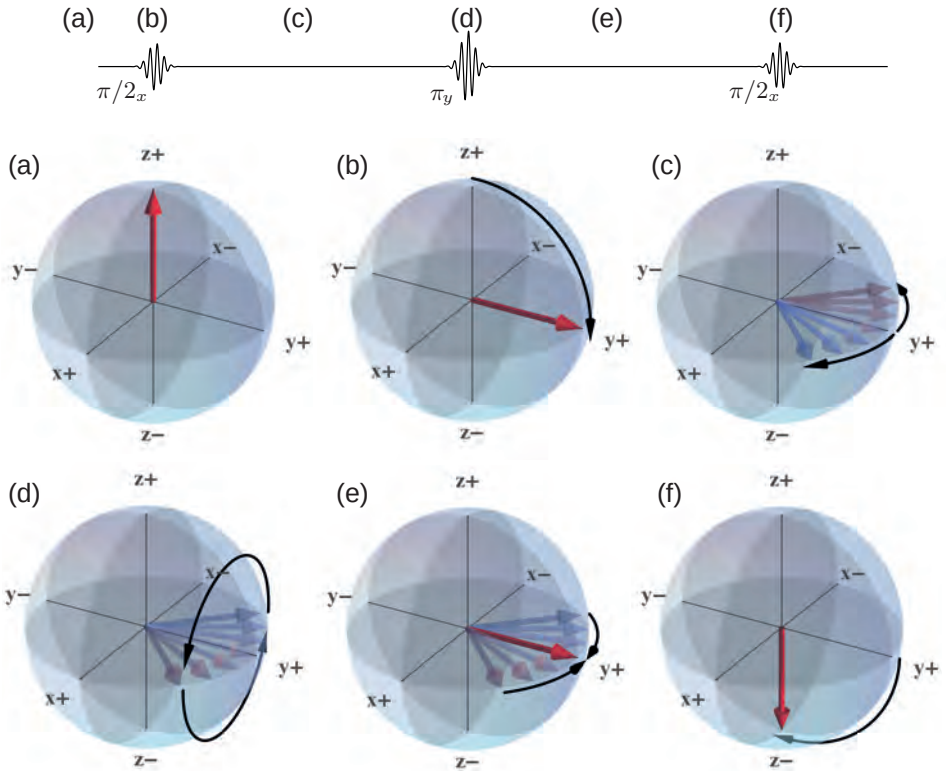

Figure B.2: Spin echo sequence: Pulse sequence (top) and evolution of the qubit state (bottom). The qubit starts in the ground state (a), and is excited to an equal superposition state (b). In the first waiting time, the state rotates due to random low-frequency noise (c). A π pulse switches the rotated state (d) which then refocuses in the subsequent waiting time (e). A final $\pi/2$ pulse (f) ideally always brings the qubit to the excited state.

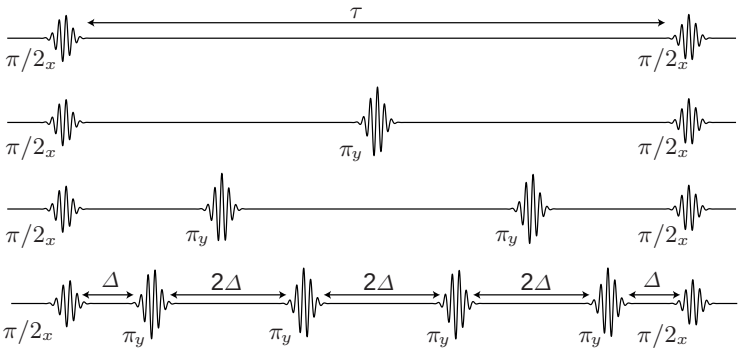

Figure B.3: Pulse sequence for (from top to bottom) a Ramsey experiment, Hahn-echo and CPMG with 2 and 4 π pulses. The spacing between the π pulses is always twice as large as the spacing between the $\pi/2$ and π pulse.

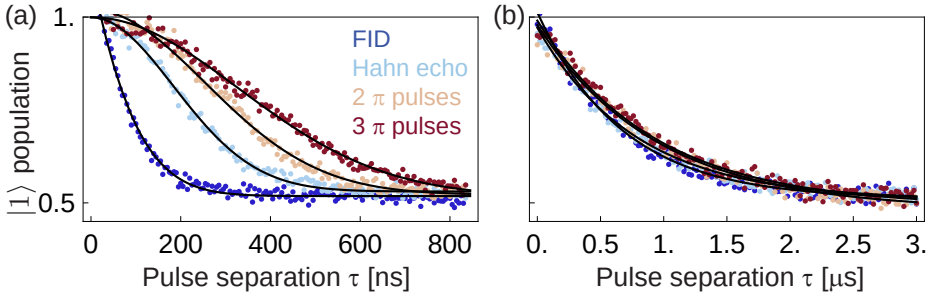

Figure B.4: Free-induction decay (FID), Hahn echo and CPMG experiments with $N = \{0, 1, 2, 3\}$ π pulses between the $\pi/2$ pulses for (a) a qubit tuned to a point with high flux noise sensitivity and (b) a qubit tuned a point of low flux noise sensitivity. Black lines are (a) Gaussian and (b) exponential fits.

An improved sequence — Uhrig dynamical decoupling (UDD) — similar to the CPMG sequence but with non-uniform spacing between the π pulses was presented in [Uhrig07, Uhrig08] and implemented in ion traps [Biercuk09b, Biercuk09a], single spin in diamond [deLange10] and superconducting circuits [Bylander11], where it showed better performance in certain noise environments than the CPMG sequence.

In superconducting circuits, spin echoes and CPMG sequences have also been studied [Vion03, Bertet05, Steffen07, Gustavsson12], used for prolonging the lifetime of a qubit [Leek07, Steffen13] or to perform noise spectroscopy [Bylander11].

C

Supplementary Material

C.1. Monte Carlo process certification

C.1.1. Input states

In the protocol for Monte Carlo process certification one has to prepare complex conjugates of eigenstates of a Pauli operator $\hat{A}_i$ as input states. Every n-qubit Pauli operator has 2^n eigenstates, half of them with eigenvalue 1, the other half with eigenvalue -1 (except for the identity operator, where all eigenvalues are 1). Both eigenspaces corresponding to the respective eigenvalue are spanned by sets of product states built from the products of the corresponding single-Pauli-operator eigenstates. It is therefore sufficient to prepare all the aforementioned product states as input states. A list of the complex conjugates of the single-Pauli-operator eigenstates is given in Tab. C.1.

To illustrate this, let's consider an example. According to Tab. 7.1, one of the relevant Pauli operators for the CNOT gate is $\hat{P} = \hat{\sigma}_x \otimes \hat{\sigma}_x \otimes \hat{\sigma}_x \otimes \mathbb{1}$. This means, that complex conjugates of eigenstates of the two-qubit Pauli-operator $\hat{A} = \hat{\sigma}_x \otimes \hat{\sigma}_x$ have to be prepared. Subsequently the CNOT operation is applied and the resulting states are measured with the operator $\hat{B} = \hat{\sigma}_x \otimes \mathbb{1}$. According to Tab. C.1, the complex conjugate eigenstates of $\hat{A}$ corresponding to the eigenvalue 1 are $|{+}{+}\rangle$ and $|{-}{-}\rangle$, the ones corresponding to eigenvalue -1 are $|{+}{-}\rangle$ and $|{-}{+}\rangle$. It is sufficient to prepare and measure these four states, since all other eigenstates are linear combi-

Pauli operator	Eigenvalue	Compl. conj. eigenstate
$\mathbb{1}$	1	$\|0\rangle$
		$\|1\rangle$
$\hat{\sigma}_x$	1	$\|+\rangle$
	-1	$\|-\rangle$
$\hat{\sigma}_y$	1	$\|-i\rangle$
	-1	$\|i\rangle$
$\hat{\sigma}_z$	1	$\|0\rangle$
	-1	$\|1\rangle$

Table C.1: List of the complex conjugates of the single-Pauli-operator eigenstates with the corresponding eigenvalue. Note that the complex conjugation affects only the eigenstates of the $\hat{\sigma}_y$ operator.

nations of these. For example the Bell state $\left|\Phi^+\right\rangle = |00\rangle + |11\rangle$, which is a $+1$ eigenstate of $\hat{\sigma}_x \otimes \hat{\sigma}_x$ is a linear combination of the aforementioned $+1$ eigenstates $\left|\Phi^+\right\rangle = |{+}{+}\rangle + |{-}{-}\rangle$.

C.1.2. Relevant operators for two sequential CPHASE gates

A sequence of two CPHASE-gates overlapping on the middle qubit has stabilizer group generators

$$\begin{aligned}
g_1 &= \hat{\sigma}_x\ \mathbb{1}\ \ \mathbb{1}\ \ \hat{\sigma}_x\ \hat{\sigma}_z\ \mathbb{1}, \\
g_2 &= \hat{\sigma}_z\ \mathbb{1}\ \ \mathbb{1}\ \ \hat{\sigma}_z\ \mathbb{1}\ \ \mathbb{1}, \\
g_3 &= \mathbb{1}\ \ \hat{\sigma}_x\ \mathbb{1}\ \ \hat{\sigma}_z\ \hat{\sigma}_x\ \hat{\sigma}_z, \\
g_4 &= \mathbb{1}\ \ \hat{\sigma}_z\ \mathbb{1}\ \ \mathbb{1}\ \ \hat{\sigma}_z\ \mathbb{1}, \\
g_5 &= \mathbb{1}\ \ \mathbb{1}\ \ \hat{\sigma}_x\ \mathbb{1}\ \ \hat{\sigma}_z\ \hat{\sigma}_x, \\
g_6 &= \mathbb{1}\ \ \mathbb{1}\ \ \hat{\sigma}_z\ \mathbb{1}\ \ \mathbb{1}\ \ \hat{\sigma}_z.
\end{aligned} \tag{C.1}$$

The relevant Pauli operators found from these generators are listed in Tab. C.2.

C.1.3. Relevant operators for the Toffoli gate

Since the Choi matrix of the Toffoli gate is not a stabilizer state, the list of relevant Pauli operators has no group structure and the relevance distribution $\Pr(i)$ is not uniform. By calculating explicitly the expectation value for all 4096 possible Pauli operators, we find only 232 operators which are non-zero. The corresponding operators are listed in Tabs. C.3 and C.4, labeld consistently with the measured values shown in Fig. 7.9.

$\mathbb{1}\,\mathbb{1}\;\;\mathbb{1}\;\;\mathbb{1}\;\;\mathbb{1}\;\;\mathbb{1}$	$\hat{\sigma}_x\,\mathbb{1}\;\;\mathbb{1}\;\;\hat{\sigma}_x\,\hat{\sigma}_z\,\mathbb{1}$	$\hat{\sigma}_y\,\mathbb{1}\;\;\mathbb{1}\;\;\hat{\sigma}_y\,\hat{\sigma}_z\,\mathbb{1}$	$\hat{\sigma}_z\,\mathbb{1}\;\;\mathbb{1}\;\;\hat{\sigma}_z\,\mathbb{1}\;\;\mathbb{1}$
$\mathbb{1}\,\mathbb{1}\;\;\hat{\sigma}_x\,\mathbb{1}\;\;\hat{\sigma}_z\,\hat{\sigma}_x$	$\hat{\sigma}_x\,\mathbb{1}\;\;\hat{\sigma}_x\,\hat{\sigma}_x\,\mathbb{1}\;\;\hat{\sigma}_x$	$\hat{\sigma}_y\,\mathbb{1}\;\;\hat{\sigma}_x\,\hat{\sigma}_y\,\mathbb{1}\;\;\hat{\sigma}_x$	$\hat{\sigma}_z\,\mathbb{1}\;\;\hat{\sigma}_x\,\hat{\sigma}_z\,\hat{\sigma}_z\,\hat{\sigma}_x$
$\mathbb{1}\,\mathbb{1}\;\;\hat{\sigma}_y\,\mathbb{1}\;\;\hat{\sigma}_z\,\hat{\sigma}_y$	$\hat{\sigma}_x\,\mathbb{1}\;\;\hat{\sigma}_y\,\hat{\sigma}_x\,\mathbb{1}\;\;\hat{\sigma}_y$	$\hat{\sigma}_y\,\mathbb{1}\;\;\hat{\sigma}_y\,\hat{\sigma}_y\,\mathbb{1}\;\;\hat{\sigma}_y$	$\hat{\sigma}_z\,\mathbb{1}\;\;\hat{\sigma}_y\,\hat{\sigma}_z\,\hat{\sigma}_z\,\hat{\sigma}_y$
$\mathbb{1}\,\mathbb{1}\;\;\hat{\sigma}_z\,\mathbb{1}\;\;\mathbb{1}\;\;\hat{\sigma}_z$	$\hat{\sigma}_x\,\mathbb{1}\;\;\hat{\sigma}_z\,\hat{\sigma}_x\,\hat{\sigma}_z\,\hat{\sigma}_z$	$\hat{\sigma}_y\,\mathbb{1}\;\;\hat{\sigma}_z\,\hat{\sigma}_y\,\hat{\sigma}_z\,\hat{\sigma}_z$	$\hat{\sigma}_z\,\mathbb{1}\;\;\hat{\sigma}_z\,\hat{\sigma}_z\,\mathbb{1}\;\;\hat{\sigma}_z$
$\mathbb{1}\,\hat{\sigma}_x\,\mathbb{1}\;\;\hat{\sigma}_z\,\hat{\sigma}_x\,\hat{\sigma}_z$	$\hat{\sigma}_x\,\hat{\sigma}_x\,\mathbb{1}\;\;\hat{\sigma}_y\,\hat{\sigma}_y\,\hat{\sigma}_z$	$\hat{\sigma}_y\,\hat{\sigma}_x\,\mathbb{1}\;\;\hat{\sigma}_x\,\hat{\sigma}_y\,\hat{\sigma}_z$	$\hat{\sigma}_z\,\hat{\sigma}_x\,\mathbb{1}\;\;\mathbb{1}\;\;\hat{\sigma}_x\,\hat{\sigma}_z$
$\mathbb{1}\,\hat{\sigma}_x\,\hat{\sigma}_x\,\hat{\sigma}_z\,\hat{\sigma}_y\,\hat{\sigma}_y$	$\hat{\sigma}_x\,\hat{\sigma}_x\,\hat{\sigma}_x\,\hat{\sigma}_y\,\hat{\sigma}_x\,\hat{\sigma}_y$	$\hat{\sigma}_y\,\hat{\sigma}_x\,\hat{\sigma}_x\,\hat{\sigma}_x\,\hat{\sigma}_x\,\hat{\sigma}_y$	$\hat{\sigma}_z\,\hat{\sigma}_x\,\hat{\sigma}_x\,\mathbb{1}\;\;\hat{\sigma}_y\,\hat{\sigma}_y$
$\mathbb{1}\,\hat{\sigma}_x\,\hat{\sigma}_y\,\hat{\sigma}_z\,\hat{\sigma}_y\,\hat{\sigma}_x$	$\hat{\sigma}_x\,\hat{\sigma}_x\,\hat{\sigma}_y\,\hat{\sigma}_y\,\hat{\sigma}_x\,\hat{\sigma}_x$	$\hat{\sigma}_y\,\hat{\sigma}_x\,\hat{\sigma}_y\,\hat{\sigma}_x\,\hat{\sigma}_x\,\hat{\sigma}_x$	$\hat{\sigma}_z\,\hat{\sigma}_x\,\hat{\sigma}_y\,\mathbb{1}\;\;\hat{\sigma}_y\,\hat{\sigma}_x$
$\mathbb{1}\,\hat{\sigma}_x\,\hat{\sigma}_z\,\hat{\sigma}_z\,\hat{\sigma}_x\,\mathbb{1}$	$\hat{\sigma}_x\,\hat{\sigma}_x\,\hat{\sigma}_z\,\hat{\sigma}_y\,\hat{\sigma}_y\,\mathbb{1}$	$\hat{\sigma}_y\,\hat{\sigma}_x\,\hat{\sigma}_z\,\hat{\sigma}_x\,\hat{\sigma}_y\,\mathbb{1}$	$\hat{\sigma}_z\,\hat{\sigma}_x\,\hat{\sigma}_z\,\mathbb{1}\;\;\hat{\sigma}_x\,\mathbb{1}$
$\mathbb{1}\,\hat{\sigma}_y\,\mathbb{1}\;\;\hat{\sigma}_z\,\hat{\sigma}_y\,\hat{\sigma}_z$	$\hat{\sigma}_x\,\hat{\sigma}_y\,\mathbb{1}\;\;\hat{\sigma}_y\,\hat{\sigma}_x\,\hat{\sigma}_z$	$\hat{\sigma}_y\,\hat{\sigma}_y\,\mathbb{1}\;\;\hat{\sigma}_x\,\hat{\sigma}_x\,\hat{\sigma}_z$	$\hat{\sigma}_z\,\hat{\sigma}_y\,\mathbb{1}\;\;\mathbb{1}\;\;\hat{\sigma}_y\,\hat{\sigma}_z$
$\mathbb{1}\,\hat{\sigma}_y\,\hat{\sigma}_x\,\hat{\sigma}_z\,\hat{\sigma}_x\,\hat{\sigma}_y$	$\hat{\sigma}_x\,\hat{\sigma}_y\,\hat{\sigma}_x\,\hat{\sigma}_y\,\hat{\sigma}_y\,\hat{\sigma}_y$	$\hat{\sigma}_y\,\hat{\sigma}_y\,\hat{\sigma}_x\,\hat{\sigma}_x\,\hat{\sigma}_y\,\hat{\sigma}_y$	$\hat{\sigma}_z\,\hat{\sigma}_y\,\hat{\sigma}_x\,\mathbb{1}\;\;\hat{\sigma}_x\,\hat{\sigma}_y$
$\mathbb{1}\,\hat{\sigma}_y\,\hat{\sigma}_y\,\hat{\sigma}_z\,\hat{\sigma}_x\,\hat{\sigma}_x$	$\hat{\sigma}_x\,\hat{\sigma}_y\,\hat{\sigma}_y\,\hat{\sigma}_y\,\hat{\sigma}_y\,\hat{\sigma}_x$	$\hat{\sigma}_y\,\hat{\sigma}_y\,\hat{\sigma}_y\,\hat{\sigma}_x\,\hat{\sigma}_x\,\hat{\sigma}_x$	$\hat{\sigma}_z\,\hat{\sigma}_y\,\hat{\sigma}_y\,\mathbb{1}\;\;\hat{\sigma}_x\,\hat{\sigma}_x$
$\mathbb{1}\,\hat{\sigma}_y\,\hat{\sigma}_z\,\hat{\sigma}_z\,\hat{\sigma}_y\,\mathbb{1}$	$\hat{\sigma}_x\,\hat{\sigma}_y\,\hat{\sigma}_z\,\hat{\sigma}_y\,\hat{\sigma}_x\,\mathbb{1}$	$\hat{\sigma}_y\,\hat{\sigma}_y\,\hat{\sigma}_z\,\hat{\sigma}_x\,\hat{\sigma}_x\,\mathbb{1}$	$\hat{\sigma}_z\,\hat{\sigma}_y\,\hat{\sigma}_z\,\mathbb{1}\;\;\hat{\sigma}_y\,\mathbb{1}$
$\mathbb{1}\,\hat{\sigma}_z\,\mathbb{1}\;\;\mathbb{1}\;\;\hat{\sigma}_z\,\mathbb{1}$	$\hat{\sigma}_x\,\hat{\sigma}_z\,\mathbb{1}\;\;\hat{\sigma}_x\,\mathbb{1}\;\;\mathbb{1}$	$\hat{\sigma}_y\,\hat{\sigma}_z\,\mathbb{1}\;\;\hat{\sigma}_y\,\mathbb{1}\;\;\mathbb{1}$	$\hat{\sigma}_z\,\hat{\sigma}_z\,\mathbb{1}\;\;\hat{\sigma}_z\,\hat{\sigma}_z\,\mathbb{1}$
$\mathbb{1}\,\hat{\sigma}_z\,\hat{\sigma}_x\,\mathbb{1}\;\;\mathbb{1}\;\;\hat{\sigma}_x$	$\hat{\sigma}_x\,\hat{\sigma}_z\,\hat{\sigma}_x\,\hat{\sigma}_x\,\hat{\sigma}_z\,\hat{\sigma}_x$	$\hat{\sigma}_y\,\hat{\sigma}_z\,\hat{\sigma}_x\,\hat{\sigma}_y\,\hat{\sigma}_z\,\hat{\sigma}_x$	$\hat{\sigma}_z\,\hat{\sigma}_z\,\hat{\sigma}_x\,\hat{\sigma}_z\,\hat{\sigma}_z\,\hat{\sigma}_x$
$\mathbb{1}\,\hat{\sigma}_z\,\hat{\sigma}_y\,\mathbb{1}\;\;\mathbb{1}\;\;\hat{\sigma}_y$	$\hat{\sigma}_x\,\hat{\sigma}_z\,\hat{\sigma}_y\,\hat{\sigma}_x\,\mathbb{1}\;\;\hat{\sigma}_y$	$\hat{\sigma}_y\,\hat{\sigma}_z\,\hat{\sigma}_y\,\hat{\sigma}_y\,\mathbb{1}\;\;\hat{\sigma}_y$	$\hat{\sigma}_z\,\hat{\sigma}_z\,\hat{\sigma}_y\,\hat{\sigma}_z\,\mathbb{1}\;\;\hat{\sigma}_y$
$\mathbb{1}\,\hat{\sigma}_z\,\hat{\sigma}_z\,\mathbb{1}\;\;\hat{\sigma}_z\,\mathbb{1}$	$\hat{\sigma}_x\,\hat{\sigma}_z\,\hat{\sigma}_z\,\hat{\sigma}_x\,\mathbb{1}\;\;\mathbb{1}$	$\hat{\sigma}_y\,\hat{\sigma}_z\,\hat{\sigma}_z\,\hat{\sigma}_y\,\mathbb{1}\;\;\mathbb{1}$	$\hat{\sigma}_z\,\hat{\sigma}_z\,\hat{\sigma}_z\,\hat{\sigma}_z\,\hat{\sigma}_z\,\hat{\sigma}_z$

Table C.2: All relevant Pauli operators for the verification of two sequential CPHASE gates

	000	001	010	011
00000	$\mathbb{1}\,\mathbb{1}\;\;\mathbb{1}\;\;\mathbb{1}\;\;\mathbb{1}\;\;\mathbb{1}$	$\mathbb{1}\;\;\hat{\sigma}_y\;\mathbb{1}\;\;\hat{\sigma}_z\;\hat{\sigma}_y\;\hat{\sigma}_x$	$\hat{\sigma}_x\;\mathbb{1}\;\;\hat{\sigma}_x\;\hat{\sigma}_x\;\hat{\sigma}_z\;\mathbb{1}$	$\hat{\sigma}_x\;\hat{\sigma}_y\;\mathbb{1}\;\;\hat{\sigma}_y\;\hat{\sigma}_x\;\hat{\sigma}_x$
	$\mathbb{1}\,\mathbb{1}\;\;\hat{\sigma}_x\;\mathbb{1}\;\;\mathbb{1}\;\;\hat{\sigma}_x$	$\mathbb{1}\;\;\hat{\sigma}_y\;\hat{\sigma}_x\;\mathbb{1}\;\;\hat{\sigma}_y\;\mathbb{1}$	$\hat{\sigma}_x\;\mathbb{1}\;\;\hat{\sigma}_x\;\hat{\sigma}_x\;\hat{\sigma}_z\;\hat{\sigma}_x$	$\hat{\sigma}_x\;\hat{\sigma}_y\;\hat{\sigma}_x\;\hat{\sigma}_x\;\hat{\sigma}_y\;\mathbb{1}$
	$\mathbb{1}\,\mathbb{1}\;\;\hat{\sigma}_y\;\mathbb{1}\;\;\mathbb{1}\;\;\hat{\sigma}_y$	$\mathbb{1}\;\;\hat{\sigma}_y\;\hat{\sigma}_x\;\mathbb{1}\;\;\hat{\sigma}_y\;\hat{\sigma}_x$	$\hat{\sigma}_x\;\mathbb{1}\;\;\hat{\sigma}_y\;\hat{\sigma}_x\;\mathbb{1}\;\;\hat{\sigma}_y$	$\hat{\sigma}_x\;\hat{\sigma}_y\;\hat{\sigma}_x\;\hat{\sigma}_x\;\hat{\sigma}_y\;\hat{\sigma}_x$
	$\mathbb{1}\,\mathbb{1}\;\;\hat{\sigma}_y\;\mathbb{1}\;\;\hat{\sigma}_z\;\hat{\sigma}_y$	$\mathbb{1}\;\;\hat{\sigma}_y\;\hat{\sigma}_x\;\hat{\sigma}_z\;\hat{\sigma}_y\;\mathbb{1}$	$\hat{\sigma}_x\;\mathbb{1}\;\;\hat{\sigma}_y\;\hat{\sigma}_x\;\hat{\sigma}_z\;\hat{\sigma}_y$	$\hat{\sigma}_x\;\hat{\sigma}_y\;\hat{\sigma}_x\;\hat{\sigma}_y\;\hat{\sigma}_x\;\mathbb{1}$
00100	$\mathbb{1}\,\mathbb{1}\;\;\hat{\sigma}_y\;\hat{\sigma}_z\;\mathbb{1}\;\;\hat{\sigma}_y$	$\mathbb{1}\;\;\hat{\sigma}_y\;\hat{\sigma}_x\;\hat{\sigma}_z\;\hat{\sigma}_y\;\hat{\sigma}_x$	$\hat{\sigma}_x\;\mathbb{1}\;\;\hat{\sigma}_y\;\hat{\sigma}_y\;\mathbb{1}\;\;\hat{\sigma}_z$	$\hat{\sigma}_x\;\hat{\sigma}_y\;\hat{\sigma}_x\;\hat{\sigma}_y\;\hat{\sigma}_x\;\hat{\sigma}_x$
	$\mathbb{1}\,\mathbb{1}\;\;\hat{\sigma}_y\;\hat{\sigma}_z\;\hat{\sigma}_z\;\hat{\sigma}_y$	$\mathbb{1}\;\;\hat{\sigma}_y\;\hat{\sigma}_y\;\mathbb{1}\;\;\hat{\sigma}_x\;\hat{\sigma}_z$	$\hat{\sigma}_x\;\mathbb{1}\;\;\hat{\sigma}_y\;\hat{\sigma}_y\;\hat{\sigma}_z\;\hat{\sigma}_z$	$\hat{\sigma}_x\;\hat{\sigma}_y\;\hat{\sigma}_y\;\hat{\sigma}_x\;\hat{\sigma}_x\;\hat{\sigma}_z$
	$\mathbb{1}\,\mathbb{1}\;\;\hat{\sigma}_z\;\mathbb{1}\;\;\mathbb{1}\;\;\hat{\sigma}_z$	$\mathbb{1}\;\;\hat{\sigma}_y\;\hat{\sigma}_y\;\mathbb{1}\;\;\hat{\sigma}_y\;\hat{\sigma}_y$	$\hat{\sigma}_x\;\mathbb{1}\;\;\hat{\sigma}_z\;\hat{\sigma}_x\;\mathbb{1}\;\;\hat{\sigma}_z$	$\hat{\sigma}_x\;\hat{\sigma}_y\;\hat{\sigma}_y\;\hat{\sigma}_x\;\hat{\sigma}_y\;\hat{\sigma}_y$
	$\mathbb{1}\,\mathbb{1}\;\;\hat{\sigma}_z\;\mathbb{1}\;\;\hat{\sigma}_z\;\hat{\sigma}_z$	$\mathbb{1}\;\;\hat{\sigma}_y\;\hat{\sigma}_y\;\hat{\sigma}_z\;\hat{\sigma}_x\;\hat{\sigma}_z$	$\hat{\sigma}_x\;\mathbb{1}\;\;\hat{\sigma}_z\;\hat{\sigma}_x\;\hat{\sigma}_z\;\hat{\sigma}_z$	$\hat{\sigma}_x\;\hat{\sigma}_y\;\hat{\sigma}_y\;\hat{\sigma}_y\;\hat{\sigma}_x\;\hat{\sigma}_y$
01000	$\mathbb{1}\,\mathbb{1}\;\;\hat{\sigma}_z\;\hat{\sigma}_z\;\mathbb{1}\;\;\hat{\sigma}_z$	$\mathbb{1}\;\;\hat{\sigma}_y\;\hat{\sigma}_y\;\hat{\sigma}_z\;\hat{\sigma}_y\;\hat{\sigma}_y$	$\hat{\sigma}_x\;\mathbb{1}\;\;\hat{\sigma}_z\;\hat{\sigma}_y\;\mathbb{1}\;\;\hat{\sigma}_y$	$\hat{\sigma}_x\;\hat{\sigma}_y\;\hat{\sigma}_y\;\hat{\sigma}_y\;\hat{\sigma}_y\;\hat{\sigma}_z$
	$\mathbb{1}\,\mathbb{1}\;\;\hat{\sigma}_z\;\hat{\sigma}_z\;\hat{\sigma}_z\;\hat{\sigma}_z$	$\mathbb{1}\;\;\hat{\sigma}_y\;\hat{\sigma}_z\;\mathbb{1}\;\;\hat{\sigma}_x\;\hat{\sigma}_y$	$\hat{\sigma}_x\;\mathbb{1}\;\;\hat{\sigma}_z\;\hat{\sigma}_y\;\hat{\sigma}_z\;\hat{\sigma}_y$	$\hat{\sigma}_x\;\hat{\sigma}_y\;\hat{\sigma}_z\;\hat{\sigma}_x\;\hat{\sigma}_x\;\hat{\sigma}_x$
	$\mathbb{1}\;\hat{\sigma}_x\;\mathbb{1}\;\;\mathbb{1}\;\;\hat{\sigma}_x\;\mathbb{1}$	$\mathbb{1}\;\;\hat{\sigma}_y\;\hat{\sigma}_z\;\mathbb{1}\;\;\hat{\sigma}_y\;\hat{\sigma}_z$	$\hat{\sigma}_x\;\hat{\sigma}_x\;\mathbb{1}\;\;\hat{\sigma}_x\;\hat{\sigma}_x\;\mathbb{1}$	$\hat{\sigma}_x\;\hat{\sigma}_y\;\hat{\sigma}_z\;\hat{\sigma}_x\;\hat{\sigma}_y\;\hat{\sigma}_z$
	$\mathbb{1}\;\hat{\sigma}_x\;\mathbb{1}\;\;\mathbb{1}\;\;\hat{\sigma}_x\;\hat{\sigma}_x$	$\mathbb{1}\;\;\hat{\sigma}_y\;\hat{\sigma}_z\;\hat{\sigma}_z\;\hat{\sigma}_x\;\hat{\sigma}_y$	$\hat{\sigma}_x\;\hat{\sigma}_x\;\mathbb{1}\;\;\hat{\sigma}_x\;\hat{\sigma}_x\;\hat{\sigma}_x$	$\hat{\sigma}_x\;\hat{\sigma}_y\;\hat{\sigma}_z\;\hat{\sigma}_y\;\hat{\sigma}_x\;\hat{\sigma}_z$
01100	$\mathbb{1}\;\hat{\sigma}_x\;\mathbb{1}\;\;\hat{\sigma}_z\;\hat{\sigma}_x\;\mathbb{1}$	$\mathbb{1}\;\;\hat{\sigma}_y\;\hat{\sigma}_z\;\hat{\sigma}_z\;\hat{\sigma}_y\;\hat{\sigma}_z$	$\hat{\sigma}_x\;\hat{\sigma}_x\;\mathbb{1}\;\;\hat{\sigma}_y\;\hat{\sigma}_y\;\mathbb{1}$	$\hat{\sigma}_x\;\hat{\sigma}_y\;\hat{\sigma}_z\;\hat{\sigma}_y\;\hat{\sigma}_y\;\hat{\sigma}_y$
	$\mathbb{1}\;\hat{\sigma}_x\;\mathbb{1}\;\;\hat{\sigma}_z\;\hat{\sigma}_x\;\hat{\sigma}_x$	$\mathbb{1}\;\;\hat{\sigma}_z\;\mathbb{1}\;\;\mathbb{1}\;\;\hat{\sigma}_z\;\mathbb{1}$	$\hat{\sigma}_x\;\hat{\sigma}_x\;\mathbb{1}\;\;\hat{\sigma}_y\;\hat{\sigma}_y\;\hat{\sigma}_x$	$\hat{\sigma}_x\;\hat{\sigma}_z\;\mathbb{1}\;\;\hat{\sigma}_x\;\mathbb{1}\;\;\mathbb{1}$
	$\mathbb{1}\;\hat{\sigma}_x\;\hat{\sigma}_x\;\mathbb{1}\;\;\hat{\sigma}_x\;\mathbb{1}$	$\mathbb{1}\;\;\hat{\sigma}_z\;\hat{\sigma}_x\;\mathbb{1}\;\;\hat{\sigma}_z\;\hat{\sigma}_x$	$\hat{\sigma}_x\;\hat{\sigma}_x\;\hat{\sigma}_x\;\hat{\sigma}_x\;\hat{\sigma}_x\;\mathbb{1}$	$\hat{\sigma}_x\;\hat{\sigma}_z\;\mathbb{1}\;\;\hat{\sigma}_x\;\mathbb{1}\;\;\hat{\sigma}_x$
	$\mathbb{1}\;\hat{\sigma}_x\;\hat{\sigma}_x\;\mathbb{1}\;\;\hat{\sigma}_x\;\hat{\sigma}_x$	$\mathbb{1}\;\;\hat{\sigma}_z\;\hat{\sigma}_y\;\mathbb{1}\;\;\mathbb{1}\;\;\hat{\sigma}_y$	$\hat{\sigma}_x\;\hat{\sigma}_x\;\hat{\sigma}_x\;\hat{\sigma}_x\;\hat{\sigma}_x\;\hat{\sigma}_x$	$\hat{\sigma}_x\;\hat{\sigma}_z\;\mathbb{1}\;\;\hat{\sigma}_x\;\hat{\sigma}_z\;\mathbb{1}$
10000	$\mathbb{1}\;\hat{\sigma}_x\;\hat{\sigma}_x\;\hat{\sigma}_z\;\hat{\sigma}_x\;\mathbb{1}$	$\mathbb{1}\;\;\hat{\sigma}_z\;\hat{\sigma}_y\;\mathbb{1}\;\;\hat{\sigma}_z\;\hat{\sigma}_y$	$\hat{\sigma}_x\;\hat{\sigma}_x\;\hat{\sigma}_x\;\hat{\sigma}_y\;\hat{\sigma}_y\;\mathbb{1}$	$\hat{\sigma}_x\;\hat{\sigma}_z\;\mathbb{1}\;\;\hat{\sigma}_x\;\hat{\sigma}_z\;\hat{\sigma}_x$
	$\mathbb{1}\;\hat{\sigma}_x\;\hat{\sigma}_x\;\hat{\sigma}_z\;\hat{\sigma}_x\;\hat{\sigma}_x$	$\mathbb{1}\;\;\hat{\sigma}_z\;\hat{\sigma}_y\;\hat{\sigma}_z\;\mathbb{1}\;\;\hat{\sigma}_y$	$\hat{\sigma}_x\;\hat{\sigma}_x\;\hat{\sigma}_x\;\hat{\sigma}_y\;\hat{\sigma}_y\;\hat{\sigma}_x$	$\hat{\sigma}_x\;\hat{\sigma}_z\;\hat{\sigma}_x\;\hat{\sigma}_x\;\mathbb{1}\;\;\mathbb{1}$
	$\mathbb{1}\;\hat{\sigma}_x\;\hat{\sigma}_y\;\mathbb{1}\;\;\hat{\sigma}_x\;\hat{\sigma}_y$	$\mathbb{1}\;\;\hat{\sigma}_z\;\hat{\sigma}_y\;\hat{\sigma}_z\;\hat{\sigma}_z\;\hat{\sigma}_y$	$\hat{\sigma}_x\;\hat{\sigma}_x\;\hat{\sigma}_y\;\hat{\sigma}_x\;\hat{\sigma}_x\;\hat{\sigma}_y$	$\hat{\sigma}_x\;\hat{\sigma}_z\;\hat{\sigma}_x\;\hat{\sigma}_x\;\mathbb{1}\;\;\hat{\sigma}_x$
	$\mathbb{1}\;\hat{\sigma}_x\;\hat{\sigma}_y\;\mathbb{1}\;\;\hat{\sigma}_y\;\hat{\sigma}_z$	$\mathbb{1}\;\;\hat{\sigma}_z\;\hat{\sigma}_z\;\mathbb{1}\;\;\mathbb{1}\;\;\hat{\sigma}_z$	$\hat{\sigma}_x\;\hat{\sigma}_x\;\hat{\sigma}_y\;\hat{\sigma}_x\;\hat{\sigma}_y\;\hat{\sigma}_z$	$\hat{\sigma}_x\;\hat{\sigma}_z\;\hat{\sigma}_x\;\hat{\sigma}_x\;\hat{\sigma}_z\;\mathbb{1}$
10100	$\mathbb{1}\;\hat{\sigma}_x\;\hat{\sigma}_y\;\hat{\sigma}_z\;\hat{\sigma}_x\;\hat{\sigma}_y$	$\mathbb{1}\;\;\hat{\sigma}_z\;\hat{\sigma}_z\;\mathbb{1}\;\;\hat{\sigma}_z\;\hat{\sigma}_z$	$\hat{\sigma}_x\;\hat{\sigma}_x\;\hat{\sigma}_y\;\hat{\sigma}_y\;\hat{\sigma}_x\;\hat{\sigma}_z$	$\hat{\sigma}_x\;\hat{\sigma}_z\;\hat{\sigma}_x\;\hat{\sigma}_x\;\hat{\sigma}_z\;\hat{\sigma}_x$
	$\mathbb{1}\;\hat{\sigma}_x\;\hat{\sigma}_y\;\hat{\sigma}_z\;\hat{\sigma}_y\;\hat{\sigma}_z$	$\mathbb{1}\;\;\hat{\sigma}_z\;\hat{\sigma}_z\;\hat{\sigma}_z\;\mathbb{1}\;\;\hat{\sigma}_z$	$\hat{\sigma}_x\;\hat{\sigma}_x\;\hat{\sigma}_y\;\hat{\sigma}_y\;\hat{\sigma}_y\;\hat{\sigma}_y$	$\hat{\sigma}_x\;\hat{\sigma}_z\;\hat{\sigma}_y\;\hat{\sigma}_x\;\mathbb{1}\;\;\hat{\sigma}_y$
	$\mathbb{1}\;\hat{\sigma}_x\;\hat{\sigma}_z\;\mathbb{1}\;\;\hat{\sigma}_x\;\hat{\sigma}_z$	$\mathbb{1}\;\;\hat{\sigma}_z\;\hat{\sigma}_z\;\hat{\sigma}_z\;\hat{\sigma}_z\;\hat{\sigma}_z$	$\hat{\sigma}_x\;\hat{\sigma}_x\;\hat{\sigma}_z\;\hat{\sigma}_x\;\hat{\sigma}_x\;\hat{\sigma}_z$	$\hat{\sigma}_x\;\hat{\sigma}_z\;\hat{\sigma}_y\;\hat{\sigma}_x\;\hat{\sigma}_z\;\hat{\sigma}_y$
	$\mathbb{1}\;\hat{\sigma}_x\;\hat{\sigma}_z\;\mathbb{1}\;\;\hat{\sigma}_y\;\hat{\sigma}_y$	$\hat{\sigma}_x\;\mathbb{1}\;\;\mathbb{1}\;\;\hat{\sigma}_x\;\mathbb{1}\;\;\mathbb{1}$	$\hat{\sigma}_x\;\hat{\sigma}_x\;\hat{\sigma}_z\;\hat{\sigma}_x\;\hat{\sigma}_y\;\hat{\sigma}_y$	$\hat{\sigma}_x\;\hat{\sigma}_z\;\hat{\sigma}_y\;\hat{\sigma}_y\;\mathbb{1}\;\;\hat{\sigma}_z$
11000	$\mathbb{1}\;\hat{\sigma}_x\;\hat{\sigma}_z\;\hat{\sigma}_z\;\hat{\sigma}_x\;\hat{\sigma}_z$	$\hat{\sigma}_x\;\mathbb{1}\;\;\mathbb{1}\;\;\hat{\sigma}_x\;\mathbb{1}\;\;\hat{\sigma}_x$	$\hat{\sigma}_x\;\hat{\sigma}_x\;\hat{\sigma}_z\;\hat{\sigma}_y\;\hat{\sigma}_x\;\hat{\sigma}_y$	$\hat{\sigma}_x\;\hat{\sigma}_z\;\hat{\sigma}_y\;\hat{\sigma}_y\;\hat{\sigma}_z\;\hat{\sigma}_z$
	$\mathbb{1}\;\hat{\sigma}_x\;\hat{\sigma}_z\;\hat{\sigma}_z\;\hat{\sigma}_y\;\hat{\sigma}_y$	$\hat{\sigma}_x\;\mathbb{1}\;\;\mathbb{1}\;\;\hat{\sigma}_x\;\hat{\sigma}_z\;\mathbb{1}$	$\hat{\sigma}_x\;\hat{\sigma}_x\;\hat{\sigma}_z\;\hat{\sigma}_y\;\hat{\sigma}_y\;\hat{\sigma}_z$	$\hat{\sigma}_x\;\hat{\sigma}_z\;\hat{\sigma}_z\;\hat{\sigma}_x\;\mathbb{1}\;\;\hat{\sigma}_z$
	$\mathbb{1}\;\hat{\sigma}_y\;\mathbb{1}\;\;\mathbb{1}\;\;\hat{\sigma}_y\;\mathbb{1}$	$\hat{\sigma}_x\;\mathbb{1}\;\;\mathbb{1}\;\;\hat{\sigma}_x\;\hat{\sigma}_z\;\hat{\sigma}_x$	$\hat{\sigma}_x\;\hat{\sigma}_y\;\mathbb{1}\;\;\hat{\sigma}_x\;\hat{\sigma}_y\;\mathbb{1}$	$\hat{\sigma}_x\;\hat{\sigma}_z\;\hat{\sigma}_z\;\hat{\sigma}_x\;\hat{\sigma}_z\;\hat{\sigma}_z$
	$\mathbb{1}\;\hat{\sigma}_y\;\mathbb{1}\;\;\mathbb{1}\;\;\hat{\sigma}_y\;\hat{\sigma}_x$	$\hat{\sigma}_x\;\mathbb{1}\;\;\hat{\sigma}_x\;\hat{\sigma}_x\;\mathbb{1}\;\;\mathbb{1}$	$\hat{\sigma}_x\;\hat{\sigma}_y\;\mathbb{1}\;\;\hat{\sigma}_x\;\hat{\sigma}_y\;\hat{\sigma}_x$	$\hat{\sigma}_x\;\hat{\sigma}_z\;\hat{\sigma}_z\;\hat{\sigma}_y\;\mathbb{1}\;\;\hat{\sigma}_y$
11100	$\mathbb{1}\;\hat{\sigma}_y\;\mathbb{1}\;\;\hat{\sigma}_z\;\hat{\sigma}_y\;\mathbb{1}$	$\hat{\sigma}_x\;\mathbb{1}\;\;\hat{\sigma}_x\;\hat{\sigma}_x\;\mathbb{1}\;\;\hat{\sigma}_x$	$\hat{\sigma}_x\;\hat{\sigma}_y\;\mathbb{1}\;\;\hat{\sigma}_y\;\hat{\sigma}_x\;\mathbb{1}$	$\hat{\sigma}_x\;\hat{\sigma}_z\;\hat{\sigma}_z\;\hat{\sigma}_y\;\hat{\sigma}_z\;\hat{\sigma}_y$

Table C.3: Elements 00000000 to 01111100 of the relevant operators for the verification of the Toffoli gate.

	100	101	110	111
00000	$\hat{\sigma}_y\ \mathbb{1}\ \ \mathbb{1}\ \ \hat{\sigma}_y\ \mathbb{1}\ \ \mathbb{1}$	$\hat{\sigma}_y\ \hat{\sigma}_x\ \hat{\sigma}_z\ \hat{\sigma}_x\ \hat{\sigma}_y\ \hat{\sigma}_z$	$\hat{\sigma}_y\ \hat{\sigma}_z\ \hat{\sigma}_y\ \hat{\sigma}_y\ \mathbb{1}\ \ \hat{\sigma}_y$	$\hat{\sigma}_z\ \hat{\sigma}_x\ \hat{\sigma}_z\ \mathbb{1}\ \ \hat{\sigma}_y\ \hat{\sigma}_y$
	$\hat{\sigma}_y\ \mathbb{1}\ \ \mathbb{1}\ \ \hat{\sigma}_y\ \mathbb{1}\ \ \hat{\sigma}_x$	$\hat{\sigma}_y\ \hat{\sigma}_x\ \hat{\sigma}_z\ \hat{\sigma}_y\ \hat{\sigma}_x\ \hat{\sigma}_z$	$\hat{\sigma}_y\ \hat{\sigma}_z\ \hat{\sigma}_y\ \hat{\sigma}_y\ \hat{\sigma}_z\ \hat{\sigma}_y$	$\hat{\sigma}_z\ \hat{\sigma}_x\ \hat{\sigma}_z\ \hat{\sigma}_z\ \hat{\sigma}_x\ \hat{\sigma}_z$
	$\hat{\sigma}_y\ \mathbb{1}\ \ \mathbb{1}\ \ \hat{\sigma}_y\ \hat{\sigma}_z\ \mathbb{1}$	$\hat{\sigma}_y\ \hat{\sigma}_x\ \hat{\sigma}_z\ \hat{\sigma}_y\ \hat{\sigma}_y\ \hat{\sigma}_y$	$\hat{\sigma}_y\ \hat{\sigma}_z\ \hat{\sigma}_z\ \hat{\sigma}_x\ \mathbb{1}\ \ \hat{\sigma}_y$	$\hat{\sigma}_z\ \hat{\sigma}_x\ \hat{\sigma}_z\ \hat{\sigma}_z\ \hat{\sigma}_y\ \hat{\sigma}_y$
	$\hat{\sigma}_y\ \mathbb{1}\ \ \mathbb{1}\ \ \hat{\sigma}_y\ \hat{\sigma}_z\ \hat{\sigma}_x$	$\hat{\sigma}_y\ \hat{\sigma}_y\ \mathbb{1}\ \ \hat{\sigma}_x\ \hat{\sigma}_x\ \mathbb{1}$	$\hat{\sigma}_y\ \hat{\sigma}_z\ \hat{\sigma}_z\ \hat{\sigma}_x\ \hat{\sigma}_z\ \hat{\sigma}_y$	$\hat{\sigma}_z\ \hat{\sigma}_y\ \mathbb{1}\ \ \mathbb{1}\ \ \hat{\sigma}_y\ \mathbb{1}$
00100	$\hat{\sigma}_y\ \mathbb{1}\ \ \hat{\sigma}_x\ \hat{\sigma}_y\ \mathbb{1}\ \ \mathbb{1}$	$\hat{\sigma}_y\ \hat{\sigma}_y\ \mathbb{1}\ \ \hat{\sigma}_x\ \hat{\sigma}_x\ \hat{\sigma}_x$	$\hat{\sigma}_y\ \hat{\sigma}_z\ \hat{\sigma}_z\ \hat{\sigma}_y\ \mathbb{1}\ \ \hat{\sigma}_z$	$\hat{\sigma}_z\ \hat{\sigma}_y\ \mathbb{1}\ \ \mathbb{1}\ \ \hat{\sigma}_y\ \hat{\sigma}_x$
	$\hat{\sigma}_y\ \mathbb{1}\ \ \hat{\sigma}_x\ \hat{\sigma}_y\ \mathbb{1}\ \ \hat{\sigma}_x$	$\hat{\sigma}_y\ \hat{\sigma}_y\ \mathbb{1}\ \ \hat{\sigma}_y\ \hat{\sigma}_y\ \mathbb{1}$	$\hat{\sigma}_y\ \hat{\sigma}_z\ \hat{\sigma}_z\ \hat{\sigma}_y\ \hat{\sigma}_z\ \hat{\sigma}_z$	$\hat{\sigma}_z\ \hat{\sigma}_y\ \mathbb{1}\ \ \hat{\sigma}_z\ \hat{\sigma}_y\ \mathbb{1}$
	$\hat{\sigma}_y\ \mathbb{1}\ \ \hat{\sigma}_x\ \hat{\sigma}_y\ \hat{\sigma}_z\ \mathbb{1}$	$\hat{\sigma}_y\ \hat{\sigma}_y\ \mathbb{1}\ \ \hat{\sigma}_y\ \hat{\sigma}_y\ \hat{\sigma}_x$	$\hat{\sigma}_z\ \mathbb{1}\ \ \mathbb{1}\ \ \hat{\sigma}_z\ \mathbb{1}\ \ \mathbb{1}$	$\hat{\sigma}_z\ \hat{\sigma}_y\ \mathbb{1}\ \ \hat{\sigma}_z\ \hat{\sigma}_y\ \hat{\sigma}_x$
	$\hat{\sigma}_y\ \mathbb{1}\ \ \hat{\sigma}_x\ \hat{\sigma}_y\ \hat{\sigma}_z\ \hat{\sigma}_x$	$\hat{\sigma}_y\ \hat{\sigma}_y\ \hat{\sigma}_x\ \hat{\sigma}_x\ \hat{\sigma}_x\ \mathbb{1}$	$\hat{\sigma}_z\ \mathbb{1}\ \ \hat{\sigma}_x\ \hat{\sigma}_z\ \mathbb{1}\ \ \hat{\sigma}_x$	$\hat{\sigma}_z\ \hat{\sigma}_y\ \hat{\sigma}_x\ \mathbb{1}\ \ \hat{\sigma}_y\ \mathbb{1}$
01000	$\hat{\sigma}_y\ \mathbb{1}\ \ \hat{\sigma}_y\ \hat{\sigma}_x\ \mathbb{1}\ \ \hat{\sigma}_z$	$\hat{\sigma}_y\ \hat{\sigma}_y\ \hat{\sigma}_x\ \hat{\sigma}_x\ \hat{\sigma}_x\ \hat{\sigma}_x$	$\hat{\sigma}_z\ \mathbb{1}\ \ \hat{\sigma}_y\ \mathbb{1}\ \ \mathbb{1}\ \ \hat{\sigma}_y$	$\hat{\sigma}_z\ \hat{\sigma}_y\ \hat{\sigma}_x\ \mathbb{1}\ \ \hat{\sigma}_y\ \hat{\sigma}_x$
	$\hat{\sigma}_y\ \mathbb{1}\ \ \hat{\sigma}_y\ \hat{\sigma}_x\ \hat{\sigma}_z\ \hat{\sigma}_z$	$\hat{\sigma}_y\ \hat{\sigma}_y\ \hat{\sigma}_x\ \hat{\sigma}_y\ \hat{\sigma}_y\ \mathbb{1}$	$\hat{\sigma}_z\ \mathbb{1}\ \ \hat{\sigma}_y\ \mathbb{1}\ \ \hat{\sigma}_z\ \hat{\sigma}_y$	$\hat{\sigma}_z\ \hat{\sigma}_y\ \hat{\sigma}_x\ \hat{\sigma}_z\ \hat{\sigma}_y\ \mathbb{1}$
	$\hat{\sigma}_y\ \mathbb{1}\ \ \hat{\sigma}_y\ \hat{\sigma}_y\ \mathbb{1}\ \ \hat{\sigma}_y$	$\hat{\sigma}_y\ \hat{\sigma}_y\ \hat{\sigma}_x\ \hat{\sigma}_y\ \hat{\sigma}_y\ \hat{\sigma}_x$	$\hat{\sigma}_z\ \mathbb{1}\ \ \hat{\sigma}_y\ \hat{\sigma}_z\ \mathbb{1}\ \ \hat{\sigma}_y$	$\hat{\sigma}_z\ \hat{\sigma}_y\ \hat{\sigma}_x\ \hat{\sigma}_z\ \hat{\sigma}_y\ \hat{\sigma}_x$
	$\hat{\sigma}_y\ \mathbb{1}\ \ \hat{\sigma}_y\ \hat{\sigma}_y\ \hat{\sigma}_z\ \hat{\sigma}_y$	$\hat{\sigma}_y\ \hat{\sigma}_y\ \hat{\sigma}_y\ \hat{\sigma}_x\ \hat{\sigma}_x\ \hat{\sigma}_y$	$\hat{\sigma}_z\ \mathbb{1}\ \ \hat{\sigma}_y\ \hat{\sigma}_z\ \hat{\sigma}_z\ \hat{\sigma}_y$	$\hat{\sigma}_z\ \hat{\sigma}_y\ \hat{\sigma}_y\ \mathbb{1}\ \ \hat{\sigma}_x\ \hat{\sigma}_z$
01100	$\hat{\sigma}_y\ \mathbb{1}\ \ \hat{\sigma}_z\ \hat{\sigma}_x\ \mathbb{1}\ \ \hat{\sigma}_y$	$\hat{\sigma}_y\ \hat{\sigma}_y\ \hat{\sigma}_y\ \hat{\sigma}_x\ \hat{\sigma}_y\ \hat{\sigma}_z$	$\hat{\sigma}_z\ \mathbb{1}\ \ \hat{\sigma}_z\ \mathbb{1}\ \ \mathbb{1}\ \ \hat{\sigma}_z$	$\hat{\sigma}_z\ \hat{\sigma}_y\ \hat{\sigma}_y\ \mathbb{1}\ \ \hat{\sigma}_y\ \hat{\sigma}_y$
	$\hat{\sigma}_y\ \mathbb{1}\ \ \hat{\sigma}_z\ \hat{\sigma}_x\ \hat{\sigma}_z\ \hat{\sigma}_y$	$\hat{\sigma}_y\ \hat{\sigma}_y\ \hat{\sigma}_y\ \hat{\sigma}_y\ \hat{\sigma}_x\ \hat{\sigma}_z$	$\hat{\sigma}_z\ \mathbb{1}\ \ \hat{\sigma}_z\ \mathbb{1}\ \ \hat{\sigma}_z\ \hat{\sigma}_z$	$\hat{\sigma}_z\ \hat{\sigma}_y\ \hat{\sigma}_y\ \hat{\sigma}_z\ \hat{\sigma}_x\ \hat{\sigma}_z$
	$\hat{\sigma}_y\ \mathbb{1}\ \ \hat{\sigma}_z\ \hat{\sigma}_y\ \mathbb{1}\ \ \hat{\sigma}_z$	$\hat{\sigma}_y\ \hat{\sigma}_y\ \hat{\sigma}_y\ \hat{\sigma}_y\ \hat{\sigma}_y\ \mathbb{1}$	$\hat{\sigma}_z\ \mathbb{1}\ \ \hat{\sigma}_z\ \hat{\sigma}_z\ \mathbb{1}\ \ \hat{\sigma}_z$	$\hat{\sigma}_z\ \hat{\sigma}_y\ \hat{\sigma}_y\ \hat{\sigma}_z\ \hat{\sigma}_y\ \hat{\sigma}_y$
	$\hat{\sigma}_y\ \mathbb{1}\ \ \hat{\sigma}_z\ \hat{\sigma}_y\ \hat{\sigma}_z\ \hat{\sigma}_z$	$\hat{\sigma}_y\ \hat{\sigma}_y\ \hat{\sigma}_z\ \hat{\sigma}_x\ \hat{\sigma}_x\ \hat{\sigma}_z$	$\hat{\sigma}_z\ \mathbb{1}\ \ \hat{\sigma}_z\ \hat{\sigma}_z\ \hat{\sigma}_z\ \hat{\sigma}_z$	$\hat{\sigma}_z\ \hat{\sigma}_y\ \hat{\sigma}_z\ \mathbb{1}\ \ \hat{\sigma}_x\ \hat{\sigma}_y$
10000	$\hat{\sigma}_y\ \hat{\sigma}_x\ \mathbb{1}\ \ \hat{\sigma}_x\ \hat{\sigma}_y\ \mathbb{1}$	$\hat{\sigma}_y\ \hat{\sigma}_y\ \hat{\sigma}_z\ \hat{\sigma}_x\ \hat{\sigma}_y\ \hat{\sigma}_y$	$\hat{\sigma}_z\ \hat{\sigma}_x\ \mathbb{1}\ \ \mathbb{1}\ \ \hat{\sigma}_x\ \mathbb{1}$	$\hat{\sigma}_z\ \hat{\sigma}_y\ \hat{\sigma}_z\ \mathbb{1}\ \ \hat{\sigma}_y\ \hat{\sigma}_z$
	$\hat{\sigma}_y\ \hat{\sigma}_x\ \mathbb{1}\ \ \hat{\sigma}_x\ \hat{\sigma}_y\ \hat{\sigma}_x$	$\hat{\sigma}_y\ \hat{\sigma}_y\ \hat{\sigma}_z\ \hat{\sigma}_y\ \hat{\sigma}_x\ \hat{\sigma}_y$	$\hat{\sigma}_z\ \hat{\sigma}_x\ \mathbb{1}\ \ \mathbb{1}\ \ \hat{\sigma}_x\ \hat{\sigma}_x$	$\hat{\sigma}_z\ \hat{\sigma}_y\ \hat{\sigma}_z\ \hat{\sigma}_z\ \hat{\sigma}_x\ \hat{\sigma}_y$
	$\hat{\sigma}_y\ \hat{\sigma}_x\ \mathbb{1}\ \ \hat{\sigma}_y\ \hat{\sigma}_x\ \mathbb{1}$	$\hat{\sigma}_y\ \hat{\sigma}_y\ \hat{\sigma}_z\ \hat{\sigma}_y\ \hat{\sigma}_y\ \hat{\sigma}_z$	$\hat{\sigma}_z\ \hat{\sigma}_x\ \mathbb{1}\ \ \hat{\sigma}_z\ \hat{\sigma}_x\ \mathbb{1}$	$\hat{\sigma}_z\ \hat{\sigma}_y\ \hat{\sigma}_z\ \hat{\sigma}_z\ \hat{\sigma}_y\ \hat{\sigma}_z$
	$\hat{\sigma}_y\ \hat{\sigma}_x\ \mathbb{1}\ \ \hat{\sigma}_y\ \hat{\sigma}_x\ \hat{\sigma}_x$	$\hat{\sigma}_y\ \hat{\sigma}_z\ \mathbb{1}\ \ \hat{\sigma}_y\ \mathbb{1}\ \ \mathbb{1}$	$\hat{\sigma}_z\ \hat{\sigma}_x\ \mathbb{1}\ \ \hat{\sigma}_z\ \hat{\sigma}_x\ \hat{\sigma}_x$	$\hat{\sigma}_z\ \hat{\sigma}_z\ \mathbb{1}\ \ \hat{\sigma}_z\ \hat{\sigma}_z\ \mathbb{1}$
10100	$\hat{\sigma}_y\ \hat{\sigma}_x\ \hat{\sigma}_x\ \hat{\sigma}_x\ \hat{\sigma}_y\ \mathbb{1}$	$\hat{\sigma}_y\ \hat{\sigma}_z\ \mathbb{1}\ \ \hat{\sigma}_y\ \mathbb{1}\ \ \hat{\sigma}_x$	$\hat{\sigma}_z\ \hat{\sigma}_x\ \hat{\sigma}_x\ \mathbb{1}\ \ \hat{\sigma}_x\ \mathbb{1}$	$\hat{\sigma}_z\ \hat{\sigma}_z\ \hat{\sigma}_x\ \hat{\sigma}_z\ \hat{\sigma}_z\ \hat{\sigma}_x$
	$\hat{\sigma}_y\ \hat{\sigma}_x\ \hat{\sigma}_x\ \hat{\sigma}_x\ \hat{\sigma}_y\ \hat{\sigma}_x$	$\hat{\sigma}_y\ \hat{\sigma}_z\ \mathbb{1}\ \ \hat{\sigma}_y\ \hat{\sigma}_z\ \mathbb{1}$	$\hat{\sigma}_z\ \hat{\sigma}_x\ \hat{\sigma}_x\ \mathbb{1}\ \ \hat{\sigma}_x\ \hat{\sigma}_x$	$\hat{\sigma}_z\ \hat{\sigma}_z\ \hat{\sigma}_y\ \mathbb{1}\ \ \mathbb{1}\ \ \hat{\sigma}_y$
	$\hat{\sigma}_y\ \hat{\sigma}_x\ \hat{\sigma}_x\ \hat{\sigma}_x\ \hat{\sigma}_y\ \mathbb{1}$	$\hat{\sigma}_y\ \hat{\sigma}_z\ \mathbb{1}\ \ \hat{\sigma}_y\ \hat{\sigma}_z\ \hat{\sigma}_x$	$\hat{\sigma}_z\ \hat{\sigma}_x\ \hat{\sigma}_x\ \hat{\sigma}_z\ \hat{\sigma}_x\ \mathbb{1}$	$\hat{\sigma}_z\ \hat{\sigma}_z\ \hat{\sigma}_y\ \mathbb{1}\ \ \hat{\sigma}_z\ \hat{\sigma}_y$
	$\hat{\sigma}_y\ \hat{\sigma}_x\ \hat{\sigma}_x\ \hat{\sigma}_y\ \hat{\sigma}_x\ \hat{\sigma}_x$	$\hat{\sigma}_y\ \hat{\sigma}_z\ \mathbb{1}\ \ \hat{\sigma}_y\ \mathbb{1}\ \ \hat{\sigma}_y$	$\hat{\sigma}_z\ \hat{\sigma}_x\ \hat{\sigma}_x\ \hat{\sigma}_z\ \hat{\sigma}_x\ \hat{\sigma}_x$	$\hat{\sigma}_z\ \hat{\sigma}_z\ \hat{\sigma}_y\ \hat{\sigma}_z\ \hat{\sigma}_z\ \mathbb{1}$
11000	$\hat{\sigma}_y\ \hat{\sigma}_x\ \hat{\sigma}_y\ \hat{\sigma}_x\ \hat{\sigma}_x\ \hat{\sigma}_z$	$\hat{\sigma}_y\ \hat{\sigma}_z\ \hat{\sigma}_x\ \hat{\sigma}_y\ \mathbb{1}\ \ \hat{\sigma}_x$	$\hat{\sigma}_z\ \hat{\sigma}_x\ \hat{\sigma}_y\ \mathbb{1}\ \ \hat{\sigma}_x\ \hat{\sigma}_y$	$\hat{\sigma}_z\ \hat{\sigma}_z\ \hat{\sigma}_y\ \hat{\sigma}_z\ \hat{\sigma}_z\ \hat{\sigma}_y$
	$\hat{\sigma}_y\ \hat{\sigma}_x\ \hat{\sigma}_y\ \hat{\sigma}_x\ \hat{\sigma}_y\ \hat{\sigma}_y$	$\hat{\sigma}_y\ \hat{\sigma}_z\ \hat{\sigma}_x\ \hat{\sigma}_x\ \hat{\sigma}_y\ \mathbb{1}$	$\hat{\sigma}_z\ \hat{\sigma}_x\ \hat{\sigma}_y\ \mathbb{1}\ \ \hat{\sigma}_y\ \hat{\sigma}_z$	$\hat{\sigma}_z\ \hat{\sigma}_z\ \hat{\sigma}_z\ \mathbb{1}\ \ \mathbb{1}\ \ \hat{\sigma}_z$
	$\hat{\sigma}_y\ \hat{\sigma}_x\ \hat{\sigma}_y\ \hat{\sigma}_y\ \hat{\sigma}_x\ \hat{\sigma}_y$	$\hat{\sigma}_y\ \hat{\sigma}_z\ \hat{\sigma}_x\ \hat{\sigma}_y\ \hat{\sigma}_z\ \hat{\sigma}_x$	$\hat{\sigma}_z\ \hat{\sigma}_x\ \hat{\sigma}_y\ \hat{\sigma}_z\ \hat{\sigma}_x\ \hat{\sigma}_y$	$\hat{\sigma}_z\ \hat{\sigma}_z\ \hat{\sigma}_z\ \mathbb{1}\ \ \hat{\sigma}_z\ \hat{\sigma}_z$
	$\hat{\sigma}_y\ \hat{\sigma}_x\ \hat{\sigma}_y\ \hat{\sigma}_y\ \hat{\sigma}_y\ \hat{\sigma}_z$	$\hat{\sigma}_y\ \hat{\sigma}_z\ \hat{\sigma}_x\ \hat{\sigma}_y\ \hat{\sigma}_x\ \mathbb{1}$	$\hat{\sigma}_z\ \hat{\sigma}_x\ \hat{\sigma}_y\ \hat{\sigma}_z\ \hat{\sigma}_y\ \hat{\sigma}_z$	$\hat{\sigma}_z\ \hat{\sigma}_z\ \hat{\sigma}_z\ \hat{\sigma}_z\ \mathbb{1}\ \ \hat{\sigma}_z$
11100	$\hat{\sigma}_y\ \hat{\sigma}_x\ \hat{\sigma}_z\ \hat{\sigma}_x\ \hat{\sigma}_x\ \hat{\sigma}_y$	$\hat{\sigma}_y\ \hat{\sigma}_z\ \hat{\sigma}_y\ \hat{\sigma}_x\ \hat{\sigma}_z\ \hat{\sigma}_z$	$\hat{\sigma}_z\ \hat{\sigma}_x\ \hat{\sigma}_z\ \mathbb{1}\ \ \hat{\sigma}_x\ \hat{\sigma}_z$	$\hat{\sigma}_z\ \hat{\sigma}_z\ \hat{\sigma}_z\ \hat{\sigma}_z\ \hat{\sigma}_z\ \hat{\sigma}_z$

Table C.4: Elements 10000000 to 11111100 of the relevant operators for the verification of the Toffoli gate.

C.2. Toffoli gate

C.2.1. Calibration procedure

Temporarily changing the frequency of a qubit by means of a flux pulse will introduce a dynamical phase between the $|0\rangle$ and the $|1\rangle$ state (see Sec. 5.2.2). This dynamical phase can be compensated for by changing the phase of all microwave pulses (including the tomography pulses) following the flux pulse.

In the Toffoli gate however, the state of the first transmon "qutrit" can be $|2\rangle$ for some finite time during the algorithm, see Sec. 7.2.1. The dynamical phase between the states $|0\rangle$ and $|2\rangle$ is in general different from the dynamical phase between $|0\rangle$ and $|1\rangle$. Therefore these phases cannot both be compensated by adjusting the phases of subsequent microwave pulses.

In other words, the phase acquired by qubit B differs, depending on the state of qubit A. The dynamical phase of the two-qubit state of qubits A and B acquired during the Toffoli gate sequence therefore depends on the input state of these qubits as

$$\begin{aligned} |00\rangle &\rightarrow |00\rangle \\ |10\rangle &\rightarrow e^{i\varphi_A}|10\rangle \\ |01\rangle &\rightarrow e^{i\varphi_B}|01\rangle \\ |11\rangle &\rightarrow e^{i\varphi_2}|11\rangle, \end{aligned}$$

where $\varphi_2 \neq \varphi_A + \varphi_B$ in general. To compensate for this effect, we adjust the phase φ_B such that the condition $\varphi_2 = \varphi_A + \varphi_B \pmod{2\pi}$ is fulfilled. This is done by an additional flux pulse just before the CPHASE gate. This flux pulse shifts the qubit to a frequency where it does not interact with any other qubit, but only acquires a dynamical phase. The amplitude and length of this pulse are calibrated in a Ramsey type experiment similar to the one presented in Fig. 8.3. The $\pi/2$ pulses are applied to qubit A, and the extra flux pulse is tuned such that the resulting traces for the input states $|0\rangle$ and $|1\rangle$ of qubit B are in phase.

C.3. Quantum teleportation

C.3.1. Calibration procedure

The standard calibration procedure for the teleportation experiment is as follows: First the single qubit operations are calibrated, followed by the calibration of the CPHASE gates (see Sec. 5.2.2) and the parametric amplifiers (see Sec. 4.4). In the experiments where feed-forward is used, this has been calibrated as presented in Sec. 8.2.6. In the following, we explain the calibration procedure for single qubit gates in detail.

Once the qubits are tuned to their approximate working frequency (determined by spectroscopic measurements), the IQ-mixers are calibrated at this frequency (see [Schmidlin09, Baur12a]). Subsequently, the following sequence of experiments is performed for each qubit individually (see also Sec. 5.1):

- Rabi oscillations: From this measurement the $\pi/2$ pulse amplitude is extracted which is used in the next experiment.
- Ramsey oscillations: The drive frequency is detuned by 4 MHz from the qubit frequency determined by spectroscopic measurements. The deviation of the oscillation frequency from the detuning allows to determine the exact qubit frequency.
- Rabi oscillations: Extract the amplitude for π and $\pi/2$ pulses at the exact qubit frequency.
- Q scaling factor needed for DRAG pulses is measured [Motzoi09, Gambetta11, Baur12a].
- Rabi oscillations to find the final amplitudes for the π and $\pi/2$ pulses.

After each experiment, the extracted parameter is used to generate the patterns of the next experiment, therefore iteratively calibrating the π and $\pi/2$ pulses. Automatizing this task[1] has reduced the amount of interaction needed to operate the experiment and greatly sped up the calibration procedure.

[1] The automatization of the calibration routine was implemented by Tim Menke, Johannes Heinsoo and Andreas Landig

C.3.2. Error budget

The finite coherence and dephasing times of our qubits are a source of error which limit the output-state fidelity. The fidelity of the measurement of Q3 through R3 affects the state fidelity of $|\psi_{\text{out}}\rangle$ directly. From the measured probabilities of correctly identifying the states $|0\rangle$ and $|1\rangle$ on Q3 we calculate the limit of the output-state fidelity through this source of error to be $\bar{\mathcal{F}}_s = 94\,\%$. In addition, the misidentification of the Bell states of Qb1 and Qb2 leads to an effective dephasing of $|\psi_{\text{out}}\rangle$. This limits the fidelity further to $\bar{\mathcal{F}}_s = 89\,\%$ and $\bar{\mathcal{F}}_s = 84\,\%$ for the respective cases in which we post-select on one Bell state only and in which we distinguish all Bell states in each measurement. Because both of these numbers are about $7-8\,\%$ higher than the actually measured fidelities, it is plausible to assign the remaining errors to the limited gate fidelities. Determining the gate errors independently shows that we perform single-qubit operations with a fidelity greater than $98\,\%$ and create Bell states with a fidelity of $92\,\%$ using two-qubit CPHASE gates with a process fidelity of 90%.

Bibliography

[Abdo13] B. Abdo, K. Sliwa, L. Frunzio, and M. Devoret. "Directional amplification with a josephson circuit." *Physical Review X*, **3**, 031001 (2013). Cited on page 141.

[Abdumalikov13] A. A. Abdumalikov, J. M. Fink, K. Juliusson, M. Pechal, S. Berger, A. Wallraff, and S. Filipp. "Experimental realization of non-abelian non-adiabatic geometric gates." *Nature*, **496**, 482 (2013). Cited on page 140.

[Aoki09] T. Aoki, G. Takahashi, T. Kajiya, J.-i. Yoshikawa, S. L. Braunstein, P. van Loock, and A. Furusawa. "Quantum error correction beyond qubits." *Nature Physics*, **5**, 541–546 (2009). Cited on page 102.

[Aspect82] A. Aspect, J. Dalibard, and G. Roger. "Experimental test of bell's inequalities using time- varying analyzers." *Physical Review Letters*, **49**, 1804–1807 (1982). Cited on page 1.

[Autodesk] Autodesk. "AutoCAD 2000 DXF Reference." `http://www.autodesk.com/techpubs/autocad/acad2000/dxf/`. Accessed on 2013-06-20. Cited on page 29.

[Awschalom13] D. D. Awschalom, L. C. Bassett, A. S. Dzurak, E. L. Hu, and J. R. Petta. "Quantum spintronics: Engineering and manipulating atom-like spins in semiconductors." *Science*, **339**, 1174–1179 (2013). Cited on page 2.

[Bao12] X.-H. Bao, X.-F. Xu, C.-M. Li, Z.-S. Yuan, C.-Y. Lu, and J.-W. Pan. "Quantum teleportation between remote atomic-ensemble quantum memories." *Proceedings of the National Academy of Sciences*, **109**, 20347–20351 (2012). Cited on pages 116 and 137.

[Barenco95] A. Barenco, C. H. Bennett, R. Cleve, D. P. DiVincenzo, N. Margolus, P. Shor, T. Sleator, J. A. Smolin, and H. Weinfurter. "Elementary gates for quantum computation." *Physical Review A*, **52**, 3457–3467 (1995). Cited on page 102.

[Barends13] R. Barends, J. Kelly, A. Megrant, D. Sank, E. Jeffrey, Y. Chen, Y. Yin, B. Chiaro, J. Mutus, C. Neill, P. OÃćâĆňâĎćMalley, P. Roushan, J. Wenner, T. C. White, A. N. Cleland, and J. M. Martinis. "Coherent josephson qubit suitable for scalable quantum integrated circuits." *Physical Review Letters*, **111**, 080502–(2013). Cited on page 140.

[Barrett04] M. Barrett, J. Chiaverini, T. Schaetz, J. Britton, W. Itano, J. Jost, E. Knill, C. Langer, D. Leibfried, R. Ozeri, and D. Wineland. "Deterministic quantum teleportation of atomic qubits." *Nature*, **429**, 737–739 (2004). Cited on pages 116 and 137.

[Baur09] M. Baur, S. Filipp, R. Bianchetti, J. M. Fink, M. Göppl, L. Steffen, P. J. Leek, A. Blais, and A. Wallraff. "Measurement of autlertownes and mollow transitions in a strongly driven superconducting qubit." *Physical Review Letters*, **102**, 243602 (2009). Cited on page 139.

[Baur12a] M. Baur. *Realizing quantum gates and algorithms with three superconducting qubits*. Ph.D. thesis, ETH Zurich (2012). Cited on pages 39, 55, 56, 74, 98, 118, 139 and 167.

[Baur12b] M. Baur, A. Fedorov, L. Steffen, S. Filipp, M. P. da Silva, and A. Wallraff. "Benchmarking a quantum teleportation protocol in superconducting circuits using tomography and an entanglement witness." *Physical Review Letters*, **108**, 040502 (2012). Cited on pages 33, 75, 93 and 118.

[Bell64] J. S. Bell. "On the Einstein Podolsky Rosen paradox." *Physics (N. Y.)*, **1**, 195 (1964). Cited on pages 1 and 141.

[Bengtsson06] I. Bengtsson. "Three ways to look at mutually unbiased bases." *arXiv:quant-ph/0610216* (2006). Cited on pages 6 and 118.

[Bennett84] C. H. Bennett and G. Brassard. "Quantum cryptography: public key distribution and coin tossing." *Int. Conf. on Computers, Systems and Signal Processing*, 175 (1984). Cited on page 2.

[Bennett93] C. H. Bennett, G. Brassard, C. Crépeau, R. Jozsa, A. Peres, and W. K. Wootters. "Teleporting an unknown quantum state via dual classical and Einstein-Podolsky-Rosen channels." *Physical Review Letters*, **70**, 1895–1899 (1993). Cited on pages 113 and 114.

[Bennett96a] C. H. Bennett, H. J. Bernstein, S. Popescu, and B. Schumacher. "Concentrating partial entanglement by local operations." *Physical Review A*, **53**, 2046–2052 (1996). Cited on page 142.

[Bennett96b] C. H. Bennett, G. Brassard, S. Popescu, B. Schumacher, J. A. Smolin, and W. K. Wootters. "Purification of noisy entanglement and faithful teleportation via noisy channels." *Physical Review Letters*, **76**, 722–725 (1996). Cited on page 142.

[Bernien13] H. Bernien, B. Hensen, W. Pfaff, G. Koolstra, M. S. Blok, L. Robledo, T. H. Taminiau, M. Markham, D. J. Twitchen, L. Childress, and R. Hanson. "Heralded entanglement between solid-state qubits separated by three metres." *Nature*, **497**, 86–90 (2013). Cited on page 2.

[Bertet05] P. Bertet, I. Chiorescu, G. Burkard, K. Semba, C. J. P. M. Harmans, D. P. DiVincenzo, and J. E. Mooij. "Dephasing of a superconducting qubit induced by photon noise." *Physical Review Letters*, **95**, 257002 (2005). Cited on pages 156 and 159.

[Bialczak10] R. C. Bialczak, M. Ansmann, M. Hofheinz, E. Lucero, M. Neeley, A. D. O'Connell, D. Sank, H. Wang, J. Wenner, M. Steffen, A. N. Cleland, and J. M. Martinis. "Quantum process tomography of a universal entangling gate implemented with josephson phase qubits." *Nature Physics*, **6**, 409–413 (2010). Cited on page 79.

[Bianchetti09] R. Bianchetti, S. Filipp, M. Baur, J. M. Fink, M. Göppl, P. J. Leek, L. Steffen, A. Blais, and A. Wallraff. "Dynamics of dispersive single-qubit readout in circuit quantum electrodynamics." *Physical Review A*, **80**, 043840 (2009). Cited on pages 3, 41, 57 and 139.

[Bianchetti10a] R. Bianchetti. *Control and readout of a superconducting artificial atom*. Ph.D. thesis, ETH Zurich (2010). Cited on pages 38, 39, 41, 44, 95 and 121.

[Bianchetti10b] R. Bianchetti, S. Filipp, M. Baur, J. M. Fink, C. Lang, L. Steffen, M. Boissonneault, A. Blais, and A. Wallraff. "Control and tomography of a three level superconducting artificial atom." *Physical Review Letters*, **105**, 223601 (2010). Cited on page 139.

[Biercuk09a] M. J. Biercuk, H. Uys, A. P. VanDevender, N. Shiga, W. M. Itano, and J. J. Bollinger. "Experimental uhrig dynamical decoupling using trapped ions." *Physical Review A*, **79**, 062324 (2009). Cited on page 159.

[Biercuk09b] M. J. Biercuk, H. Uys, A. P. VanDevender, N. Shiga, W. M. Itano, and J. J. Bollinger. "Optimized dynamical decoupling in a model quantum memory." *Nature*, **458**, 996–1000 (2009). Cited on page 159.

[Blais04] A. Blais, R.-S. Huang, A. Wallraff, S. M. Girvin, and R. J. Schoelkopf. "Cavity quantum electrodynamics for superconducting electrical circuits: An architecture for quantum computation." *Physical Review A*, **69**, 062320 (2004). Cited on pages 3, 16, 63 and 122.

[Blais07] A. Blais, J. Gambetta, A. Wallraff, D. I. Schuster, S. M. Girvin, M. H. Devoret, and R. J. Schoelkopf. "Quantum-information processing with circuit quantum electrodynamics." *Physical Review A*, **75**, 032329 (2007). Cited on pages 55 and 62.

[Blume-Kohout10] R. Blume-Kohout. "Optimal, reliable estimation of quantum states." *New Journal of Physics*, **12**, 043034 (2010). Cited on page 90.

[Boissonneault08] M. Boissonneault, J. M. Gambetta, and A. Blais. "Nonlinear dispersive regime of cavity qed: The dressed dephasing model." *Physical Review A*, **77**, 305–305 (2008). Cited on page 51.

[Boixo13a] S. Boixo, T. Albash, F. M. Spedalieri, N. Chancellor, and D. A. Lidar. "Experimental signature of programmable quantum annealing." *Nature Communications*, **4**, 2067 (2013). Cited on page 141.

[Boixo13b] S. Boixo, T. F. Rønnow, S. V. Isakov, Z. Wang, D. Wecker, D. A. Lidar, J. M. Martinis, and M. Troyer. "Quantum annealing with more than one hundred qubits." *arXiv:1304.4595* (2013). Cited on page 141.

[Borrelli11] M. Borrelli, L. Mazzola, M. Paternostro, and S. Maniscalco. "Simple trapped-ion architecture for high-fidelity toffoli gates." *Physical Review A*, **84**, 012314 (2011). Cited on page 103.

[Bouchiat98] V. Bouchiat, D. Vion, P. Joyez, D. Esteve, and M. H. Devoret. "Quantum coherence with a single Cooper pair." *Physica Scripta*, **T76**, 165–170 (1998). Cited on page 13.

[Bouwmeester97] D. Bouwmeester, J. W. Pan, K. Mattle, M. Eibl, H. Weinfurter, and A. Zeilinger. "Experimental quantum teleportation." *Nature*, **390**, 575–579 (1997). Cited on pages 114 and 137.

[Bozyigit10] D. Bozyigit. *Correlation Function Measurements of a Microwave Frequency Single Photon Source*. Master's thesis, ETH Zurich (2010). Cited on page 59.

[Bozyigit11] D. Bozyigit, C. Lang, L. Steffen, J. M. Fink, C. Eichler, M. Baur, R. Bianchetti, P. J. Leek, S. Filipp, M. P. da Silva, A. Blais, and A. Wallraff. "Antibunching of microwave-frequency photons observed in correlation measurements using linear detectors." *Nature Physics*, **7**, 154–158 (2011). Cited on pages 33 and 139.

[Brassard98] G. Brassard, S. L. Braunstein, and R. Cleve. "Teleportation as a quantum computation." *Physica D: Nonlinear Phenomena*, **120**, 43–47 (1998). Cited on page 122.

[Braunstein98] S. L. Braunstein and H. J. Kimble. "Teleportation of continuous quantum variables." *Physical Review Letters*, **80**, 869–872 (1998). Cited on page 135.

[Briegel98] H.-J. Briegel, W. Dür, J. I. Cirac, and P. Zoller. "Quantum repeaters: The role of imperfect local operations in quantum communication." *Physical Review Letters*, **81**, 5932–5935 (1998). Cited on page 114.

[Brune96] M. Brune, F. Schmidt-Kaler, A. Maali, J. Dreyer, E. Hagley, J. M. Raimond, and S. Haroche. "Quantum Rabi oscillation: A direct test of field quantization in a cavity." *Physical Review Letters*, **76**, 1800–1803 (1996). Cited on page 61.

[Burkhard12] S. Burkhard. "Optimization of transmon design for longer coherence time." (2012). Cited on page 23.

[Bylander11] J. Bylander, S. Gustavsson, F. Yan, F. Yoshihara, K. Harrabi, G. Fitch, D. G. Cory, Y. Nakamura, J.-S. Tsai, and O. W. D. "Noise spectroscopy through dynamical decoupling with a superconducting flux qubit." *Nature Physics*, **7**, 565–570 (2011). Cited on pages 156 and 159.

[Campagne-Ibarcq13] P. Campagne-Ibarcq, E. Flurin, N. Roch, D. Darson, P. Morfin, M. Mirrahimi, M. H. Devoret, F. Mallet, and B. Huard. "Persistent control of a superconducting qubit by stroboscopic measurement feedback." *Physical Review X*, **3**, 021008 (2013). Cited on page 141.

[Carr54] H. Y. Carr and E. M. Purcell. "Effects of diffusion on free precession in nuclear magnetic resonance experiments." *Physical Review*, **94**, 630–638 (1954). Cited on page 156.

[Castellanos-Beltran08] M. A. Castellanos-Beltran, K. D. Irwin, G. C. Hilton, L. R. Vale, and K. W. Lehnert. "Amplification and squeezing of quantum noise with a tunable Josephson metamaterial." *Nature Physics*, **4**, 929–931 (2008). Cited on pages 44 and 126.

[Chang13] J. B. Chang, M. R. Vissers, A. D. Corcoles, M. Sandberg, J. Gao, D. W. Abraham, J. M. Chow, J. M. Gambetta, M. B. Rothwell, G. A. Keefe, M. Steffen, and D. P. Pappas. "Improved superconducting qubit coherence using titanium nitride." *Applied Physics Letters*, **103**, 012602 (2013). Cited on page 140.

[Chiaverini04] J. Chiaverini, D. Leibfried, T. Schaetz, M. Barrett, R. Blakestad, J. Britton, W. Itano, J. Jost, E. Knill, C. Langer, R. Ozeri, and D. Wineland. "Realization of quantum error correction." *Nature*, **432**, 602–605 (2004). Cited on page 102.

[Choi75] M.-D. Choi. "Completely positive linear maps on complex matrices." *Linear Algebra and its Applications*, **10**, 285 – 290 (1975). Cited on page 90.

[Chow09] J. M. Chow, J. M. Gambetta, L. Tornberg, J. Koch, L. S. Bishop, A. A. Houck, B. R. Johnson, L. Frunzio, S. M. Girvin, and R. J. Schoelkopf. "Randomized benchmarking and process tomography for gate errors in a solid-state qubit." *Physical Review Letters*, **102**, 090502 (2009). Cited on page 85.

[Chow10a] J. M. Chow, L. DiCarlo, J. M. Gambetta, F. Motzoi, L. Frunzio, S. M. Girvin, and R. J. Schoelkopf. "Optimized driving of superconducting artificial atoms for improved single-qubit gates." *Physical Review A*, **82**, 040305 (2010). Cited on pages 56 and 57.

[Chow10b] J. M. Chow, L. DiCarlo, J. M. Gambetta, A. Nunnenkamp, L. S. Bishop, L. Frunzio, M. H. Devoret, S. M. Girvin, and R. J. Schoelkopf. "Detecting highly entangled states with a joint qubit readout." *Physical Review A*, **81**, 062325 (2010). Cited on pages 68, 70, 74 and 95.

[Chow12] J. M. Chow, J. M. Gambetta, A. D. Córcoles, S. T. Merkel, J. A. Smolin, C. Rigetti, S. Poletto, G. A. Keefe, M. B. Rothwell, J. R. Rozen, M. B. Ketchen, and M. Steffen. "Universal quantum gate set approaching fault-tolerant thresholds with superconducting qubits." *Physical Review Letters*, **109**, 060501 (2012). Cited on pages 3, 83, 84 and 140.

[Chow13] J. M. Chow, J. M. Gambetta, A. W. Cross, S. T. Merkel, C. Rigetti, and M. Steffen. "Microwave-activated conditional-phase gate for superconducting qubits." *New Journal of Physics*, **15**, 115012 (2013). Cited on page 140.

[Chuang97] I. L. Chuang and M. A. Nielsen. "Prescription for experimental determination of the dynamics of a quantum black box." *Journal of Modern Optics*, **44**, 2455–2467 (1997). Cited on page 80.

[Clariant GmbH] Clariant GmbH. "AZ 5214 E Product Data Sheet." `http://www.microchemicals.com/products/photoresists/azr_5214e.html`. Accessed on 2013-06-21. Cited on pages 30 and 32.

[Clarke08] J. Clarke and F. K. Wilhelm. "Superconducting quantum bits." *Nature*, **453**, 1031–1042 (2008). Cited on pages 2, 12 and 155.

[Clauser69] J. F. Clauser, M. A. Horne, A. Shimony, and R. A. Holt. "Proposed experiment to test local hidden-variable theories." *Physical Review Letters*, **23**, 880–884 (1969). Cited on page 1.

[Collett93] E. Collett. *Polarized light : fundamentals and applications*. Marcel Dekker New York (1993). Cited on page 69.

[Córcoles11] A. D. Córcoles, J. M. Chow, J. M. Gambetta, C. Rigetti, J. R. Rozen, G. A. Keefe, M. B. Rothwell, M. B. Ketchen, and M. Steffen. "Protecting superconducting qubits from radiation." *Applied Physics Letters*, **99**, 181906 (2011). Cited on page 39.

[Córcoles13] A. D. Córcoles, J. M. Gambetta, J. M. Chow, J. A. Smolin, M. Ware, J. Strand, B. L. T. Plourde, and M. Steffen. "Process verification of two-qubit quantum gates by randomized benchmarking." *Physical Review A*, **87** (2013). Cited on page 85.

[Cory98] D. G. Cory, M. D. Price, W. Maas, E. Knill, R. Laflamme, W. H. Zurek, T. F. Havel, and S. S. Somaroo. "Experimental quantum

error correction." *Physical Review Letters*, **81**, 2152–2155 (1998). Cited on page 102.

[Das08] A. Das and B. K. Chakrabarti. "*Colloquium* : Quantum annealing and analog quantum computation." *Reviews of Modern Physics*, **80**, 1061–1081 (2008). Cited on page 141.

[daSilva11] M. P. da Silva, O. Landon-Cardinal, and D. Poulin. "Practical characterization of quantum devices without tomography." *Physical Review Letters*, **107**, 210404 (2011). Cited on pages 89, 90, 91, 92 and 109.

[deLange10] G. de Lange, Z. H. Wang, D. RistÃÍ, V. V. Dobrovitski, and R. Hanson. "Universal dynamical decoupling of a single solid-state spin from a spin bath." *Science*, **330**, 60–63 (2010). Cited on page 159.

[Deutsch85] D. Deutsch. "Quantum theory, the Church-Turing principle and the universal quantum computer." *Proceedings of the Royal Society of London. Series A, Mathematical and Physical Sciences*, **400**, 97–117 (1985). Cited on page 1.

[Deutsch92] D. Deutsch and R. Jozsa. "Rapid solution of problems by quantum computation." *Proceedings: Mathematical and Physical Sciences*, **439**, 553–558 (1992). Cited on page 2.

[Devoret85] M. H. Devoret, J. M. Martinis, and J. Clarke. "Measurements of macroscopic quantum tunneling out of the zero-voltage state of a current-biased Josephson junction." *Physical Review Letters*, **55**, 1908–1911 (1985). Cited on page 12.

[Devoret13] M. Devoret and R. J. Schoelkopf. "Superconducting circuits for quantum information: An outlook." *Science*, **339**, 1169–1174 (2013). Cited on pages 2, 3 and 140.

[Dewes12] A. Dewes, R. Lauro, F. R. Ong, V. Schmitt, P. Milman, P. Bertet, D. Vion, and D. Esteve. "Quantum speeding-up of computation demonstrated in a superconducting two-qubit processor." *Physical Review B*, **85**, 140503 (2012). Cited on page 3.

[DiCarlo09] L. DiCarlo, J. M. Chow, J. M. Gambetta, L. S. Bishop, B. R. Johnson, D. I. Schuster, J. Majer, A. Blais, L. Frunzio, S. M. Girvin, and R. J. Schoelkopf. "Demonstration of two-qubit algorithms with a superconducting quantum processor." *Nature*, **460**, 240–244 (2009). Cited on pages 59, 63, 64, 74 and 140.

[DiCarlo10] L. DiCarlo, M. D. Reed, L. Sun, B. R. Johnson, J. M. Chow, J. M. Gambetta, L. Frunzio, S. M. Girvin, M. H. Devoret, and R. J. Schoelkopf. "Preparation and measurement of three-qubit entanglement in a superconducting circuit." *Nature*, **467**, 574–578 (2010). Cited on pages 63, 64, 70 and 75.

[Dickson13] N. G. Dickson, M. W. Johnson, M. H. Amin, R. Harris, F. Altomare, A. J. Berkley, P. Bunyk, J. Cai, E. M. Chapple, P. Chavez, F. Cioata, T. Cirip, P. deBuen, M. Drew-Brook, C. Enderud, S. Gildert, F. Hamze, J. P. Hilton, E. Hoskinson, K. Karimi, E. Ladizinsky, N. Ladizinsky, T. Lanting, T. Mahon, R. Neufeld, T. Oh, I. Perminov, C. Petroff, A. Przybysz, C. Rich, P. Spear, A. Tcaciuc, M. C. Thom, E. Tolkacheva, S. Uchaikin, J. Wang, A. B. Wilson, Z. Merali, and G. Rose. "Thermally assisted quantum annealing of a 16-qubit problem." *Nature Communications*, **4**, 1903 (2013). Cited on page 140.

[DiVincenzo09] D. P. DiVincenzo. "Fault-tolerant architectures for superconducting qubits." *Physica Scripta*, **2009**, 014020 (2009). Cited on page 140.

[Duan10] L.-M. Duan and C. Monroe. "Colloquium: Quantum networks with trapped ions." *Reviews of Modern Physics*, **82**, 1209–1224 (2010). Cited on page 2.

[Dutra05] S. M. Dutra. *Cavity Quantum Electrodynamics*. John Wiley & Sons, New York (2005). Cited on page 3.

[Efron81] B. Efron. "Nonparametric estimates of standard error: The jackknife, the bootstrap and other methods." *Biometrika*, **68**, 589–599 (1981). Cited on page 110.

[Eichler11] C. Eichler, D. Bozyigit, C. Lang, M. Baur, L. Steffen, J. M. Fink, S. Filipp, and A. Wallraff. "Observation of two-mode squeezing in the microwave frequency domain." *Physical Review Letters*, **107**, 113601 (2011). Cited on pages 48, 127 and 139.

[Eichler13a] C. Eichler. *Experimental Characterization of Quantum Microwave Radiation and its Entanglement with a Superconducting Qubit*. Ph.D. thesis, ETH Zurich (2013). Cited on pages 45, 49 and 141.

[Eichler13b] C. Eichler and A. Wallraff. "Controlling the dynamic range of a josephson parametric amplifier." *arXiv:1305.6583* (2013). Cited on pages 45 and 141.

[Fedorov12] A. Fedorov, L. Steffen, M. Baur, M. P. da Silva, and A. Wallraff. "Implementation of a Toffoli gate with superconducting circuits." *Nature*, **481**, 170–172 (2012). Cited on pages 75, 89, 93, 103 and 139.

[Feynman82] R. P. Feynman. "Simulating physics with computers." *International Journal of Theoretical Physics*, **21**, 467–488 (1982). Cited on page 1.

[Filipp09] S. Filipp, P. Maurer, P. J. Leek, M. Baur, R. Bianchetti, J. M. Fink, M. Göppl, L. Steffen, J. M. Gambetta, A. Blais, and A. Wallraff. "Two-qubit state tomography using a joint dispersive readout." *Physical Review Letters*, **102**, 200402 (2009). Cited on pages 3, 74, 95, 122 and 139.

[Fink08] J. M. Fink, M. Göppl, M. Baur, R. Bianchetti, P. J. Leek, A. Blais, and A. Wallraff. "Climbing the Jaynes-Cummings ladder and observing its nonlinearity in a cavity QED system." *Nature*, **454**, 315–318 (2008). Cited on page 63.

[Fink10a] J. Fink. *Quantum nonlinearities in strong coupling circuit QED*. Ph.D. thesis, ETH Zurich (2010). Cited on pages 23 and 61.

[Fink10b] J. M. Fink, L. Steffen, P. Studer, L. S. Bishop, M. Baur, R. Bianchetti, D. Bozyigit, C. Lang, S. Filipp, P. J. Leek, and A. Wallraff. "Quantum-to-classical transition in cavity quantum electrodynamics." *Physical Review Letters*, **105**, 163601 (2010). Cited on pages 61 and 139.

[Flammia11] S. T. Flammia and Y.-K. Liu. "Direct fidelity estimation from few pauli measurements." *Physical Review Letters*, **106**, 230501 (2011). Cited on pages 89, 90, 91 and 92.

[Fowler12] A. G. Fowler, M. Mariantoni, J. M. Martinis, and A. N. Cleland. "Surface codes: Towards practical large-scale quantum computation." *Physical Review A*, **86**, 032324 (2012). Cited on page 140.

[Freedman72] S. J. Freedman and J. F. Clauser. "Experimental test of local hidden-variable theories." *Physical Review Letters*, **28**, 938–941 (1972). Cited on page 1.

[Frey12] T. Frey, P. J. Leek, M. Beck, A. Blais, T. Ihn, K. Ensslin, and A. Wallraff. "Dipole coupling of a double quantum dot to a microwave resonator." *Physical Review Letters*, **108**, 046807 (2012). Cited on page 141.

[Fuchs03] C. A. Fuchs and M. Sasaki. "Squeezing quantum information through a classical channel: measuring the "quantumness" of a set of quantum states." *Quantum Information & Computation*, **3**, 377–404 (2003). Cited on page 118.

[Furusawa98] A. Furusawa, J. L. Sørensen, S. L. Braunstein, C. A. Fuchs, H. J. Kimble, and E. S. Polzik. "Unconditional quantum teleportation." *Science*, **282**, 706–709 (1998). Cited on pages 116 and 135.

[Gaebler12] J. P. Gaebler, A. M. Meier, T. R. Tan, R. Bowler, Y. Lin, D. Hanneke, J. D. Jost, J. P. Home, E. Knill, D. Leibfried, and D. J. Wineland. "Randomized benchmarking of multiqubit gates." *Physical Review Letters*, **108**, 260503 (2012). Cited on page 85.

[Gambetta11] J. M. Gambetta, F. Motzoi, S. T. Merkel, and F. K. Wilhelm. "Analytic control methods for high-fidelity unitary operations in a weakly nonlinear oscillator." *Physical Review A*, **83**, 012308 (2011). Cited on pages 56, 57, 105, 122 and 167.

[Georgescu13] I. M. Georgescu, S. Ashhab, and F. Nori. "Quantum simulation." *arXiv:1308.6253* (2013). Cited on page 142.

[Gevorgian95] S. Gevorgian, L. J. P. Linnér, and E. L. Kollberg. "CAD models for shielded multilayered CPW." *IEEE Transactions on Microwave Theory and Techniques*, **43(2)**, 772 (1995). Cited on pages 19 and 20.

[Gisin02] N. Gisin, G. Ribordy, W. Tittel, and H. Zbinden. "Quantum cryptography." *Reviews of Modern Physics*, **74**, 145–195 (2002). Cited on pages 114, 138 and 141.

[Göppl08] M. Göppl, A. Fragner, M. Baur, R. Bianchetti, S. Filipp, J. M. Fink, P. J. Leek, G. Puebla, L. Steffen, and A. Wallraff. "Coplanar waveguide resonators for circuit quantum electrodynamics." *Journal of Applied Physics*, **104**, 113904 (2008). Cited on pages 18, 21, 23, 24, 26 and 119.

[Göppl09] M. Göppl. *Engineering Quantum Electronic Chips - Realization and Characterization of Circuit Quantum Electrodynamics Systems*. Ph.D. thesis, ETH Zurich (2009). Cited on page 23.

[Gottesman97] D. Gottesman. *Stabilizer Codes and Quantum Error Correction*. Ph.D. thesis, California Institute of Technology (1997). Cited on pages 91 and 97.

[Gottesman99] D. Gottesman and I. L. Chuang. "Demonstrating the viability of universal quantum computation using teleportation and single-qubit operations." *Nature*, **402**, 390–393 (1999). Cited on pages 91, 97, 114 and 138.

[Groen13] J. P. Groen, D. Rista, L. Tornberg, J. Cramer, P. C. de Groot, T. Picot, G. Johansson, and L. DiCarlo. "Partial-measurement backaction and nonclassical weak values in a superconducting circuit." *Physical Review Letters*, **111**, 090506 (2013). Cited on page 97.

[Grover96] L. K. Grover. "A fast quantum mechanical algorithm for database search." In "Proceedings of the twenty-eighth annual ACM symposium on Theory of computing," 212–219. ACM, Philadelphia, Pennsylvania, United States (1996). Cited on page 2.

[Gustavsson12] S. Gustavsson, F. Yan, J. Bylander, F. Yoshihara, Y. Nakamura, T. P. Orlando, and W. D. Oliver. "Dynamical decoupling and dephasing in interacting two-level systems." *Physical Review Letters*, **109**, 010502 (2012). Cited on page 159.

[Gywat06] O. Gywat, F. Meier, D. Loss, and D. D. Awschalom. "Dynamics of coupled qubits interacting with an off-resonant cavity." *Physical Review B*, **73**, 125336 (2006). Cited on page 63.

[Häffner08] H. Häffner, C. F. Roos, and R. Blatt. "Quantum computing with trapped ions." *Physics Reports-review Section of Physics Letters*, **469**, 155–203 (2008). Cited on page 2.

[Hahn50] E. L. Hahn. "Spin echoes." *Physical Review*, **80**, 580–594 (1950). Cited on page 156.

[Hanson07] R. Hanson, L. P. Kouwenhoven, J. R. Petta, S. Tarucha, and L. M. K. Vandersypen. "Spins in few-electron quantum dots." *Reviews of Modern Physics*, **79**, 1217–1265 (2007). Cited on page 2.

[Haroche06] S. Haroche and J.-M. Raimond. *Exploring the Quantum: Atoms, Cavities, and Photons*. Oxford University Press, New York, USA (2006). Cited on pages 3 and 16.

[Häusler12] S. Häusler. *Extension of a printed circuit board and sample holder for experiments in circuit quantum electrodynamics*. Master's thesis, ETH Zurich (2012). Cited on page 39.

[Helmer09] F. Helmer, M. Mariantoni, A. G. Fowler, J. von Delft, E. Solano, and F. Marquardt. "Cavity grid for scalable quantum computation with superconducting circuits." *EPL (Europhysics Letters)*, **85**, 50007 (2009). Cited on pages 28, 119 and 140.

[Hinton86] G. E. Hinton, J. L. McClelland, and D. E. Rumelhart. "Distributed representations." In "Parallel Distributed Processing: Explorations in the Microstructure of Cognition. Volume 1: Foundations," 77–109. MIT Press (1986). Cited on page 101.

[Hofheinz08] M. Hofheinz, E. M. Weig, M. Ansmann, R. C. Bialczak, E. Lucero, M. Neeley, A. D. O'Connell, H. Wang, J. M. Martinis, and A. N. Cleland. "Generation of Fock states in a superconducting quantum circuit." *Nature*, **454**, 310–314 (2008). Cited on page 61.

[Hogan12] S. D. Hogan, J. A. Agner, F. Merkt, T. Thiele, S. Filipp, and A. Wallraff. "Driving Rydberg-Rydberg transitions from a coplanar microwave waveguide." *Physical Review Letters*, **108**, 063004 (2012). Cited on page 141.

[Horodecki99] M. Horodecki, P. Horodecki, and R. Horodecki. "General teleportation channel, singlet fraction, and quasidistillation." *Physical Review A*, **60**, 1888 (1999). Cited on page 91.

[Ithier05a] G. Ithier. *Manipulation, lecture et analyse de la décohérence d'un bit quantique supraconducteur*. Ph.D. thesis, Service de Physique de l'Etat Condensé, CEA-Saclay (2005). Cited on pages 153, 154 and 156.

[Ithier05b] G. Ithier, E. Collin, P. Joyez, P. J. Meeson, D. Vion, D. Esteve, F. Chiarello, A. Shnirman, Y. Makhlin, J. Schriefl, and G. Schön. "Decoherence in a superconducting quantum bit circuit." *Physical Review B*, **72**, 134519 (2005). Cited on pages 154 and 155.

[Ivanović81] I. D. Ivanović. "Geometrical description of quantal state determination." *Journal of Physics A: Mathematical and General*, **14**, 3241 (1981). Cited on page 6.

[Jamiołkowski72] A. Jamiołkowski. "Linear transformations which preserve trace and positive semidefiniteness of operators." *Reports on Mathematical Physics*, **3**, 275 – 278 (1972). Cited on page 90.

[Ježek03] M. Ježek, J. Fiurášek, and Z. Hradil. "Quantum inference of states and processes." *Physical Review A*, **68**, 012305 (2003). Cited on pages 74 and 106.

[Johansson06] J. Johansson, S. Saito, T. Meno, H. Nakano, M. Ueda, K. Semba, and H. Takayanagi. "Vacuum Rabi oscillations in a macroscopic superconducting qubit LC oscillator system." *Physical Review Letters*, **96**, 127006 (2006). Cited on page 61.

[Johnson11] M. W. Johnson, M. H. S. Amin, S. Gildert, T. Lanting, F. Hamze, N. Dickson, R. Harris, A. J. Berkley, J. Johansson, P. Bunyk, E. M. Chapple, C. Enderud, J. P. Hilton, K. Karimi, E. Ladizinsky, N. Ladizinsky, T. Oh, I. Perminov, C. Rich, M. C. Thom, E. Tolkacheva, C. J. S. Truncik, S. Uchaikin, J. Wang, B. Wilson, and G. Rose. "Quantum annealing with manufactured spins." *Nature*, **473**, 194 (2011). Cited on pages 140 and 141.

[Josephson62] B. D. Josephson. "Possible new effects in superconductive tunnelling." *Physics Letters*, **1**, 251–253 (1962). Cited on page 12.

[Josephson74] B. D. Josephson. "The discovery of tunnelling supercurrents." *Reviews of Modern Physics*, **46**, 251–254 (1974). Cited on page 12.

[Kamat08] P. V. Kamat. "Quantum dot solar cells. semiconductor nanocrystals as light harvesters." *The Journal of Physical Chemistry C*, **112**, 18737–18753 (2008). Cited on page 143.

[Kim01] Y. H. Kim, S. P. Kulik, and Y. Shih. "Quantum teleportation of a polarization state with a complete bell state measurement." *Physical Review Letters*, **86**, 1370–1373 (2001). Cited on pages 116 and 137.

[Kirchmair13] G. Kirchmair, B. Vlastakis, Z. Leghtas, S. E. Nigg, H. Paik, E. Ginossar, M. Mirrahimi, L. Frunzio, S. M. Girvin, and R. J. Schoelkopf. "Observation of quantum state collapse and revival due to the single-photon kerr effect." *Nature*, **495**, 205–209 (2013). Cited on page 140.

[Knill01] E. Knill, R. Laflamme, R. Martinez, and C. Negrevergne. "Benchmarking quantum computers: The five-qubit error correcting code." *Physical Review Letters*, **86**, 5811–5814 (2001). Cited on page 102.

[Knill08] E. Knill, D. Leibfried, R. Reichle, J. Britton, R. B. Blakestad, J. D. Jost, C. Langer, R. Ozeri, S. Seidelin, and D. J. Wineland. "Randomized benchmarking of quantum gates." *Physical Review A*, **77**, 012307 (2008). Cited on pages 85 and 87.

[Koch07] J. Koch, T. M. Yu, J. Gambetta, A. A. Houck, D. I. Schuster, J. Majer, A. Blais, M. H. Devoret, S. M. Girvin, and R. J. Schoelkopf. "Charge-insensitive qubit design derived from the Cooper pair box." *Physical Review A*, **76**, 042319 (2007). Cited on pages 12, 13, 15, 16, 17 and 18.

[Kok07] P. Kok, W. J. Munro, K. Nemoto, T. C. Ralph, J. P. Dowling, and G. J. Milburn. "Linear optical quantum computing with photonic qubits." *Reviews of Modern Physics*, **79**, 135–174 (2007). Cited on page 2.

[Koster89] N. Koster, S. Koblowski, R. Bertenburg, S. Heinen, and I. Wolff. "Investigations on air bridges used for mmics in cpw technique." In "Microwave Conference, 1989. 19th European," 666–671 (1989). Cited on page 27.

[Krupka94] J. Krupka, R. Geyer, M. Kuhn, and J. Hinken. "Dielectric properties of single crystals of Al_2O_3 , $LaAlO_3$, $NdGaO_3$, $SrTiO_3$, and mgo at cryogenic temperatures." *Microwave Theory and Techniques, IEEE Transactions on*, **42**, 1886–1890 (1994). Cited on page 20.

[Kubo11] Y. Kubo, C. Grezes, A. Dewes, T. Umeda, J. Isoya, H. Sumiya, N. Morishita, H. Abe, S. Onoda, T. Ohshima, V. Jacques, A. Dréau, J.-F. Roch, I. Diniz, A. Auffeves, D. Vion, D. Esteve, and P. Bertet. "Hybrid quantum circuit with a superconducting qubit coupled to a spin ensemble." *Physical Review Letters*, **107**, 220501 (2011). Cited on page 141.

[Ladd10] T. D. Ladd, F. Jelezko, R. Laflamme, Y. Nakamura, C. Monroe, and J. L. O'Brien. "Quantum computers." *Nature*, **464**, 45–53 (2010). Cited on page 2.

[Lang13a] C. Lang, D. Bozyigit, Y. Salathe, C. Eichler, and A. Wallraff. "Quantum signal analyzer for itinerant microwave radiation." *in preparation* (2013). Cited on page 130.

[Lang13b] C. Lang, C. Eichler, L. Steffen, J. M. Fink, M. J. Woolley, A. Blais, and A. Wallraff. "Correlations, indistinguishability and entanglement in Hong-Ou-Mandel experiments at microwave frequencies." *Nature Physics*, **9**, 345–348 (2013). Cited on page 33.

[Lanyon09] B. P. Lanyon, M. Barbieri, M. P. Almeida, T. Jennewein, T. C. Ralph, K. J. Resch, G. J. Pryde, J. L. O'Brien, A. Gilchrist, and A. G. White. "Simplifying quantum logic using higher-dimensional hilbert spaces." *Nature Physics*, **5**, 134–140 (2009). Cited on page 103.

[Las Heras13] U. Las Heras, A. Mezzacapo, L. Lamata, S. Filipp, A. Wallraff, and E. Solano. "Digital quantum simulation of spin systems in superconducting circuits." *arXiv:1311.7626* (2013). Cited on page 142.

[Lee11] N. Lee, H. Benichi, Y. Takeno, S. Takeda, J. Webb, E. Huntington, and A. Furusawa. "Teleportation of nonclassical wave packets of light." *Science*, **332**, 330–333 (2011). Cited on pages 116 and 135.

[Leek07] P. J. Leek, J. M. Fink, A. Blais, R. Bianchetti, M. Göppl, J. M. Gambetta, D. I. Schuster, L. Frunzio, R. J. Schoelkopf, and A. Wallraff. "Observation of Berry's phase in a solid-state qubit." *Science*, **318**, 1889 (2007). Cited on page 159.

[Leek09] P. J. Leek, S. Filipp, P. Maurer, M. Baur, R. Bianchetti, J. M. Fink, M. Göppl, L. Steffen, and A. Wallraff. "Using sideband transitions for two-qubit operations in superconducting circuits." *Physical Review B*, **79**, 180511 (2009). Cited on page 139.

[Leek10] P. J. Leek, M. Baur, J. M. Fink, R. Bianchetti, L. Steffen, S. Filipp, and A. Wallraff. "Cavity quantum electrodynamics with separate photon storage and qubit readout modes." *Physical Review Letters*, **104**, 100504 (2010). Cited on page 139.

[Liu12] Y. Liu. *Implementation and Characterization of 16-port Devices in Circuit Quantum Electrodynamics*. Master's thesis, ETH Zurich (2012). Cited on page 39.

[Lucero12] E. Lucero, R. Barends, Y. Chen, J. Kelly, M. Mariantoni, A. Megrant, P. O'Malley, D. Sank, A. Vainsencher, J. Wenner, T. White, Y. Yin, A. N. Cleland, and J. M. Martinis. "Computing prime factors with a josephson phase qubit quantum processor." *Nature Physics*, **8**, 719–723 (2012). Cited on page 3.

[Ma12] X.-S. Ma, T. Herbst, T. Scheidl, D. Wang, S. Kropatschek, W. Naylor, B. Wittmann, A. Mech, J. Kofler, E. Anisimova, V. Makarov, T. Jennewein, R. Ursin, and A. Zeilinger. "Quantum teleportation over 143 kilometres using active feed-forward." *Nature*, **489**, 269–273 (2012). Cited on pages 114 and 137.

[Magesan12] E. Magesan, J. M. Gambetta, B. R. Johnson, C. A. Ryan, J. M. Chow, S. T. Merkel, M. P. da Silva, G. A. Keefe, M. B. Rothwell, T. A. Ohki, M. B. Ketchen, and M. Steffen. "Efficient measurement of quantum gate error by interleaved randomized benchmarking." *Physical Review Letters*, **109**, 080505 (2012). Cited on page 85.

[Majer07] J. Majer, J. M. Chow, J. M. Gambetta, J. Koch, B. R. Johnson, J. A. Schreier, L. Frunzio, D. I. Schuster, A. A. Houck, A. Wallraff, A. Blais, M. H. Devoret, S. M. Girvin, and R. J. Schoelkopf. "Coupling superconducting qubits via a cavity bus." *Nature*, **449**, 443–447 (2007). Cited on pages 3 and 63.

[Mallet09] F. Mallet, F. R. Ong, A. Palacios-Laloy, F. Nguyen, P. Bertet, D. Vion, and D. Esteve. "Single-shot qubit readout in circuit quantum electrodynamics." *Nature Physics*, **5**, 791–795 (2009). Cited on pages 44 and 97.

[Marcikic03] I. Marcikic, H. de Riedmatten, W. Tittel, H. Zbinden, and N. Gisin. "Long-distance teleportation of qubits at telecommunication wavelengths." *Nature*, **421**, 509–513 (2003). Cited on page 114.

[Mariantoni11] M. Mariantoni, H. Wang, T. Yamamoto, M. Neeley, R. C. Bialczak, Y. Chen, M. Lenander, E. Lucero, A. D. O'Connell, D. Sank, M. Weides, J. Wenner, Y. Yin, J. Zhao, A. N. Korotkov, A. N. Cleland, and J. M. Martinis. "Implementing the quantum von Neumann architecture with superconducting circuits." *Science*, **334**, 61–65 (2011). Cited on pages 53, 103, 106 and 141.

[Martinis85] J. M. Martinis, M. H. Devoret, and J. Clarke. "Energy-level quantization in the zero-voltage state of a current-biased josephson junction." *Physical Review Letters*, **55**, 1543–1546 (1985). Cited on page 12.

[Martinis05] J. M. Martinis, K. B. Cooper, R. McDermott, M. Steffen, M. Ansmann, K. D. Osborn, K. Cicak, S. Oh, D. P. Pappas, R. W. Simmonds, and C. C. Yu. "Decoherence in Josephson qubits from dielectric loss." *Physical Review Letters*, **95**, 210503 (2005). Cited on page 140.

[Marx09] S. Marx. *Optimization of the microwave properties of a cryostat sample holder*. Master's thesis, ETH Zurich (2009). Cited on page 39.

[Massar95] S. Massar and S. Popescu. "Optimal extraction of information from finite quantum ensembles." *Physical Review Letters*, **74**, 1259–1263 (1995). Cited on page 116.

[Meiboom58] S. Meiboom and D. Gill. "Modified spin-echo method for measuring nuclear relaxation times." *Review of Scientific Instruments*, **29**, 688–691 (1958). Cited on page 156.

[MicroChem Corp.] MicroChem Corp. "NANO PMMA and Copolymer." `http://microchem.com/pdf/PMMA_Data_Sheet.pdf`. Accessed on 2013-06-21. Cited on page 31.

[Monroe13] C. Monroe and J. Kim. "Scaling the ion trap quantum processor." *Science*, **339**, 1164 (2013). Cited on page 2.

[Monz09] T. Monz, K. Kim, W. Hänsel, M. Riebe, A. S. Villar, P. Schindler, M. Chwalla, M. Hennrich, and R. Blatt. "Realization of the quantum Toffoli gate with trapped ions." *Physical Review Letters*, **102**, 040501 (2009). Cited on page 103.

[Motzoi09] F. Motzoi, J. M. Gambetta, P. Rebentrost, and F. K. Wilhelm. "Simple pulses for elimination of leakage in weakly nonlinear qubits." *Physical Review Letters*, **103**, 110501 (2009). Cited on pages 56, 57, 105, 122 and 167.

[Murch13] K. W. Murch, S. J. Weber, C. Macklin, and I. Siddiqi. "Observing single quantum trajectories of a superconducting qubit." *Nature*, **502**, 211–214 (2013). Cited on page 140.

[Mutus13] J. Y. Mutus, T. C. White, E. Jeffrey, D. Sank, R. Barends, J. Bochmann, Y. Chen, Z. Chen, B. Chiaro, A. Dunsworth, J. Kelly, A. Megrant, C. Neill, P. J. J. O'Malley, P. Roushan, A. Vainsencher, J. Wenner, I. Siddiqi, R. Vijay, A. N. Cleland, and J. M. Martinis. "Design and characterization of a lumped element single-ended superconducting microwave parametric amplifier with on-chip flux bias line." *Applied Physics Letters*, **103**, 122602 (2013). Cited on page 141.

[Nakamura97] Y. Nakamura, C. D. Chen, and J. S. Tsai. "Spectroscopy of energy-level splitting between two macroscopic quantum states of charge coherently superposed by josephson coupling." *Physical Review Letters*, **79**, 2328–2331 (1997). Cited on pages 3 and 12.

[Neeley10] M. Neeley, R. C. Bialczak, M. Lenander, E. Lucero, M. Mariantoni, A. D. O'Connell, D. Sank, H. Wang, M. Weides, J. Wenner, Y. Yin, T. Yamamoto, A. N. Cleland, and J. M. Martinis. "Generation of three-qubit entangled states using superconducting phase qubits." *Nature*, **467**, 570–573 (2010). Cited on page 70.

[Nielsen98] M. A. Nielsen, E. Knill, and R. Laflamme. "Complete quantum teleportation using nuclear magnetic resonance." *Nature*, **396**, 52–55 (1998). Cited on pages 116 and 122.

[Nielsen00] M. A. Nielsen and I. L. Chuang. *Quantum Computation and Quantum Information*. Cambridge University Press (2000). Cited on pages 1, 2, 5, 22, 68, 70 and 102.

[Nölleke13] C. Nölleke, A. Neuzner, A. Reiserer, C. Hahn, G. Rempe, and S. Ritter. "Efficient teleportation between remote single-atom quantum memories." *Physical Review Letters*, **110**, 140403 (2013). Cited on pages 116 and 137.

[Oliver13] W. D. Oliver. "Superconducting qubits." In D. DiVincenzo (Ed.), "Quantum Information Processing," Lecture Notes of the 44$^{\text{th}}$ IFF Spring School 2013 (2013). Cited on pages 153, 154 and 156.

[Olmschenk09] S. Olmschenk, D. N. Matsukevich, P. Maunz, D. Hayes, L.-M. Duan, and C. Monroe. "Quantum teleportation between distant matter qubits." *Science*, **323**, 486–489 (2009). Cited on pages 116 and 137.

[Oxford Instruments] Oxford Instruments. "High Access Dilution Refrigerator - Kelvinox400HA." http://www.oxford-instruments.com/products/cryogenic-environments/dilution-refrigerator/wet-dilution-refrigerators/high-access-dilution-refrigerator-kelvinoxha. Accessed on 2013-06-25. Cited on page 36.

[Paik11] H. Paik, D. I. Schuster, L. S. Bishop, G. Kirchmair, G. Catelani, A. P. Sears, B. R. Johnson, M. J. Reagor, L. Frunzio, L. I. Glazman, S. M. Girvin, M. H. Devoret, and R. J. Schoelkopf. "Observation of high coherence in Josephson junction qubits measured in a three-dimensional circuit QED architecture." *Physical Review Letters*, **107**, 240501 (2011). Cited on page 140.

[Pavan97] P. Pavan, R. Bez, P. Olivo, and E. Zanoni. "Flash memory cells-an overview." *Proceedings of the IEEE*, **85**, 1248–1271 (1997). Cited on page 143.

[Pechal13] M. Pechal, C. Eichler, S. Zeytinoglu, S. Berger, A. Wallraff, and S. Filipp. "Microwave-controlled generation of shaped single photons in circuit quantum electrodynamics." *arXiv:1308.4094* (2013). Cited on pages 141 and 142.

[Peterer12] M. Peterer. *Investigating the suppression of external sources of decoherence in transmon quibits*. Master's thesis, ETH Zurich (2012). Cited on page 39.

[Pittman05] T. B. Pittman, B. C. Jacobs, and J. D. Franson. "Demonstration of quantum error correction using linear optics." *Physical Review A*, **71**, 052332 (2005). Cited on page 102.

[Pobell06] F. Pobell. *Matter and Methods at Low Temperatures*. Springer, 3rd edition, (2006). Cited on page 36.

[Pozar11] D. M. Pozar. *Microwave engineering*. John Wiley & Sons, Inc., 4th edition (2011). Cited on pages 18, 19, 21, 22 and 24.

[Preskill97] J. Preskill. "Fault-tolerant quantum computation." *arXiv:quant-ph/9712048* (1997). Cited on page 140.

[Rabi37] I. I. Rabi. "Space quantization in a gyrating magnetic field." *Physical Review*, **51**, 652–654 (1937). Cited on page 56.

[Ralph07] T. C. Ralph, K. J. Resch, and A. Gilchrist. "Efficient Toffoli gates using qudits." *Physical Review A*, **75**, 022313 (2007). Cited on pages 103 and 106.

[Ramsey50] N. F. Ramsey. "A molecular beam resonance method with separated oscillating fields." *Physical Review*, **78**, 695–699 (1950). Cited on page 57.

[Redfield57] A. G. Redfield. "On the theory of relaxation processes." *IBM Journal of Research and Development*, **1**, 19–31 (1957). Cited on page 154.

[Reed12] M. D. Reed, L. DiCarlo, S. E. Nigg, L. Sun, L. Frunzio, S. M. Girvin, and R. J. Schoelkopf. "Realization of three-qubit quantum error correction with superconducting circuits." *Nature*, **482**, 382–385 (2012). Cited on pages 3, 53, 64, 102, 103 and 140.

[Riebe04] M. Riebe, H. Häffner, C. F. Roos, W. Hänsel, J. Benhelm, G. P. T. Lancaster, T. W. Körber, C. Becher, F. Schmidt-Kaler, D. F. V. James, and R. Blatt. "Deterministic quantum teleportation with atoms." *Nature*, **429**, 734–737 (2004). Cited on page 116.

[Rigetti12] C. Rigetti, J. M. Gambetta, S. Poletto, B. L. T. Plourde, J. M. Chow, A. D. Córcoles, J. A. Smolin, S. T. Merkel, J. R. Rozen, G. A. Keefe, M. B. Rothwell, M. B. Ketchen, and M. Steffen. "Superconducting qubit in a waveguide cavity with a coherence time approaching 0.1 ms." *Physical Review B*, **86**, 100506 (2012). Cited on pages 3 and 140.

[Ristè12a] D. Ristè, C. C. Bultink, K. W. Lehnert, and L. DiCarlo. "Feedback control of a solid-state qubit using high-fidelity projective measurement." *Physical Review Letters*, **109**, 240502 (2012). Cited on page 53.

[Ristè12b] D. Ristè, J. G. van Leeuwen, H.-S. Ku, K. W. Lehnert, and L. DiCarlo. "Initialization by measurement of a superconducting quantum bit circuit." *Physical Review Letters*, **109**, 050507 (2012). Cited on pages 52 and 140.

[Ristè13] D. Ristè, M. Dukalski, C. A. Watson, G. de Lange, M. J. Tiggelman, Y. M. Blanter, K. W. Lehnert, R. N. Schouten, and L. DiCarlo. "Deterministic entanglement of superconducting qubits by parity measurement and feedback." *Nature*, **502**, 350–354 (2013). Cited on pages 3, 140 and 141.

[Rivest78] R. L. Rivest, A. Shamir, and L. Adleman. "A method for obtaining digital signatures and public-key cryptosystems." *Commun. ACM*, **21(2)**, 120–126 (1978). Cited on page 2.

[Rubin94] S. M. Rubin. "Computer Aids for VLSI Design." `http://www.rulabinsky.com/cavd/text/chapc.html` (1994). Accessed on 2013-06-20. Cited on page 29.

[Saffman10] M. Saffman, T. G. Walker, and K. Mølmer. "Quantum information with Rydberg atoms." *Reviews of Modern Physics*, **82**, 2313–2363 (2010). Cited on page 2.

[Salathe13] Y. Salathe. *in preparation* (2013). Cited on page 130.

[Sandberg13] M. Sandberg, M. R. Vissers, T. A. Ohki, J. Gao, J. Aumentado, M. Weides, and D. P. Pappas. "Radiation-suppressed superconducting quantum bit in a planar geometry." *Applied Physics Letters*, **102**, 072601 (2013). Cited on page 140.

[Schmidlin09] S. Schmidlin. *Generation of amplitude and phase controlled microwave pulses for qubit manipulation in Circuit QED*. Master's thesis, ETH Zurich (2009). Cited on pages 56 and 167.

[Schumacher95] B. Schumacher. "Quantum coding." *Physical Review A*, **51**, 2738–2747 (1995). Cited on page 2.

[Schumacher96] B. Schumacher. "Sending entanglement through noisy quantum channels." *Physical Review A*, **54**, 2614–2628 (1996). Cited on pages 82 and 91.

[Scully97] M. O. Scully and M. S. Zubairy. *Quantum Optics*. Cambridge University Press (1997). Cited on page 60.

[Shende09] V. V. Shende and I. L. Markov. "On the CNOT-cost of TOFFOLI gates." *Quantum Information & Computation*, **9**, 461–486 (2009). Cited on page 102.

[Shi03] Y. Shi. "Both toffoli and controlled-not need little help to do universal quantum computing." *Quantum Info. Comput.*, **3**, 84–92 (2003). Cited on pages 11 and 102.

[Shor94] P. W. Shor. "Algorithms for quantum computation: Discrete logarithms and factoring." In "Proceedings, 35th Annual Symposium on Foundations of Computer Science, Santa Fe," 124. IEEE Computer Society Press (1994). Cited on page 2.

[Siddiqi04] I. Siddiqi, R. Vijay, F. Pierre, C. M. Wilson, M. Metcalfe, C. Rigetti, L. Frunzio, and M. H. Devoret. "RF-driven Josephson bifurcation amplifier for quantum measurement." *Physical Review Letters*, **93**, 207002 (2004). Cited on page 44.

[Sillanpää07] M. A. Sillanpää, J. I. Park, and R. W. Simmonds. "Coherent quantum state storage and transfer between two phase qubits via a resonant cavity." *Nature*, **449**, 438–442 (2007). Cited on page 63.

[Simons01] R. N. Simons. *Coplanar waveguide circuits, components and systems*. Wiley Series in Microwave and Optical Engineerging. Wiley Inter-Science (2001). Cited on pages 18, 19, 22 and 27.

[Smolin12] J. A. Smolin, J. M. Gambetta, and G. Smith. "Efficient method for computing the maximum-likelihood quantum state from measurements with additive gaussian noise." *Physical Review Letters*, **108**, 070502 (2012). Cited on pages 74, 90, 98 and 106.

[Spörl07] A. Spörl, T. Schulte-Herbrüggen, S. J. Glaser, V. Bergholm, M. J. Storcz, J. Ferber, and F. K. Wilhelm. "Optimal control of coupled josephson qubits." *Physical Review A*, **75**, 012302 (2007). Cited on page 104.

[Srinivasan13] S. J. Srinivasan, N. M. Sundaresan, D. Sadri, Y. Liu, J. M. Gambetta, T. Yu, S. M. Girvin, and A. A. Houck. "Time-reversal symmetrization of spontaneous emission for high fidelity quantum state transfer." *arXiv:1308.3471* (2013). Cited on pages 141 and 142.

[Steffen06a] M. Steffen, M. Ansmann, R. C. Bialczak, N. Katz, E. Lucero, R. McDermott, M. Neeley, E. M. Weig, A. N. Cleland, and J. M. Martinis. "Measurement of the entanglement of two superconducting qubits via state tomography." *Science*, **313**, 1423–1425 (2006). Cited on page 79.

[Steffen06b] M. Steffen, M. Ansmann, R. Mcdermott, N. Katz, R. C. Bialczak, E. Lucero, M. Neeley, E. M. Weig, A. N. Cleland, and J. M. Martinis. "State tomography of capacitively shunted phase qubits with high fidelity." *Physical Review Letters*, **97**, 050502 (2006). Cited on page 97.

[Steffen07] L. Steffen. *Spin Echo Measurements in a Superconducting Qubit.* Semester Thesis, ETH Zürich (2007). Cited on page 159.

[Steffen08] L. Steffen. *Local Qubit Control in Circuit Quantum Electrodynamics.* Master's thesis, ETH Zurich (2008). Cited on page 56.

[Steffen11] M. Steffen, D. DiVincenzo, J. M. Chow, T. Theis, and M. Ketchen. "Quantum computing: An IBM perspective." *IBM Journal of Research and Development*, **55**, 13:1–13:11 (2011). Cited on page 140.

[Steffen12] L. Steffen, M. P. da Silva, A. Fedorov, M. Baur, and A. Wallraff. "Experimental Monte Carlo quantum process certification." *Physical Review Letters*, **108**, 260506 (2012). Cited on pages 75, 89, 93 and 139.

[Steffen13] L. Steffen, Y. Salathe, M. Oppliger, P. Kurpiers, M. Baur, C. Lang, C. Eichler, G. Puebla-Hellmann, A. Fedorov, and A. Wallraff. "Deterministic quantum teleportation with feed-forward in a solid state system." *Nature*, **500**, 319–322 (2013). Cited on pages 3, 113, 116, 139, 140, 141 and 159.

[Stojanović12] V. M. Stojanović, A. Fedorov, A. Wallraff, and C. Bruder. "Quantum-control approach to realizing a toffoli gate in circuit qed." *Physical Review B*, **85**, 054504 (2012). Cited on page 104.

[Stokes52] G. G. Stokes. "On the composition and resolution of streams of polarized light from different sources." *Trans. Camb. Phil. Soc.*, **9**, 399 (1852). Cited on page 69.

[Strauch03] F. W. Strauch, P. R. Johnson, A. J. Dragt, C. J. Lobb, J. R. Anderson, and F. C. Wellstood. "Quantum logic gates for coupled superconducting phase qubits." *Physical Review Letters*, **91**, 167005 (2003). Cited on page 63.

[Sun07] Q. Sun, Y. A. Wang, L. S. Li, D. Wang, T. Zhu, J. Xu, C. Yang, and Y. Li. "Bright multicoloured light-emitting diodes based on quantum dots." *Nature Photonics*, **1**, 717–722 (2007). Cited on page 143.

[Takeda13] S. Takeda, T. Mizuta, M. Fuwa, P. van Loock, and A. Furusawa. "Deterministic quantum teleportation of photonic quantum bits by a hybrid technique." *Nature*, **500**, 315–318 (2013). Cited on pages 116 and 135.

[Thompson92] R. J. Thompson, G. Rempe, and H. J. Kimble. "Observation of normal-mode splitting for an atom in an optical cavity." *Physical Review Letters*, **68**, 1132–1135 (1992). Cited on page 61.

[Toffoli80] T. Toffoli. *Reversible computing*, volume 85 of *Lecture Notes in Computer Science*. Springer Berlin / Heidelberg (1980). Cited on page 102.

[Troyer13] M. Troyer. "Quantum annealing." Talk at Microsoft Research Faculty Summit 2013, July 15-16, 2013, Redmond, Washington, United States (2013). Cited on page 141.

[Uhrig07] G. S. Uhrig. "Keeping a quantum bit alive by optimized π-pulse sequences." *Physical Review Letters*, **98**, 100504 (2007). Cited on page 159.

[Uhrig08] G. S. Uhrig. "Exact results on dynamical decoupling by π pulses in quantum information processes." *New Journal of Physics*, **10**, 083024 (2008). Cited on page 159.

[Underwood12] D. L. Underwood, W. E. Shanks, J. Koch, and A. A. Houck. "Low-disorder microwave cavity lattices for quantum simulation with photons." *Physical Review A*, **86**, 023837 (2012). Cited on page 140.

[Vaidman94] L. Vaidman. "Teleportation of quantum states." *Physical Review A*, **49**, 1473–1476 (1994). Cited on page 135.

[Valenzuela06] S. O. Valenzuela, W. D. Oliver, D. M. Berns, K. K. Berggren, L. S. Levitov, and T. P. Orlando. "Microwave-induced cooling of a superconducting qubit." *Science*, **314**, 1589–1592 (2006). Cited on page 53.

[Vandersypen04] L. M. K. Vandersypen and I. L. Chuang. "NMR techniques for quantum control and computation." *Reviews of Modern Physics*, **76**, 1037 (2004). Cited on page 2.

[vanEnk07] S. J. van Enk, N. Lütkenhaus, and H. J. Kimble. "Experimental procedures for entanglement verification." *Physical Review A*, **75**, 052318 (2007). Cited on pages 116, 117 and 118.

[Vijay09] R. Vijay, M. H. Devoret, and I. Siddiqi. "Invited review article: The josephson bifurcation amplifier." *Review of Scientific Instruments*, **80**, 111101 (2009). Cited on page 44.

[Vijay11] R. Vijay, D. H. Slichter, and I. Siddiqi. "Observation of quantum jumps in a superconducting artificial atom." *Physical Review Letters*, **106**, 110502 (2011). Cited on pages 44, 51 and 97.

[Vion03] D. Vion, A. Aassime, A. Cottet, P. Joyez, H. Pothier, C. Urbina, D. Esteve, and M. H. Devoret. "Rabi oscillations, Ramsey fringes and spin echoes in an electrical circuit." *Fortschritte der Physik*, **51**, 462–468 (2003). Cited on pages 56, 57, 156 and 159.

[Voss81] R. F. Voss and R. A. Webb. "Macroscopic quantum tunneling in 1-μm Nb Josephson junctions." *Physical Review Letters*, **47**, 265 (1981). Cited on page 12.

[Wallraff04] A. Wallraff, D. I. Schuster, A. Blais, L. Frunzio, R.-S. Huang, J. Majer, S. Kumar, S. M. Girvin, and R. J. Schoelkopf. "Strong coupling of a single photon to a superconducting qubit using circuit quantum electrodynamics." *Nature*, **431**, 162–167 (2004). Cited on pages 3, 16 and 61.

[Walls08] D. F. Walls and G. J. Milburn. *Quantum Optics*. Springer Verlag, Berlin, 2nd edition (2008). Cited on pages 17 and 60.

[Wangsness53] R. K. Wangsness and F. Bloch. "The dynamical theory of nuclear induction." *Physical Review*, **89**, 728–739 (1953). Cited on page 154.

[Wen69] C. Wen. "Coplanar waveguide: A surface strip transmission line suitable for nonreciprocal gyromagnetic device applications." *IEEE Trans. Microwave Theory Tech.*, **17**, 1087–1090 (1969). Cited on page 18.

[Wenner11] J. Wenner, R. Barends, R. C. Bialczak, Y. Chen, J. Kelly, E. Lucero, M. Mariantoni, A. Megrant, P. J. J. O'Malley, D. Sank, A. Vainsencher, H. Wang, T. C. White, Y. Yin, J. Zhao, A. N. Cleland, and J. M. Martinis. "Surface loss simulations of superconducting coplanar waveguide resonators." *Applied Physics Letters*, **99**, 113513 (2011). Cited on page 140.

[Wolff06] I. Wolff. *Coplanar Microwave Integrated Circuits*. Wiley InterScience (2006). Cited on pages 18, 22, 26 and 27.

[Xiang13] Z.-L. Xiang, S. Ashhab, J. Q. You, and F. Nori. "Hybrid quantum circuits: Superconducting circuits interacting with other quantum systems." *Reviews of Modern Physics*, **85**, 623–653 (2013). Cited on page 141.

[Yamamoto99] Y. Yamamoto and A. Imamoğlu. *Mesoscopic Quantum Optics*. Wiley (1999). Cited on page 60.

[Yin12] J. Yin, J.-G. Ren, H. Lu, Y. Cao, H.-L. Yong, Y.-P. Wu, C. Liu, S.-K. Liao, F. Zhou, Y. Jiang, X.-D. Cai, P. Xu, G.-S. Pan, J.-J. Jia, Y.-M. Huang, H. Yin, J.-Y. Wang, Y.-A. Chen, C.-Z. Peng, and J.-W. Pan. "Quantum teleportation and entanglement distribution over 100-kilometre free-space channels." *Nature*, **488**, 185–188 (2012). Cited on page 114.

[Yurke06] B. Yurke and E. Buks. "Performance of cavity-parametric amplifiers, employing Kerr nonlinearites, in the presence of two-photon loss." *J. Lightwave Technol.*, **24**, 5054–5066 (2006). Cited on page 44.

[Żukowski93] M. Żukowski, A. Zeilinger, M. A. Horne, and A. K. Ekert. ""Event-ready-detectors" Bell experiment via entanglement swapping." *Physical Review Letters*, **71**, 4287–4290 (1993). Cited on page 142.

List of Symbols

Constants

c	$299\,792\,458\,\mathrm{m\ s^{-1}}$	Speed of light in vacuum
e	$1.602\,18 \times 10^{-19}\,\mathrm{C}$	Elementary charge
h	$6.626\,07 \times 10^{-34}\,\mathrm{J\ s}$	Planck constant
$\hbar$	$1.054\,57 \times 10^{-34}\,\mathrm{J\ s}$	Reduced Planck constant ($\hbar = h/2\pi$)
k_B	$1.380\,65 \times 10^{-23}\,\mathrm{J\ K^{-1}}$	Boltzmann constant
ε_0	$8.854\,19 \times 10^{-12}\,\mathrm{F\ m^{-1}}$	Vacuum permittivity, electric constant
Φ_0	$2.067\,83 \times 10^{-15}\,\mathrm{Wb}$	Flux quantum ($\Phi_0 = h/(2e)$)
μ_0	$4\pi \times 10^{-7}\,\mathrm{H\ m^{-1}}$	Vacuum permeability, magnetic constant

Variables

ν	[Hz]	Frequency
ω	$[\mathrm{rad\,s^{-1}}]$	Angular frequency
T	[K]	Temperature

Operators, mathematical Functions

$\mathbb{1}, \hat{\sigma}_0$	Identity operator
$\hat{\sigma}_x$	Pauli x-operator
$\hat{\sigma}_y$	Pauli y-operator
$\hat{\sigma}_z$	Pauli z-operator
Tr	Trace
$\hat{\sigma}, \hat{\rho}$	Density matrices

Abbreviations

a.u.	Arbitrary units
AWG	Arbitrary waveform generator
CPB	Cooper pair box
CPW	Coplanar waveguide
DAQ	Data acquisition
DMSO	Dimethyl sulfoxide
DUV	Deep ultraviolet
EL	Ethyl lactate
FPGA	Field-programmable gate array
HEMT	High-electron-mobility transistor
IVC	Inner vacuum chamber
JC	Jaynes-Cummings
JPA	Josephson parametric amplifier
OFC	Oxygen-free copper
PCB	Printed circuit board
PTM	Pauli transfer matrix

QED	Quantum electrodynamics
QUDEV	Quantum Device
RB	Randomized benchmarking
SMA	SubMiniature version A connection standard
SMP	SubMiniature version P connection standard
SPAM	State preparation and measurement
SQUID	Superconducting quantum interference device
TEM	Transverse electromagnetic
UV	Ultraviolet

List of Equipment

Experimental setup

Cryostat	Oxford Instruments	Kelvinox 400HA
Signal generators	Agilent	PSG E8257D
	Rohde & Schwarz	SMF100A
Arbitrary waveform generators	Tektronix	AWG5014
	Tektronix	AWG520
Semi-rigid coax cables		
Stainless-steel	Micro-coax	UT-85-SS-SS
SPCW	Micro-coax	UT-85-SS
Copper	Micro-coax	UT-85-TP
NbTi	Keycom	NbTiNbTi085A
PCB-SMP connectors	Rosenberger	19S102-40ML5
SMP bullets	Rosenberger	19K101-K00L5

Fabrication

PVD system	Plassys	MEB550S
Mask aligner	ABM	DUV
	Karl Süss	MA6
Wire bonder	Westbond	7476D
Reactive ion etching	Oxford Instruments	Plasmalab 80
Plasma asher	Technis Plasma	100-E

Samples

Chapter 7, Monte Carlo process certification, Toffoli gate	M14Q4
Chapter 8, Teleportation	M23G2
Appendix B.2, Dynamical Decoupling, high noise sensitivity	M4C4
Appendix B.2, Dynamical Decoupling, low noise sensitivity	M3E3

List of Publications

Most relevant publications for this thesis

1. **L. Steffen**, Y. Salathe, M. Oppliger, P. Kurpiers, M. Baur, C. Lang, C. Eichler, G. Puebla-Hellmann, A. Fedorov, A. Wallraff, "Deterministic quantum teleportation with feed-forward in a solid state system", *Nature* **500**, 319-322 (2013)

2. **L. Steffen**, M. P. da Silva, A. Fedorov, M. Baur, A. Wallraff, "Experimental Monte Carlo Quantum Process Certification", *Physical Review Letters* **108**, 260506 (2012)

3. A. Fedorov, **L. Steffen**, M. Baur, M. P. da Silva, A. Wallraff, "Implementation of a Toffoli gate with superconducting circuits", *Nature* **481**, 170–172 (2012)

4. M. Baur, A. Fedorov, **L. Steffen**, S. Filipp, M. P. da Silva, A. Wallraff, "Benchmarking a Quantum Teleportation Protocol in Superconducting Circuits Using Tomography and an Entanglement Witness", *Physical Review Letters* **108**, 040502 (2012)

5. J. M. Fink, **L. Steffen**, P. Studer, Lev S. Bishop, M. Baur, R. Bianchetti, D. Bozyigit, C. Lang, S. Filipp, P. J. Leek, A. Wallraff, "Quantum-To-Classical Transition in Cavity Quantum Electrodynamics", *Physical Review Letters* **105**, 163601 (2010)

Other publications

6. S. Berger, M. Pechal, A. A. Abdumalikov Jr., C. Eichler, **L. Steffen**, A. Fedorov, A. Wallraff, S. Filipp, "Exploring the effect of noise on the Berry phase", *Physical Review A* **87**, 060303(R) (2013)

7. C. Lang, C. Eichler, **L. Steffen**, J. M. Fink, M. J. Woolley, A. Blais, A. Wallraff, "Correlations, indistinguishability and entanglement in Hong-Ou-Mandel experiments at microwave frequencies", *Nature Physics* **9**, 345–348 (2013)

8. J. A. Mlynek, A. A. Abdumalikov, J. M. Fink, **L. Steffen**, M. Baur, C. Lang, A. F. van Loo, A. Wallraff, "Demonstrating W-type entanglement of Dicke states in resonant cavity quantum electrodynamics", *Physical Review A* **86**, 053838 (2012)

9. S. Berger, M. Pechal, S. Pugnetti, A. A. Abdumalikov Jr., **L. Steffen**, A. Fedorov, A. Wallraff, S. Filipp, "Geometric phases in superconducting qubits beyond the two-level-approximation", *Physical Review B* **85**, 220502(R) (2012)

10. M. Pechal, S. Berger, A. A. Abdumalikov Jr., J. M. Fink, J. A. Mlynek, **L. Steffen**, A. Wallraff, S. Filipp, "Geometric Phase and Nonadiabatic Effects in an Electronic Harmonic Oscillator", *Physical Review Letters* **108**, 170401 (2012)

11. S. Filipp, A. F. van Loo, M. Baur, **L. Steffen**, A. Wallraff, "Preparation of subradiant states using local qubit control in circuit QED", *Physical Review A* **84**, 061805 (2011)

12. C. Eichler, D. Bozyigit, C. Lang, M. Baur, **L. Steffen**, J. M. Fink, S. Filipp, A. Wallraff, "Observation of Two-Mode Squeezing in the Microwave Frequency Domain", *Physical Review Letters* **107**, 113601 (2011)

13. S. Filipp, M. Göppl, J. M. Fink, M. Baur, R. Bianchetti, **L. Steffen**, A. Wallraff, "Multimode mediated qubit-qubit coupling and dark-state symmetries in circuit quantum electrodynamics", *Physical Review A* **83**, 063827 (2011)

14. C. Lang, D. Bozyigit, C. Eichler, **L. Steffen**, J. M. Fink, A. A. Abdumalikov Jr., M. Baur, S. Filipp, M. P. da Silva, A. Blais, A. Wallraff, "Observation of Resonant Photon Blockade at Microwave Frequencies Using Correlation Function Measurements", *Physical Review Letters* **106**, 243601–4 (2011)

15. C. Eichler, D. Bozyigit, C. Lang, **L. Steffen**, J. Fink, A. Wallraff, "Experimental State Tomography of Itinerant Single Microwave Photons", *Physical Review Letters* **106**, 220503 (2011)

16. D. Bozyigit, C. Lang, **L. Steffen**, J. M. Fink, C. Eichler, M. Baur, R. Bianchetti, P. J. Leek, S. Filipp, A. Wallraff, M. P. da Silva, A. Blais, "Correlation measurements of individual microwave photons emitted from a symmetric cavity", *Journal of Physics: Conference Series* **264**, 012024 (2011)

17. D. Bozyigit, C. Lang, **L. Steffen**, J. M. Fink, C. Eichler, M. Baur, R. Bianchetti, P. J. Leek, S. Filipp, M. P. da Silva, A. Blais, A. Wallraff, "Antibunching of microwave-frequency photons observed in correlation measurements using linear detectors", *Nature Physics* **7**, 154–158 (2011)

18. R. Bianchetti, S. Filipp, M. Baur, J. M. Fink, C. Lang, **L. Steffen**, M. Boissonneault, A. Blais, A. Wallraff, "Control and Tomography of a Three Level Superconducting Artificial Atom", *Physical Review Letters* **105**, 223601–4 (2010)

19. P. J. Leek, M. Baur, J. M. Fink, R. Bianchetti, **L. Steffen**, S. Filipp, A. Wallraff, "Cavity Quantum Electrodynamics with Separate Photon Storage and Qubit Readout Modes", *Physical Review Letters* **104**, 100504 (2010)

20. J. M. Fink, M. Baur, R. Bianchetti, S. Filipp, M. Göppl, P. J. Leek, **L. Steffen**, A. Blais, A. Wallraff, "Thermal Excitation of Multi-Photon Dressed States in Circuit Quantum Electrodynamics", *Physica Scripta* **T137**, 014013 (2009)

21. R. Bianchetti, S. Filipp, M. Baur, J. M. Fink, M. Göppl, P. J. Leek, **L. Steffen**, A. Blais, A. Wallraff, "Dynamics of dispersive single-qubit

readout in circuit quantum electrodynamics", *Physical Review A* **80**, 043840 (2009)

22. J. M. Fink, R. Bianchetti, M. Baur, M. Göppl, **L. Steffen**, S. Filipp, P. J. Leek, A. Blais, A. Wallraff, "Dressed Collective Qubit States and the Tavis-Cummings Model in Circuit QED", *Physical Review Letters* **103**, 083601–4 (2009)

23. M. Baur, S. Filipp, R. Bianchetti, J. M. Fink, M. Göppl, **L. Steffen**, P. J. Leek, A. Blais, A. Wallraff, "Measurement of Autler-Townes and Mollow Transitions in a Strongly Driven Superconducting Qubit", *Physical Review Letters* **102**, 243602–4 (2009)

24. P. J. Leek, S. Filipp, P. Maurer, M. Baur, R. Bianchetti, J. M. Fink, M. Göppl, **L. Steffen**, A. Wallraff, "Using sideband transitions for two-qubit operations in superconducting circuits", *Physical Review B* **79**, 180511 (2009)

25. S. Filipp, P. Maurer, P. J. Leek, M. Baur, R. Bianchetti, J. M. Fink, M. Göppl, **L. Steffen**, J. M. Gambetta, A. Blais, A. Wallraff, "Two-Qubit State Tomography Using a Joint Dispersive Readout", *Physical Review Letters* **102**, 200402–4 (2009)

26. M. Göppl, A. Fragner, M. Baur, R. Bianchetti, S. Filipp, J. M. Fink, P. J. Leek, G. Puebla, **L. Steffen**, A. Wallraff, "Coplanar Waveguide Resonators for Circuit Quantum Electrodynamics", *Journal of Applied Physics* **104**, 113904 (2008)

Acknowledgments

Throughout the years I spent working on this thesis, I received invaluable support from many people. Without them, the realization of this thesis would not have been possible.

First and foremost I like to express my gratitude to Andreas Wallraff who offered me the opportunity to perform my PhD thesis in the Quantum Device Lab at ETH. I could benefit greatly from his vast knowledge of experimental techniques, his experience in analyzing and solving technical problems and his advice for writing papers or presenting my results. As my supervisor, he provided the optimal mixture of freedom and guidance, allowing me to grow personally and professionally. I also like to thank him for his continuous interest in and support of my projects as well as for the patience needed for some of the projects to show results.

I want to thank Leonardo DiCarlo, the co-examiner of my thesis, for his careful reading of and commenting on the draft of this thesis. Leo's comments were all very helpful, and implementing his suggestions greatly enhanced the quality of the written thesis.

One of the most important factors at work are of course the co-workers. I always perceived the QUDEV-team with all its individuals as a very positive and stimulating environment. Thank you all for making work and life in the lab and office great fun and an excellent experience!

Peter Leek introduced me to cleanroom work, microwave electronics, the handling of the dilution refrigerator and the secrets of *Mathematica*, which are all amongst the most useful technical skills I needed for my thesis. Peter taught me a lot about scientific working and I always admired his clear and concise way of arguing in discussions (not only about science). Johannes Fink and Romeo Bianchetti taught me a lot of practical skills in the laboratory. With Johannes I worked on the quantum-to-classical project and from Romeo I also learned how to manage the group's IT-infrastructure. In my first years, I also collaborated with Deniz Bozyigit and Christian Lang on the first version of the fluxpulse shaping. Most of what I know about Fourier transformation I learned from these guys. Christian's expertise in FPGA programming was also essential when realizing the teleportation project. Moreover he is the person I shared the office with for the longest period of time, and I like to thank him for making it pleasant to work in "D 7". With Arkady Fedorov and Matthias

Baur I worked together on all quantum computation projects: the Toffoli gate, Monte Carlo process certification and the teleportation experiment. Together we solved many problems our fridge prepared for us, designed and carried out the experiments, fabricated samples and analyzed the data. Arkady contributed many crucial ideas to the projects and his calm and focused way of working made it enjoyable to work with him. When Matthias worked on something, he always did it with great care and accuracy. The work he has done for cleaning up our measurement software, making it much more modular and programmer-friendly than it was before, made life easier for everyone in our lab. Thank you both so much! Marcus da Silva is one of the inventors of the Monte Carlo quantum process certification technique. I greatly appreciate his help in understanding the scheme and designing the corresponding experiments, as well as his contribution to the writing of the paper. Yves Salathé joined the quantum computing team in the second phase of the teleportation experiment. It is due to him that the feed-forward could be realized. Moreover, he will be an excellent successor as responsible person for the QUDEV IT-infrastructure. Also in the second phase of the teleportation experiment, Markus Oppliger and Philipp Kurpiers joined the team and helped getting the experiment running. With the integration of his parametric amplifiers, Christopher Eichler contributed in an essential way to the realization of the teleportation project. Gabriel Puebla-Hellmann was the fab expert in our group. I greatly appreciate his support, especially also in adapting his airbridge process to our needs. Jonas Mlynek was a great office mate. Together we were responsible for the Plassys evaporator who kept us busy with all his minor and major problems.

A very big "Thank you!" goes to the members of the "D 17"-office. In addition to Philipp and Yves, these are Anna Stockklauser, Arjan van Loo, Marek Pechal and Simon Berger. I will never forget the fun we had at the countless adventures, e.g. our never-ending victories at the AMP pub quiz, our training for the SOLA (together with Arkady), movie nights, concert visits and many more things. You made QUDEV a more nerdy and awesome place.

I also like to thank QUDEV's technical and administrative staff Hans Rudolf Aeschbach, Janis Lütolf, Gabriela Strahm and Francesca Bay for their help in various occasions and their contribution to the good atmosphere in the group. Thanks go to the post-docs Abdufarrukh Ab-

DUMALIKOV, JULIEN BASSET, MILAN ALLAN, MINTU MONDAL and STEFAN FILIPP for the various discussions about scientific and other matters during the time of my PhD. And thanks to all my friends from outside the lab for all the common activities.

My most sincere and heartfelt thanks go to my parents EDITH AND DANIEL STEFFEN, and my brother JAN for their great support at every stage of my life, and to SARAH for her patience, support and understanding.